COMPUTATIONAL MODELING OF STRUCTURAL DYNAMICS AND ENERGETICS OF TWO ALLOSTERIC PROTEINS:

Kinesins and Acetylcholine Receptors

by

Srirupa Chakraborty

October 2016

A dissertation submitted to the

Faculty of the Graduate School of the

University of Buffalo, State University of New York

in partial fulfillment of the requirements for the degree of

Doctor of Philosophy

For Maa, Baba, Didi and Anoop …

सा विद्या या विमुक्तये… विद्यान्या शिल्पनैपुणम् ।।
sā vidyā yā vimuktaye … vidya'nyā śilpanaipuṇam.

It is the pursuit of knowledge that liberates… all else are merely trivial skills.

-ancient Sanskrit saying.
(Origin: Mahapurana, ca. 400 BCE, estimated)

Acknowledgements

This discourse would be incomplete without me acknowledging some very important people, who have been such big driving forces towards the all-around realization of my work and this thesis.

Foremost, I would like to thank my advisors, Dr. Wenjun Zheng and Dr. Anthony Auerbach, for all their advice and support. Dr. Zheng’s patience with me during my initial days of learning, and all the scientific discussions I have had with him will be cherished by me. The most important skill which I hope I have been able to learn from him, is his attention to even the minutest detail, and I thank him for that.

I thank Dr. Auerbach for taking the leap of faith in me and agreeing to add a computational aspect in a traditionally well-known experimental lab. My time working with him have been wonderfully inspiring. Having gone through the rigors of the initial training already, I could spread my wings here. The daily discussions of science, both related to our work and otherwise, and Dr. Auerbach’s contagious enthusiasm, all honed my knowledge, ability and creativity.

I would also like to express my gratitude to my university and my department for providing all the wonderful research facilities and allowing the flexibility to perform cross-departmental research even at graduate level. My acknowledgements also to the Center for Computational Research at UB, not only for providing and maintaining the supercomputing facility, but also for keeping up with our constant demands of support with installing, updating or benchmarking different computational packages.

My earnest thanks to Dr. Arnd Pralle and Dr. Feng Qin – members of my thesis committee for going through my thesis and supplying immensely valuable advice and suggestions.

Coming to all my colleges and lab members – life and work would not have been as good without them. Mustafa, Jeffery and Minghui from the Zheng Lab, all of whom had taught me a lot in the field of computational biology. My juniors there – Paul, Sushree, Han Wen and Han Ding – hopefully I have been successful in sharing some of my knowledge with them. I know I ended up learning a lot in the process.

Prasad, Tapan, Iva, Ridhima and Shaweta from the Auerbach Lab – I cannot begin to tell how much each of them have helped towards this dissertation. Thanks to them, I could smoothly fit in within an experimental setting and pick up quickly on an entirely new system in the middle of my PhD years. My appreciation for bench-work has gone up manifold, by observing, learning and discussing with them. Moreover, the wonderful scientific discussions I have had with our neighbors, especially Phil and Krishna, have enhanced my graduate school experience.

To complement all this, was the constant support of some wonderful ladies – Jan, Marlene, Mary Meritt, Mary Jo, Mary Teeling and Bev. They made life wonderful on third floor Cary, with all their love, laughter, and general camaraderie.

Life at lab has of course been the prime focus for the past few years. But I have been lucky to have made some other wonderful friends that made life outside the lab amazingly fulfilling. Heartiest thanks and cheers to all my friends in Buffalo, for seeing me through it all.

The biggest driving force towards my work has been my family. My Maa, Baba and Didi, with their constant support and indulgence, have shaped my entire life, and now this thesis too. It is only fitting that I dedicate this work to them. If I can live and work to be the way they taught me, and, go even slightly close to how awesome my Didi is, I will consider myself successful. Lots of love and thanks also to my brother-in-law Tathagata Da, and my darling nephew Rio (in whom I see a little bit of myself and my childhood) – your thoughts have helped keep me going through bleak days. The same goes for my wonderful in-laws – Momsy, Popsy, for all their support, love and help. Thank you for being there. Arvind has become like a brother of my own, and it all began with life together at UB.

Lastly, but most importantly, thanks to Anoop, my husband, best friend, comrade-in-arms through the travails and travels of life. You have had my back through the thick and thin of my grad-days. I cannot imagine being able to finish this dissertation without your support and love. Thank you for everything.

My journey with the thesis has been long and humbling, and at the same time, extremely rewarding. I hope, along the way, I have been able to make a little outward dent in the periphery of human knowledge, however minute that may be. I also thank you, Reader, for picking this up for reading, and I look forward to hearing any suggestions, corrections or ideas that this may stimulate in you.

- Srirupa Chakraborty

Buffalo, NY

List of Abbreviations

ACh	Acetylcholine
ADP	adenosine diphosphate
AMD	accelerated molecular dynamics
ATP	adenosine triphosphate
CCC	cross-correlation coefficient
CMD	classical molecular dynamics
CNS	central nervous system
CSA	contact surface area
ECD	extracellular domain
EM	electron microscopy
GABAR	gamma-aminobutyric acid receptor
GluCl	glutamate gated chloride channel
HA	high affinity
HB	hydrogen bond
ICD	intracellular domain
iGluR	ionotropic glutamate receptor
KIN	Kinesin
KNF	Koshland – Nemethy – Filmer model
LA	low affinity
LGIC	ligand gated ion channel
MD	molecular dynamics
MT	Microtubule
MWC	Monod – Wyman – Changeux model
nAChR	nicotinic acetylcholine receptor
PCA	principal component analysis
PDB	Protein Data Bank
Pi	inorganic phosphate
RMSD	root mean squared deviation
RMSF	root mean squared fluctuation
SMD	steered molecular dynamics
TBS	transmitter binding site
TMA	tetramethyl ammonium
TMD	transmembrane domain
TMD	targeted molecular dynamics
ZAC	zinc-activated ion channel
5-HT$_3$R	5-hydroxytryptamine (serotonin) receptor

Table of Contents

Contents **Page No.**

Chapter 6: Investigating the Structural and Energetic Bases of the Differences between the Primary ATPase States of a Kinesin-Tubulin Complex by All-Atom Molecular Dynamics Simulation ……………………………..…………………... 59

Chapter 8: Structural correlates of affinity in fetal versus adult endplate nicotinic receptors …………………………………………………………………………………………. 130

List of Figures

Figure number and caption **Page No.**

List of Tables

THESIS SYNOPSIS

To quote famous physicist and Nobel laureate, Dr. Richard Feynman, "…everything that living things do can be understood in terms of the jigglings and wigglings of atoms." It is these jigglings and wigglings of atoms that form the focus of my dissertation, which studies the structural dynamics of two different allosteric proteins through computational simulations. Protein allostery is a field that has been investigated widely. But the structural details of how signals initiating at one site transmit through the network of residues in different proteins and result in the alteration of their functional states, still remains largely unresolved. Here, we independently study the kinesin motor protein and the neuromuscular acetylcholine receptor (nAChR) – both of which play crucial roles in cellular signaling. Kinesins are intracellular porters, carrying organelles, molecules and other cargo within the cell, while nAChRs are transmembrane receptors that aid in intercellular communication at nerve-to-muscle synapses. These two protein families are structurally and functionally very different, but both are allosteric in nature, with interesting protein dynamics that efficiently convert chemical energy to mechanical motions in order to perform their cellular functions.

The total timescale of an entire allosteric transition is currently too long for complete all-atom molecular dynamics simulations. Thus, in this dissertation, for both the projects, we begin at different equilibrium states of the proteins and carry out comparative analyses of conformation and dynamics at those states, which aids in elucidating the structural and functional correlates for these systems.

For the kinesin-microtubule (KIN-MT) system, we have built atomistic structure models for the key nucleotide-binding states of the kinesin-MT complex from lower resolution cryo-EM maps, by suitably modifying the MD potential with the EM map force. We have also studied ligand-protein (ADP/ATP-kinesin) interactions and predicted the sequence of structural changes in kinesin-MT complex during its conformational transitions between important biochemical states and pinpointed key contributing residues.

Simultaneously, we have also characterized the transmitter binding sites of neuromuscular acetylcholine receptors and analyzed the energy asymmetries between the fetal and adult endplate receptors. Through large-scale simulations of the fetal and adult binding sites, we have come across compelling evidence of the structural causes that explain these asymmetries and were successful in identifying the minimum construct that is both necessary and sufficient to exchange the function between adult and fetal binding sites in AChRs. Our *in silico* models and predictions act as important tools to further guide mutational and functional experiments.

.

Chapter 1: INTRODUCTION

Proteins are not the static objects we are generally used to seeing in pictures. They are instead dynamic entities, whose movements play fundamental roles in their functions. In fact, the dynamic nature of each protein imparts a ‘personality’ [1] and versatility to it, which is essential towards function. These dynamics vary in magnitude, from side chain rotations, fluctuations of loops and motifs, to large-scale domain motions, and span a wide spectrum of timescales, from picoseconds to milliseconds and even hours (Table 1.1). Since proteins are central to cellular function and perform crucial tasks in almost all biological processes, it is of utmost importance to try and determine their detailed structure *and* dynamics, in order to completely understand these processes.

Most proteins can exist in more than one geometric conformation, despite having the same atomic content. The modern generalization of Anfinsen’s dogma [2] is that, **a protein adopts an ensemble of structures, determined by its amino acid sequence and cellular environment.** The average of this large ensemble of conformations at equilibrium forms a *static picture* of the protein. These average static pictures are now known for a large number of proteins, thanks to the revolutionizing modern techniques of X-ray crystallography, nuclear magnetic resonance (NMR) spectroscopy, small-angle X-ray scattering and cryo-electron microscopy, which provide atomic and near-atomic level resolutions. However, these techniques do not always correctly mimic the cellular environment or provide answers about the dynamic and temporal behaviors of the protein.

The *dynamic picture* of a protein is determined by the variance within the equilibrium population of different conformers (thermodynamics) and the transitions over energy barriers between these conformers (kinetics) (Figure 1.1). Conditions in the cellular environment that may affect these two factors include temperature, pH, voltage, ionic concentration, binding of a ligand, etc. These conformers may be iso-energetic, in which case the protein usually exists as an ensemble of states that are in equilibrium with each other through thermal motions. Or, the conformers can be separated by energy barriers of different heights (Figure 1.1), thus having different probabilities of shifting between states. In that case, some external environmental change may provide the energy necessary to overcome the barrier. For many proteins, this external perturbation is in the form of an effector molecule binding.

Table 1.1: Hierarchy of protein dynamics (Gerstein et. al., 1994; Palmer, 2004; Bu Callaway, 2011)

Scale of motion	Function	Timescale	Amplitude
Local:	Ligand docking flexibility	fs to ps	
Atomic fluctuation	Thermal diffusion	$10^{-15} – 10^{12}$ s	< 1 Å
Side-chain motion			
Medium-scale:	Active site conformation adaption	ns to μs	
Loop motion		$10^{-9} – 10^{-6}$ s	1 – 5 Å
Helix motion	Hinge-bending		
Large-scale:	Ligand binding	μs to ms	
Domain motion	Allosteric transitions	$10^{-6} – 10^{-3}$ s	5 – 10 Å
Subunit motion			
Transition motion:	Ligand binding	ms to hours	
Helix-coil	Protein-protein interaction	$10^{-3} – 10^{4}$ s	> 10 Å
Dissociation/Association			
Folding-unfolding			

To understand proteins in action, one must study the time-dependent change in the atomic coordinates, including both equilibrium fluctuations and non-equilibrium transitions. Various experimental techniques and assays like fluorescence microscopy, FRET spectroscopy, electrophysiology, optical tweezers, quantum dots, etc. are used to study the effects of various perturbations (light, voltage, mutations, etc.) on the observable protein functions, and hence deduce reasonable conclusions about their dynamics. But **the ultimate goal would be to 'watch' proteins in real time at femtosecond and angstrom resolution.**

Computational studies of proteins can do this, by (i) using reasonably modeled static coordinates as a starting point, (ii) completely defining the potential energy and forces felt by each constituent domain and (iii) studying the precise positions of each domain as a response to the defined potential field and time. The domain size can vary from individual atoms to larger coarse-grained units, depending on the computational abilities and the phenomenon under study. Thus, *in-silico* analyses act as a third pillar to *in-vivo* and *in-vitro* measurements to understand protein dynamics, by making rational hypotheses as to how and why things move, and giving outlines to guide further experimental inquiries.

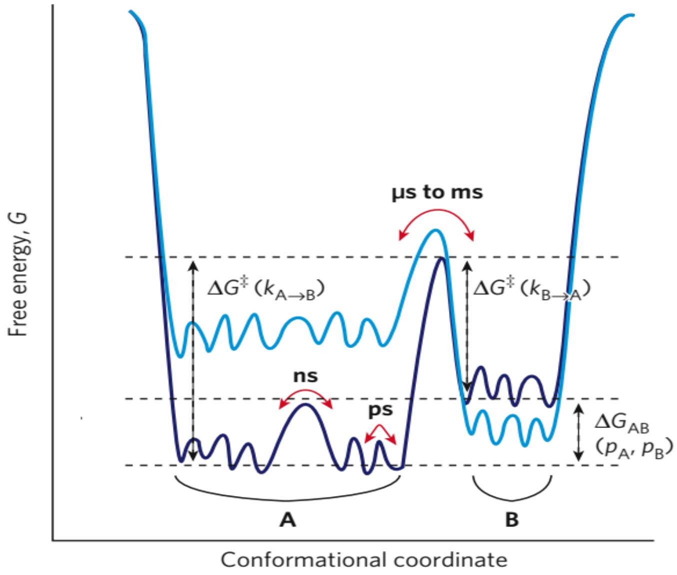

Figure 1.1: Representative energy landscape comparing the different orders of protein dynamics and energy barriers (Adapted from Kern *et. al*. 2007 [1]). The barriers $\Delta G^{\ddagger}$ determine the rate of interconversion between states. An external perturbation (like ligand binding) can be large enough to alter the landscape (from dark blue to light blue).

This dissertation deals with two independent projects, targeting two very important classes of proteins, using all-atom computational molecular dynamics simulations. The first project involves the study and characterization of kinesin (KIN) motor proteins, which are molecular nanomachines involved in many important cellular functions including cell division, transport of organelles, vesicles and other cellular cargo. In the second project, we have characterized the transmitter binding sites of neuromuscular nicotinic acetylcholine receptors (nAChRs) which are ligand gated ion channels that play an important role in nerve to muscle signaling. Both the systems are structurally and functionally very different, but both are allosteric in nature, with interesting protein dynamics that efficiently convert chemical energy to mechanical motions in order to perform their cellular functions.

1.1 - Objectives of this study

This dissertation has been able to address the following issues and objectives:

(1) Understanding the structural basis of kinesin-microtubule (MT) interactions by –

1. Building atomistic structure models for the key binding states of the kinesin-MT complex from lower resolution cryo-EM maps using MD simulations, by suitably modifying the MD potential with the EM map force.
2. Predicting the sequence of structural changes in the KIN-MT complex during its conformational transitions between important biochemical states.
3. Pin-pointing key residues that contribute to the KIN-MT and KIN-nucleotide binding.

(2) Analyzing the energy asymmetries between fetal and nAChRs by –

i. Building homology models of these ligand-binding interfaces from known AChBP structures, docking different agonists to the binding sites, and corroborating the *in silico* results by *in vitro* kinetic analysis.
ii. Studying the structural causes that explain the differences in ligand binding between these interfaces.
iii. Identifying the key contributing residues, their relative positions and orientations around the ligand and their correlations with the binding energies.
iv. Using simulations to get the minimum construct that is both necessary and sufficient to exchange the function between adult and fetal binding sites in AChRs
v. Identifying key structural factors that determine interactions between binding-site core residues and the surrounding residues not in direct contact with the ligand.

(3) Studying correlated harmonic motions between the M1 helix and the pore-lining M2 helix in the AChR transmembrane domain using a coarse grained elastic network model.

Chapter 2: LONG DISTANCE COMMUNICATION AND PROTEIN ALLOSTERY

When the perturbation by an effector molecule at one structural site leads to a functional change at a topographically distinct second site, it is called allosteric modulation. Allosteric regulation is an important mechanism of long distance communication in proteins and is very efficient in controlling various protein activities [3-5] including metabolic pathways, gene regulation and cellular signaling. It is an effective instrument by which the environment can affect function [6], equipping living organisms to adapt to changing conditions. Monod recognized the importance of this regulatory process [7] and described allostery as ‘the second secret of life’, the first of course, being the genetic code[8]. The term “allosteric” was initially coined to explain the mechanism of feedback inhibition in bacterial regulatory enzymes by ligands [9] – in contrast to direct or “steric” interaction. But it has now been extended to motor proteins, neurotransmitter receptors, and a large number of other proteins involved in communication within and in between cells.

According to the classical view, allosteric interactions, mediated by the binding of an effector molecule, leads to a series of discrete changes that alter protein structure and hence, function [10-12]. Quantifiable representations of allostery are given by the classic concerted Monod-Wyman-Changeux (MWC) model [13] and the sequential Koshland-Némethy-Filmer (KNF) model [14]. In contrast to the ‘induced fit’ theory of KNF model, where the fit occurs “only after a change in shape of the enzyme molecule had been induced by the substrate” [15], the MWC model proposed that, the conformational transition is established as an already existing equilibrium between the states, with the ligand selectively shifting the equilibrium towards one side. In the absence of ligand, the two states, R and R*, are conjectured to spontaneously transition between each other, which can be defined by an intrinsic equilibrium constant, E_0, called the allosteric constant.

2.1 – Theory of MWC model

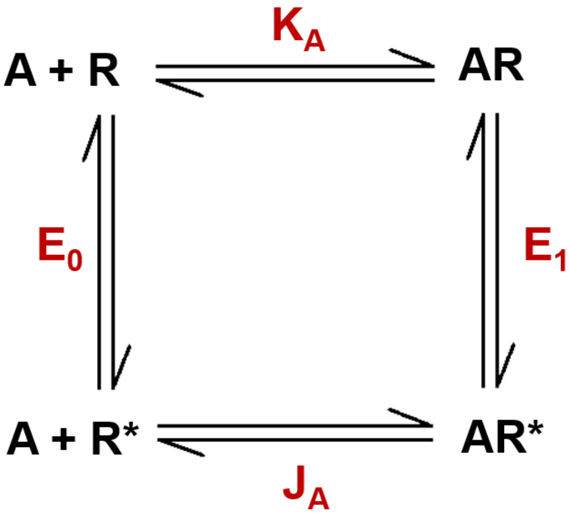

Figure 2.1: Thermodynamic cycle of two-state MWC model

The closed thermodynamic cycle of a simple two-state MWC model is shown in Figure 2.1. The four binding constants in Figure 2.1 are related, because the change in free energy during the R to AR* conversion must be the same, whether A binds to R, or R* activation happens first [16]. **The difference between the free energy of activation of R → R* in the presence versus absence of A, is a measure of allostery.**

$$E_0 = \frac{[R^*]}{[R]}; \qquad E_1 = \frac{[AR^*]}{[AR]};$$

$$K_A = \frac{[AR]}{[A][R]}; \qquad J_A = \frac{[AR^*]}{[A][R^*]};$$

∴

………………………. Eq. 2.1

$$\frac{J_A}{K_A} = \frac{[AR^*].[R]}{[AR].[R^*]} = \frac{E_1}{E_0} = \lambda$$

………………………. Eq. 2.2

λ, which is the ratio of activation of R → R* in the presence versus absence of A is called the **allosteric coupling constant**. If $\lambda > 1$, the effector causes increased probability of activation. If $\lambda < 1$, the effector causes decreased probability of activation. If $\lambda = 1$, A and R are not allosterically coupled.

If the biological response of the system is a measurable observable, all the parameters defining the MWC cycle can be calculated from the equations above. Going by the conjecture that the biological response, f_R^* is proportional to the fraction of receptors in the activated state, we can write [17]:

$$f_R^* = \frac{[R^*] + [AR^*]}{[R] + [AR] + [R^*] + [AR^*]}$$

………………………. Eq. 2.3

Using equations 2.1 and 2.2 in equation 2.3,

$$f_R^* = \frac{E_0[R] + E_1K_A[A][R]}{E_0[R] + E_1K_A[A][R] + [R] + K_A[A][R]}$$

Cancelling [R] and rearranging, we get response, f_R^*, in terms of agonist concentration [A], as:

$$f_R^* = \frac{E_0 + E_1K_A[A]}{1 + E_0 + K_A[A] + E_1K_A[A]}$$

………………………. Eq. 2.4

Equation 2.4 gives the typical sigmoidal dose-response of observable biological response as a function of the logarithm of agonist concentration, as shown in Figure 2.2. This sigmoidal curve has three points of interest. The basal activity at [A]→0, where equation 2.4 is reduced to:

$$f_R^*(basal) = \frac{E_0}{1+E_0}$$

……………………… Eq. 2.5a

If E_0 is smaller than the experimentally measurable resolution limit, $f_R^*(basal)$ effectively reduces to zero. The maximum activity at **[A]→∞**, gives the efficacy of the agonist.

$$f_R^*(maximal) = \frac{E_1}{1+E_1}$$

……………………… Eq. 2.5b

The efficacy is equal to $\frac{E_n}{1+E_n}$ for a (n+1)-state system.

At midpoint, where activity is half-maximal, $f_R^*(half\ max) = \frac{1}{2}[f_R^*(basal) + f_R^*(maximal)]$. This point is determined by the agonist concentration, EC_{50}.

$$[A]_{midpoint} = \frac{(1+E_0)}{K_A(1+E_1)}$$

……………………… Eq. 2.5c

Keeping in mind equation 2.2, E_0 and E_1 can be expressed in terms of each other in these series of equations, since they are related by the coupling constant. These equations and the concept of the coupling constant will be recalled again when we discuss nAChRs (page 35). It must be noted here that **as a corollary of the MWC model, the spontaneous R↔R* equilibrium can be shifted not just by ligands, but by mutations too.**

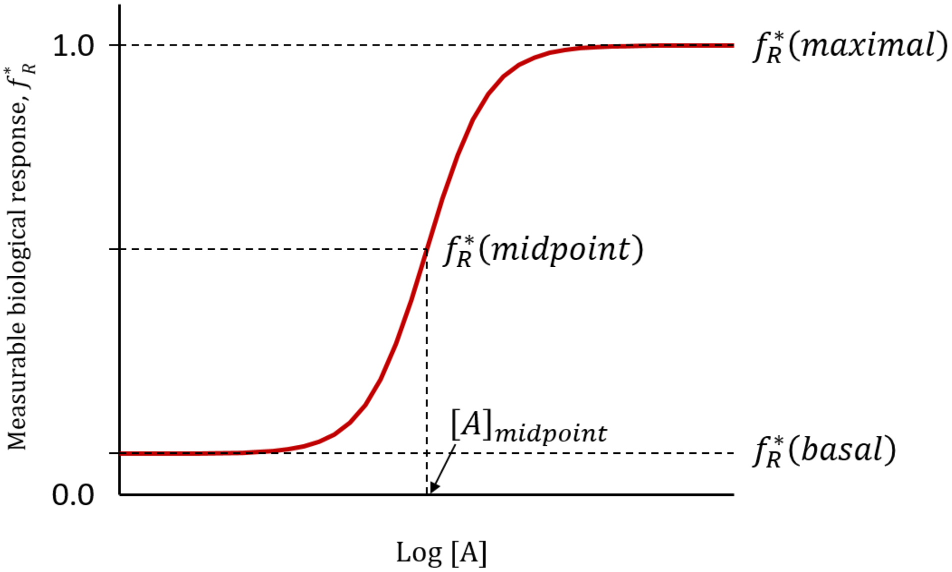

Figure 2.2: Typical dose response curve of an allosteric system (inspired from Tsai et. al., 2014 [17]).

Allostery being fundamentally thermodynamic in nature, long-range information propagation may be mediated not only from a change in the protein conformation and bonding interactions (enthalpic contribution) but also from a change in the dynamic fluctuations about the mean position (entropic contribution) [18-20]. In fact, experimental evidence backs the idea that allostery can even be solely entropy-driven by changes in protein dynamics [21]. Therefore, summarizing the modern view of allostery, (i) the native state is an ensemble of conformations instead of a structure; (ii) the allosteric perturbation can not only be brought about by the binding of a molecule, but also by other changes in the environment like pH, temperature, voltage, ionic concentration, covalent modifications like glycosylation, phosphorylation, tethering, etc; (iii) spatially separated sites can be energetically coupled; and (iv) the strain energy from the perturbation event can be relayed to the functional site by enthalpy, entropy or a combination of both.

This long distance communication is brought about by transfer of energy through quaternary (large-scale collective), tertiary (residue-wise interactions) and backbone network of motions [22]. Modulating these responses hold promise for drug design. But details of how signals arising due to a perturbation can transmit through the structural network still remains elusive. As shown in Table 1.1, the total timescale of an entire allosteric transition is too long for complete all-atom molecular dynamics simulations (with standard computational power). Thus, in this dissertation, for both the kinesin-MT system and the nAChR ligand binding, we begin at different equilibrium states and carry out comparative analyses of conformation and dynamics at those states, which sheds light in the structural and functional correlates for these systems.

Chapter 3: KINESIN MOTOR PROTEINS

Motor proteins are enzyme-based molecular nanomachines that power most of the movements by living organisms. A common feature that they share is that they can convert the chemical energy of ATP (or GTP) hydrolysis (Figure 3.1) to mechanical work, and result in producing coordinated, directed (oftentimes macroscopic) motions. These motor proteins are some of the most efficient known energy transducers and have been well studied, though the exact structural details of how they work still remains an outstanding mystery.

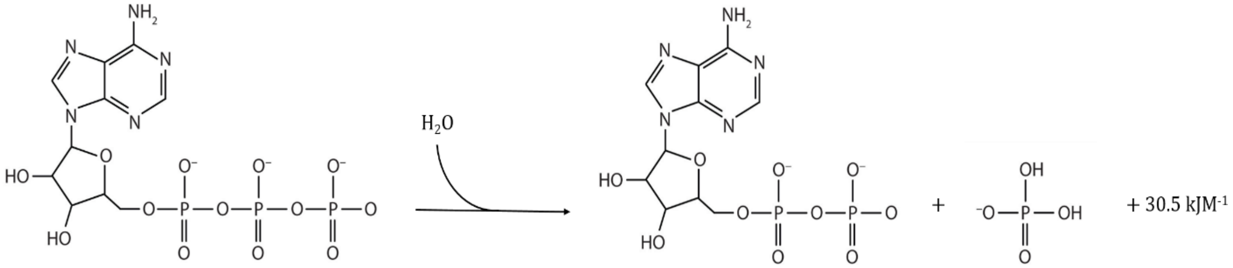

Figure 3.1: ATP to ADP hydrolysis reaction leads to release of 30.5 kJ M^{-1} of energy, which is utilized to perform mechanical work by motor proteins.

Dozens of different kinds of motor protein coexist in every eukaryotic cell and are usually associated with the cellular cytoskeletal filaments - actin or microtubules. The myosin-superfamily [23] of motor proteins are actin-associated, and are crucial for bringing about muscle contraction. Their study dates back to 1864 [24] and have served as model systems to study motility for decades. Kinesins [25] and dyneins [26] are the microtubule associated motor proteins, participating in cargo transport. The motor protein system is critical for the cellular organization and function, breakdown of which leads to diseases like Alzheimer's, and also acts as tools for developing powerful anticancer agents.

3.1 - Microtubules

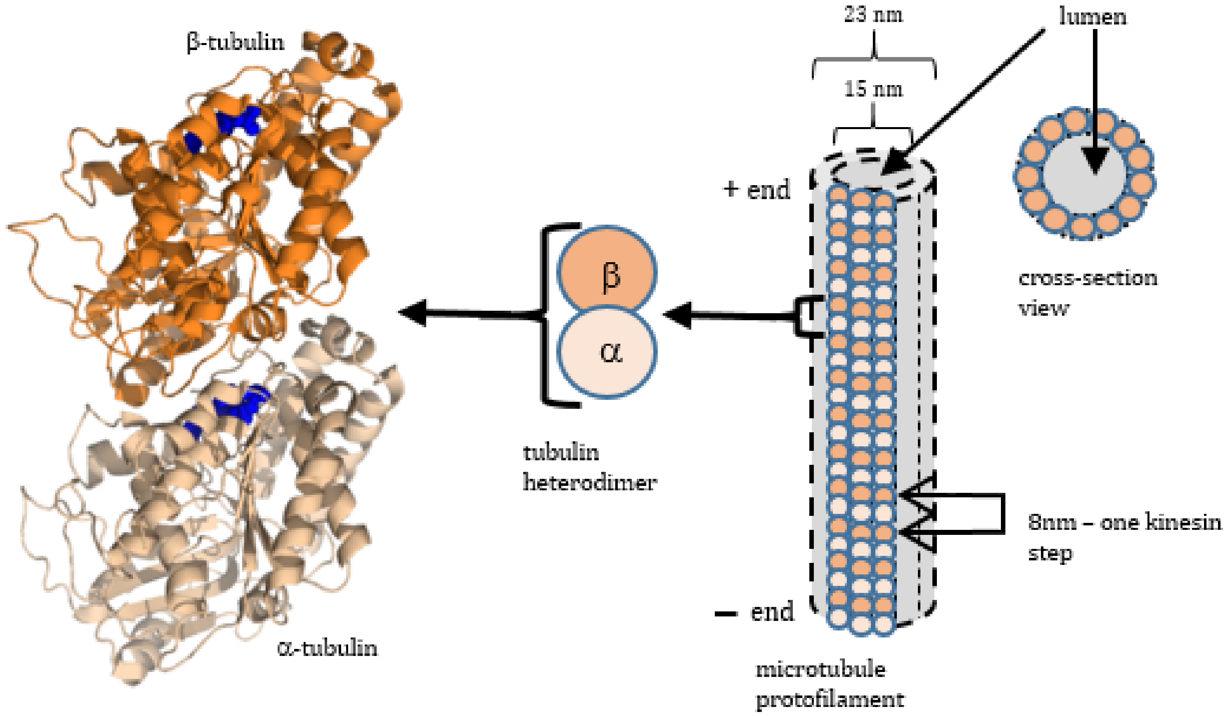

Figure 3.2: Microtubule assembly on proto-filament. β-tubulin is at plus end and α-tubulin at minus end. Cartoon protein structure of tubulin heterodimer is from bovine microtubule (PDB ID: 1JFF). Blue spheres represent the vdW radii of nucleotide atoms in each tubulin. It cycles between GTP and GDP to sustain MT growth.

Microtubules are filamentous tubular structures that are an essential part of the cytoskeleton. These filaments are ~23 nm in diameter and built from 13 parallel protofilaments, each composed of alternating α-tubulin and β-tubulin proteins, tightly bound together by noncovalent bonds [27] (Figure 3.2). Each of the subunits in the protofilament point in the same direction, rendering a distinct structural polarity to microtubule, with α-tubulins exposed at the 'minus'-end (center of the cell) and β-tubulins exposed at the 'plus'-end (periphery of the cell) [28]. The microtubule network radiates outwards from the central nucelus, acting as tracks for a molecular-scale "railway" network [29] , on which kinesins and dyneins haul their cargoes.

3.2 - Kinesins

The kinesin superfamily was first identified in the giant axon of squid in 1985 [30] using *in vitro* motility assays, laying aside a long-standing misconception that transport of material within the cell cytoplasm is simply diffusion-driven. Functionally, kinesins are responsible for a wide variety of tasks [31] – intracellular transport of cargo including vesicles and organelles, cytoskeletal reorganization, mitotic and meiotic spindle formation and chromosome segregation. In contrast to dyneins that move to the microtubules' minus end, kinesins mostly show 'anterograde transport', moving towards the plus end and transporting material from inside the cell to outside [31]. The kinesin superfamily is large, with at least 14 distinct families and hundreds of subtypes. As an illustration to the types of kinesin proteins, the yeast *Saccharomyces cerevisiae* has 6 distinct kinesins, the nematode *Caenorhabditis elegans* has 16 kinesins and the human genome has about 45 distinct kinesin genes [32]. Of these, kinesin-1, also called KIF5 or the conventional kinesin, is the best studied, and is known to work against a load of up to ~7 pN [33]. There are a lot of variations from the general properties, within this large super-family. Some kinesins like *Drosophila* NCD, budding yeast KAR3, etc. have the motor domains at the C-terminus and walks in the opposite direction (plus to minus end). Some kinesins lack a coiled-coil region and function as monomers. Some others are heterodimers. However, the conventional kinesin (kinesin-1) can be considered as a good prototype, and was our target system.

3.2.1 - Kinesin structure:

Almost all kinesin proteins have a similar core structure, common also to the myosin core, and have comparable conformation change strategy, indicating a common evolutionary origin [34]. The conventional kinesin exists as a dimer (Figure 3.3), with each monomer consisting of a head group or catalytic core domain which binds to the microtubule and exhibits ATPase activity [35], a neck linker functioning as a mechanical amplifier [36], a coiled-coil stalk domain for dimerization, and a tail domain for cargo binding. There are two kinesin-light- chains (KLC) associated with this heavy chain dimer that they act as adapter molecules for the cargo [37].

The conventional kinesin dimer ‘walks’ stepwise on the microtubule tracks in a ‘hand-over-hand’ manner [38], and is highly processive [39], having the ability to take several hundred steps before detaching. Each step size utilizes 1 ATP molecule hydrolysis and is about 8 nm [40], which is the exact distance between two neighboring tubulin dimers. The speed varies widely between different kinesin proteins, ranging from 0.02 to 2 μm/s, with conventional kinesin-1 known to have an average *in vitro* velocity of ~800 nm/s [41], indicating it can take 100 steps each second (~10ms/step). This leads to the required rapid transport of the kinesin cargo – mitochondria, secretory vesicles, various synaptic components, over long distances down the microtubule. The different domains of the kinesin-1 core is given in Figure 3.4, along with the residue numbers.

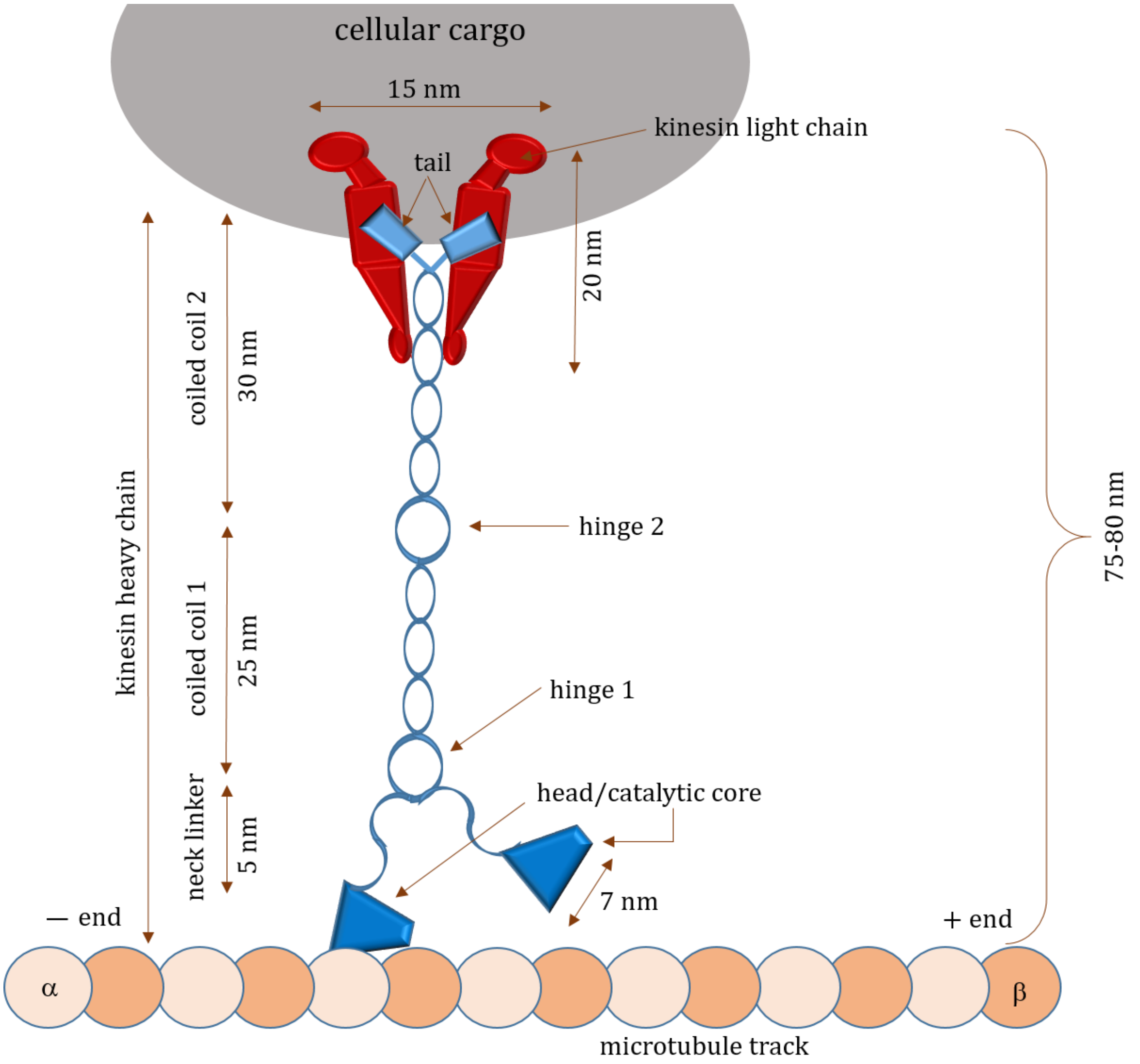

Figure 3.3: Diagrammatic representation of conventional kinesin model. Details of each structural domain and their geometric dimensions shown here [42] have been determined by X-ray diffraction, optical trap and other single-molecule experimental techniques.

Switch I, switch II and P-loop are involved in nucleotide binding. The switches also act as gates and sensors for nucleotide entry, release and hydrolysis. The α4 helix, loops 7, 8, 11, 12 are involved with microtubule association. The α6 helix attaches to the neck linker which can become structured (docked along the central beta-sheet) or unstructured (undocked) as the kinesin cycles through its various nucleotide-bound states. The highly conserved relay or α4 helix was found to have different orientations and conformations in the crystal structures of kinesin (without MT) and may have a role in the communication between the nucleotide and MT binding sites.

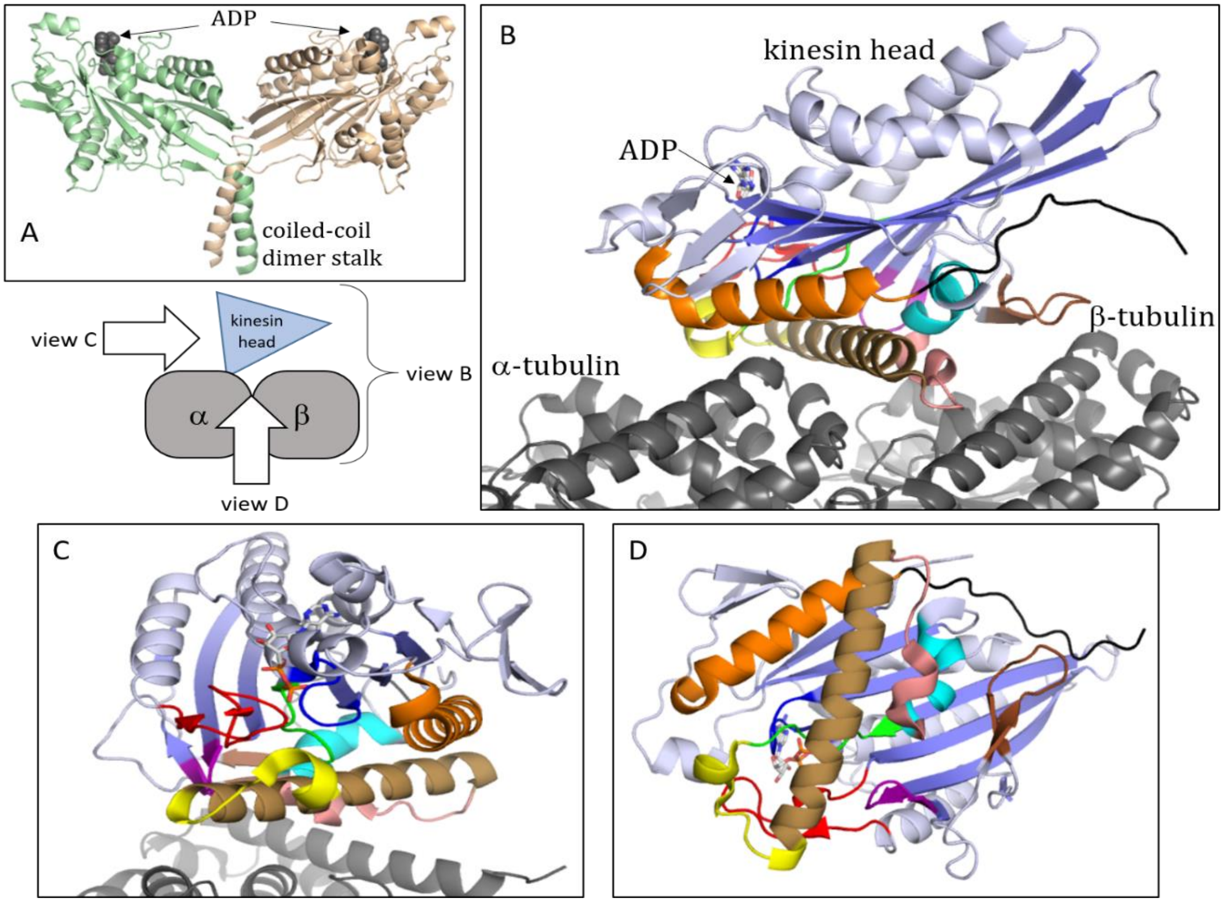

Figure 3.4: Structural details of human kinesin-1 catalytic core domain. (A). Dimer structure of kinesin head (PDB ID 2Y65). ADP molecules shown by grey spheres. (B, C, D). Views of a monomeric kinesin head (PDB ID 4HNA) from 3 different orientations as shown in the schematic. B – Side view with MT heterodimer (grey) at the bottom of the panel. C – view from the back of the kinesin head looking towards the direction of motion. D – Bottom view, looking at the MT-binding interface of kinesin. The colors used here will be maintained in the rest of the thesis unless otherwise mentioned. Green: P-loop (res. 85-92); red: Switch I (res. 190-204); dark blue: Switch II (res. 231-236); purple: loop-7 (res. 138-142); tan: loop-8 (res. 155-165); yellow: loop-11 (res. 237-246); tan: α4 helix (res. 247-271); pink: loop-12 (res. 271-281); cyan: α5 helix (res. 282-290); orange: α6 helix (res. 300-325) black: neck linker (res. 236 onward). ADP molecule is shown by sticks. The extended β-sheet domain is highlighted in light blue.

Kinesin activity must be regulated to prevent unnecessary usage of ATP or blocking of microtubule tracks. Studies have unraveled that this regulation is through a mechanism of ‘autoinhibition’ [43-45], where the kinesin tail folds back on itself and binds to the MT binding site, undergoing an overall quarternary structural change from an extended active conformation at high ionic concentrations to a folded inactive conformation at physiological concentrations.

3.2.2 – Kinesin biochemical pathway:

Numerous studies have finally led to a model of the kinesin walking, by a ‘mechano-chemical coupling’ mechanism [46]. The primary biochemical pathway is outlined in Figure 3.5, which has been obtained through various kinetic studies [47, 48]. Cycling through these biochemical states, the kinesin head undergoes a series of conformational changes brought about by allosteric coupling between nucleotide and microtubule binding. Of the three main MT-bound states, (ATP bound, ADP bound and nucleotide-free APO states), the ATP and APO states have strong MT binding, while the binding of MT in the ADP state is very weak. Through extensive experimental assays such as radio-labelling, crystallography, NMR, cryo-EM spectroscopy, and single-molecule optical trap studies, much has been unraveled about kinesin functioning. It is now understood that, the protein cycles through filament binding, conformational change, filament release, conformational relaxation, and filament rebinding, that requires a series of highly coordinated allosteric steps where nucleotide, kinesin head and microtubule work in close partnership.

I will go over the currently established kinesin-walking model [49, 50] step by step (Figure 3.5):

i. In solution, both kinesin heads contain tightly bound ADP (**K-ADP** state), and moves randomly by Brownian motion.
ii. When one head encounters a microtubule, MT-stimulated ADP release occurs [51] leading from **M-K-ADP** to a strong MT-binding APO state (**M-K**).
iii. This is followed by ATP binding (**M-K-ATP** state) at that MT-bound head. This is believed to trigger force generation via docking of neck linker along the catalytic core domain [36, 52]. This flings the unbound trailing head forward, on to the next kinesin binding site on the microtubule (8 nm away).
iv. ATP hydrolysis occurs in the first head (which is now the trailing head), forming intermediate **M-K-ADP-Pi** state, and subsequent γ-phosphate Pi release and neck linker undocking, finally leading to the **M-K-ADP** state again, where MT is weakly bound. Meanwhile, the leading head has reached step (ii) and the cycle continues.

There are a few important features to note here. The leading head must remain bound to MT until the trailing head detaches, ‘zippers’ forward and rebinds to the next MT site in front. Also, the two heads are always in different nucleotide states to keep the processive kinetic cycle going. The two heads function independently in solution, suggesting MT plays an important role in bringing about the coordination. The neck linker and coiled-coil domain seem to coordinate the mechano-chemical cycle of the heads and also determine the directionality of motion, through docking and undocking (order-disorder transition). The small movements in the switch loops at the nucleotide binding site determines the docking and undocking of the neck linker at a distance (~20Å). Thus, small conformational changes (angstrom-scale) are amplified through the motor head, to bring about neck linker docking and subsequent ‘zippering’ forward of the trailing head (nanometer-scale).

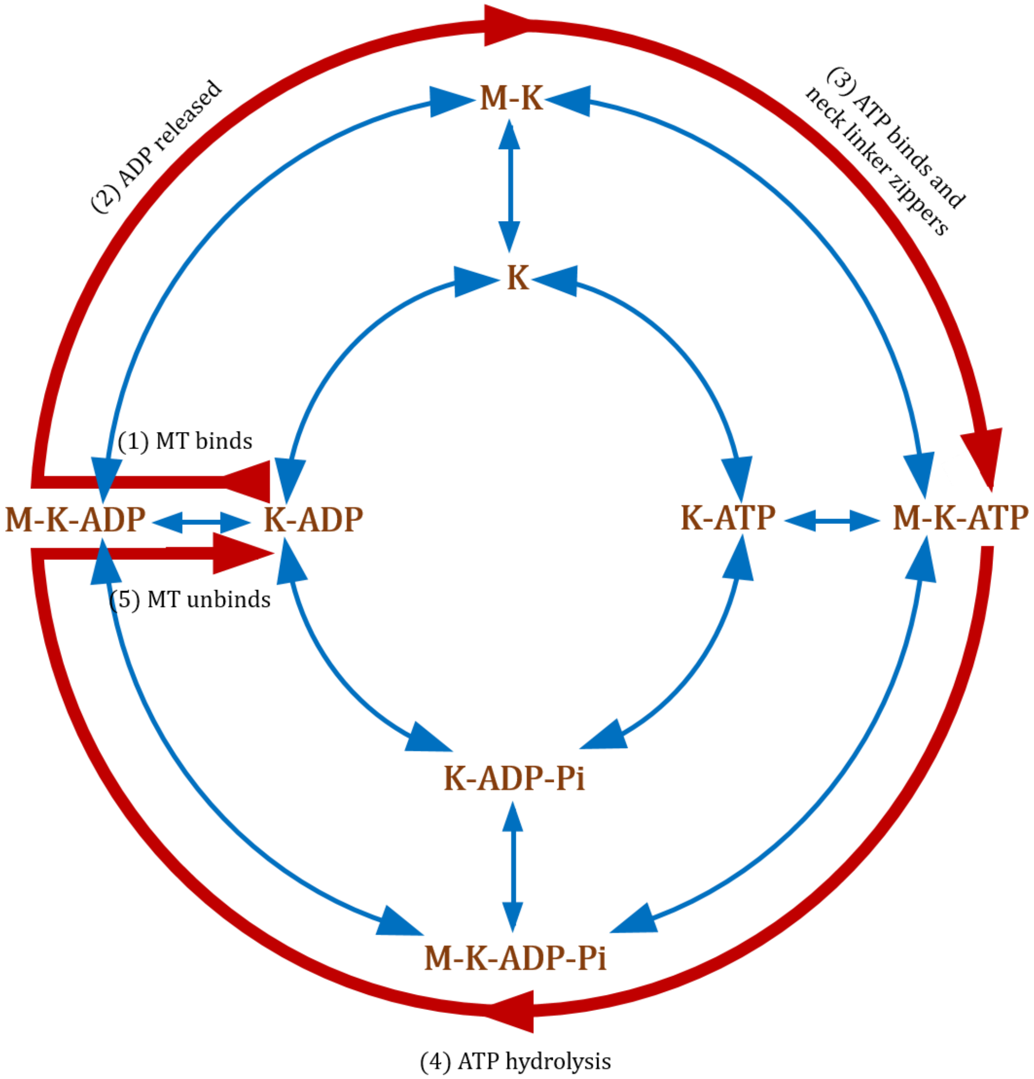

Figure 3.5: Primary biochemical cycle of kinesin – microtubule complex. The physiologically relevant pathway is marked in red.

In order to fully elucidate the fundamental basis of this long-distance transmission and amplification of information, we need to know the structural details of the important biochemical states. However, it has been extremely difficult to obtain high resolution structural and dynamic information. As outlined in the kinesin-walking algorithm, MT binding is very important for key kinesin processes, including MT-simulated ADP release, ATP-induced force generation and active detachment of kinesin from MT. Despite intense efforts by structural biologists, kinesin crystal structures have been solved almost always in the absence of MT. Only recently have MT-attached structures been obtained for ATP-analog state (PDB ID 4HNA [53] in the year 2013) and APO state (PDB ID 4LNU at the beginning of 2015, after the work shown in the thesis was already published). Even with these structures there are considerable uncertainties, as the crystallization was carried out in the presence of synthetic DARPIN construct, and on single tubulin dimer instead of long filaments. The tubulin in these PDB structures seems to be more curved than when in a microtubule filament, as shown by cryo-EM maps.

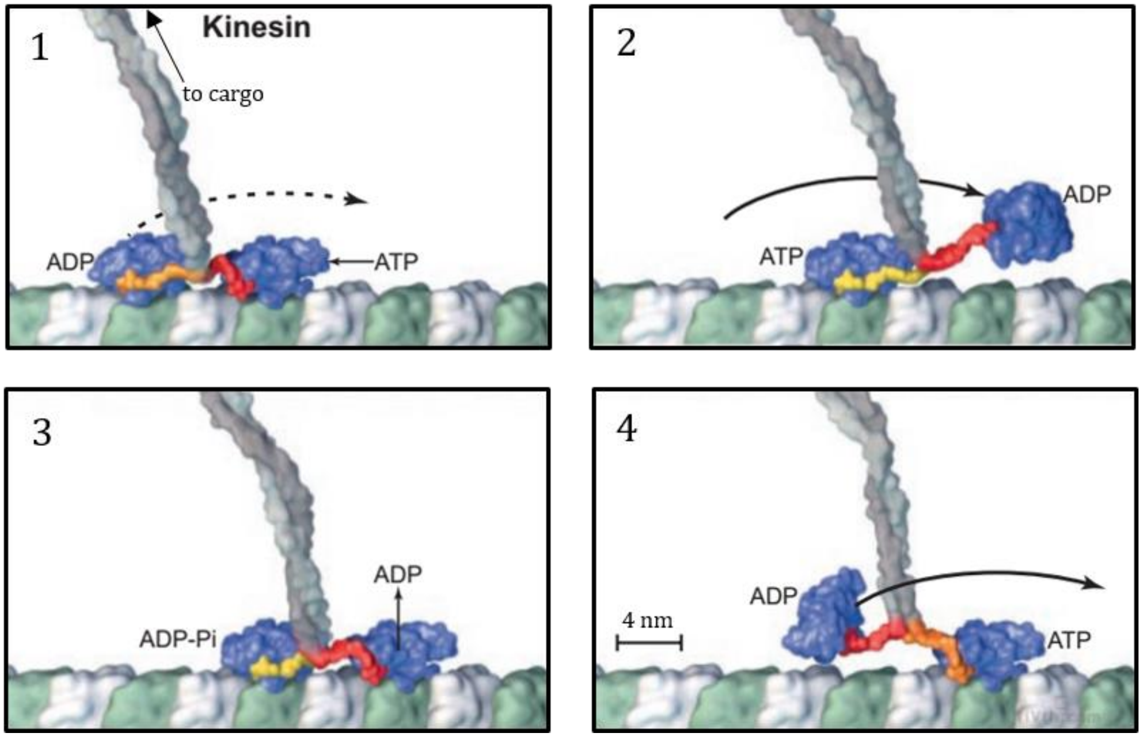

Figure 3.5: Model of conventional kinesin forward-stepping (adapted from Vale & Milligan, *Science*, 2000 [50]). Grey coiled-coil stalk leads up to the tail domain and cargo (not shown in figure). Kinesin catalytic heads (blue) bind to MT dimer (green, β-subunit; white, α-subunit). The two neck-linkers are shown in orange and red. Docked neck-linker shown in yellow. (1) Trailing head is ADP-bound. ATP binds to leading head and causes neck-linker to dock. (2) Trailing head zippers forward and becomes the leading head. (3) ATP hydrolysis leads to K-ADP state which does not bind tightly to MT. (4) Trailing ADP-bound head unbinds from MT and a forward-step is complete.

To solve the enigma of extensive communication and allosteric coupling between nucleotide binding site and MT binding site, a synergistic interplay between computational simulations and experimental investigations, is required. To this end, we built atomistic structural models for key kinesin-MT states, and identified residues and domain motions that drive this coupling which can be further tested by experiment.

Chapter 4: NEUROMUSCULAR ACETYLCHOLINE RECEPTORS

Motor proteins mediate transport and communication within a cell. But how about communication between cells? To that end, a high speed mechanism has evolved in which the transmitting cell releases a chemical signal, which diffuses to the receptor proteins on the target cell membrane, eliciting a suitable response. The ligand-gated ion channel (LGIC) superfamily is a principal example of such synaptic receptors, mediating intercellular communication, by rapid conversion of a chemical signal from a presynaptic cell to an electrical flux in a postsynaptic cell. There are broadly three categories of LGICs – the trimeric P2X receptors where ATP is the ligand, the tetrameric ionotropic glutamate receptors (iGluR), and the pentameric 'Cys-loop' receptors [54] comprising of the glutamate-gated chloride channel (GluCl) in invertebrates, the anionic γ-aminobutyric acid (GABA) and glycine receptors, and the cationic nicotinic acetylcholine receptors (nAChR), 5-hydroxytryptamine receptors (5-HT3 R) and the zinc-activated channels (ZAC). These are called 'Cys-loop' receptors, due to the presence of a signature loop of about 13 residues in the extracellular domain, flanked by two cysteines that are crosslinked by a disulphide bridge. All subunits of the pentameric LGIC superfamily are homologous and bear this canonical cys-loop motif, suggesting a common evolutionary ancestor [55].

4.1 – Neuromuscular communication and nAChRs

Of all the LGICs, nAChRs have been the best studied with regard to function, and are present in a variety of synapses – neurons of the Central Nervous System (CNS), in autonomic ganglia, and the neuromuscular junction. The name ‘nicotinic’ comes from the fact that these receptors can bind and be stimulated by the alkaloid nicotine, as opposed to the other ‘muscarinic’ type of AChR (a G-protein coupled receptor) that responds to muscarine instead. Though acetylcholine released from a nerve terminal acts as the physiological ligand, these ion channels can be modulated by a large variety of other small molecules, making it a target for toxins and drugs. Of these, the neuromuscular nAChR has been an important case study, and plays a crucial role in mediating fast signal transduction from motor neurons to skeletal muscles, ultimately working towards bringing about muscle contraction. These receptors are densely packed on the skeletal muscle plasma membrane at the neuromuscular junction, at more than 10,000 receptors per μm^2 [56]. To better understand the function of this protein, let me review the cascading sequence of events [57] that occur during neuromuscular signal transduction (Figure 4.1).

1. An action potential reaches the nerve terminal and the plasma membrane is depolarized.
2. This depolarization triggers opening of voltage gated Ca^{2+} channels. Influx of Ca^{2+} ions occurs along the concentration gradient from outside to inside the terminal.
3. Increased Ca^{2+} ion concentration prompts ~100 vesicles containing ~10^3 to 10^4 neurotransmitter acetylcholine molecules each [58] to fuse with the presynaptic membrane and release a pulse of acetylcholine in the synaptic cleft [59].
4. The released acetylcholine molecules travel across the synaptic cleft (~ 20 to 50 nm) by diffusion and bind to AChRs on the post-synaptic muscle membrane. These cation channels transiently open, Na^+ ions flow in and K^+ ions flow out due to respective concentration gradients. Since this gradient is higher for Na^+ than for K^+, there is a net inward flux of positive charge, causing a local depolarization.

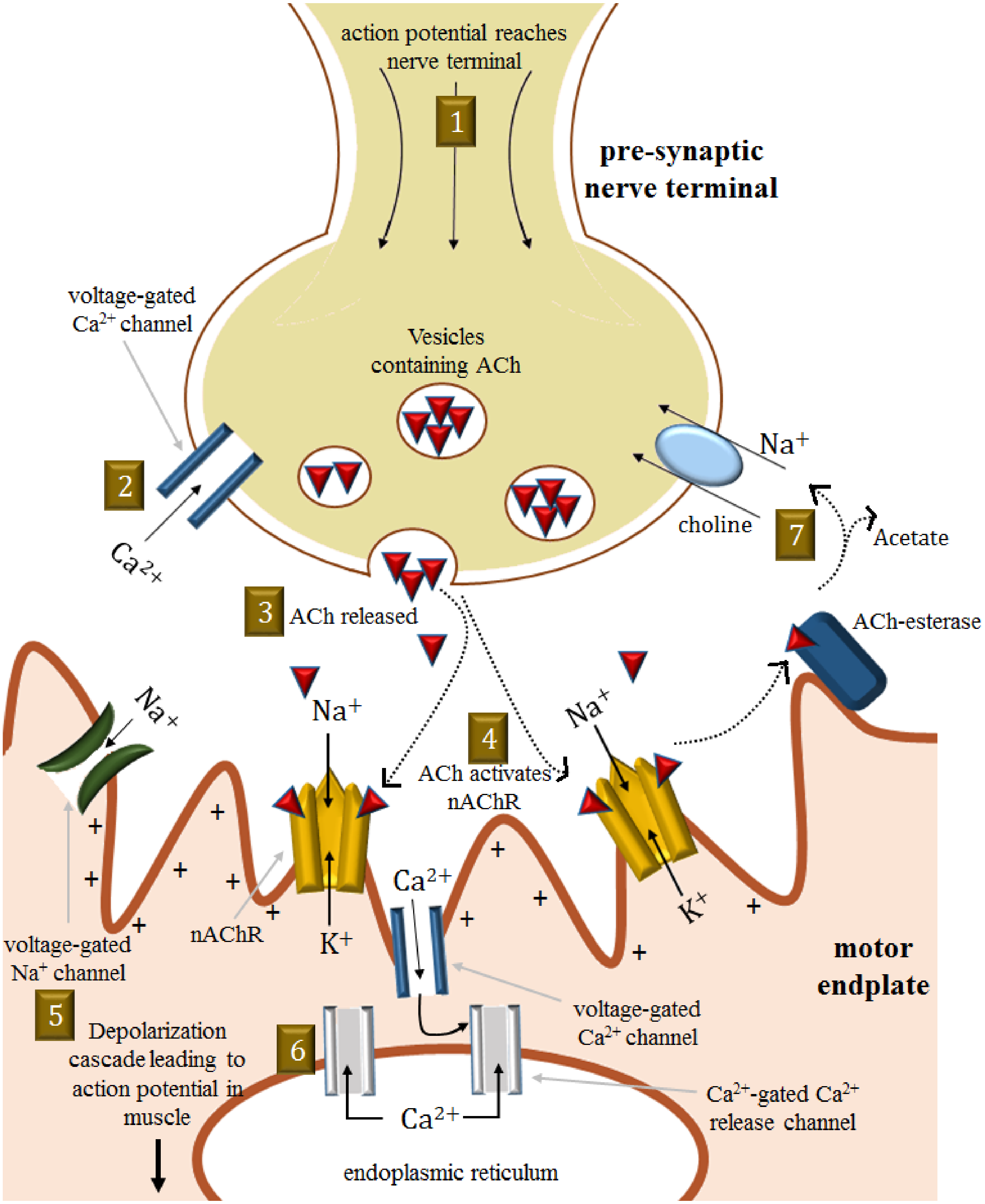

Figure 4.1: Schematic diagram of events at a neuromuscular junction. The numbers given here follow the sequence of steps outlined in text.

5. If the threshold potential is reached by the depolarization, voltage gated Na^+ channels are activated. More Na^+ ions enter the cell and the membrane is further depolarized. This depolarization self-propagates by opening other neighboring Na^+ channels, and thus spreads across entire muscle membrane.
6. Voltage gated Ca^{2+} channels are opened by this surge of depolarization, triggering further Ca^{2+} gated Ca^{2+} channels on the ER, bringing about the necessary cytoplasmic Ca^{2+} concentration for myofibril contraction.
7. Meanwhile, the acetylcholine molecules are removed (in ~ 0.2 ms) from the synaptic cleft by diffusion or broken down into ACh hydrolysis products (choline and acetate), and reused and recycled by the nerve terminal.

4.2 – Historical importance of neuromuscular AChRs

After being postulated as a protein (Nachmansohn, 1955) and biochemically characterized by Changeux, Kasai & Lee (1970), the neuromuscular AChR has borne titles of many firsts in ion channel history. It was the first ion channel whose single open-channel conductance was recorded (Neher and Sakmann, 1976), the first ion channel gene to be isolated, cloned and sequenced (Noda *et. al.*, 1982), the first to be expressed in foreign cells by mRNA injection (Mishina *et. al.*, 1984), and the first to be reconstituted into synthetic lipid bilayer (Montal *et. al.*, 1986). The reasons for this rapid progress in its characterization could be due to the ease of obtaining large quantities of the protein. The electric organs of the electric eel (*Electrophorus*) and electric ray (*Torpedo*) are rich sources of this receptor, having a density of ~16,000 per μm^2 [60]. Moreover, neurotoxins like a-bungarotoxin binds with high affinity ($K_d=10^{-8}$ to 10^{-12} M) [61] and specificity [62], making it easy to extract the protein by chromatography.

4.3 – Structure of nAChRs

Despite these swift advancements in deducing nAChR properties, a complete atomistic structure determination has remained elusive. Its large size, heteropentameric quaternary structure and hydrophobic nature of the transmembrane region makes it difficult to obtain well-diffracting crystals for X-ray crystallography. Other direct and indirect methods, like freeze-fracture micrographs (as far back as 1978) [63], cryo-electron microscopy [64] and extraction with subunit-specific antibodies [65] have resulted in the overall structure being known, albeit at a low resolution, for quite some time. Then, further refinements of the cryo-EM technique has led to a 4Å resolution structure determination (PDB ID 2BG9) of the Torpedo AChR in 2005 [66]. This resolution is good enough to localize the secondary structures, and even though there may be some uncertainties in the loops and exact helix locations, it has given an abundance of information regarding the structural details. Moreover, high resolution x-ray crystal structures of acetylcholine binding proteins (AChBP) which are soluble homologues of the AChR extracellular domain, (PDB ID 3WIP from *Lymnaea stagnalis* [67] and PDB ID 2BYQ from *Aplysia californica* [68] for example) crystal structures of prokaryotic relatives of AChR – the ELIC (PDB ID 2VL0 [69], 3RQW [70] and GLIC (PDB ID 4HFI [71], 4NPQ [72]) proteins, and more recently, *C. elegans* glutamate-gated chloride channels (GluCl) (PDB ID 3RIF, 3RHW, 4TNW, 4TNV) in various open and closed forms [73, 74] among others have shed light on the structural details of nAChRs.

It is now known that the receptor is a large 290 kDa cylindrical glycoprotein [75], approximately 8 nm in diameter and ~12 nm in length, with a large extracellular domain, a transmembrane domain and an intracellular region, all surrounding a central ion permeation pathway. As opposed to neuronal AChRs, which can be both homopentamers and heteropentamers, the muscle-type AChRs form a heteropentameric system consisting of two α

subunits, a β subunit, a δ subunit, and a γ subunit [76]. The γ subunit is replaced by a homologous ε subunit in adult mammalian or amphibian muscle cells [77]. These subunits are assembled in a stoichiometric ratio of 2:1:1:1 and share about ~40% sequence identity with each other [78]. The arrangement of the subunits is clockwise in the order α–ε/γ–α–β–δ (Figure 4.2) around a pseudo five-fold symmetry axis [60].

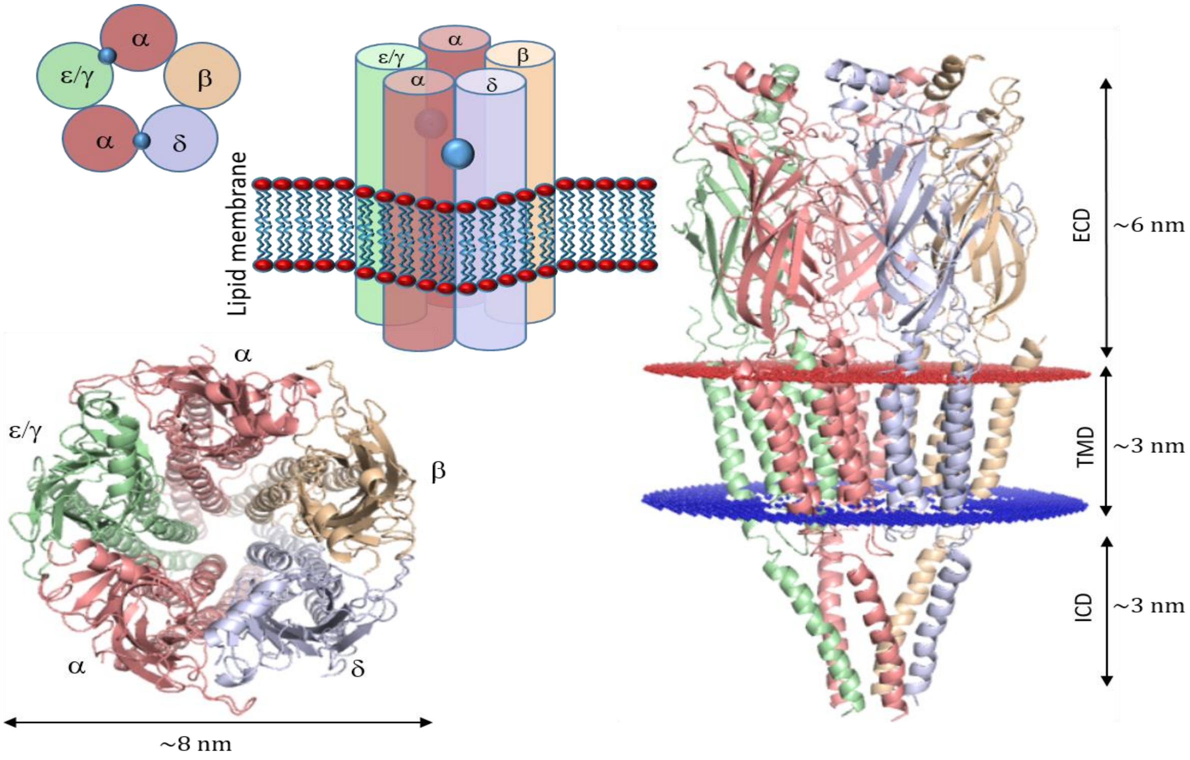

Figure 4.2: Representation of overall structure of AChRs. 4A resolution *Torpedo* AChR (PDB ID 2BG9) shown. Top view on left and side view on right. The schematic diagram shows the order of the chains and positions of transmitter binding sites (blue spheres). The lipid-embedded TMD region location is identified by OPM database and denoted by the blue and red boundaries.

The transmembrane domain consists of 4 hydrophobic helices (M1-M4) joined by short hydrophilic loops or 'linkers'. Of these, the M2-M3 linker at the ECD-TMD interface is suspected to play a role in coupling between agonist binding and gating [79]. The large and variable M3-M4 linker is more than 100 residues long and is important for efficient subunit assembly [80] and the locational distribution of receptors on the cell surface [81]. The M2 helix from each of the subunits line the channel lumen [82], which forms a narrow pore in the transmembrane region but expands to wider vestibules above and below. Clusters of negatively charged residues in M2 line the pore on both ends [83], and help in preventing negative ions from passing through. Orientations of the residues also help in forming the size selectivity filter, cutting off ions above 0.65 nm diameter [84], thus restricting the physiological traffic to Na^+, K^+ and Ca^{2+} ions. The ‘gate’ that acts as a physical barrier occluding the pore and preventing ions from passing through in the ‘closed’ conformation as opposed to the ‘open’ conformation, consists of 3 hydrophobic residues in the 9’, 13’ and 17’ positions of M2 (L251, V255 and V259 on mouse alpha AChR)[85]. Bordering the M2 helix are the M1 and M3 helices. Here, at the subunit interfaces, secondary allosteric binding sites for drugs (propofol in prokaryotic pLGICs [86]; ivermectin in GluCl [74]) have been recently identified. At the extreme periphery is the M4 helix, interacting with the lipid bilayer [87]and showing the most variance between available structures.

4.4 - nAChR transmitter binding site

It has been known from early biochemical experiments [88] that each pentamer has two “orthosteric” transmitter binding sites (TBS) on the extracellular domain, ~ 45 Å above the gate. Each site is located at the interface of two subunits – the principal α subunit forming the “+” side, the complementary δ subunit and the ε subunit (γ subunit in fetal AChRs) forming the “–” side. This arrangement was further confirmed by the advent of the crystal structures discussed above, especially the ACh-binding proteins (AChBPs), which are produced and secreted by the glial cells of mollusks [68, 89]. As determined from the AChBP structures, the ECD, which is ~200 amino acids long, is composed of a twisted beta sandwich-like structure, with 10 rigid β-strands, and a number of flexible loops at the subunit interfaces [89]. Three loops from the principal side (loops A, B, C) and four from the complementary side (loops D, E, F and G) together constitute the ligand binding pocket [90]. In AChRs, a tyrosine in loop A, a tryptophan in loop B, two tyrosines in loop C, and another tryptophan in the complementary side loop D form an aromatic "cage" [91]. These aromatic residues participate in direct cation-pi interactions with the quaternary ammonium group of ACh, establishing the main sources of free energy for ligand binding [92]. The ECD from AChBP structure is shown in Figure 4.3.

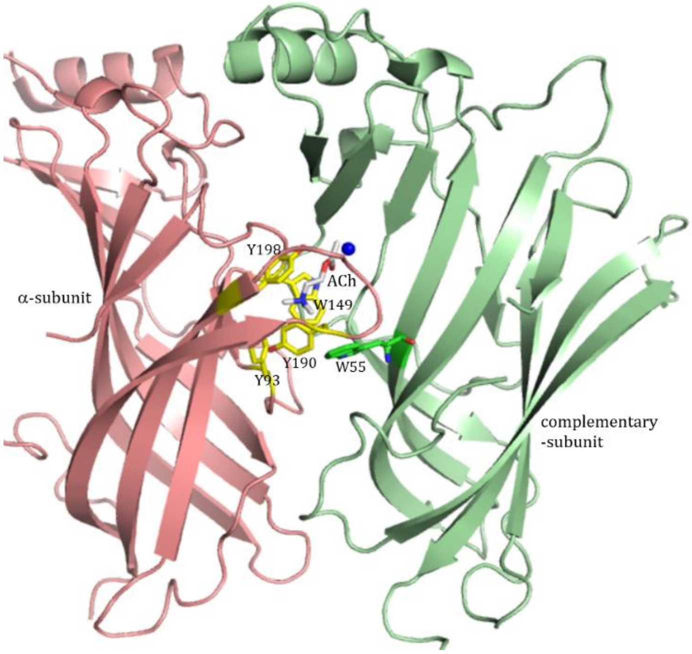

Figure 4.3: Extracellular domain of *Lymnaea* AChBP (PDB ID 3WIP). Only one α- and complementary subunit is shown. The 5 residues forming the aromatic cage around the quarternary ammonium of ACh (white) are shown. Blue sphere indicates a crystal water that participates in H-bonding with ligand and protein. More about this will be discussed in Chapters 7 and 8.

4.5 - nAChR Gating

The nAChRs, like all LGICs ‘gate’: they can switch between ion-permeable (functionally open) and ion-impermeable (closed or desensitized) states in a controlled manner. These allosteric structural changes between resting and active conformations can occur spontaneously, by random samplings of microstates by thermal motions, albeit with very low probability, due to the large energy barrier between C (closed) and O (open) states (apo state opening rate in mouse muscle AChR is very small at 0.008 s^{-1}; see Figure 4.5). Since the small ACh molecule reaches the binding pocket by diffusion, it does not have enough momentum to impart to the protein which would allow the receptor to cross this barrier. However, binding of the ligand molecule leads to local conformational arrangements that is understood to lower this C↔O transition barrier [93], increasing the gating probability (diliganded opening rate in mouse muscle AChR is 65,000 s^{-1}; see Figure 4.5) . In other words, the random sampling motions driven by temperature alone, is now sufficient to overcome the lowered energy barrier between C and O states.

The gating transition occurs in microsecond to millisecond timescale and is one of the fastest occurring conformational changes observed in such large oligomeric proteins [59]. Evidence from the crystal structures of ‘closed’ vs ‘open’ LGIC structures, especially the prokaryotic GLIC [71, 72] and the eukaryotic GluCl structures [73, 74] suggest that the C↔O gating isomerization involves global quaternary structural reorganizations (Figure 4.4) , including a twisting motion of the ECD around the central symmetry axis, and an un-blooming motion of the pentamer (“resembling the closure of a blossom”), coupled with the tilting of M2 and M3 helices that ultimately results in opening the gate. The third stable state, the long-lifetime ‘desensitized’ or D state is non-conducting and can be entered from the O-state, and has similar high affinity for ligand as the O-conformation [94]. This state occurs on a time-scale of 0.1s to

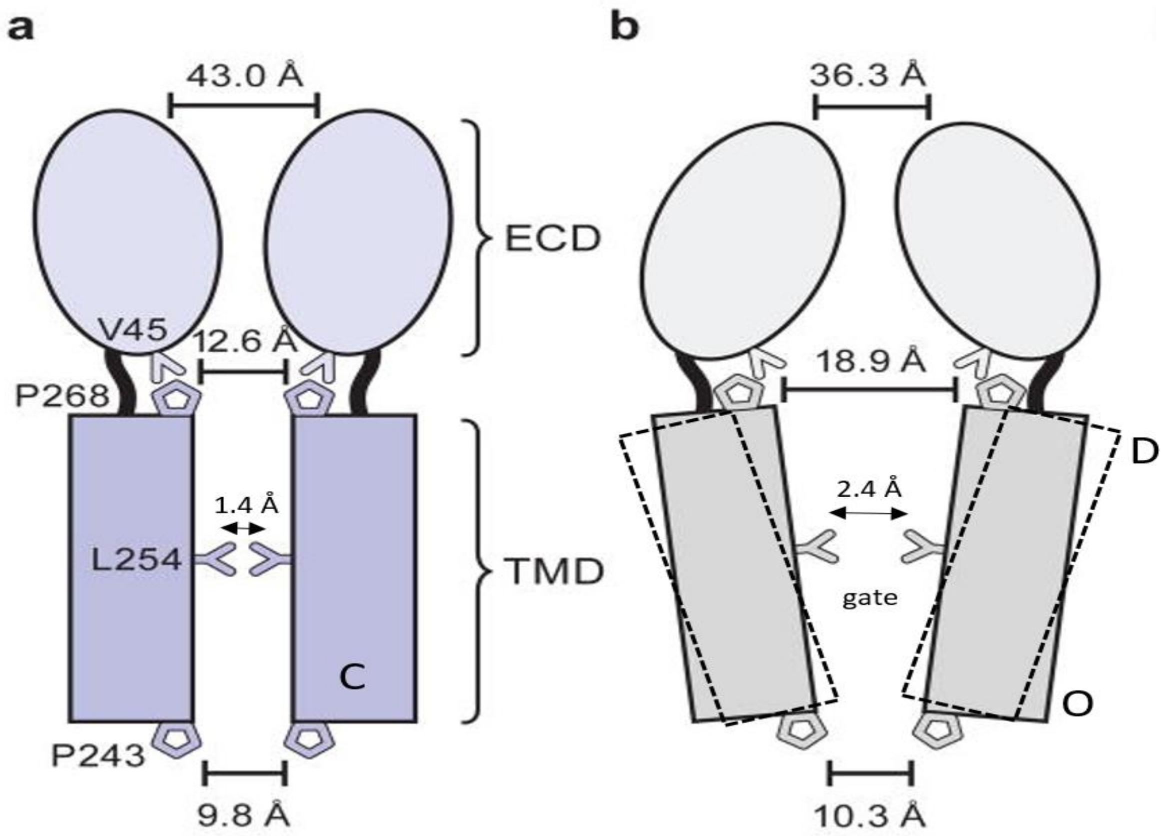

Figure 4.4: Model of 'Closed' (a, left) and 'Open' (b, right) conformations from GluCl crystal structures (PDB IDs 4TNV and 3RHW). In the C↔O transition, the twisting and unblooming of ECD is shown. The pore-lining M2 of TMD bends out to open the gate at L254 (9'-position) from 1.4Å to 2.4Å, enough for monovalent sodium and potassium ions to pass. The current hypothesis for the desensitized 'D' state is that the TMD bends further so that the pore is occluded at the base even though the gate is 'open', as shown by dotted lines at right. (Figure modified from Figure 5, Althoff *et. al.,* Nature, 2014 [73]).

several seconds while the open-form is transient for ~ 1ms. This, along with the fact that the D-state can be reached more easily from O-state than the C-state (by a factor of > 100) [94], seem to suggest that the Open conformation is only a short lived intermediate between Closed and Desensitized conformations. Desensitization seems to be the evolutionary design to prevent over-stimulation when the agonist persists for long in the local environment. Though the structural basis of the D-state is not known, it is hypothesized that the non-conducting state occurs when the M2 helices bend further than in the O-state and occlude the channel at the base [95] as speculated in Figure 4.4. Details about the D-state remain unanswered and not many mutations have been identified that affect desensitization.

4.6 – Applying MWC model to nAChRs

That MWC can be a plausible model to explain nAChR gating was recognized by Karlin as far back as 1967 [96]. The equilibrium dissociation constant for ACh binding to a C-state site (K_d) is ~175μM at both αδ and αε (adult) and ~8μM at the fetal, αγ site [91]. In comparison, that for binding to the O-state site (J_d) is 25 nM in adult AChRs. In the absence of any external source of energy, this difference in energy between K_d and J_d is the energy available to modify the phase space landscape and stabilize the 'Open' structure. When certain mutations are present, unliganded AChRs have been known to open with the same ionic conductance as receptors under saturated ligand concentrations [97], making this AChR system a successful candidate for the MWC cycle of allostery [98] (as discussed in Chapter 2 before). A simplified 2-step MWC cycle of neuromuscular AChR is shown in Figure 4.5.

When a ligand binds more strongly to the channel in the open state, than in the closed state, the presence of ligand molecules shifts the gating equilibrium and increases the open probability of the channel. Equation 2.2 in page 10 for the simple two-state model can also be extended to a 3-state model or more. In case of a system like Figure 4.5, where the ligand binding to the two sites are considered as separate incidents, path independence of work done (conservation of energy) and Hess' Law still holds and equation 2.2 can be further extended as:

$$\frac{E_1}{E_0} = \frac{K_D}{J_D} = \lambda;$$

$$\frac{E_2}{E_0} = \left(\frac{K_D}{J_D}\right)^2 = \lambda^2$$

………………………. Eq. 4.1

Here, $\lambda = K_D/J_D$ ratio is referred as the 'coupling constant', and E_0 is referred as the 'allosteric constant'. These 4 parameters together completely define the kinetics and activity of the channel.

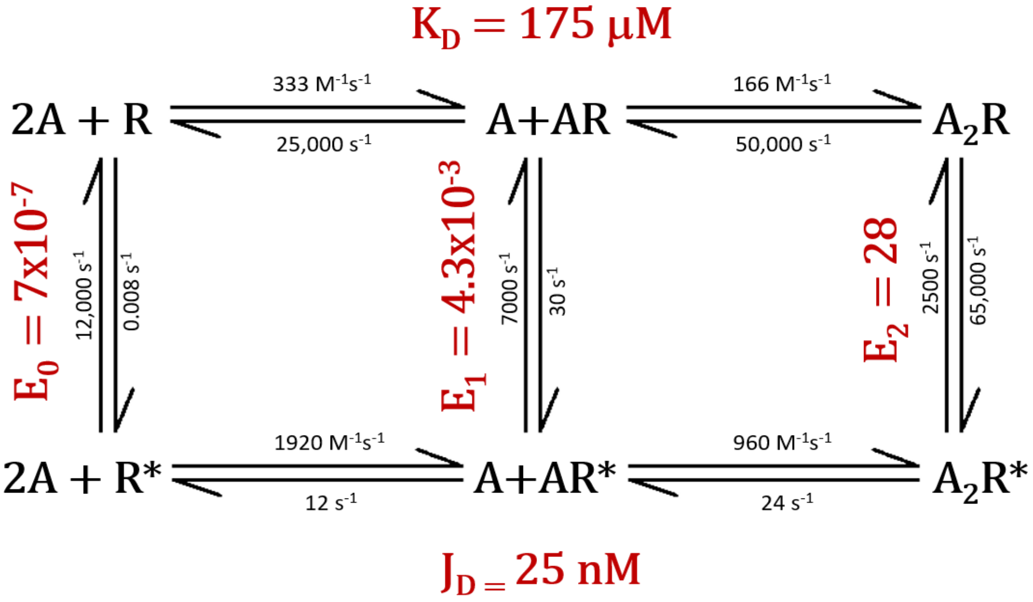

Figure 4.5: Simplified two-step MWC cycle for mouse nAChR. The desensitization cycle is not shown. A is the agonist AChR, R is the receptor, and R* is the activated receptor (rate-constant numbers and cycle from Auerbach, J. Physiol., 2012 [99]).

4.6.1 - Experimental measurement of parameters

By electrophysiology measurements, it is relatively easy to estimate E_2. In the presence of high concentration of agonists, AChRs express single channel currents that occur as clusters of openings arising from multiple binding-gating cycles as shown in a sample current-time plot in Figure 4.6. The basal-current epochs in between these clusters shown in the figure are periods of desensitization. The intra-cluster current on-off kinetics gives E_2. For wild-type (WT) mouse neuromuscular AChRs, $E_2 \approx 28$ (at -100 mV, 23 °C) [100].

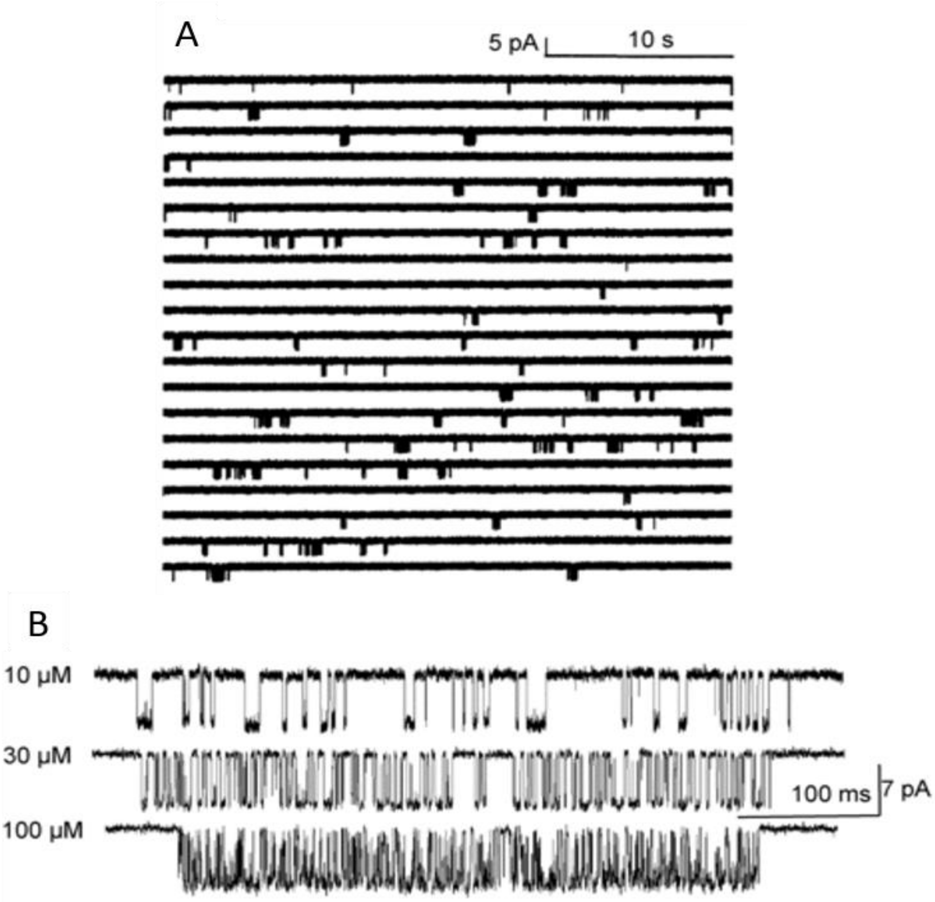

Figure 4.6: Sample current clusters in adult mouse WT AChRs. A. Channels open in short bursts (downward), followed by long intervals of desensitization (1mM ACh). B. Close-up of open clusters at different ACh concentrations. Channel opening probability decreases with agonist concentrations lower than saturation, because mono- and unliganded states are also present with higher probabilities. Experimental conditions are 23 C, -70 mV, cell-attached patch (adapted from Auerbach, *J. Physiol*., 2012 [99]).

The ‘allosteric constant’ $\mathbf{E_0}$ is more difficult to measure, since the unliganded spontaneous openings occur with very low probability and are very brief. Early ion-flux measurements in 1982 [101] estimated $\mathbf{E_0}$ to be of the order $\sim 10^{-7}$. Interestingly, there are many naturally occurring mutations known in humans, causing slow-channel congenital myasthenic syndromes (SCCMS) which lead to an increased $\mathbf{E_0}$ and spontaneous channel activity [102]. Multiple mutations have also been identified that increase $\mathbf{E_2}$ by known amounts [103]. When these mutations are far from the binding site and do not affect the ratio of the binding constants $\mathbf{K_D/J_D}$, equation 4.1 dictates that $\mathbf{E_0}$ should increase by the same amount. Combining a number of such mutations which are energetically independent of each other, $\mathbf{E_0}$ can be increased sufficiently to bring it within experimentally measurable limits. Extrapolating back to zero fold-change, the WT value of $\mathbf{E_0}$ is $\approx 7.5 \times 10^{-7}$ in adult and $\sim 5.2\times 10^{-8}$ in fetal AChRs [91].

With the identification of mutations like αW149M [104] and ε/γP121R (δ123R) [105] which knock out the ACh binding ability at the transmitter binding sites, with negligible effect on $\mathbf{E_0}$, it is now possible to measure the mono-liganded gating constant $\mathbf{E_1}$. When the complimentary side P121 mutation is used, that particular site is knocked out. When the W149 mutant is used, which is present on the α-subunit, the cell is transfected with both WT and mutant α-subunit varieties, and 4 types of AChRs are expressed – both sites WT, both sites knocked out and each of the two sites knocked out separately. The intriguing observation here is that, the single-site knock-out populations are indistinguishable. Moreover, with the ability of forming receptors with only one functional binding site, the measurement of binding energies at each site separately is now feasible. For all agonists, the energies obtained from WT receptors are equal to the sum of those obtained from each of the two sites. Both these observations suggest that **the two sites are**

mutually independent in function. The gating equilibrium of mono-liganded AChR for acetylcholine is: **E_1** ≈ 4.3 × 10^{-3} [106].

Again, by the conservation of work done in each of the two cycles of Figure 4.5, we obtain

$$\frac{E_1}{E_0} = \frac{E_2}{E_1}$$

……………………… Eq. 4.2

This gives us another way to determine **E_0**, by measuring **E_2** and **E_1**.

4.6.2 - Statistical mechanics of equilibrium constant

An equilibrium constant is related to the Gibbs free energy (ΔG) of the chemical transition. The logarithm of equilibrium constant is proportional to this free energy. The basis of this relation derives from the principles of statistical mechanics.

The observable macrostate of a system in thermodynamic equilibrium can be defined completely by 3 parameters – the total number of particles N, the total volume V and the total energy E. But statistically, there can be a number of ways in which total energy E can be distributed among N particles within the same volume V. Each of these ways is called a **microstate Ω**, and according to the postulate of "equal *a priori* probabilities", at any particular time without any external constraints, the system is equally likely to be in any of these microstates. The total entropy, S of the system is a function of all possible microstates Ω, as was first explicitly shown by Max Planck:

$$S = Nk_B . \ln\Omega$$

where $k_B = R/N_A$ is the Boltzmann constant (R → universal gas constant and N_A → Avogadro number). For a thermodynamic reaction, the change in entropy, $\Delta S = k_B . \ln[\frac{\text{number of final states}}{\text{number of initial states}}]$.

The number of states is inversely proportional to the concentration, for a dilution reaction. Therefore, the term within parenthesis becomes equal to $[\frac{reactant\ concentration}{product\ concentration}]$. The change in entropy can hence be written as:

$$\Delta S = -Nk_B . \ln\left[\frac{product\ concentration}{reactant\ concentration}\right] = -nR . \ln Q$$

………………………. Eq. 4.3

Here, Q gives the reaction coefficient, which under equilibrium conditions is the equilibrium constant, and n is the total number of moles of substance in the system.

We know the Gibbs free energy change, ΔG, is equal to $\Delta H - T\Delta S$, where ΔH is the enthalpy change, and ΔS is the entropy change of the system, at temperature T.

Taking derivatives of both sides with respect to temperature T, we get:

$$\frac{\partial(\Delta G)}{\partial T} = \frac{\partial(\Delta H)}{\partial T} - T\frac{\partial(\Delta S)}{\partial T} - \Delta S\frac{\partial T}{\partial T}$$

Now, from thermodynamic definitions, the specific heats at constant volume C_v and at constant pressure C_p can be shown to be [107]:

$$C_v = T\left.\frac{\partial S}{\partial T}\right|_{N,V} ; \quad C_p = \left.\frac{\partial H}{\partial T}\right|_{N,P}$$

For non-compressible systems like ours, $C_v = C_p$ and the first two terms in the right hand side of our Gibbs energy derivative above cancel each other.

$$\frac{\partial(\Delta G)}{\partial T} = -\Delta S$$

Integrating, and using our definition of entropy change from equation 4.3,

$$\Delta G = \Delta G^0 + nRT.\ln Q$$

At equilibrium when $\Delta G = 0$ and Q is the equilibrium constant K_{eq}, **the standard change in Gibbs free energy (ΔG^0) per mole** is given by:

$$\Delta G^0 = -RT.\ln K_{eq}$$

………………………. Eq. 4.4a

In our case, K_{eq} can be substituted by any of the 4 equilibrium constants of Figure 4.5. With $R=1.98\text{x}10^{-3}$ kcal $M^{-1}K^{-1}$, T the standard temperature 23^0C and $K_{eq} = 1/K_D$ (dissociation constant is the inverse of equilibrium constant for ligand binding),

$$\Delta G^0 = +0.59.\ln K_D \ \ in\ kcal\ M^{-1}$$

………………………. Eq. 4.4b

Being able to calculate free energy of binding from the agonist dissociation constant thus gives us the important advantage of being able to compare *in silico* binding results with experimentally obtained data. There are two standard ways of getting dissociation constant K_D from electrophysiology. Equation 2.5c in page 11 demonstrates that the agonist concentration at half maximal response of a dose-response curve can be used to obtain K_d.

$$K_D = \frac{(1+E_1)}{(1+E_0)}[A]_{half-max}$$

………………………. Eq. 4.5

For the alternative approach, in which we get a fairly precise approximation of K_D, we go back to equation 4.1 again. As discussed later in this chapter, the high affinity binding energy measured by the natural log of J_D is found to be about double that of the low affinity binding energy measured by the natural log of K_D [108, 109]. This means $J_D \approx (K_D)^2$. Equation 4.1 can therefore be reduced to $\frac{E_1}{E_0} \approx \frac{K_D}{(K_D)^2}$.

$$\therefore \quad \frac{E_0}{E_1} \approx K_D$$

……………………… Eq. 4.6

This method makes experimental measurement simpler, since it does not involve cross-concentration fitting. Comparison of K_D values measured by both these techniques (equations 4.5 and 4.6) have given similar results (see Chapter 8).

ΔG_0 and ΔG_2 are the unliganded and diliganded gating free energies respectively, corresponding to E_0 and E_2, while ΔG_{LA} and ΔG_{HA} are the low affinity and high affinity binding free energies corresponding to K_d and J_d. Again from detailed balance of the cycle, taking natural log of equation 4.1 and multiplying both sides by –RT:

$$\Delta G_2 - \Delta G_0 = 2\Delta G_{HA} - 2\Delta G_{LA}$$

……………………… Eq. 4.7a

Defining $(\Delta G_{HA} - \Delta G_{LA})$ as ΔG_B,

$$2\Delta G_B = \Delta G_2 - \Delta G_0$$

……………………… Eq. 4.7b

ΔG_B is the net free energy available due to the affinity change of the agonist at the binding site, between O and C structures, and is equal to –RTlnλ. Equation 4.7b shows that this available energy ultimately leads to increased stability of the diliganded gating compared to unliganded gating [110]. This energy has been measured to be -10.4 kcal M^{-1} when there are agonists present at both binding sites. Single site knock-outs show that each site individually contributes ~5.2 kcal M^{-1}

further reinforcing the observation that the two sites function independent of each other [111]. Choline, on the other hand, which is a low efficacy partial agonist, provides ~3.3 kcal M^{-1} per binding site [111].

Experimentally, the single channel or multi-channel currents are measured by an electrophysiological technique called patch clamp. The first AChR currents were measured by using two electrodes to maintain the voltage across the membrane, and then measuring the current with third independent probe by Neher and Sakmann [112]. But this technique had poor signal-to-noise ratio. Further developments led to improving of the technique and the attainment of the giga-ohm seal was possible [113], wherein, a polished glass micropipette is attached to the membrane by the application of air-suction, leading to a high resistance contact with negligible current leakage. It was also possible to directly maintain the voltage through the same micropipette, which eliminated the need for an independent voltage-sensing electrode. This, along with advancement in the electronic circuitry [114]), now allows for measurement of single channel currents, with temporal resolution of 10μs and stability for of 10s of seconds or longer. The rise-times of microsecond duration, the currents of millisecond scales and the desensitization sojourns of several seconds now became accessible by this technique.

4.7 - Using computational techniques to study pLGICs

To compliment the laboratory techniques, pLGICs have been studied quite extensively using computational methods, like equilibrium MD simulations [59, 115-118], targeted MD simulations [119] and steered MD simulations [120]. These simulation times have ranged from nanosecond range [117, 119] to 1 microsecond [121] shedding light on some key structural dynamics involved in the channel functions. They have been successful in identifying key sequence of structural events that proceed from the ligand binding site, to the ECD-TMD interface and then finally further down to the TMD helices M2, M4 and M3. However the accessible timescales so far have been much smaller compared to the millisecond range channel gating in neuromuscular AChRs [122]. Coarse grained elastic network models [123-125] have also been useful to study the global large amplitude motions of these channels and have helped in identifying overall transition pathways, than seem to match fairly well with electrophysiological phi-value analyses [126].

There is a large set of different AChBP structures now available, and these have been used extensively to computationally study structure-function relationships of the extracellular domains of pLGICs with fairly good accuracy [127, 128]. Having more than 60% sequence similarity with nAChRs, these structures also act as good templates for making homology models for the ECDs of the acetylcholine receptors, opening avenues for large-scale drug screening and other computational studies of the binding sites. Here we have done the same and were successful in building reasonably precise homology models of the mouse adult and fetal-type binding site on a single pentameric extracellular domain structure. Comparison of results obtained from our *in-silico* model with those in physiological *in-vitro* conditions is justified by the following assertions that define the premise of our study:

(1) The two binding sites are independent of each other in function (discussed earlier), as evidenced by the fact that binding energies obtained from the two sites combined is equal to the sum of the individual binding energies from each site.

(2) Mutations in the TMD do not generally affect the binding site and the ECD [129]. Hence, the lack of TMD in our model should not affect the phenomenon of ligand binding, though

it does not help in shedding light in the gating process. In fact, all observations so far lead to the conclusion that most mutations away from the binding site affect only the allosteric constant $\mathbf{E_0}$ and not the binding affinities or the coupling constant [93].

(3) For different agonists and mutations at the binding site, ΔG_{LA} and ΔG_{HA} are correlated. The high affinity binding energy has been found to be approximately double that of the low affinity binding ($\Delta G_{HA} \approx 2\Delta G_{LA}$) [108, 109], which suggests that the two are just different steps of a single mechanism ("catch-and-hold"). Using this relation in equations 4.4a and 4.4b, we get $\Delta G_B \approx \Delta G_{LA}$. Since the binding energies obtained from simulations are equivalent to the low affinity closed state agonist binding, these can be compared to the experimentally obtained ΔG_B values.

(4) The *in vitro* free energies of binding for acetylcholine with muscle AChRs is mainly enthalpy driven, with a negligible entropic component [130]. Hence, even though the binding energy calculated *in silico* does not account for entropy, it is possible to compare these with the *in vitro* energies measured.

4.8 - Fetal vs. adult AChRs

As discussed earlier here, the γ-subunit in amphibian and mammalian muscle AChRs is replaced by the ε-subunit during postnatal development from fetal-type to adult-type cells [77]. The γ-subunit is required for proper synaptic development [131], normal innervation patterns [132] and muscle fiber composition [133]. Their importance in embryonic development is further exemplified by the fact that the γ-subunit knockout is lethal in mice [134] and mutations to the human gamma CHRNG gene are associated with various lethal and non-lethal multiple pterygium and Escobar syndromes [135-137].

While the two binding sites within a single receptor are independent of each other, in adult channels, the $\alpha-\delta$ and the $\alpha-\varepsilon$ sites have similar binding energies to ACh and provide equivalent energies to channel gating [106]. But this is not the case for the $\alpha-\gamma$ site. The fetal $\alpha-\gamma$ site has a G_B value ~7.0 kcal.M^{-1} from ACh binding as compared to ~5.1 kcal/mol in adult $\alpha-\varepsilon/\delta$ sites [91]. The fetal-type γ-channels also have a smaller conductance [138], a lower Ca^{2+} permeability [139] and a longer open channel lifetime as compared to adult ε-AChRs [77].

The peak acetylcholine concentration generally available at the adult neuromuscular synapse is ~ 1mM [140]. But during synaptic development, the available ACh concentration at the end-plate junction is significantly reduced due to the reduced amount of ACh released by the presynaptic vesicles, and the pre- and post-synaptic cells being farther from each other. Due to the lower [ACh], only γ-AChRs can generate significant current, due to its greater ACh affinity, making it a perfect evolutionary design to allow for proper synaptic development and signaling. Moreover, interestingly, choline, which is both a precursor and a breakdown product of ACh, is present in higher concentrations in fetal serum, which could also act synergistically with ACh, during embryonic development.

Chapter 5: COMPUTATIONAL SIMULATIONS OF PROTEINS

With the fast progress of computational power, many physical problems which are still beyond the reach of conventional experimental methods can now be studied through simulations. For example, in the case of structural dynamics of proteins, the time-scales and space-scales of some of the properties of interest are difficult to probe or beyond the scope of the current experimental methods available. If an accurate computational model can be constructed, it can be used to predict and provoke further experiments, explain experimentally obtained results, and even in some cases replace experiments completely. Computational simulations have therefore become useful complements to experimental studies of biomolecules.

The time and length scales over which biomolecular activities occur vary over a wide range as shown in Table 1.1, page 4. Depending on what we want to study, a hierarchy of methods can be applied to capture the dynamics on different scales. Molecular dynamics simulations can, in principle, provide atomic-scale spatial resolution and femto-second scale time resolution, which is not easy to achieve by other experiments. However, to study the behavior of large proteins over long periods of time, MD simulations would require computational power which is not commonly available. In fact, since such high spatio-temporal resolution may not always be relevant for the question at hand, various other simulation techniques have also been developed. For example, there can be coarse-graining of the system where groups of atoms are considered as one unit, instead of being examined individually; or random sampling of an equilibrium ensemble of a system using Monte Carlo techniques. For the purpose of this thesis, we were interested in the dynamics within nanosecond time scales and hence all-atom classical molecular dynamic simulations were used.

5.1 - Classical molecular dynamics (MD) simulations

MD simulations involve the solving of Newton's 2nd equation of motion for a defined potential function, which can be integrated over time to obtain the evolution of atomic coordinates of the system.

$$\vec{F_i} = -\nabla_i V$$

Or,

$$m_i \frac{d^2 X_i(t)}{dt^2} = -\frac{dV}{dX_i}$$

……………………… Eq. 5.1

Here, X_i is a generalized coordinate of the system, m_i is the mass, $\vec{F_i}$ is the force experienced by atom i, and V is the empirical potential defining the system. This method was first applied on the interactions of hard spheres in the late 1950's by Alder and Wainwright [141, 142]. Later it was developed further by Rahman and Stillinger for the study of simple liquids with more realistic potentials as in liquid argon [143] and and water [144]. It was first applied in the case of protein simulations in 1977 by McCammon and Karplus [145] on the bovine pancreatic trypsin inhibitor protein. Currently, MD simulation is one of the most common tools to study time dependent (and independent) behavior of biomolecules. It has been used for modeling proteins, nucleic acids and their complexes, to study the folding and stability of these molecules, enzyme reactions, design of drug activation, conformational changes and even construction of 3D structures (by homology modeling, X-ray diffraction and NMR).

The central idea of molecular dynamics simulations comes from the fact that macroscopic observables measurable in experiments are the statistical outcome of microscopic behavior at the atomic level. Thus statistical mechanics forms the governing theory of MD simulations, which give rigorous calculations of macroscopic properties like pressure, free energy, heat capacities, etc. from the distribution of motion of the constituent atoms and molecules. On page 39 I had defined microstates Ω. In statistical mechanics, an ensemble is defined as a collection of all possible microstates that have the same identical macroscopic or thermodynamic state. In other words, a system with a particular observable value of macroscopic property can be in any combination of the available microstates. It is the average value of the ensemble of microstates that determines the observable macrostate.

The average over the ensemble is not trivial. Here, the **Ergodic hypothesis** comes to our rescue, which states that the ensemble average of a parameter is equal to the time average, for a system [107]. Or, in other words, if a system is allowed to evolve long enough in time, it will eventually pass through all possible microstates.

$$\langle A\rangle_{ensemble} = \langle A\rangle_{time}$$

………………………. Eq. 5.2

Averages of macroscopic parameters like potential energy, kinetic energy, pressure, etc. can therefore be calculated from MD simulations, averaging over time. We use this technique in Chapters 6, 7 and 8 to define our ensemble in order to estimate binding affinity of proteins.

5.1.1 - The force field

The basic functional form of the potential energy used in equation 5.1 is a summation of bonded (covalent bond lengths, bond angles, dihedral angles) and nonbonded (electrostatic, van der Waals) terms, which are parameterized empirically from existing datasets or quantum mechanical calculations. Though the details are different for different standardized force fields like AMBER, CHARMM, GROMACS, OPLS-AA, etc., the basic form of the equation remains the same. The CHARMM force field equation [146] is shown here in equation 5.3, and is used for all our simulations.

$$
\begin{aligned}
V = \sum_{bonds} k_b(b-b_0)^2 + \sum_{angles} k_\theta(\theta-\theta_0)^2 + \sum_{dihedrals} k_\varphi[1+\cos(n\varphi-\delta)] \\
+ \sum_{impropers} k_\omega(\omega-\omega_0)^2 + \sum_{Urey-Bradley} k_u(u-u_0)^2 \\
+ \sum_{nonbonded\,pairs} \epsilon\left[\left(\frac{R_{ij}^{min}}{r_{ij}}\right)^{12} - \left(\frac{R_{ij}^{min}}{r_{ij}}\right)^{6}\right] + \frac{q_i q_j}{4\pi\varepsilon\varepsilon_0 r_{ij}}
\end{aligned}
$$

……………………… Eq. 5.3

In equation 5.3, k denotes the various force constants and the subscript 0 indicates the equilibrium position. In the dihedral term δ is the phase shift, n is the periodicity and φ is the torsional angle. The non-bonded term is given by standard van der Waals (Lennard Jones) and electrostatic (Coulombic) interactions between atoms i and j, with r_{ij} as the spatial distance between them. These terms together define the potential felt by each atom in the system, and its gradient gives the force exerted on the atoms, forming the basis of the integration step of MD simulations, given in equation 5.1.

5.1.2 - Simulation preparation:

Figure 5.1 shows the schematic algorithm of MD simulation giving a simplistic explanation of the steps involved. Before the simulations can begin, the system must be set up. This includes, choosing or building a model of the protein structure, and then building its environment, which closely replicates its physiological condition. This generally involves immersion of the protein in

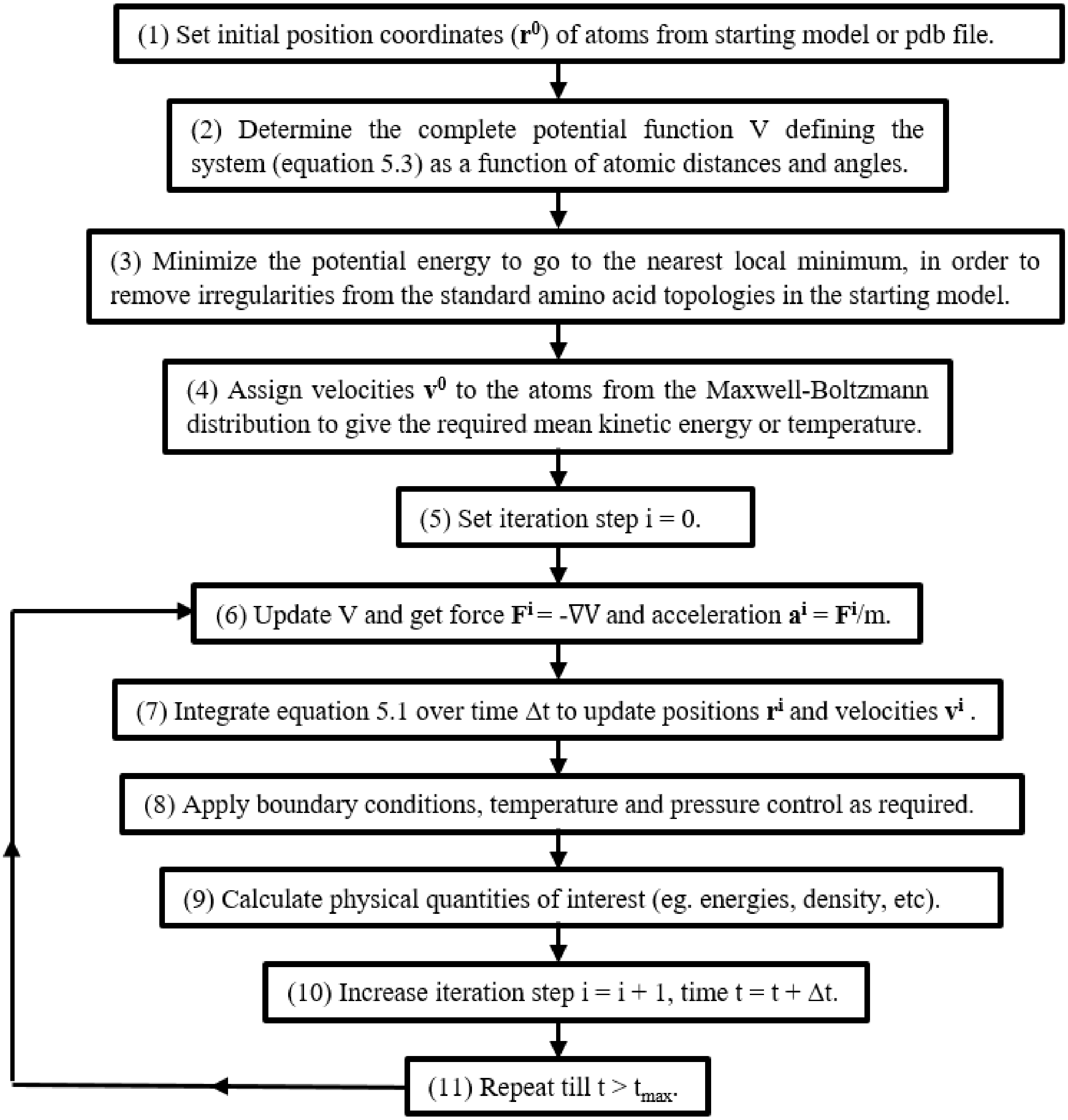

Figure 5.1: Schematic flow chart of steps of a standard classical molecular dynamics simulation

a water box (Figure 5.2) and adding of charged ions to neutralize the system and mimic the salt concentration. If it is a membrane protein, it needs to be embedded in a lipid bilayer. All the atoms of water, ions and lipids, along with the protein now become a part of the system, and interact with each other, contributing to the force field. As shown in step 3 (Figure 5.1), this assembly now needs to be relaxed in order to remove steric clashes and other inappropriate geometry. This is done through a process called local energy minimization, where the local potential field around the starting configuration is searched for a minimum in energy, which should be a local equilibrium state corresponding to a stable conformer of the protein. There are various numerical techniques that are commonly used for energy minimization, by iteratively calculating the gradient of the potential function, as in the Newton-Raphson method [147], the steepest descent method [147, 148] and the conjugate gradient method [148, 149].

After the initial position coordinates of the protein conformer is thus determined, the initial velocities as assigned as shown in step 4. This is generally a random assignment, satisfying two criteria: (i) the resultant overall momentum is zero;

$$P = \sum_{i=1}^{N} m_i v_i = 0$$

……………………… Eq. 5.4a

(ii) The velocities are distributed in Maxwell-Boltzmann distribution such that the average kinetic energy gives a measure of the temperature of the system.

$$P(v_i) = 4\pi \left[\frac{m_i}{2\pi k_B T}\right]^{3/2} v_i^2 \, exp\left(-m_i v_i^2 / 2k_B T\right)$$

……………………… Eq. 5.4b

The temperature of the system can thus be calculated from the velocities as:

$$T = \frac{1}{(3N)} \sum_{i=1}^{N} \frac{|p_i|}{2m_i}$$

……………………… Eq. 5.4c

In equations 5.4 a, b, c, N is the total number of atoms, i is the index of atom with mass m_i and momentum p_i, T is the temperature and $P(v_i)$ is the probability of velocity v_i.

5.1.3 - The integration step

The equation 5.1, with potential function V given by equation 5.3, is too complex in nature to have an analytical solution. Hence, this time integration is solved numerically, where the positions, velocities and accelerations are approximated by a Taylor series expansion, using a number of standard algorithms like Verlet, Leap-frog and Beeman's integrators [150, 151]. For the work in this thesis, the Verlet algorithm has been used, where position r_i is calculated at $\pm\Delta t$:

$$r_i(t + \Delta t) = r_i(t) + v_i(t)(\Delta t) + \frac{1}{2} a_i(t)(\Delta t)^2$$

$$r_i(t - \Delta t) = r_i(t) - v_i(t)(\Delta t) + \frac{1}{2} a_i(t)(\Delta t)^2$$

Adding the two equations, we obtain:

$$r_i(t + \Delta t) = 2r_i(t) - r_i(t - \Delta t) + a_i(t)(\Delta t)^2$$

………………………. Eq. 5.5

Equation 5.5 demonstrates that the position at time step Δt can be iterated from the previous two steps and the acceleration at time t. The step size Δt is a rate limiting factor in MD calculations. It cannot be made larger than the period of the highest vibrational frequency in the system. By fixing the bond length involving hydrogen atoms, the maximum usable Δt is 2 fs.

5.1.4 - Periodic boundary conditions

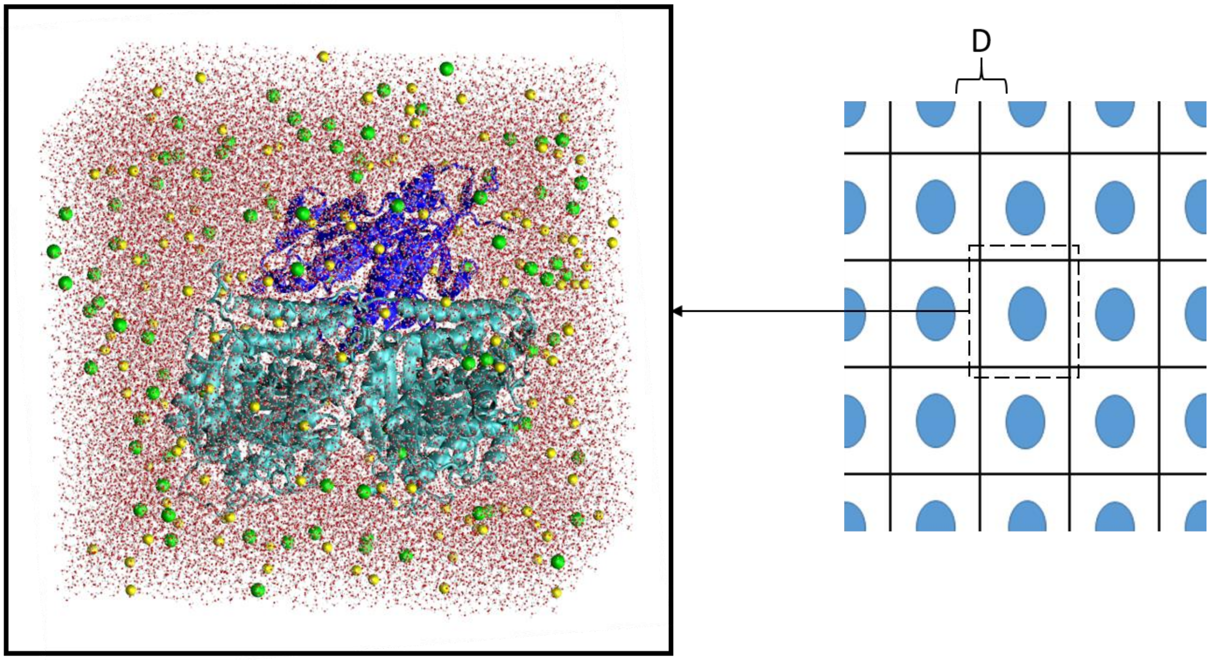

Figure 5.2: Unit cell of a MD simulation system. Kinesin-MT protein (pdb 4HNA) immersed in a water box. Yellow spheres are positive sodium ions and green spheres negative chloride ions, added to neutralize the system at 150 mM salt concentration. The infinite arrangement of unit cells are shown in 2-dimensions on the right. Blue circle represents the protein, and black lines, the water box boundary. Distance D between two neighboring protein images should be more than the non-bonded interaction cut-off distance.

Since the protein-surrounding assembly (as shown in figure 5.2) has a well-defined finite boundary between water and vacuum, there will be edge effects in the integration, leading to distortion of system and rapid "evaporation" of water molecules. To minimize such effects, the system is surrounded by space filling translated copies of itself on all sides, making this an infinite system with uniformly repeated unit cell, and no boundaries [152]. The drawback of this approach is that, the number of atoms is effectively increased to infinity, and each molecule can interact with its own image in a neighboring unit cell. To counter these problems, and to reduce the required computational power, the non-bonded interactions given in equation 5.3 are considered only within a particular cut-off distance (Figure 5.2), beyond which the potential smoothly switches to zero [153]. The solvation box has to be made thick enough such that a molecule and its neighboring image is separated by more than this cut-off distance.

5.1.5 - Modified Molecular Dynamics

Classical MD simulations have branched out into different paths where the classical potential is modified to accelerate the process under study to simulation time scales (ns), such that longer processes can be approximately mimicked within nano-second range simulations. Some of these common methods are Targeted MD (TMD), Accelerated MD (AMD) and Steered MD (SMD). In all these non-equilibrium techniques, an extra potential term is added to the classical force field, the gradient of which, applies a steering force on the atoms. In TMD [154], structural transitions are studied between an ‘initial’ and a ‘final’ structure, where a subset (or all) of the atoms in the simulation is guided towards the final ‘target’ geometry. The TMD potential is proportional to the difference in actual RMSD of the coordinates at each step and a targeted RMSD obtained by linear interpolation between the initial and final structures through the total number of TMD steps. AMD [155] on the other hand, allows for augmented sampling of the conformational space, by reducing the energy barriers needed to be overcome between states. The classical MD potential energy landscape is modified by decreasing the well depths at those regions where the energy wells are deeper than a certain threshold. The system thus spends less time in these originally deep wells and as a result, can sample a wider conformation space.

Another commonly used modified MD is Steered Molecular Dynamics (SMD) [156]. The basic idea behind SMD is to virtually replicate atomic force microscopy, optical tweezer or other similar pulling experiments. A force is applied to one or more atoms, while another subset of atoms is kept fixed, and the behavior of the system under this stress is studied. For constant velocity pulling, force is applied by means of a virtual dummy spring,

$$U_{SMD} = \frac{1}{2}k[vt - (\vec{r} - \vec{r_0}).\hat{n}]^2$$

……………………… Eq. 5.6

Here, U_{SMD} is the added SMD term to the MD potential, k is the spring constant, v is the pulling velocity, t is the time, $\vec{r_0}$ is the initial position vector of the atom being pulled, $\vec{r}$ is the present position vector, and $\hat{n}$ is a unit vector that gives the direction of pulling. The negative gradient of this potential term gives the force on the atoms. For constant force pulling, no dummy springs are used. Rather, a constant force term is added on top of the classical MD forces to the atoms being pulled. SMD has been applied to study many of non-equilibrium conformational changes, like protein unfolding, binding-unbinding, large scale domain motions, etc. [120, 157, 158]. This technique is currently being used as a follow-up of the study in Chapter 6, to understand the force-regulation of kinesin-microtubule binding. In this dissertation, another similar technique of modifying the classical MD potential function has been applied to flexibly fit kinesin-microtubule models in experimentally obtained cryo-EM density maps and has been described in page 66.

5.1.6 - Limitations of MD

It must be borne in mind that like most computational techniques, there are many limitations to MD simulations. For example, (i) the calculations assume a classical system, whereas, in reality, some particles like hydrogen atoms are small enough to exhibit quantum effects, like tunneling through energy barriers. (ii) All electrons are assumed to be in ground state, and electronic motions are not considered; (iii) the force fields are approximate and do not explicitly incorporate polarizabilities; (iv) boundary conditions are unnatural and interactions are cut off beyond a particular distance. But despite all these limitations, MD simulations have evolved to be a very potent tool to study and guide biomolecular experiments.

5.2 – Homology modeling

The exact 3-dimensional structure is not available for most proteins that have been isolated and identified so far, despite continuous efforts by crystallographers. Building on the Anfinsen's dogma (page 3) we can however, get clues to the native structure of a protein, if the amino acid sequence is known. Homology modeling [159] is a computational technique where a reasonably accurate quaternary geometry of a protein can be modeled by comparison with another protein whose structure is known, if the two proteins share high sequence similarity. The critical first step to homology modeling is to judiciously identify one or more template structures by multiple sequence alignment [160, 161] which are homologous to the target protein that needs to be modeled. It has been observed that evolutionarily related proteins show high conservation of secondary structures, greater than even the amino acid sequences [162]. An accurate sequence alignment thus gives a one-to-one correspondence between the template and the target residues. The 3-dimensional Cartesian coordinates of the backbone atoms of the target can be extrapolated based on this alignment. The most common technique used is 'fragmentation' where segments of the sequence are matched to separate templates from structures in the Protein Data Bank. For guessing the coordinates, further help from experimentally available data may be used. The spatial restraints can be thus guided by NMR spectroscopy, EM maps and mutational studies which can shed light on interacting regions. After the initial guess of the backbone, side chain atoms are added. The internal coordinates of the proteins are spatially restrained and the overall structure optimized to match empirically parameterized datasets of bond lengths, angles, dihedral, etc. The more challenging part is to guess coordinates for insertions and adjust for deletions in the sequence alignments. Therefore, insertion of a loop longer than a few residues is a common source of error in modeling [163]. The overall structure obtained is further verified by various quantifiable criteria like energy stabilization, presence of steric clashes etc. MODELLER [164] and ROSETTA [165] are two standard packages commonly used in literature for performing homology modeling.

5.3 – Ligand docking

Ligand docking is a method of computationally predicting the interaction of a small molecule with a protein by modeling a putative structural orientation [166] of the two molecules relative to each other. Geometric shapes of the ligand and protein are matched by searching the 'solvent accessible surface areas' and finding the complimentary alignments, like a "lock-and-key" approach [167]. The search space is usually identified based on pre-existing available knowledge about the protein. All possible orientations and conformations of the ligand molecule within that search space are explored by various search-algorithms like Monte Carlo, molecular dynamics or various Genetic Algorithms [168]. This is a common approach used for scanning molecules as potential drug targets for a protein, and like most computational techniques, there is a trade-off between accuracy of calculations and higher data throughput. AutoDock is one such tool for the application of ligand docking that was used in this study. AutoDock uses a Lamarckian Genetic Algorithm for search, and an in-built empirical free-energy scoring function for optimization [169].

Chapter 6:

Investigating the Structural and Energetic Bases of the Differences between the Primary ATPase States of a Kinesin-Tubulin Complex by All-Atom Molecular Dynamics Simulation*

*Work presented in this chapter has been published:

Chakraborty S., Zheng W., *Biochemistry*, **2015**, *54* (3), pp 859–869

ABSTRACT:

Kinesin- microtubule interactions vary during the stepping action of the motor protein and depends on the nucleotide state. But due to the limited number of high resolution structures, not much is known about the structural basis of the kinesin – tubulin binding. Here we have employed flexible fitting of cryo-electron microscopy maps to build all-atom structural models of human kinesin-1 monomer in the three major ATPase states (ADP, APO and ATP state) while in complex with a tubulin dimer. We have applied extensive molecular dynamics (MD) simulations (total 400 ns for each state) to investigate the structural dynamics and energetics of the nucleotide-dependent regulation of kinesin – microtubule interactions. In this study, we have determined the key structural changes of the nucleotide-binding pocket, the tubulin-binding site, and allosterically coupled motions driving the APO to ATP transition. Moreover, we have identified key hydrogen bonds that play important functional roles and also pin-pointed the key residues involved in kinesin-tubulin binding. This study has provided a comprehensive structural and dynamic picture of kinesin's major ATPase states, addressed several outstanding issues in kinesin study and offered promising targets for future mutational and functional studies to investigate the molecular mechanism of kinesin motors.

6.1 - Introduction

Kinesin proteins are molecular motors that utilize the chemical energy from ATP hydrolysis to perform important cellular functions, including cell division and transport of cellular cargo [170]. Of the 14 kinesin families, kinesin-1 was the first to be identified, and is known as the conventional kinesin [30]. Conventional kinesin is a highly processive motor protein, driven by ATP hydrolysis. It can take several 8-nm steps along microtubule tracks before dissociating from it. This processive nature was initially demonstrated by Howard *et. al.* using a gliding assay in 1989 [39]. Later, Block *et. al*. established that single kinesin motors attached to glass beads traveled over a micron distance along MT tracks without dissociation [38]. Since kinesins utilize one ATP molecule per step, the number of ATP molecules hydrolyzed, or the number of cycles of the kinesin biochemical pathway a kinesin head goes through while staying associated with a microtubule, is defined as its processivity [171]. It has been observed that the average processivity of the conventional kinesin is ~ 125 [172]. This indicates that the ability to continue 'walking' on the MT tracks comes from a coordinated variation of the binding affinity of the kinesin head with tubulin in different nucleotide states.

There is general agreement that within each biochemical cycle, the two identical motor heads move in a hand-over-hand manner [173], with the leading head remaining stationary while the trailing head passes it, triggered by the docking of a ~ 14-residues long neck linker [52] . There have been several theories as to the coordination between the two heads, either by 'chemical gating' or mechanical actions [174, 175]. The main ATPase pathway of a kinesin monomer (in the presence of MT) has been extensively probed by kinetic studies [47, 48, 176-178], and has been described in detail in Chapter 3 (page 20). Kinesin bound to ATP and kinesin free from nucleotide

(APO state) show strong MT binding, while kinesin bound to ADP can only bind weakly to microtubule [51]. The docking of the neck linker along the catalytic core domain occurs in the ATP state [36, 52]. To fully understand the molecular mechanism of kinesin motility, it is critical to investigate the above three states and the transitions between them with high spatio-temporal resolutions.

Since most high-resolution structures of kinesin were solved in the absence of tubulin [179-181], questions about structural details of the allosteric modulation of kinesin activity by microtubules have largely remained open. Recently, the Knossow lab succeeded in solving a crystal structure of ATP-like kinesin–tubulin complex [53], which answered many of these questions on kinesin-MT strong binding, and opened avenues of new structural studies. Cryo-electron microscopy (cryo-EM) maps in various MT-bound kinesin ATPase states have been available for some time [182-187], which do not yet have resolutions high enough to completely determine the secondary structures and amino acid side chain orientations. But the map density information can be used to guide computational modeling to accurately determine the global and local structural changes between ADP, APO and ATP states. A number of flexible fitting techniques have been developed to optimize the fitting of a given initial protein structure with a cryo-EM map [188-196]. Molecular dynamics flexible fitting (MDFF) program is one such technique that that we use in this study [197, 198]. We try to answer some of the open questions of cyro-EM based flexible fitting, such as, the convergence of different fitting techniques and their accuracy in distinguishing the structural features that separate the different kinesin-MT ATPase states.

To compliment various experimental studies like optical trap and other single-molecule techniques, structure-based computer simulation have been used to study the structure-function relationships of kinesin motor proteins. Various coarse-grained modeling studies [199-206] and tens of nanoseconds-scale all-atom MD simulations have been performed to investigate the structural dynamics of conventional kinesin in the absence [207-214] or presence [213, 215-217] of tubulin. However, such a time scale is much shorter than the millisecond range kinetics of kinesin ATPase cycle. Here we perform 100 ns range simulations of kinesin-tubulin complex, after exhaustive flexible fitting with cryo-EM maps, which has helped shed light on greater details of the structural dynamics of the system. We also build on a previous study from our lab [217] by improving the modeling and flexible fitting protocol and performing longer unconstrained MD simulations (total 400 ns per state), allowing for adequate equilibration of the system and meaningful analysis of the energetics and dynamics of kinesin in different ATPase states.

We have been successful in obtaining a detailed structural and dynamic picture of kinesin's three major ATPase states, which has revealed nucleotide-dependent changes in the structure and flexibility of the nucleotide-binding pocket and the tubulin-binding site, and allosterically coupled motions driving the APO to ATP transition. We have also performed a detailed analysis of key hydrogen bonds (see Appendix 1) involved in kinesin-nucleotide and kinesin–tubulin interactions, and the calculation of the polar contribution to the kinesin–tubulin binding free energy. On the basis of our findings, we have been able to shed light on some of the long outstanding questions in kinesin study, like the role of the central β-sheet twist in MT binding and ADP release, the allosteric connections between the neck linker docking and nucleotide binding, the structural variations of the α4 relay helix during the ATPase cycle, and other mechanistic features of MT-regulated kinesin activity.

6.2 - Methods

6.2.1 - Building the starting structures

The initial structures of the three important ATPase states of human kinesin-1 motor domain (referred as kinesin here on; see Figure 6.1) in association with tubulin dimer was built as follows, before being subjected to flexible-fitting into cryo-EM maps.

ADP State: The kinesin head was built from the ADP-bound kinesin-1 structure (PDB id: 1BG2) with neck linker truncated at residue 325 [218]. Being in the MT-free state, the a4 helix is shorter in this structure. To mimic the MT-bound ADP state, the N-terminal segment of α4 helix (residues 247 to 256) was extended by the Modeller program [219] based on the ADP-bound kinesin-5 structure (PDB id: 1II6) as template (similar to ref [217]). Residues 243 to 246 of loop L11 were remodeled *ab initio* by Modeller to join the extended α4 helix with the already-existing section of loop L11 (residues 237 to 242). The tubulin dimer model was taken from an ATP-like structure of kinesin–tubulin complex (PDB id: 4HNA) [53].

ATP State: The newly available ATP-like structure of kinesin–tubulin dimer complex (PDB id: 4HNA)[53] was used as the initial model for ATP state. Here the ATP state is defined as the state visited after ATP-binding and before ATP hydrolysis, which corresponds to experimental structures of kinesin bound with ADP-AlF_4 and tubulin/MT in the literature [53, 186]. AlF_4 molecule is an analogue of γ-phosphate of ATP. This ATP analogue (i.e., ADP-AlF_4), together with Mg^{2+} ion and two crystal waters at the active site of 4HNA, was kept in our model to stabilize the closed nucleotide-binding pocket characteristic of ATP state [220]. Two different constructs were modeled for the ATP state, one with the neck linker (up to residue 337) in a docked conformation, another with the neck linker truncated at residue 325 to match the number of residues in the ADP and APO states. This helped us to investigate the extent of the neck-linker contribution to ATP state properties.

APO State: Since no nucleotide-free crystal structure of kinesin was available up to the time of this study (kinesin is structurally unstable in the absence of nucleotide and MT [221]), the ATP-like kinesin–tubulin structure (PDB id: 4HNA) was also used as the initial model for APO state. This approximation is reasonable, as both ATP state and APO state of kinesin protein is known to have high MT binding affinity. The docked neck linker in the PDB structure was truncated at residue 325 because it is disordered in the APO state. The ATP analogue, Mg ion and crystal waters at the active site of 4HNA were deleted to make the nucleotide binding pocket empty.

All three states had the same tubulin dimer model, obtained from the 4HNA structure. Missing residues in the models (residues 438–451 of α tubulin, 442–455 of β tubulin, 1–4 of kinesin) were modeled with the help of Modloop [222]. However, a missing loop in α tubulin (residues 39 to 45) was modeled by Modeller using the corresponding region of β tubulin as template. The protonation states of histidines were determined by the pK_a calculation using the PDB2PQR Web server (http://nbcr-222.ucsd.edu/pdb2pqr_1.9.0/).

6.2.2 - Flexible Fitting of the initial models into Cryo-EM Maps

Extensive conformational changes are expected to transform the initial structures to more accurate models for the three states through flexible fitting of cryo-EM maps. To this end, the initial models of the APO and ATP state were rigidly fitted into the corresponding cryo-EM maps [184] of MT filaments decorated by nucleotide-free and ADP-AlF_4-bound kinesin using the Chimera program [223]. For ADP state, a sequential fitting protocol was used to fit kinesin and tubulin dimer separately as two rigid bodies, in order to avoid atomic clashes between them. The ligands (Mg and ADP or ADP-AlF$_4$) were included when fitting the cryo-EM maps of ADP or ATP state. To further refine the kinesin-tubulin models, flexible fitting of the structures into the cryo-EM maps was performed with the MDFF program [198].

To prepare for the MDFF run, hydrogen atoms were added and each kinesin–tubulin model was immersed into a rectangular box of TIP3 water molecules extending to 12 Å from the protein periphery in *x*, *y* and *z* direction with the VMD program [224]. The three systems were neutralized at the physiological ionic concentration of 150 mM by adding Na$^+$ and Cl$^-$ ions. Energy minimization of 2000 steps was performed using the conjugate gradient method to remove bad contacts and optimize the initial models under the constraint of cryo-EM maps.

We performed a 10 ns MDFF simulation using the NAMD program [225] and the CHARMM27 force field [146], with gradual release of the map constraints. Water molecules were described by the TIP3P model [226]. The particle-mesh Ewald summation method [227] was used to evaluate long-range electrostatic forces with a grid size of <1 Å and an integration time step of 1 fs was used. A 12-Å cutoff distance was used for nonbonded interactions, and a temperature of 300 K was maintained using the Langevin thermostat [228] which was coupled to all heavy atoms with a damping coefficient of 5.0 ps^{-1}.

MDFF adds an external potential (U_{EM}) derived from the EM density map, to the usual MD potential [197].

$$U_{EM} = \sum_j \omega_j V_{EM}(\boldsymbol{r}_j)$$

where,

$$V_{EM}(\boldsymbol{r}_j) = \begin{cases} \xi\left[1 - \dfrac{\Phi(\boldsymbol{r}_j) - \Phi_{thr}}{\Phi_{max} - \Phi_{thr}}\right] & \text{if } \Phi(\mathbf{r}_\mathrm{j}) \geq \Phi_\mathrm{thr} \ ; \\ \xi & \text{if } \Phi(\mathbf{r}_\mathrm{j}) < \Phi_\mathrm{thr} \end{cases}$$

……………………… Eq. 6.1

Here, ω_j is a weight factor for each atom j, generally set to the atomic mass; ξ is a variable scaling factor to the potential; $\Phi(\mathbf{r}_\mathrm{j})$ is the EM map density at position $\mathbf{r}_\mathrm{j}$; Φ_{max} is the maximum EM density and Φ_{thr} is a cut-off threshold density, added to remove the solvent contribution to the map density. Each atom thus feels a force depending on the gradient of the electron density. In order to prevent over-fitting, another potential term U_{ss} is added, that enforces harmonic restraints to preserve secondary structure elements such as α-helices and β-strands. The parameters for U_{EM} and U_{SS} were set to be $\xi = 0.3$ kcal mol^{-1} and $k_{ss} = 300$ kcal mol^{-1} Å^{-2}, as recommended in ref [197]. To gradually release the cryo-EM restraints and allow a smooth transition to subsequent unconstrained MD simulation, ξ was lowered by 0.05 every 2 ns.

In order to investigate the convergence of cryo-EM-fitted models by different flexible fitting methods (including MDFF), two additional flexible fitting methods were also applied on the APO-state: EMFF [195] and Rosetta density fitting [196], resulting in two other APO-state models of kinesin–tubulin complex alternative to the MDFF-generated models.

6.2.3 - Classical MD Simulation

Following 8 ns MDFF simulation with gradual release of map restraints to zero, we continued with regular classical MD simulation of 100 ns at constant temperature and pressure. During the MD simulation, to stabilize the tubulin dimer structure and prevent global translational and rotational motions, while allowing for full flexibility of kinesin and kinesin–tubulin interface, we restrained the Cα atoms of tubulin residues which are greater than 12 Å away from kinesin by harmonic springs with force constant of 1 kcal mol^{-1} Å^{-2}. Four independent MD simulations were conducted following four MDFF runs, resulting in total 400 ns MD trajectories for each state, in the NPT ensemble. The Nose–Hoover algorithm [229] was used to maintain the temperature at 300 K and pressure at 1 atm. Periodic boundary conditions were applied to minimize the edge effects. A 10-Å switching distance and a 12-Å cutoff distance were used for nonbonded interactions. The SHAKE algorithm was used to constrain bond lengths involving hydrogen atoms, which allowed a time step of 2 fs for MD simulation. The frames of the trajectories were saved every 20 ps during MD simulation for later analysis, resulting in 5000 snapshots per trajectory. The NAMD program [225] with CHARMM27 force field [146] was used to run the simulations.

6.2.4 - RMSD and RMSF Analysis

To assess the conformational stability of the simulations, the root mean squared deviations (RMSD) of the structures from the initial models were calculated for the Cα atoms. For each snapshot *m*, the RMSD value is given by:

$$RMSD_m = \sqrt{\frac{1}{N}\sum_{n=1}^{N}|\vec{r}_{nm} - \vec{r}_{ni}|^2}$$

………………………. Eq. 6.2

where $\vec{r}_{nm}$ is the C_α atomic position of residue *n* in snapshot *m*, $\vec{r}_{ni}$ is the C_α atomic position of residue *n* in initial reference model *i*, and N is the total number of residues.

To quantify the local flexibility of kinesin residues in ADP, APO, and ATP state based on the equilibrium simulations, the root mean squared fluctuation (RMSF) was calculated for the last 50 ns of the four MD trajectories together for each state. The C_α coordinates of kinesin alone or kinesin–tubulin complex (excluding the floppy C-terminal loops of αβ-tubulin) were spatially aligned with minimal RMSD and the variance from the mean structure was calculated at each residue *n*:

$$RMSF_n = \sqrt{\frac{1}{M}\sum_{m=1}^{M} |\vec{r}_{mn} - \langle\vec{r}_n\rangle|^2}$$

……………………… Eq. 6.3

where $\vec{r}_{mn}$ is the C_α atomic position of residue *n* in snapshot *m*, $\langle\vec{r}_n\rangle = (\frac{1}{M})\sum_{m=1}^{M}\vec{r}_{mn}$ is the average C_α atomic position of residue *n*. The ensemble for each state consisted of 4 × 2500 snapshots. amaking *M* = 10000 snapshots for each of the three states.

6.2.5 - Principal Component Analysis (PCA)

Principal component analysis (PCA) was performed on the last 50 ns of the 4 trajectories in each state to identify dominant modes of structural fluctuations in the kinesin–tubulin complex during MD simulation. The ensemble used was similar to that used for the RMSF calculations, with 10000 snapshots for each state, and the C_α coordinates of kinesin–tubulin complex (excluding the floppy C-terminal loops of αβ-tubulin) superimposed with minimal RMSD. A covariance matrix comprised of the following 3 × 3 blocks was obtained:

$$C_{nn'} = \frac{1}{M}\sum_{m=1}^{M} (\vec{r}_{mn} - \langle\vec{r}_n\rangle) \otimes (\vec{r}_{mn'} - \langle\vec{r}_{n'}\rangle)$$

………………………. Eq. 6.4

Diagonalizing this covariance matrix gives the eigenvectors describing the directions of maximal fluctuations, each of which translates to a specific conformational change sampled within the ensemble. The eigenvalue of each mode gives the fractional contribution of that mode to the total structural fluctuations. We analyzed the top two modes with the highest eigenvalues.

6.2.6 - Kinesin–Tubulin Binding Free Energy Calculations

Kinesin-MT binding free energy was calculated for each trajectory using a continuum solvent model [230], where the total binding free energy ΔG is written as a linear combination of the electrostatic and van der Waals interactions. The scaling factors for this linear combination had been empirically parameterized for the kinesin-MT system previously in our lab [216, 217].

$$\Delta G = \Delta G_{np} + \Delta G_{elec} = \alpha E_{vdw} + \beta \Delta E_{elec}$$

………………………. Eq. 6.5

Here, E_{vdW} is the van der Waals interaction energy between kinesin and tubulin dimer leading to the non-polar contribution (ΔG_{np}) in the free energy. ΔE_{elec} is the change in electrostatic energy from unbound kinesin and tubulin to bound kinesin-tubulin complex. 10000 snapshots for each state was used from the last 50 ns of the simulations. E_{elec} was calculated using the Poisson–Boltzmann (PB) method [231, 232]. $\alpha = 0.158$ and $\beta = 0.153$ were calibrated using alanine-scanning data in lab [216]. Because of the high uncertainty in entropy calculation, the entropic contribution was not included to ΔG, which resulted in a negative shift of ΔG by 7–15 kcal/mol relative to true ΔG [207].

The CHARMM program [233] was used to obtain the residue-wise partitioning of ΔG, E_{vdW}, and ΔE_{elec}. Details of the method can be found in the CHARMM documentation (analys.doc and pbeq.doc at http://www.charmm.org/documentation/c37b1/index.html). Ranking the kinesin residues by the contribution to binding (ΔG_n), the top 5% (which corresponds to a p value of 0.05, a widely accepted standard for significance level) was predicted to be important to kinesin–tubulin binding.

6.3 - Results and Discussion

6.3.1 - Cryo-EM Map-fitted models of ADP, APO, and ATP States

In 2010, Sindelar and Downing obtained subnanometer-resolution (~8.9 Å) cryo-EM maps for kinesin-1 decorated MT filaments in all three states that we study here, namely, ADP, ADP-AlF_4 and nucleotide-free APO states [186]. This resolution gave a better picture of the secondary structural organizations and enabled the detection of certain structural differences at the nucleotide binding pocket and the MT binding interface between the tubulin-bound and unbound pictures of kinesins. Cryo-EM maps with similar resolution have also been obtained for kinesin-5 in different states [185, 187]. At such a resolution, these maps help in accurate modeling of protein structures by providing useful constraints and guiding the rearrangement of structural features by the electron density gradient. We used the kinesin-1 maps to perform rigid and flexible fitting of cryo-EM maps as described in the Methods section.

Starting off from the rigidly fitted initial models of the kinesin-tubulin complex in the three different states (ADP, APO and ATP states), we used the map densities [186] to further optimize the structures using the Molecular Dynamics Flexible Fitting (MDFF) program [197, 198]. Four independent MDFF simulations with different random seeds were performed for each of the three states. Each of the MDFF runs were 10ns long, and involved a gradual release of the cryo-EM map restraints, in order to prevent any sharp changes in the structural perturbation by the fitting forces and allow for a smooth transition to subsequent unconstrained MD simulations.

As a measure of the fitting quality, the local cross-correlation coefficient (CCC) was calculated between the cryo-EM map densities and the electron densities within 8.9 Å of the molecular surface of the modeled kinesin-tubulin structures. As predicted, the MDFF did indeed improve the fitting the structural models over rigid fitting (Figure 6.2). The CCC values improved between rigid and flexible fitting from 0.65 to 0.72 in ADP state, from 0.67 to 0.79 in APO state, and from 0.80 to 0.86 in ATP state, supporting the advantage of using a flexible fitting protocol.

The MDFF simulations induced extensive conformational changes to transform the initial structures to the final models. Indeed, the largest conformational changes were observed in the APO state, which underwent an overall RMSD of ~ 3.5 Å over the course of the flexible fitting. This is not surprising, since the initial model started out from an ATP-like structure. The primary transformations involved a clockwise rotation of kinesin on top of tubulin dimer (Figure 6.2(b)), and restructuring of the tubulin-binding interface (Figure 6.3(a)) and the nucleotide-binding pocket (Figure 6.3(b)).

The flexible cryo-EM fitting thus gives us a better match to the physiological structures. However, to test the reliability of a model built through such extensive structural perturbations, we analyzed the convergence of such cryo-EM map fitted models obtained through different flexible fitting methods, using the APO state as our test case. The APO structure obtained through the MDFF runs were compared to those from two other standard techniques, namely, EMFF [195] and Rosetta density fitting [196]. The four independent MDFF runs generated very similar models of APO state (RMSD ≤ 1 Å between each MDFF model and the average structure of four MDFF models). The alternative models generated by EMFF and Rosetta were also fairly similar to the MDFF models (RMSD ≤ 1.9 Å relative to the average structure of four MDFF models). The conformational changes predicted by the three flexible fitting methods were also very similar at the tubulin-binding interface (e.g., in loop L11, loop L12, sideward shift in α4 helix and rotation of α6 helix; Figure 6.3(a)) and the nucleotide-binding pocket (e.g., in switch I and II; Figure

6.3(b)). Therefore, the flexible fitting of kinesin-tubulin complex in sub-nanometer cryo-EM maps indeed enable robust structural modeling by presenting sufficient geometric constraints.

6.3.2 - Conformational Differences between ADP, APO, and ATP States

We looked into the structural differences between the flexible-fitted models of ADP, APO and ATP states. These differences reveal the key conformational features that distinguish the different ATPase events of kinesin (ADP release and ATP binding). Large global conformational changes were observed between ADP/APO and ATP states, highlighting a counterclockwise rotation of kinesin on top of the microtubule (Figure 6.4(a)), and a seesaw-like rotation of kinesin as viewed along the MT axis (Figure 6.4(b)). These key features have also been observed in previous cryo-EM studies of kinesin-1 [186] and kinesin-5 [185]. A tilting motion of kinesin towards tubulin was observed in a previous study of kinesin-5 [187], from ADP to APO state, which was not replicated in our current kinesin-1 study.

The local changes observed between the states will be discussed separately for the kinesin-tubulin interface and the nucleotide-binding pocket.

The Kinesin–Tubulin Interface (Figure 6.4(c))

The MDFF-generated kinesin–tubulin models in three ATPase states were superimposed along the tubulin dimer in order to determine the key structural differences that distinguish the states. Loop L7 was found to move further away from tubulin in the weak MT-binding ADP state, as compared to the APO and ATP states. In these two states, loop L7 moves closer to MT, supporting its role in sensing and facilitating strong MT binding [234]. Loop L8 has been predicted in literature to be an anchor point of kinesin on tubulin during the ATPase cycle [179]. We found loop L8 barely moves between these states, supporting its role as a pivot for kinesin on MT. Similarly, the position and orientation of the α4 helix remained roughly stable and fixed in all three states, as has been observed before [185, 186]. But we also noticed a slight bending of its C-terminal region and adjacent loop L12 closer to tubulin in APO state than ADP and ATP state. The N-terminal region of loop L11, where the residues have been known to play a role in enabling strong MT binding [180], moves closer to tubulin in APO and ATP state than ADP state. α6 helix was found to adopt different orientations between ATP state and the other two states, moving closer and aligning with the central beta sheet, thus accommodating a distinct docked neck linker conformation in the ATP state.

The Nucleotide-Binding Pocket (Figure 6.4(d))

Next, we studied the nucleotide-dependent structural changes of switch I and II, by superimposing the MDFF-generated kinesin models of three ATPase states along P-loop, since P-loop is known to be relatively stable between these states. There is a short helical turn in Switch I in the ADP state, and it moves away from P-loop. Switch I is extended and close to P-loop in APO and ATP states. In other words, switch I undergoes a large open-to-close movement from ADP state to APO state, and further close in the ATP state. Thus, in the APO state, switch I adopts an intermediate conformation between the open position of ADP state and the closed position of ATP state, whereas switch II adopts a more open position than ADP and ATP state. This supports a previous proposal that a fully open switch II enables complete release of Mg and ADP [235]. However, these are *static* pictures of switch I and II determined by cryo-EM fitting, whereas, under physiological conditions the two switch regions sample an ensemble of *dynamic* conformations. The considerable variations in switch I among different kinesin crystal structures [236] further indicate its dynamic nature. The MD simulation studies of these states and the analysis of the fluctuations of the nucleotide binding pocket (involving key residues of P-loop, switch I, and switch II) will thus shed light on the dynamic properties.

6.3.3 - MD Simulations of ADP, APO, and ATP States

While the MDFF-generated models provide reasonable static structural pictures, the dynamic information is absent. Moreover, the cryo-EM fitting forces may lead to minor distortions and clashes in local structures or the resultant structures may still retain some residual features of the initial models. Therefore, in order to further optimize the structures, and explore the dynamic behaviors of kinesin interacting with tubulin dimer under physiological conditions, we performed four independent 100 ns-long MD simulations of kinesin–tubulin complex in the presence of solvents and ions progressing from the MDFF-generated models of ADP, APO, and ATP state (see Methods).

At the end of the 100ns simulations, we calculated the RMSD for C_α atoms relative to the starting MDFF models in order to assess the conformational stability and to make sure that the systems have reached a local equilibrium (Figure 6.5). For all MD trajectories, the system stabilized within <50 ns as indicted by saturating RMSD ∼2 Å. The variance in the RMSDs between different trajectories was less than 1 Å. So we kept 4 × 2500 snapshots of the last 50 ns of four MD trajectories in each state, and combined them to construct a structural ensemble for each state for further analysis of the trajectories. As a control for robustness of our MD-based calculations, we repeated all the analyses for the last 25 ns of MD trajectories to ensure the results are not sensitive to the chosen lengths of the trajectories.

As a further test of the stability of the binding interface between kinesin and tubulin dimer during MD simulation, we calculated the kinesin–tubulin contact surface area (CSA) for four MD trajectories in ADP, APO, and ATP state (Figure 6.6). The CSA is defined here as half the difference between the solvent accessible surface areas of unbound proteins (kinesin and tubulin separately) and the bound complex using the SASA program [237]. Although the CSA values are highly fluctuating (Table 6.1), the overall mean of CSA remained stable during the last 50 ns of the MD simulation, suggesting no destabilization of the kinesin–tubulin interface during MD simulation. Consistent with stronger MT binding in APO and ATP state than ADP state, the CSA values are significantly higher in APO and ATP state than ADP state (see Table 6.1). The fluctuations between the trajectories is also significantly higher in the ADP state, further suggesting a less stable kinesin-MT interaction.

6.3.4 - Flexibility Analysis of Kinesin Residues

The root mean squared fluctuations (RMSF) of individual kinesin residues was measured as an average of all four trajectories for each of the three ATPase states, for the last 50ns of the MD simulations. The amplitude of fluctuations was measured both with respect to the mean kinesin-tubulin structure to highlight the effects of kinesin and tubulin relative motions (Figure 6.7(a)), as well as with respect to an average structure of kinesin alone in order to focus on fluctuations within kinesin itself (Figure 6.7(b)). The flexibilities in all three states are comparable within kinesin (Figure 6.7(b)), which is in contrast to an earlier finding [214] where the kinesin was found to be more flexible in the nucleotide-free APO state than the ADP and ATP states. Our finding supports the fact that it is the binding of tubulin that dictates the kinesin dynamics. Overall, kinesin is more flexible in ADP state than APO and ATP state (see Figure 6.7(a)), which can be mainly due to a greater mobility of the weakly bound kinesin relative to tubulin dimer in ADP state [238], with lesser interactions with MT to rigidly hold the kinesin head. On the basis of the RMSF calculation, we further analyzed nucleotide-dependent changes in local flexibility at the kinesin-tubulin interface and the nucleotide-binding pocket.

The Kinesin–Tubulin Interface

Consistent with the weak MT binding nature of the ADP state, the tubulin-binding interface (e.g., loop L7, L8, L11, and α4 helix) exhibits higher flexibility than in the APO and ATP states (Figure 6.7a). Loop L11 is also quite flexible in the strong MT-binding APO and ATP states (Figure 6.7). The functional importance of L11 flexibility in communicating between MT sensing and nucleotide interactions was highlighted by an S to G substitution in residue position 239 of a fast fungal kinesin [239]. α6 helix is much less flexible in ATP than in ADP and APO states (Figure 6.7), which is consistent with distinct neck-linker docked conformation in the ATP state, as compared to being disordered in the other two states.

Some structural studies [180, 181, 240] speculate that the N-terminal region of α4 helix undergoes nucleotide-dependent extension and shortening, while the cryo-EM studies of kinesin-decorated MT filaments [185, 186] suggest otherwise. To address this issue, we compared the RMSF in this region between three ATPase states, and found similar RMSF distribution with comparable flexibility in APO and ATP state (Figure 6.7(b)). Visual observation of the MD simulations of tubulin-binding interface in ADP, APO, and ATP state also showed α4 helix to be structurally stable except for transient unwinding of one turn at the N-terminus, supporting the idea that the change in the length of α4 helix is insignificant between various ATPase states.

The Nucleotide-Binding Pocket

At the nucleotide-binding pocket, switch I is more flexible in the APO state than in the ATP and ADP states (Figure 6.7). The higher dynamics here is due to the absence of nucleotide interacting with switch I. The 'front door' of the pocket can thus dynamically open to allow for nucleotide entry, in preparation for the next step in the ATPase cycle. In contrast, switch II (along with loop L11 that immediately follows) is more flexible in ADP state than ATP and APO state (Figure 6.7). This indicates that there is an allosteric connection between destabilization of switch II – nucleotide interactions and weak MT binding in the ADP state. The destabilization of switch II may aid in opening the 'backdoor' to the pocket, which may be a path of eventual release of ADP. A disordered switch II in ADP state has also been observed in a recent cryo-EM study of kinesin-5 [187].

6.3.5 - Analysis of the Twist of Central β-Sheet in Kinesin

There have been some proposals that suggest that a twist of central β-sheet facilitates strong MT binding and ADP release in kinesin [235, 241], similar to that observed in myosin protein. We quantified this twist of the β-sheet in the MDFF and MD simulated structures of ADP, APO, and ATP state (Table 6.2), and analyzed them in in comparison with crystal structures of kinesin and myosin (Table 6.3). This twist angle was defined as the angle between strands β1 and β4. β1 was represented as a vector joining the Cα atom of residue K10 to that of R14, and β4 was represented as a vector joining the Cα atom of residue V132 to that of E136. All 4 residues used as markers here are structurally conserved between kinesin and myosin (Figure 6.8).

Crystal structures of myosin are available in three ATPase states (ADP-Pi state, ATP state, and APO state). The twist angle was found to increase in total by about 25° in the order of ADP-Pi < ATP < APO. In comparison, within crystal structures of kinesin (available in ATP-like and ADP-like states), the twist angle increases by <10° from ATP-like to ADP-like state. In our MD simulations, the twist angle was found to increase from 63.8 ± 2.5° in ATP state to 68.3 ± 3.5° in ADP state, a similar order of change as in the crystal structures. The APO state showed a greater twist (70.6 ± 3.2°) than both ADP and ATP state, which is greater than even the maximum twist angle (~69°) observed in a KIF14 crystal structure [242]. The MDFF-generated models showed lesser twist in β-sheet compared to that in the MD simulations, highlighting the importance of dynamic fluctuations in guiding the β-sheet twist in kinesin.

Interestingly, one of the MD trajectories in ADP state (trajectory # 4) showed an unusually large twist angle (72.3 ± 2.7°). A detailed structural analysis of this trajectory indicated a more open switch I at the nucleotide-binding pocket (Table 6.5), paired with a larger kinesin-tubulin contact surface area (Table 6.1). Our findings together support the fact that the twisting of the central β-sheet plays an important role in strong MT binding of kinesin, similar to that observed in myosin [235, 241].

In another recent study [213], the twist of the central β-sheet was analyzed through MD simulations by calculating the tilt angles between adjacent β strands (i.e., β3-β4, β4-β5, and β5-β6) (see Figure 6.8). For a direct comparison with the results of ref [213], we also calculated the tilt angles ϕ_{34}, ϕ_{45}, and ϕ_{56} between neighboring β strands (i.e., β3-β4, β4-β5, and β5-β6) (see

Table 6.4). Similar to this study, we found that the ϕ_{34} angle was largest in ATP and smallest in ADP state. Angle ϕ_{56} was the largest in ADP and smallest in APO state for both the studies. However, in contrast to ref [213], we found that the ϕ_{45} angle was largest in ATP and smallest in APO states, while ref [213] found the smallest ϕ_{45} in ATP state. It is not clear if this disagreement is caused by differences in modeling and simulation or the fact that kinesin-3 molecule was used in ref [213].

6.3.6 - Allosterically Coupled Motions through PCA of the APO state

It is generally believed that the ATPase-driven motility of kinesin is primarily guided by allosteric couplings between the nucleotide-binding pocket, the MT-binding site and the neck linker, with the ATPase activity being facilitated by the presence of MT binding. In order to study the major conformational changes among various kinesin crystal structures, principal component analysis (PCA) has previously employed [214, 243]. However, the applicability of the results of these studies was limited by the lack of tubulin binding in these structures. Thanks to our extensive MD simulation of the kinesin–tubulin complex in three ATPase states, we are now able to address this outstanding issue. We performed PCA on the MD-generated structural ensemble of APO state as described in the Methods section, and identified the dominant modes of structural fluctuations which may allosterically couple distant sites of kinesin and initiate conformational transitions between different ATPase states.

For the APO system, the top two dominant PCA modes accounted for 32% and 18% of the overall structural fluctuations respectively, and we focused on these. Mode 1 predicts extensive global and local conformational changes, including a clockwise rotation of kinesin on tubulin dimer, with α4 helix roughly anchored in place, a reorientation of α6 helix to allow docking of neck linker, closing of switch I on the nucleotide pocket relative to P-loop, and a movement of loop L11 toward the nucleotide-binding site, away from MT (Figure 6.9(a)). Interestingly, all these conformational changes are similar to the features of the ATP state simulations, suggesting that our extensive MD simulation in APO state was able to sample conformational space in the direction of ATP state even in the absence of ATP binding.

Mode 2 primarily predicts the local conformational changes involving the opening of switch I relative to P-loop and a movement of loop L11 toward tubulin (Figure 6.4(b)). Similar local conformational changes were also observed in the PCA of ADP state. This may suggest that MT binding triggers opening of the nucleotide-binding pocket to allow ADP release. This finding supports the proposed role of switch I displacement in stimulating Mg-ADP release [239]. The dominant PCA modes revealed high flexibility of switch I in APO state in agreement with the analysis of RMSF and dynamics of the nucleotide-binding pocket (Figure 6.7 and Table 6.5). L8 in both the modes showed very little change.

Our PCA based on the APO-state MD simulation thus indicates large global and local structural fluctuations that bring about the conformational transition toward ATP state, and elucidate how MT binding facilitates opening of the nucleotide-binding pocket to allow ADP release.

6.3.7 - Opening and closing of the nucleotide-binding pocket in MD simulations

In order to study the dynamic picture of the nucleotide-binding pocket and its variation between ADP, ATP, and APO state states (Figure 6.4(d)), we further analyzed the fluctuations of the nucleotide-binding pocket during MD simulation in these states, which involve opening/closing movements of switch I and II (relative to P-loop), coupled with a change in the coordination with the nucleotide. Following ref [242], we measured the following key atomic distances between selected nucleotide-binding residues and ADP:

$D_{85,234}$: the distance between C_α atoms of residues G85 (P-loop) and G234 (switch II), which gives a measure of the openness of switch II relative to P-loop.

$D_{91,202}$: the distance between C_α atoms of residues K91 (P-loop) and S202 (Switch I) to study the opening/closing of switch I relative to P-loop.

$D_{203,236}$: the minimal distance between NH1/NH2 atom of R203 (Switch I) and OE1/OE2 atom of E236 (Switch II) to assess the formation of a key salt bridge between switch I and II (using a criterion of $D_{203,236}<4.5$Å).

$D_{P\beta,202}$: the distance between P_β atom of ADP and C_α atom of residue S202 to assess the closeness ADP to switch I.

$D_{P\beta,91}$: the distance between P_β atom of ADP and C_α atom of residue K91 to assess the closeness of ADP to P-loop. The results are summarized as follows (see Table 6.5):

ADP state: Switch II seems to open up from the MDFF-generated configuration during the MD simulations (as indicated by $D_{85,234}$), especially in the 2nd and 3rd trajectory. In contrast, switch I is on average more closed during the MD simulations (as indicated by $D_{91,202}$). The 4th trajectory however, shows a more open switch I compared to the others and it also has the weakest coordination of ADP by switch I (as indicated by $D_{P\beta,202}$). The 4th trajectory also shows a greater twist of central β−sheet (Table 6.2) accompanying a larger kinesin-tubulin contact surface area

(Table 6.1). These together give compelling evidence of allosteric coupling between MT-interactions and nucleotide binding pocket. The key salt bridge between R203 of switch I and E236 of switch II only forms in two of the four trajectories, suggesting that the ‘backdoor’ of the pocket remains partially open in ADP state. In qualitative agreement with our finding, a recent cryo-EM study of kinesin-5 [187] observed an open nucleotide binding pocket with disordered switch II in ADP state.

ATP state: Compared to the ADP state, both switch I and switch II are on average more closed and less variable in the ATP state simulations (as measured by $D_{91, 202}$ and $D_{85, 234}$ respectively). Although the R203-E236 salt bridge is present in all four MDFF-generated models, it is removed in two of the four trajectories during the MD simulations. The above finding suggests that this salt bridge is highly dynamic in ATP state, despite the nucleotide-binding pocket being most closed and less flexible in ATP state. Even though some studies suggest that the formation of this salt bridge is required to lock the ‘backdoor’ of a closed nucleotide-binding pocket for ATP hydrolysis in kinesin [240, 244], our findings indicate otherwise. To probe the role of neck linker docking in allosteric regulation of the nucleotide-binding pocket [245, 246], we performed four 100-ns-long MD simulations for an alternative kinesin construct with neck linker truncated at the end of α6 (residue 325) in ATP state, and then analyzed the dynamics of nucleotide-binding pocket. The neck-linker truncation led to a more open and flexible switch I and weaker coordination of ADP by switch I in one of four MD trajectories. This preliminary finding supports the role of neck linker docking in allosterically stabilizing the nucleotide in the binding pocket.

APO state: Switch II is the most open and flexible in the APO state (as indicated by $D_{85,234}$), which is consistent with our RMSF results and the observation from the cryo-EM-fitted models (Figure 6.4(d)). Switch I is also more open and flexible than ADP and ATP state (as indicated by

$D_{91,202}$), which can be attributed to the higher flexibility during the MD simulations (Figure 6.7). Trajectory # 4 shows the maximum openness, with $D_{91,202}$>10Å which is comparable to an open switch-I conformation observed in a recently published KIF14 structure [242]. The switch I-switch II salt bridge forms partially in two out of four trajectories.

Summarizing, both switch I and switch II are most flexible in the nucleotide free APO state, undergoing a transient opening, less so in the ADP state, while the ATP state (in the presence of docked neck linker) features the most closed and the least flexible nucleotide-binding pocket.

6.3.8 - Calculation and Partition of Binding Free Energy

It has been established by various biochemical measurements [177, 247], that kinesin binds MT variably during the different ATPase states, with strong kinesin-MT affinity in APO and ATP state, and weak MT affinity in ADP state. It is this difference in MT-binding affinity that allosterically drives the structural changes that lead to events like ADP release, ATP binding and hydrolysis, neck linker docking and force generation, bringing about the processive stepping action of kinesins. In previous studies from our lab [216, 217], an empirical binding free energy measurement protocol for the kinesin-tubulin complex was established (see Methods), which yielded stronger (more negative) binding free energy (denoted ΔG) for APO and ATP state than ADP state. Here we recalculated ΔG based on the new kinesin–tubulin models and more extensive MD simulations. While the ΔG value of APO or ATP state is similar to the old value from ref [217], ΔG is weaker (less negative) for ADP state (see Table 6.6). The longer and unrestrained simulations makes the kinesin more mobile in the weak-binding ADP state, resulting in its moving further away from tubulin dimer. However, the higher mobility of kinesin also involves more favorable entropy (not considered in our calculation) which partially compensates the unfavorable binding energy. From our breakdown of ΔG into electrostatic (polar) and van der Waals (nonpolar) contribution, we observed that both polar and nonpolar contribution follows the order of ADP < ATP ≤ APO, which correlates well with ΔG (see Table 6.6) and the kinesin–tubulin contact surface area (see Table 6.1). The magnitude of the non-polar contribution is higher than the polar contribution, indicating the importance of van der Waals interactions in kinesin-tubulin binding. The polar contribution correlates with hydrogen bond (HB) analysis (see Figure 6.10 and Appendix 1) which can also be used to distinguish between weak and strong MT-binding states, and identifying key residues involved in kinesin–tubulin binding.

To understand which residues contribute most to differential kinesin-tubulin binding among the states, we partitioned ΔG among individual kinesin residues (see Methods and ref [248]) and kept the top 5% kinesin residues for each state (Table 6.7). As expected, they are distributed over known MT-binding motifs including loop L2 (K44), L7 (K141), L8 (K159, R161, and K166), L11 (K237, V238, S239, K240, and L248), L12 (Y274 and R278), α4 (K252, N255, K256, and N263), α5 (K281 and R284), and α6 helix (K313 and R321). A large number of them are positively charged residues with a few polar (S239, N255, and N263) and nonpolar residues (V238, L248, and Y274). This highlights the importance of extensive electrostatic interactions and local nonpolar interactions to kinesin–tubulin binding. Many of them were also identified by the HB analysis (Figure 6.10 and Appendix 1). Some of residues, such as K159, K237, V238, S239, K240, L248, K252, N255, K256, Y274, R278, K281, and R284, contribute more to the strong MT-binding APO and ATP state than the weak MT-binding ADP state. Thus, through this *in silico* study, we are now armed with a comprehensive list of mutational targets that can be targeted and tested through *in vitro* experiments to further understand kinesin-MT binding.

6.4 - Addressing Outstanding Issues in Kinesin Study

Twist of the Central β-Sheet

Myosin which is another type of motor protein and shares common evolutionary ancestors with kinesin has been shown to display a higher twist of the central β-sheet in its APO-like rigor-conformation while simultaneously displaying stronger actin-binding and the opening of the nucleotide pocket to release Pi and ADP [249, 250]. These findings led to speculations that the kinesin catalytic core may undergo a similar twist of its central β-sheet to enable strong MT binding [241] and MT-activated ADP release [235]. Some studies have corroborated these speculations. For example, a large twist of the central β-sheet was observed in a recent ADP-bound K1F14 crystal structure [242], cryo-EM investigation of kinesin-14 motors displayed differences in the central β-sheet [183], and computational MD simulations of KIF1A (kinesin-3) demonstrated nucleotide-dependent β-sheet twisting [213]. However, some other studies have failed to replicate such nucleotide-dependent central β-sheet twisting in kinesin-1 [186] and kinesin-5 [185]. To address this issue, we examined the angle of twist in the central β-sheet of kinesin-1 during the MD simulation in ADP, APO, and ATP state in comparison with various crystal structures of kinesin and myosin (Table 6.2 and Table 6.3). In our simulations, we observed a more twisted β-sheet in APO state than ADP and ADP state. The MDFF structures did not show twist angles as high as the MD simulations, which corroborates the importance of structural dynamics in the central β-sheet twisting. Also, one of our ADP-state simulations indicated a correlation of the β-sheet twist (Table 6.2) with opening of switch I (Table 6.5) and stronger kinesin–tubulin area of contact (Table 6.1). In fact, a current preliminary study from our lab also demonstrates a strong negative correlation between the central β-sheet twist and the electrostatic energy of kinesin-tubulin binding. Our findings thus support the proposed role of β-sheet twist in enabling strong MT binding [241] and ADP release [235].

Stability of α4 Helix

It is established that the α4 helix undergoes lengthening by ~3 turns, with the L11 simultaneously shortening, as the kinesin head transitions from free to MT-bound conformation. Moreover, a recent structural study of a KIF4 motor [240] proposed that the length of α4 helix (and adjacent loop L11) undergoes a nucleotide-dependent change during the ATPase cycle of kinesin, while being bound to MT and coupled with the ATPase state and nucleotide-binding pocket conformation changes. Additionally, a cryo-EM study of an APO-state kinesin-14 motor protein [183] observed a structural melting of a single turn of the α4 helix. However, no such extension or shortening of α4 helix was observed in cryo-EM studies [185, 186] of kinesin-1 and 5. To address this issue, we analyzed the structural flexibility of α4 helix during our MD simulations (Figure 6.7). α4 helix was found to be structurally stable in all three states, with a slight bend at the C-terminal end (towards L12) in the APO state. In fact α4 helix acts like a pivot for other global conformational rotations on top of the MT.

Importance of Neck Linker Docking

Neck linker docking is established to play a role in ATP hydrolysis and subsequent stepping forward of the trailing kinesin head [245, 246]. However, the structural and dynamic basis of the effect of neck linker docking remains undetermined. To probe this, we have compared MD simulation for kinesin ATP state with two different neck-linker constructs: one with an extended and docked neck linker and the other with the neck linker truncated after α6 helix, at residue 325. Interestingly, the construct with no neck linker exhibited a more flexible and open switch I, suggesting that neck linker docking is allosterically coupled with a closed nucleotide-binding pocket, thus allowing for stabilizing the nucleotide, leading to ATP hydrolysis.

MT-Activated ADP Release

Our simulation results confirm that kinesin-MT interactions lead allosteric modulation at the nucleotide-pocket and subsequent stimulation of ADP release [251], by revealing an open and highly flexible switch I in APO and ADP state (Table 6.5 and Figure 6.8). Our simulations also predict a more open switch II in APO state than ADP state (see Table 6.5 and Figure 6.4(d)), which may further destabilize Mg-ADP coordination by switch II [236, 244]. Moreover, the number and occupancy of hydrogen bonds at the nucleotide binding motifs with each other and with the nucleotide is significantly lower at the ADP state compared to the ATP state. All these indicate that MT binding is structurally and dynamically coupled with ADP release.

6.5 - Future Direction

We have corroborated the proposal that kinesin- microtubule binding depends on nucleotide state. But it has been widely suggested that it is also affected by the direction of strain applied by the neck linker joining the two catalytic heads [252, 253]. This strain acts as the coordinator that helps in processive walking of the motor protein along microtubule tracks. As the natural subsequent step or our study, we are currently studying the effect of this strain by applying steered molecular dynamics to mimic the intramolecular force: in the backward direction for the nucleotide-tree APO state, and in the forward direction for the ATP-bound state. We aim to determine the variation of kinesin-MT binding due to the external force, elucidate the primary structural differences that occur under these conditions, and identify the key residues involved in the force-regulation of kinesin-microtubule binding affinities. This shall complement the study already described in unraveling the details of processivity that guides kinesin transport on microtubules.

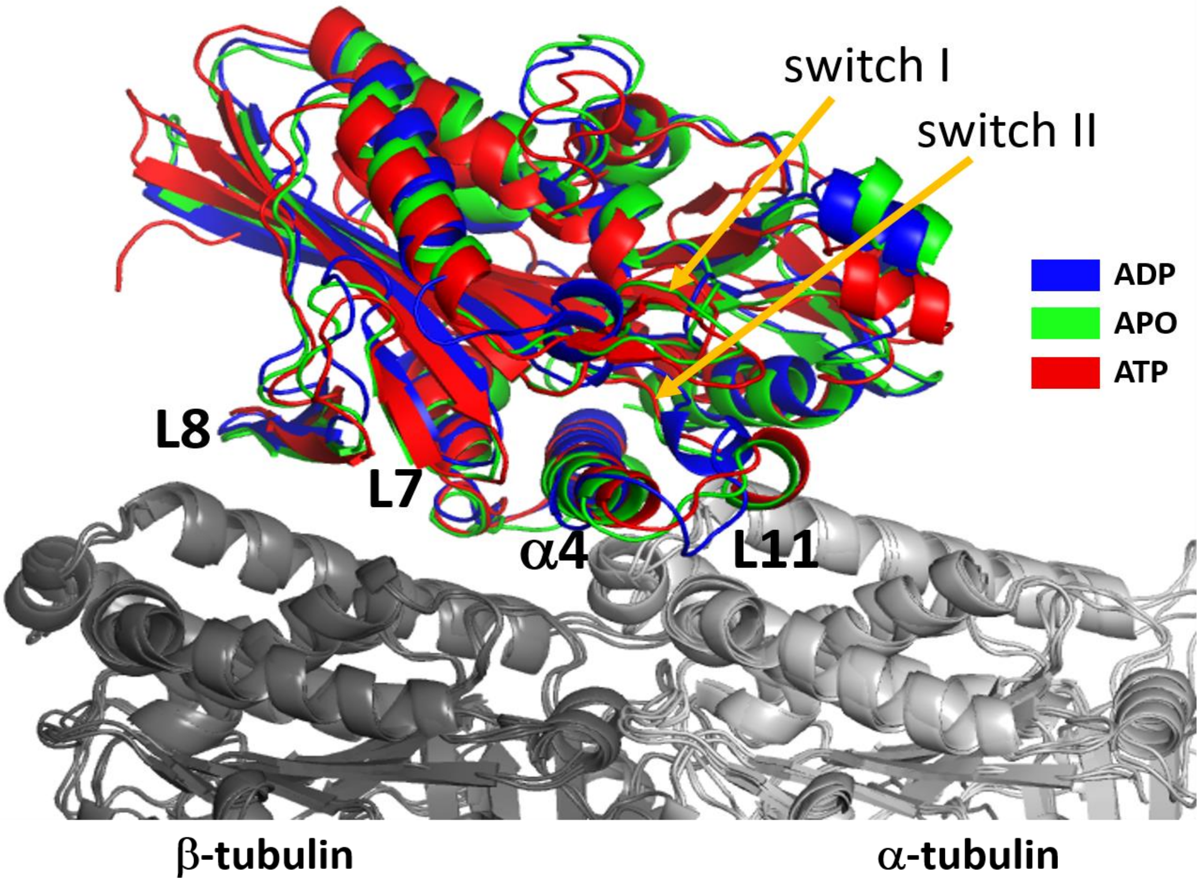

Figure 6.1: **Comparison of cryo-EM fitted models of kinesin head in APO, ADP- and ATP-like states, bound to a microtubule dimer.**

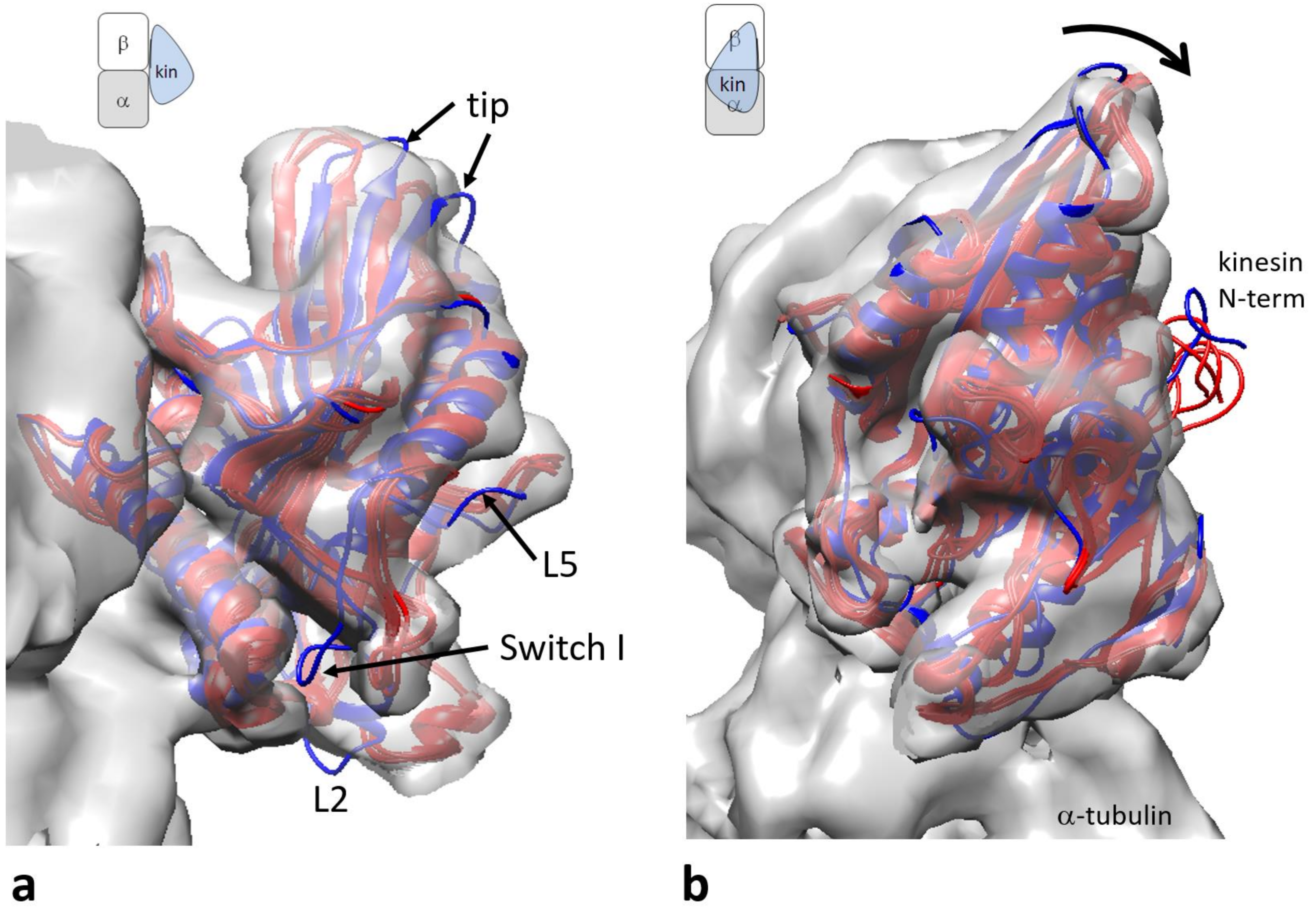

Figure 6.2: **Comparison of rigid-fitted and flexible-fitted kinesin-tubulin models overlaid with cryo-EM map** in APO state: (a) side view; (b) top view. The rigidly fitted model (PDB id: 4HNA) is colored blue, and four flexibly fitted models generated by MDFF are colored red. Several regions of the rigidly fitted model which are not fitted within the cryo-EM densities are labeled. In panel (b), the arrow indicates the clockwise rotation of kinesin on MT.

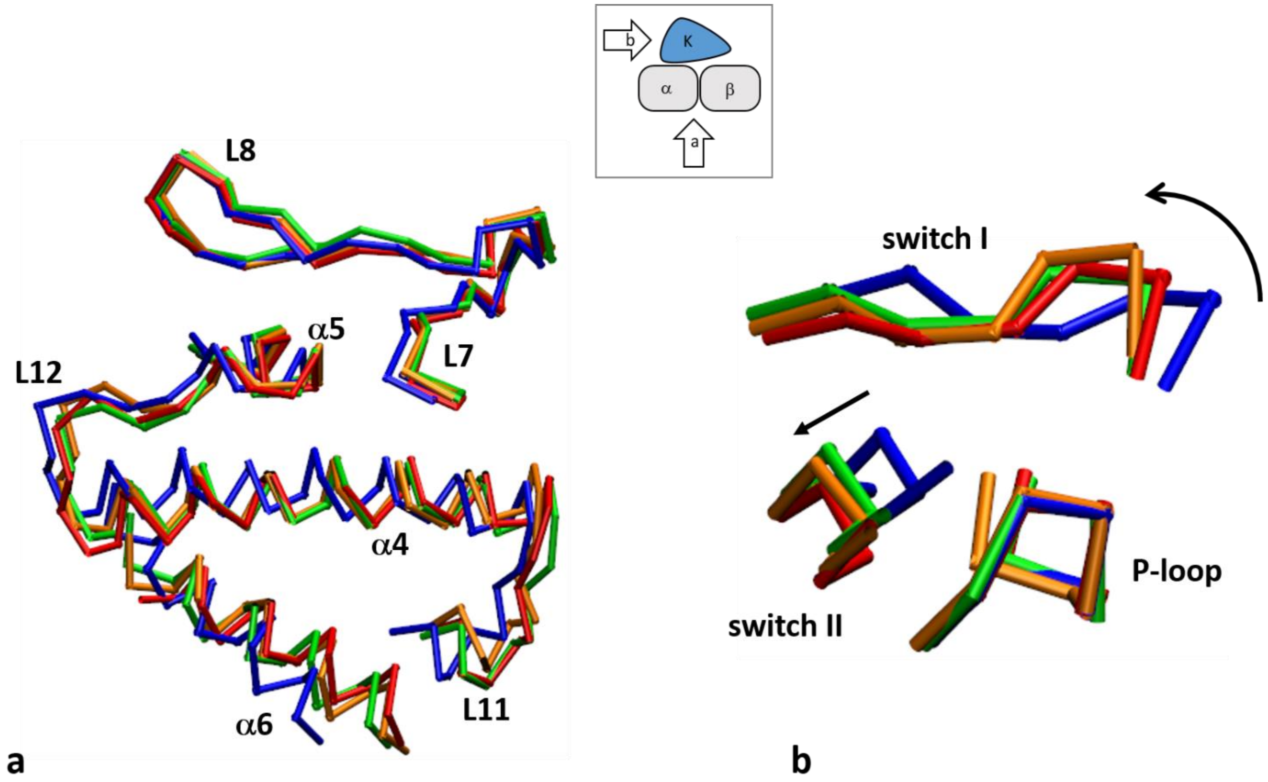

Figure 6.3: Comparative visualization of APO-state kinesin-tubulin models built by rigid fitting (blue) and three flexible fitting methods --- MDFF (red), EMFF (green) and Rosetta (orange); the directions of viewing given in inset cartoon: (a) at tubulin-binding interface (with tubulin dimer removed); (b) at nucleotide-binding pocket. The MDFF model shown here is an average structure of four models independently generated by MDFF. The three flexibly fitted models are more similar to each other (with RMSD<1.5Å) than they are to the rigidly fitted model (RMSD=3.3-3.6Å). In panel (a), important tubulin-binding motifs are labeled. In panel (b), opening movements of switch I and II during flexible fitting are indicated by arrows.

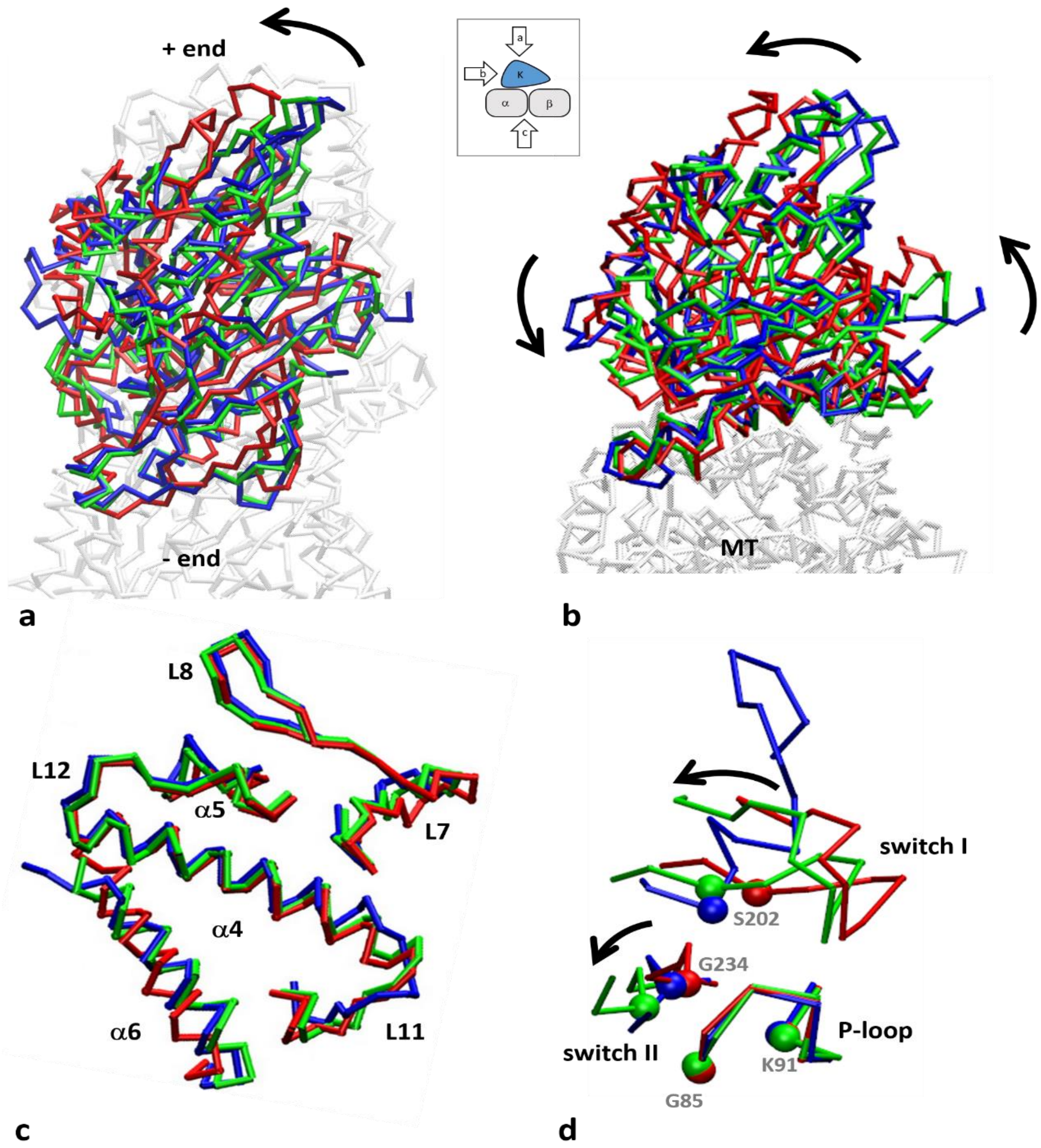

Figure 6.4: Conformational differences between flexibly fitted models of kinesin–tubulin complex in ADP, APO, and ATP state: (a) top view of a rotation of kinesin relative to tubulin (from ADP and APO state to ATP state, indicated by arrow); (b) side view of a seesaw rotation of kinesin relative to tubulin (from ADP and APO state to ATP state, indicated by black arrows); (c) bottom view (with tubulin dimer removed) of movements of tubulin-binding motifs in kinesin (including loop L7, L8, L11, L12, and α4, α5, α6 helix as labelled); (d) movements of switch I and II in the nucleotide-binding pocket (with P-loop as reference and key residues shown as spheres and labelled). Models of ADP, APO, and ATP state are colored blue, green, and red, respectively. The viewing directions of panels (a)–(c) are shown in a cartoon inset.

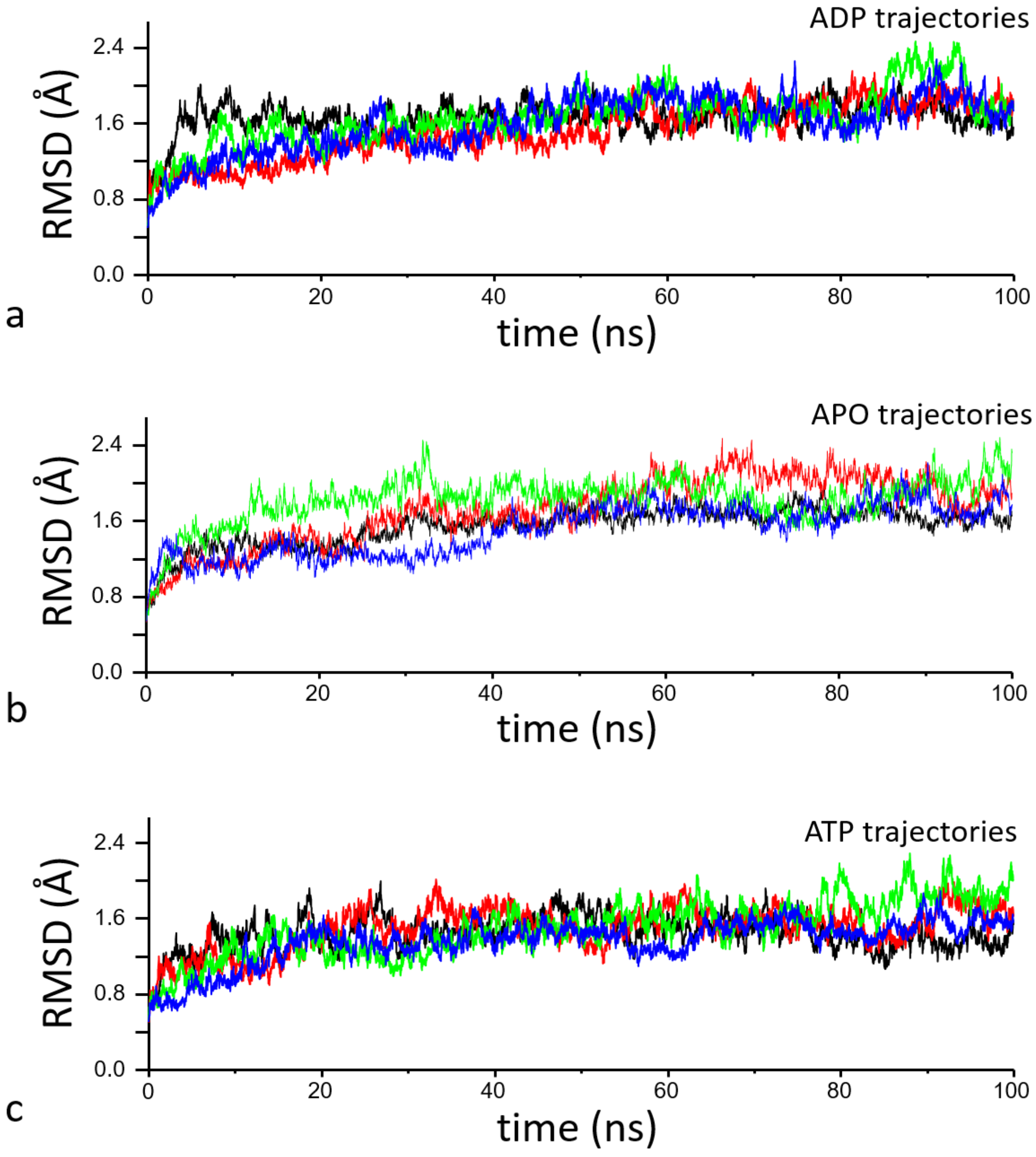

Figure 6.5: Root mean squared deviation (RMSD) as a function of time for each MD trajectory in: (a) ADP state, (b) APO state, (c) ATP state. The 1st, 2nd, 3rd and 4th trajectories are colored black, red, green and blue, respectively.

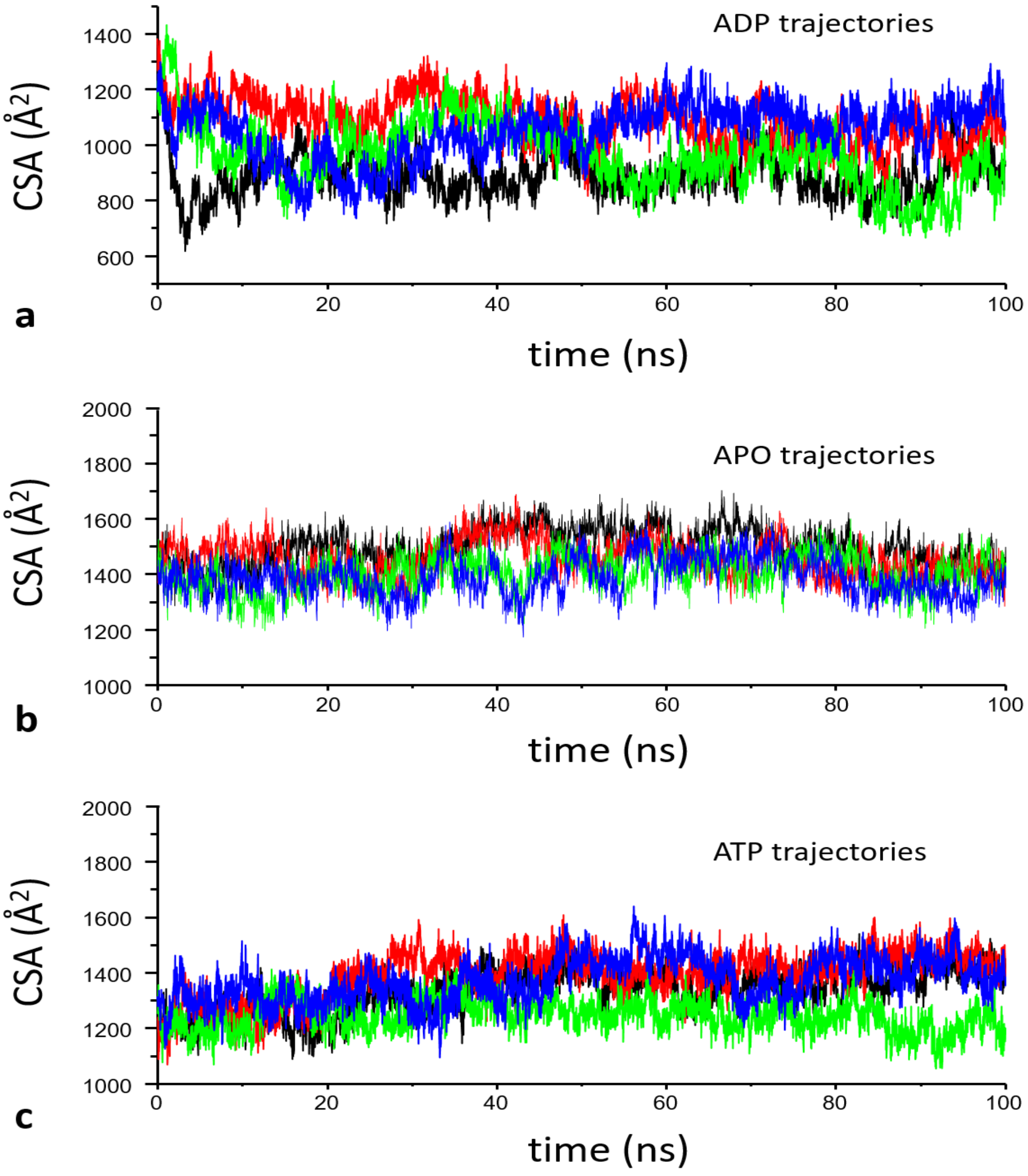

Figure 6.6: Kinesin-tubulin contact surface area (CSA) as a function of time for each MD trajectory in: (a) ADP state, (b) APO state, (c) ATP state. The 1st, 2nd, 3rd and 4th trajectory are colored black, red, green, and blue, respectively.

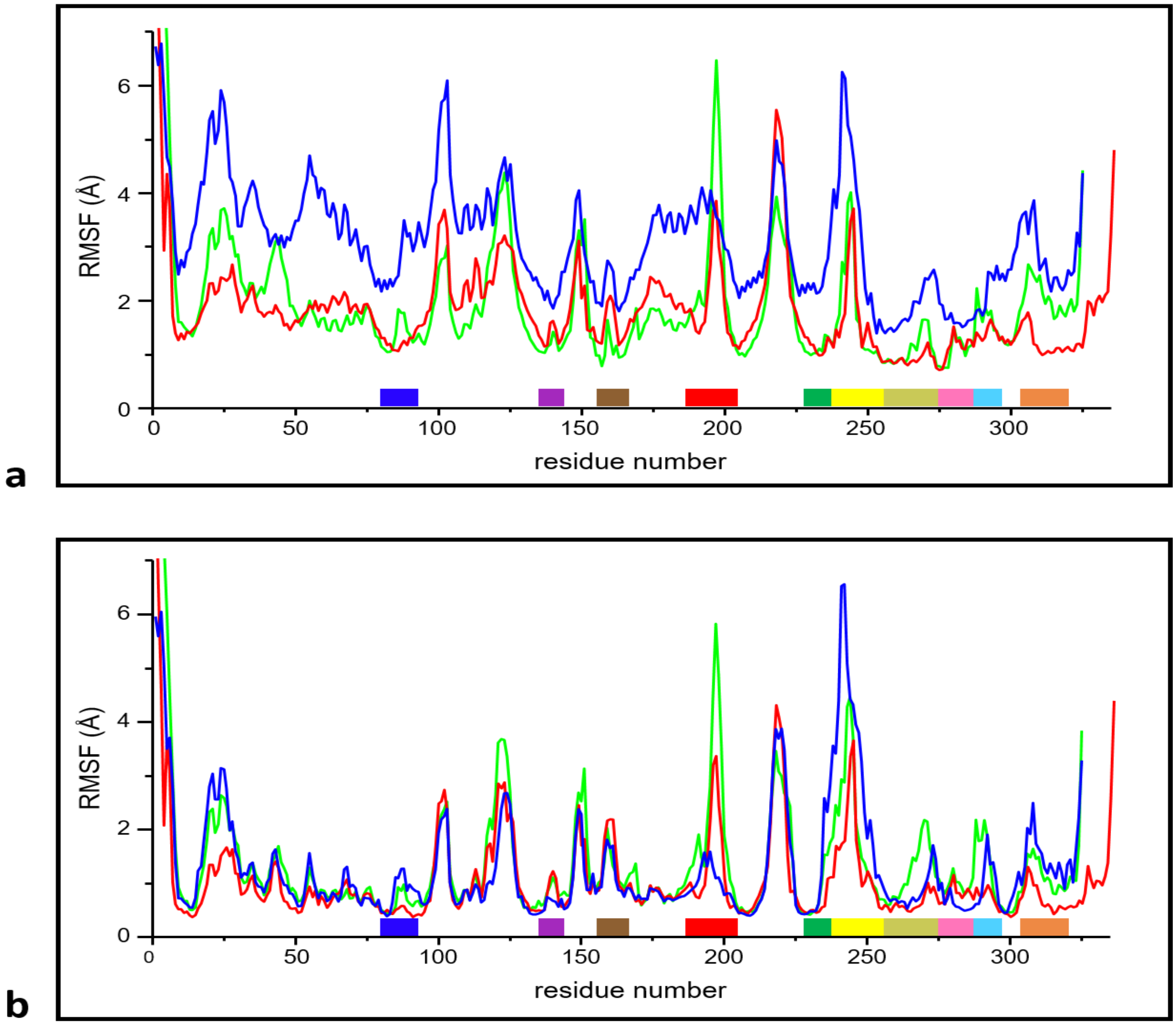

Figure 6.7: Root Mean Squared structural fluctuations of kinesin residues: (a) with respect to an average kinesin–tubulin structure; (b) with respect to an average kinesin structure. RMSF curves of ADP, APO, and ATP state are colored blue, green, and red, respectively. Key kinesin motifs are marked and colored as follows: P-loop (blue), switch I (red), switch II (green), loop L7 (purple), loop L8 (tan), loop L11 (yellow), α4 helix (dark yellow), L12 (pink), α5 helix (cyan) and α6 helix (orange).

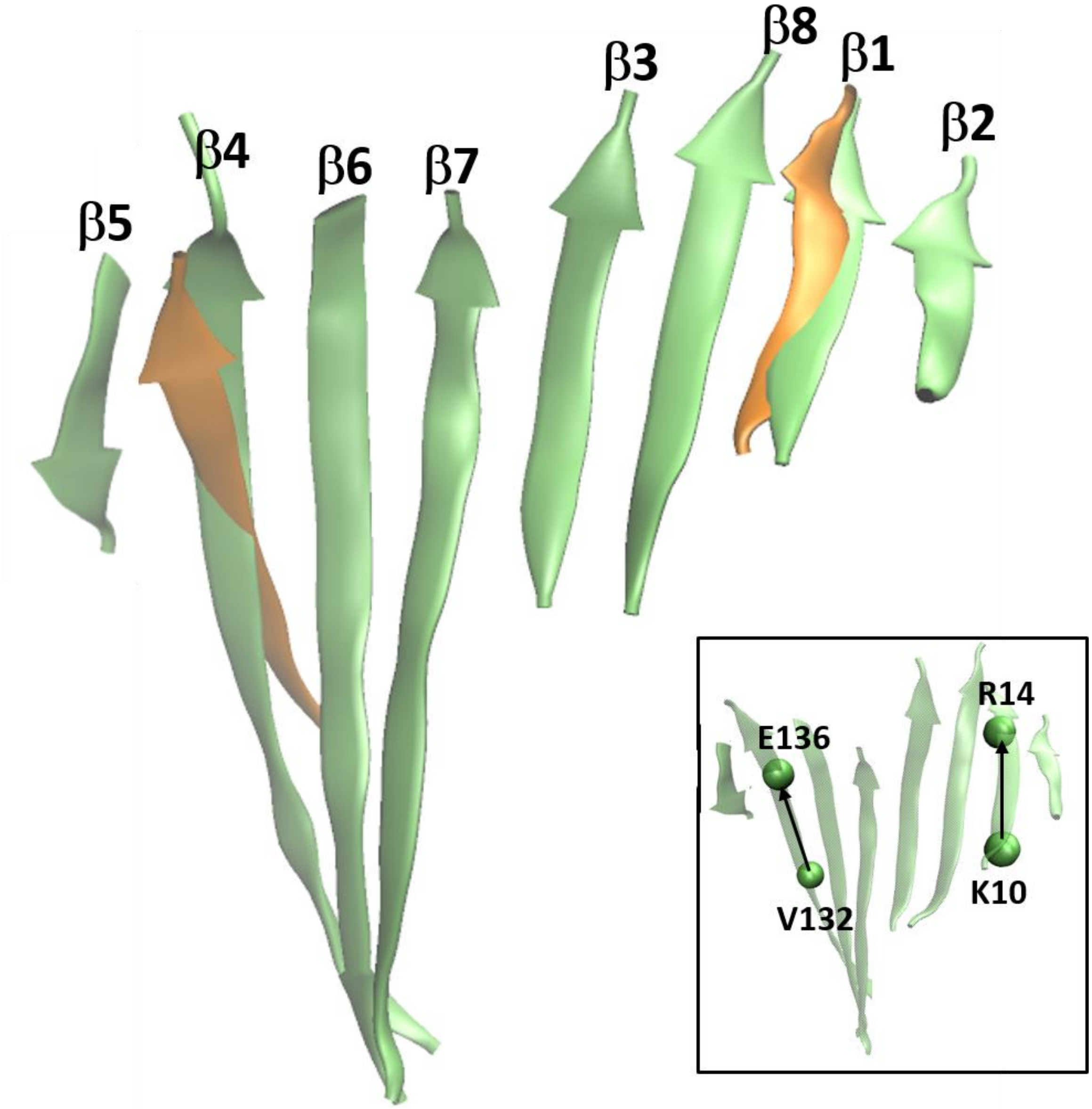

Figure 6.8: The central β-sheet (β1-β8) of an ATP-like kinesin structure (PDB id: 4HNA).

Four residues (K10, R14, V132 and E136) used to define the twist angle between β1 and β4 strand are shown by spheres, with two vectors connecting them (inset). For comparison, the β1 and β4 strand of a rigor-like myosin V structure (PDB id: 1OE9) are also shown (colored in orange).

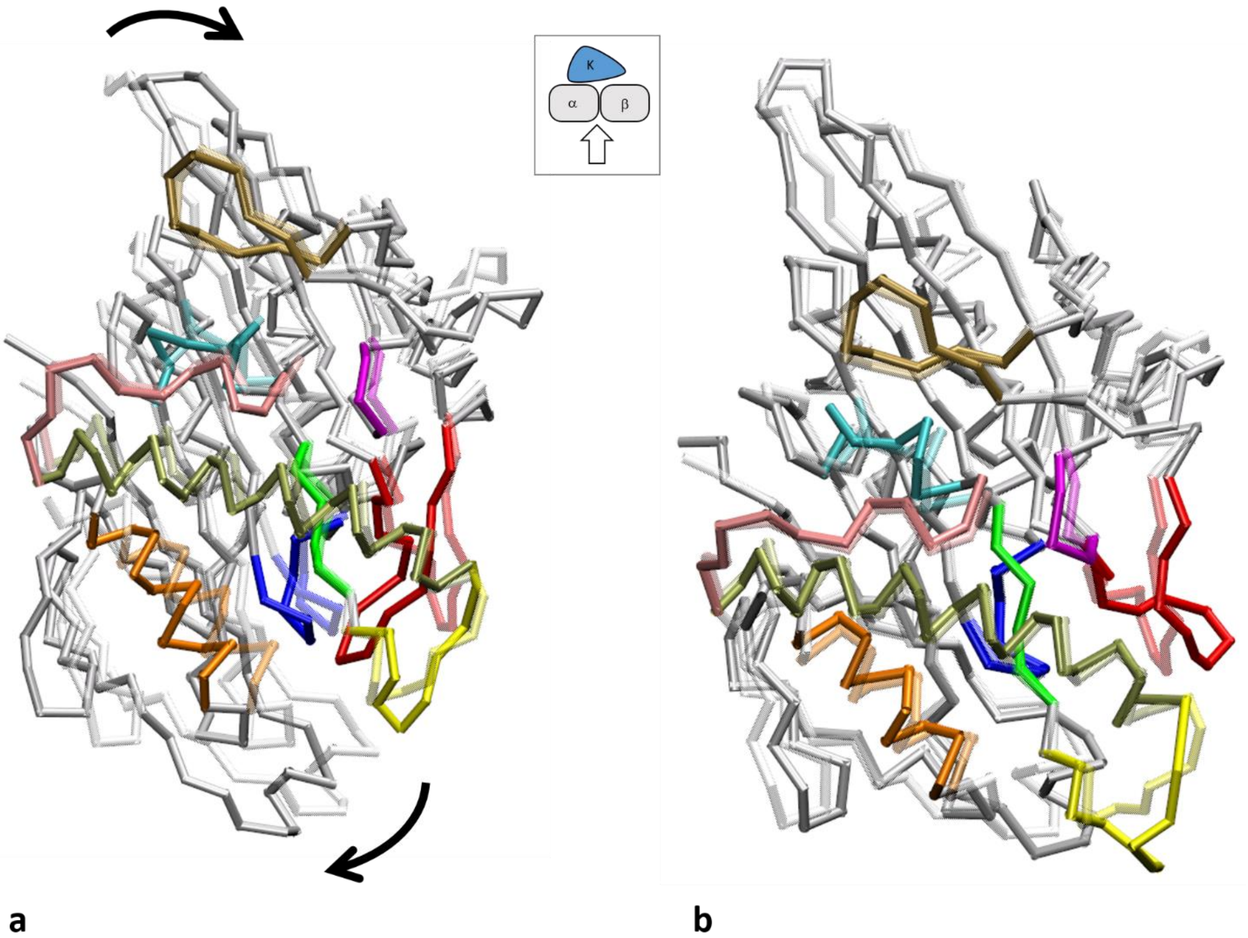

Figure 6.9: Conformational changes in kinesin predicted by the top two PCA modes in APO state: (a) mode 1 (b) mode 2. Kinesin structure before and after the predicted conformational changes are shown as transparent and opaque, respectively, viewing direction given in inset. Key kinesin motifs are colored as: P-loop (blue), switch I (red), switch II (green), L7 (purple), L8 (tan), L11 (yellow), L12 (pink), α4 (dark yellow), α5 (cyan), α6 (orange).

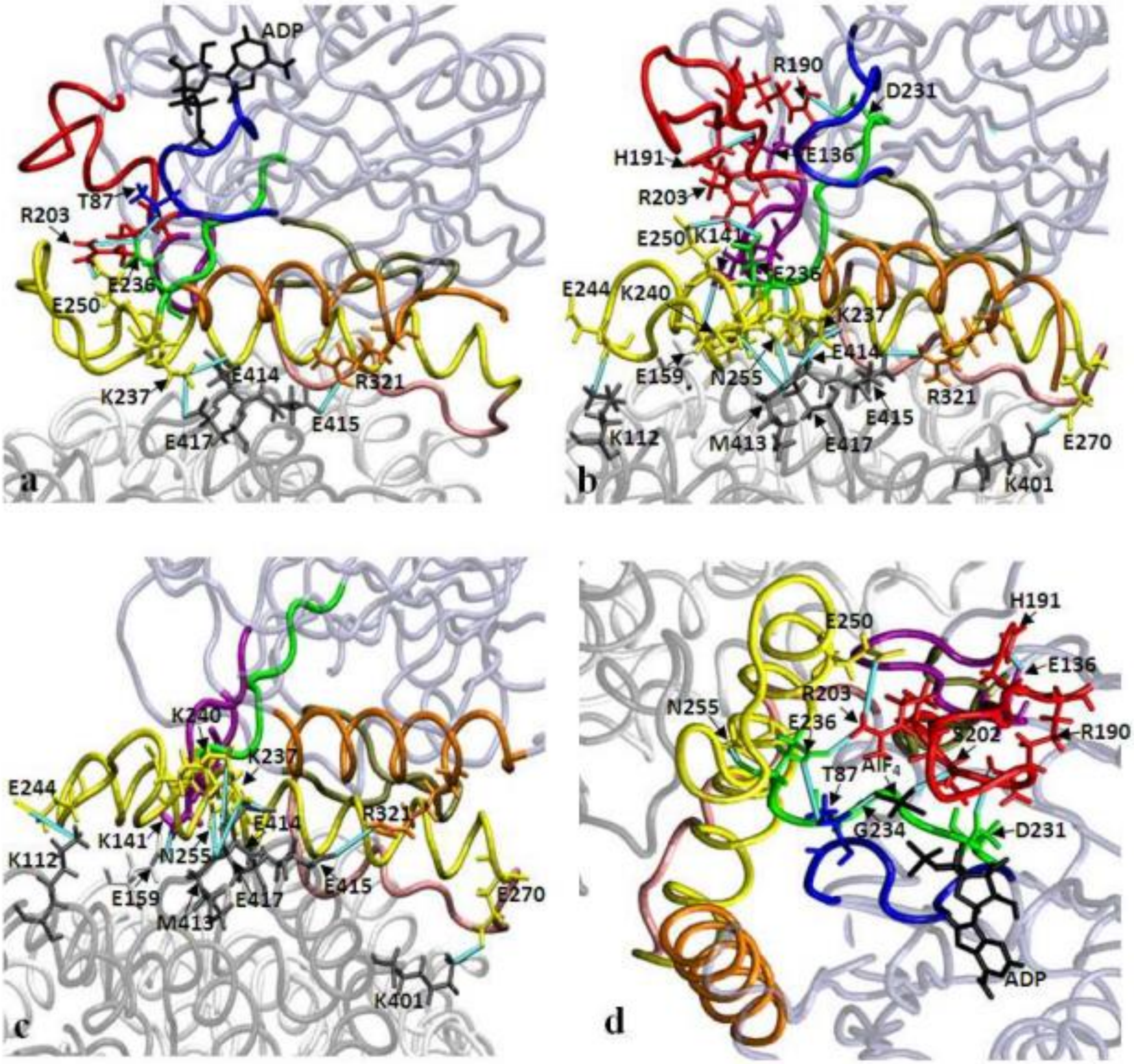

Figure 6.10: Selected hydrogen bonds formed in (a) ADP, (b) APO, (c) ATP state (at the kinesin-tubulin interface) and (d) ATP state (at the nucleotide-binding pocket). Key structural motifs of kinesin are colored as follows: P-loop (blue), switch I (red), switch II (green), α4 helix and loop L11 (yellow), α6 helix (orange), loop L7 (purple), loop L8 (tan), and loop L12 (pink). The ligands (ADP and AlF_4) are colored black. The rest of structure is transparent and colored as follows: kinesin (ice blue), α-tubulin (gray) and β-tubulin (white). Hydrogen bonds are shown as short lines colored in cyan. Residues involved in these hydrogen bonds are shown as sidechains and labeled. The viewing directions of panel (a)-(c) are similar to Figure 6.4(b), and the viewing direction of panel (d) is similar to Figure 6.4(d).

Table 6.1. The kinesin-tubulin contact surface area from the MD trajectories in ADP, APO and ATP states.

MD Trajectory #	**Contact surface area mean ± s.d. (Å^2)**
ADP state 1	919.1 ± 72.7
ADP state 2	1073.4 ± 78.1
ADP state 3	924.0 ± 83.7
ADP state 4	1124.7 ± 63.8
Mean ADP state	**1010.3 ± 117.6**
APO state 1	1492.6 ± 65.2
APO state 2	1431.8 ± 52.3
APO state 3	1417.0 ± 59.0
APO state 4	1402.1 ± 69.8
Mean APO state	**1435.9 ± 70.8**
ATP state 1	1461.0 ± 59.4
ATP state 2	1432.3 ± 53.8
ATP state 3	1313.6 ± 56.9
ATP state 4	1535.8 ± 69.3
Mean ATP state	**1435.7 ± 100.0**

Table 6.2. The twist angle of central β–sheet calculated based on four MDFF-generated models and four MD trajectories in ADP, APO and ATP state.

Trajectory #	**Twist Angle: mean ± s.d. (degree)**	
	MDFF traj.	**MD traj.**
ADP state 1	61.5	66.4 ± 2.3
ADP state 2	66.8	68.0 ± 2.4
ADP state 3	63.7	66.5 ± 2.6
ADP state 4	65.6	72.3 ± 2.7
Mean ADP state	**64.4 ± 2.3**	**68.3 ± 3.5**
APO state 1	64.3	70.6 ± 2.4
APO state 2	64.0	73.0 ± 2.3
APO state 3	66.3	67.1 ± 2.2
APO state 4	62.0	71.7 ± 2.4
Mean APO state	**64.2 ± 1.8**	**70.6 ± 3.2**
ATP state 1	60.5	63.0 ± 2.3
ATP state 2	58.2	62.7 ± 2.3
ATP state 3	59.8	64.6 ± 2.5
ATP state 4	59.8	65.1 ± 2.0
Mean ATP state	**59.6 ± 1.0**	**63.8 ± 2.5**

Table 6.3. The twist angle of central β−sheet calculated for crystal structures of myosin and kinesin.

PDB id of myosin	**β-sheet twist angle (degree)**		
	ADP-Pi state	**APO state**	**ATP state**
1VOM	65.9		
1BR1	65.5		
1QVI	67.5		
1Q5G		90.4	
3I5G		92.1	
2OS8		90.1	
1OE9		85.2	
1W8J		86.0	
1FMW			73.9
1KK7			75.5
1W7J			73.4
PDB id of kinesin	**ATP-like state**		**ADP-like state**
4HNA	59.9		
1VFV	60.0		
1VFW	60.9		
3HQD	63.5		
1BG2			65.4
1I5S			60.3
1II6			68.9
4OZQ			69.2

Table 6.4. Comparison of the tilt angles (mean ± standard deviation) with the results of ref [213]

β-strands	**Tilt Angle: mean ± s.d. (degree)**	
	MD trajectories	**Ref [213] results**
ADP state ϕ_{34}	13.1 ± 2.2	8.6 ± 0.5
ADP state ϕ_{45}	10.9 ± 4.6	18 ± 1.0
ADP state ϕ_{56}	19.4 ± 3.8	17 ± 1.2
APO state ϕ_{34}	13.6 ± 1.9	9.3 ± 2.0
APO state ϕ_{45}	5.4 ± 2.8	19 ± 1.8
APO state ϕ_{56}	16.3 ± 4.7	15 ± 1.8
ATP state ϕ_{34}	16.9 ± 1.5	20 ± 1.0
ATP state ϕ_{45}	14.9 ± 3.1	10 ± 0.7
ATP state ϕ_{56}	16.7 ± 4.0	16 ± 1.3

Table 6.5 Atomic distances in the nucleotide-binding pocket calculated from MD trajectories in comparison with MDFF-generated models.

State	**traj#**	$D_{85,234}$	$D_{P\beta,202}$	$D_{P\beta,91}$	$D_{91,202}$	$D_{203,236}$
		mean ± standard deviation (value of MDFF model), unit: Å				
ADP	1st	5.6 ± 0.3(6.2)	6.8 ± 0.2(7.1)	4.5 ± 0.1(4.4)	9.6 ± 0.2(9.8)	8.3 ± 2.2(5.9)
	2nd	6.9 ± 0.5(6.2)	6.8 ± 0.2(7.3)	4.4 ± 0.1(4.5)	9.6 ± 0.2(10.2)	3.8 ± 1.2(8.0)
	3rd	7.1 ± 0.4(5.7)	6.9 ± 0.3(6.7)	4.5 ± 0.1(4.5)	9.7 ± 0.3(9.8)	7.9 ± 2.2(3.1)
	4th	5.9 ± 0.5(5.6)	8.3 ± 0.7(8.7)	4.6 ± 0.2(5.1)	9.8 ± 0.7(10.7)	4.4 ± 1.3(2.7)
	All	6.4 ± 0.7	7.2 ± 0.7	4.5 ± 0.1	9.7 ± 0.4	6.2 ± 2.6
ATP	1st	6.2 ± 0.3(5.5)	6.9 ± 0.1(7.0)	4.5 ± 0.1(4.3)	9.3 ± 0.2(9.2)	2.9 ± 0.4(2.7)
	2nd	6.4 ± 0.4(6.1)	6.9 ± 0.2(6.8)	4.4 ± 0.1(4.2)	9.2 ± 0.2(9.3)	6.3 ± 1.2(2.7)
	3rd	6.7 ± 0.3(6.1)	6.9 ± 0.1(6.6)	4.5 ± 0.1(4.3)	9.4 ± 0.2(9.0)	5.0 ± 1.1(2.6)
	4th	6.1 ± 0.3(5.4)	6.8 ± 0.1(6.9)	4.4 ± 0.1(4.3)	9.3 ± 0.2(9.4)	3.8 ± 1.0(2.8)
	All	6.3 ± 0.4	6.9 ± 0.2	4.4 ± 0.1	9.3 ± 0.2	4.8 ± 1.7
ATP (no NL)	1st	6.1 ± 0.4	9.1 ± 0.2	4.3 ± 0.1	11.1 ± 0.3	4.2 ± 1.7
	2nd	6.5 ± 0.4	6.8 ± 0.1	4.5 ± 0.1	9.4 ± 0.2	6.5 ± 1.8
	3rd	6.4 ± 0.5	6.8 ± 0.1	4.4 ± 0.1	9.3 ± 0.1	6.0 ± 1.3
	4th	5.8 ± 0.3	6.9 ± 0.1	4.4 ± 0.1	9.3 ± 0.1	3.3 ± 0.8
	All	6.2 ± 0.5	7.4 ± 1.0	4.4 ± 0.1	9.8 ± 0.8	5.2 ± 2.1
APO	1st	6.5 ± 0.4(5.2)			9.3 ± 0.3(11.1)	8.9 ± 5.3(2.7)
	2nd	6.8 ± 0.5(5.2)			10.0 ± 0.4(10.5)	3.5 ± 0.9(4.8)
	3rd	7.2 ± 0.9(5.7)			9.4 ± 0.4(10.6)	9.3 ± 2.2(2.6)
	4th	6.2 ± 0.5(5.0)			10.5 ± 0.5(10.6)	3.3 ± 0.7(2.8)
	All	6.7 ± 0.7			9.8 ± 0.6	6.3 ± 4.0

Table 6.6. Results of kinesin-tubulin binding free energy calculation for ADP, APO and ATP state

Traj #	E_{vdW} ΔE_{elec} ΔG mean ± standard deviation, unit: kcal/mol		
	ADP state	**APO state**	**ATP state**
1	-55.1±8.2 -26.8±4.0 -12.8±1.0	-103.2±10.5 -37.8±5.2 -22.1±1.2	-108.0±7.4 -30.5±3.8 -21.7±1.1
2	-71.3±7.7 -24.8±4.9 -15.1±1.1	-110.8±8.1 -33.7±3.9 -22.7±1.1	-106.9±8.3 -34.4±4.2 -22.1±1.1
3	-61.0±7.8 -18.7±4.2 -12.5±1.2	-117.4±7.8 -19.8±3.7 -21.6±1.0	-101.5±7.7 -26.4±3.2 -20.1±1.1
4	-72.1±7.6 -31.2±4.3 -16.2±1.1	-106.5±8.6 -34.4±5.1 -22.1±1.2	-88.0±9.8 -46.9±3.9 -21.1±1.3
All	-65.0±10 -25.4±6.2 -14.2±1.9	-107.6±11.1 -32.4±8.9 -22.0±1.2	-101.1±11.5 -34.5±8.6 -21.3±1.4
Ref [217]	-18.9±0.4	-21.9±0.2	-21.5±0.4

Table 6.7. Results of partition of kinesin-tubulin binding free energy for APO, ADP and ATP state

residue	APO state			residue	ADP state			residue	ATP state		
	ΔG_n(s.d.)	$E_{vdw,\ n}$	$\Delta E_{elec,n}$		ΔG_n(s.d.)	$E_{vdw,\ n}$	$\Delta E_{elec,n}$		ΔG_n(s.d.)	$E_{vdw,\ n}$	$\Delta E_{elec,n}$
K141	-0.33(0.19)	+0.31	-2.47	K44	-0.24(0.15)	+0.06	-1.66	K141	-0.33(0.16)	-0.05	-2.11
K159	-0.30(0.16)	-1.42	-0.50	K141	-0.27(0.10)	-0.17	-1.58	K159	-0.27(0.13)	-1.34	-0.37
R161	-0.54(0.26)	-1.10	-2.39	R161	-0.50(0.27)	-0.70	-2.57	R161	-0.49(0.34)	-0.83	-2.33
K237	-0.74(0.27)	+0.03	-4.85	K166	-0.16(0.05)	-0.16	-0.90	K237	-0.84(0.37)	-0.02	-5.47
V238	-0.37(0.07)	-2.20	-0.17	K237	-0.53(0.32)	+0.42	-3.90	V238	-0.43(0.07)	-2.55	-0.21
S239	-0.24(0.09)	-1.37	-0.17	K240	-0.26(0.19)	-0.17	-1.54	S239	-0.25(0.08)	-1.24	-0.33
K240	-0.45 (0.33)	-0.07	-2.84	L248	-0.17(0.12)	-1.18	+0.08	K240	-0.54(0.31)	+0.04	-3.56
L248	-0.42(0.09)	-2.80	+0.16	K252	-0.64(0.15)	-2.38	-1.76	L248	-0.34(0.08)	-2.29	+0.12
K252	-0.75(0.15)	-2.92	-1.90	N255	-0.40(0.12)	-2.58	+0.04	K252	-0.80(0.20)	-2.81	-2.32
N255	-0.49(0.09)	-2.89	-0.22	K256	-0.54(0.14)	-1.85	-1.59	N255	-0.46(0.08)	-2.62	-0.30
K256	-0.73(0.10)	-2.78	-1.91	N263	-0.18(0.09)	-1.04	-0.10	K256	-0.74(0.11)	-2.84	-1.92
Y274	-0.86(0.17)	-5.07	-0.37	Y274	-0.58(0.19)	-3.15	-0.53	Y274	-0.84(0.17)	-4.91	-0.44
R278	-1.17(0.18)	-4.32	-3.20	R278	-0.83(0.25)	-2.46	-2.85	R278	-1.16(0.20)	-4.25	-3.18
K281	-0.40(0.08)	-0.31	-2.31	K281	-0.31(0.11)	-0.06	-1.96	K281	-0.40(0.10)	-0.27	-2.37
R284	-0.48(0.21)	-0.32	-2.79	R284	-0.35(0.12)	-0.36	-1.94	R284	-0.49(0.25)	+0.03	-3.23
K313	-0.46(0.24)	+0.54	-3.54	K313	-0.45(0.22)	+0.46	-3.44	K313	-0.39(0.17)	+0.51	-3.05
R321	-0.56 (0.24)	-1.62	-1.99	R321	-0.44(0.25)	-0.14	-2.71	R321	-0.27(0.19)	-0.25	-1.51

The color scheme is the same as that used in Page 19. L7: purple, L8: tan, L11: yellow, L12: pink, $\alpha 4$: dark yellow, $\alpha 5$: cyan, $\alpha 6$: orange

Chapter 7:

Structural differences between neurotransmitter binding sites of muscle acetylcholine receptors*

*This chapter is a part of a published article:

Proc Natl Acad Sci U S A, 2014. 111(49): p. 17660-5.

Only the *in silico* simulations are discussed here.

ABSTRACT

A muscle acetylcholine receptor (AChR) has two neurotransmitter binding sites located in the extracellular domain, at αδ and either αε (adult) or αγ (fetal) subunit interfaces. The two binding sites behave independently in both adult and fetal AChRs. Single-channel electrophysiology measurements have helped determine that, for at least four different agonists including ACh and choline, ΔG_{B1} is ∼−2 kcal/mol more favorable at fetal αγ compared with at αε and αδ. The same five conserved aromatic residues form the binding core in all three interfaces, but their contributions to binding energies vary. We used computational modeling and MD simulation to investigate the structural dynamics and energetics of these 3 different binding interfaces. Starting from an *Aplysia* AChBP crystal structure (PDB id 2BYQ), we used homology modeling to build all-atom dimer and pentamer models of the extracellular domain, and docked acetylcholine (ACh) as the ligand. ACh binding energies estimated from molecular dynamics simulations are consistent with experimental values from electrophysiology and suggest that the αγ site is more compact, better organized, and less dynamic than αε and αδ. We speculate that the different sensitivities of the fetal αγ site versus the adult αε and αδ sites to ACh are important for the proper maturation and function of the neuromuscular synapse.

7.1 - Introduction

For AChR receptors at cholinergic synapses, the main chemical signals are ACh released from nerve terminals and choline, which is an ACh precursor, hydrolysis product, and stable component of serum [254]. The muscle AChR has central pore surrounded by five subunits of composition $\alpha_2\beta\delta\varepsilon$ in adult-type and $\alpha_2\beta\delta\gamma$ in fetal-type (Figure 7.1A) [60]. The fetal γ subunit is essential for proper synapse maturation, and the adult ε subunit is necessary for proper function of mature synapses [134, 255, 256]. Each AChR pentamer has two agonist binding sites in the extracellular domain, at αδ and either αε (adult) or αγ (fetal) subunit interfaces. On the α-side of each site, there are four aromatics known to influence agonist affinity: αY190 (in loop C), αY198 (loop C), αY93 (loop A), and αW149 (loop B) (Figure 7.1B)) [89, 92, 159, 258, 259]. In addition, there is a conserved tryptophan in the non-α subunit, W55 (at position 57 in the δ subunit) [89, 260-262]. These aromatic residues have been shown to stabilize the quaternary ammonium of the agonist by cation-π forces [92, 259, 263].

Single-channel electrophysiology experiments done by our group have led to the findings that only three of the aromatics contribute significantly to ΔG_{B1} at the adult sites (αY190, αY198, and αW149), but all five do so at αγ (as well as αY93 and γW55). γW55 makes a particularly large contribution only at αγ that is coupled energetically to those contributions of some of the α-subunit aromatics. The hydroxyl and benzene groups of loop C residues αY190 and αY198 behave similarly with regard to ΔG_{B1} at all three sites. Appendix 2 summarizes the experimentally obtained results.

Given the central role of receptors at synapses, we thought it important to understand in detail the underlying structural dissimilarities that bring about the binding free energy differences in the three kinds of agonist sites present in mouse muscle nicotinic acetylcholine receptors (AChRs). Our goal was to use homology models (with AChBP as template) for the extracellular domains of the three binding interfaces (αδ, αε and αγ), test the models against experimentally obtained results and use molecular dynamics simulations to identify structural correlates that explain the differences in ligand binding affinity.

7.2 - Methods

7.2.1 - Model preparation and ligand docking

Our initial model of the mouse muscle AChR was an α plus a non-α subunit dimer of the extracellular domain (residues 17-209) that was built according to the x-ray structure of the *Aplysia california* ACh binding protein (AChBP) bound with epibatidine (PDB code 2BYQ; (9)). Homology models were constructed by using the ZMM program (http://www.zmmsoft.com), which employs the Monte Carlo minimization algorithm (MCM) to search for energetically favorable conformations (10). The homology model was minimized until 5000 consecutive energy minimizations did not decrease the apparent global minimum. During energy minimization, the α carbons of the protein were constrained to the template structure by harmonic restraints with the spring constants gradually released from 10 kcal $M^{-1}Å^{-2}$ to 1 kcal $M^{-1}Å^{-2}$. For docking, we searched for the optimal positions and orientations of ACh using a Lamarckian Genetic Algorithm for optimization with Autodock Tools [264]. Details of constructing the pentamer model is given in chapter 8, page 136.

7.2.2 - MD simulation protocol

The three systems of αδ, αε and αγ were further optimized and equilibrated using MD simulation. The systems were solvated in a water box with TIP3P water model [265] and the box was extended at least 10 Å from the periphery of the protein in each direction. Na^+ and Cl^- ions were added to neutralize the system and bring it to an ionic concentration of 150 mM of NaCl. The simulations were conducted using NAMD [225] version 2.8, with CHARMM27 force field [146].

First, a 20,000-step minimization was done using the steepest descent method, and with gradual release of restraints on the protein backbone. Then the systems were subjected to 20ns MD simulation performed in the NPT ensemble. The Nosé-Hoover method [266] was used with a temperature of 300K and a pressure of 1 atm. Harmonic constraints (force constant =1kcalM^{-1}Å^{-2}) were applied on the backbone atoms of residues which were atleast 20 Å away from the acetylcholine molecule at the binding site. These constraints maintain the global backbone conformation of the model while allowing relaxation of all side chains and the residues in the key loops of the ACH-binding interface. Periodic boundary conditions were applied. A 10 Å switching distance and a 12 Å cutoff distance were used for non-bonded interactions. The particle mesh Ewald (PME) method [267] was used to calculate long-range electrostatic interactions. The SHAKE algorithm [268] was used to constrain bond lengths of hydrogen-containing bonds, which allows a time step of 2 fs for MD simulations. Four MD simulation trajectories were obtained for each of the $\alpha\delta$, $\alpha\varepsilon$ and $\alpha\gamma$ models. The coordinates of the systems were saved every 1ps during MD simulations for later analysis.

7.2.3 - Calculation of ACh-protein binding free energy

The ACh-protein binding free energy was calculated using a continuum solvent model [230]. The binding free energy, ΔG, is expressed as $\Delta G_{np}+\Delta G_{elec}$, similar to that is the kinesin-MT system (as explained in page 70). Here, the nonpolar contribution ΔG_{np} ($=\lambda E_{VDW}$) is empirically written as a fraction ($\lambda<1$) of the van der Waals (VDW) interaction energy. λ is small because the gain in favorable VDW interaction energy between ACh and protein is largely compensated by a loss of VDW interaction energy between the free protein and ACh, and water. We used the empirically estimated value of $\lambda = 0.17$ in [230]. This energy calculation method was improved and specifically parameterized for nAChR, later in Chapter 8. The ACh molecule remained close its equilibrium position at all 3 sites, with the nitrogen deviating by an average of 1.0±0.4 Å. ΔG_{elec} was calculated using the Poisson−Boltzmann (PB) method [231, 232] where a probe radius of 1.4 Å was used to define the molecular surface corresponding to the dielectric boundary. The salt concentration was set to 140 mM, corresponding to the buffer condition for experimental measurements. All the PB calculations were performed using the PBEQ module [232] of the CHARMM program [233]. Each PB calculation was conducted by using bilinear interpolation to construct the boundary potential. The atomic Born radii used were previously calibrated and optimized to reproduce the electrostatic free energy of the 20 amino acids in MD simulations with explicit water molecules [269]. The binding energy calculations were done on snapshots extracted every 20 ps over the last 10 ns of each trajectory. The ensemble for each state therefore contained 2,000 snapshots, which were used to perform all quantitative analyses. We also calculated the binding energy using AUTODOCK-4 (epdb module; [264]) and the MMPBSA method [270]. In MMPBSA, the VDW term is unscaled and a non-polar surface area term is added, so that the energy is over-estimated [271]. The comparison is shown in Table 7.1.

7.2.4 - Structural parameters and dynamics

For structural analyses, the geometric centers of the aromatic and indole rings of interest and the ACh quaternary amine (QA) nitrogen were used as reference points.

***Angle between Tryptophans*:** The angle between the αW149 and W55 indole rings was defined as the angle between the perpendiculars to the planes of the rings for each residue.

***Volume*:** The ligand pocket in the ACh bound state is outlined by αW149, αY93, αY190, αY198 and W55 in the non-α subunit (Figure 7.1B). The volume of this pocket was estimated by joining the centroids of the aromatic rings to form two adjoining tetrahedra (Figure 7.5A). The volume of each tetrahedron was estimated using the 3-simplex determinant method from the coordinates of the vertices.

***Hydrogen bonds and cation-π interactions*:** We used the following geometric criteria: H-bond, a donor−acceptor distance of <3.5 Å and a donor-hydrogen-acceptor angle of < 60°; cation-π interaction, a distance cutoff of less than 6 Å between the ACh QA nitrogen and the geometric center of the phenyl ring, and an angle cutoff of less than 45° between the normal to the phenyl ring and the vector joining the ring center and the ACh nitrogen [257]. We used VMD program [224] to identify and calculate the above parameters in the last 10 ns ensemble**.**

***RMSF*:** To compare the flexibility of the ligand binding interface between the three sites, we performed root-mean-square fluctuation (RMSF) analysis based on the last 10 ns of the MD simulations. RMSF of Cα atoms of each residue was calculated with respect to the mean of the ensemble using VMD version-1.9.

7.3 - Results

In wild-type (WT) AChRs having two agonist binding sites, the total free energy from both affinity changes was experimentally estimated by our group from single-channel current interval durations obtained at a saturating agonist concentration, using constructs having known unliganded gating equilibrium constants (Figure 7.2A). Affinity changes were also obtained for single site knock-outs for different agonists (Figure 7.2B). Appendix 2 shows this total energy from two-site and single-site AChRs for four different agonists. Fetal-type AChRs, which have a γ-subunit rather than a ε-subunit, provide >1.5 kcal/mol more favorable free energy for all agonists compared with adult-type. Summarizing the experimentally obtained results (Figure 7.2 and Appendix 2), the aromatic groups of the two loop C tyrosines and αW149 provide similar free energies at all three binding sites (∼−2 kcal/mol). However, the aromatic group of αY93 and, in particular, W55 has more favorable effects at αγ. Only three of the aromatics contribute to $\Delta G_{B1}{}^{ACh}$ at the αε and αδ sites, whereas all five contribute at the fetal, αγ, site.

7.3.1 - MD simulations

To explore possible mechanistic bases for the experimental free energy measurements, we carried out MD simulations using simple homology models of each of the three kinds of agonist site. There are two issues to consider in making comparisons between simulated and experimental energy estimates. First, the simulations estimate a bound vs. unbound energy difference, whereas the ΔG_{B1} measurements from electrophysiology give a difference in binding free energy: HA minus LA (Equations 4.7a and 4.7b, page 42). In adult-type AChRs, for the agonists and mutations used in this study, the HA and LA equilibrium dissociation constants are correlated and have the relationship G_{HA}~$2G_{LA}$ [109]. Combining this with equation 4.7, we get ΔG_{B1}~G_{LA}. Hence, in this regard, the energy difference from the affinity change can be compared with the bound vs. unbound energy difference. A second issue is that energies from simulations are enthalpies (ΔH_{B1}) that do not incorporate entropy (ΔS_{B1}), whereas ΔG_{B1} measurements from electrophysiology are free energies that report both enthalpy and entropy contributions ($\Delta G_{B1} = \Delta H_{B1} - T\Delta S_{B1}$, where T is the absolute temperature). Previously, energy measurements as a function of temperature showed that relative to ACh, the change in ($\Delta G_{B1}+\Delta G_{B2}$) was approximately equal to the change in ($\Delta H_{B1} + \Delta H_{B2}$) for both CCh and Cho [130]. This suggests that the entropy component of the agonist's free energy change is small and, hence, that it is appropriate to compare free energies from experiments with enthalpies from simulations.

Figure 7.3A shows the root mean square deviations (RMSD) of the MD simulation trajectories. The protein RMSD got equilibrated by the first 6ns and therefore all analyses and binding energy calculations were done on snapshots extracted every 20ps over the last 10 ns of each trajectory. The ensemble for each state therefore contained 2500 snapshots of the system.

Binding energies: Figure 7.4A shows the distributions of simulated ΔG_{B1}^{ACh} values for each site. As with the electrophysiology ΔG_{B1}^{ACh} values, the population means were in the order αγ>αδ~αε. Moreover, experiments and simulations produced results that were in good quantitative agreement, with both indicating ~33% more energy from αγ relative to αδ/αε (Figure 7.4B). A breakdown of the simulated enthalpy at each site into its various components is shown in Figure 7.4C, 7.4D and Table 7.1. While ΔG_{elec} are comparable for all of the binding sites, ΔG_{VDW} is significantly different at αγ vs αε/αδ. While classical Class 1 additive force fields like CHARMM do not account for cation-π interactions explicitly, the charge separation in aromatic rings (negative on carbon atoms and positive on hydrogen atoms) gives them a dipole-like (or higher order) behavior. The cation-π electrostatic interactions can thus be mimicked as dipole-dipole van der Waals interactions.

RMSF analysis: The three binding sites were broadly similar in their dynamics, as evidenced by the similar root-mean-square fluctuations profiles (Figure 7.3B). As expected, loop regions in both sides of the binding pocket were more flexible at all three sites. The most flexible regions on the α-side were loops C and F, which were less dynamic in αγ compared with αδ and αε.

Geometry of the core: Figure 7.5B shows snapshots (lowest RMSD from centroid structures) of the two fetal-type AChR agonist sites, αγ and αδ, obtained from MD simulations of heteropentamers. Simulations results of αε compared to αδ, and αγ dimers are shown in Figure 7.5C and Table 7.2, 7.3. At αγ, the five aromatic side chains make up a tight pocket that is ∼22% smaller than at αδ (Figure 7.6B) and is similar to the starting acetylcholine binding protein structure. In contrast, in the course of the simulations, the W55, αY93, and αW149 side chains at the αδ and αε sites separate from ACh quaternary ammonium (QA). Also, as seen in Table 7.3, in general, the average distances between the core residues and the QA are smaller at αγ vs αε/αδ. The angle between the two indole planes becomes less orthogonal in αε/αδ as compared to αγ (Figure 7.6A and Table 7.2). Greater orthogonality of indole rings is an indication of a stronger cation-π interaction [272]. This suggests that W55 interacts strongly with W149 in fetal binding site, but not so in adult sites.

Geometric analysis of hydrogen bonds and cation-π interactions: Using the geometric criteria outlined (see Methods), the frequencies of H-bond interactions and cation-π interactions between the core aromatic residues and the acetylcholine were calculated (Figure 7.6C, 7.6D). The number of H-bonds followed the trend of αγ > αδ > αε, which again consolidated the fact that the core pocket at αγ is the most compact. There is a similar general trend for cation-π interactions, except for Y190, which shows a higher frequency for αδ site.

7.4 - Discussion

The MD results were broadly consistent with those obtained by electrophysiology. The relative energy differences for ACh at αγ, αε, and αδ were similar (Figure 7.4; Table 7.1). Simulations of dimers vs. pentamers (details in Chapter 8, Methods) produced similar energies and structural parameters, as predicted by the electrophysiology results showing site independence. The model side chain orientations and experimental free energies were also congruent. At all three sites, αY190 and αY198 adopted similar configurations relative to the QA in the simulations and also showed similar experimental free energy values. Likewise, W55, αY93, and αW149 showed the largest structural differences as well as the most free energy variation between sites. The general correspondence between simulations and electrophysiology suggests that the mean structural snapshots from the simulations (Figure 7.6) can be used as a provisional basis for interpreting the experimental ΔG_{B1}^{ACh} differences between the agonist sites. Further examination of the correspondence between simulation predictions and experimental results should reveal the value and limitations of the simple model used in this study.

The forces that undergird the free energy (structure) differences between the three agonist sites are not known. The fact that ACh and tetramethylammonium (TMA) provide about the same amount of extra free energy at αγ suggests that an interaction of the "tail" of the agonist with the non-α subunit is probably not the reason for the larger energy contributions from W55, αY93, and αW149. Further, the homology models used in the MD simulations were from the same ACh binding protein crystal structure, so neither the overall alignment between the α and non-α subunits nor differences between the backbones of the non-α subunits are likely reasons for the differences between αγ and αδ/αε. By elimination, we postulate that side chains in the ε/δ subunit, which have yet to be identified but probably are in the vicinity of the pocket, make ΔG_{B1}^{ACh} less favorable at αδ/αε compared with αγ. From our experiments, we cannot distinguish whether forces from these side chains generate a stable binding pocket even before the arrival of the agonist or whether the arrival of the ligand is an organizing principle that rearranges the αε/αδ site into a suboptimal configuration.

Synapse Development and Physiology: One aspect of cation-π forces is that they only derive from protein–ligand interactions and, unlike H-bonds, are newfound energies that are not traded off with those from the solvent. Given the all-or-none nature of the vertebrate neuromuscular synapse, it is curious that neither of the two adult sites (αδ and αε) derive the maximum free energy from the neurotransmitter molecule. It seems that through natural selection, the fetal αγ site has been so optimized, but as a consequence, it responds to Cho as well as ACh. Perhaps the ε subunit, which is evolutionarily more recent than γ [273, 274], has been selected specifically because it does not respond to Cho (see Appendix 2). We speculate that the differential sensitivity to Cho, which is higher at αγ and lower at αε, is a reason for the γ→ε subunit swap that is required for synapse development [254, 275]. Fetal and adult AChRs also differ in conductance, open-channel lifetime, voltage sensitivity, frequency of spontaneous openings, and Ca^{2+} permeability [77]. Which of these differences in function are necessary for healthy nerve–muscle synapse development and function remains to be determined.

Analysis of our in silico model suggests that they form a reasonable replication of experimental results at the binding site. This forms the basis of our next study where we look for the minimum construct necessary to interchange fetal and adult binding sites.

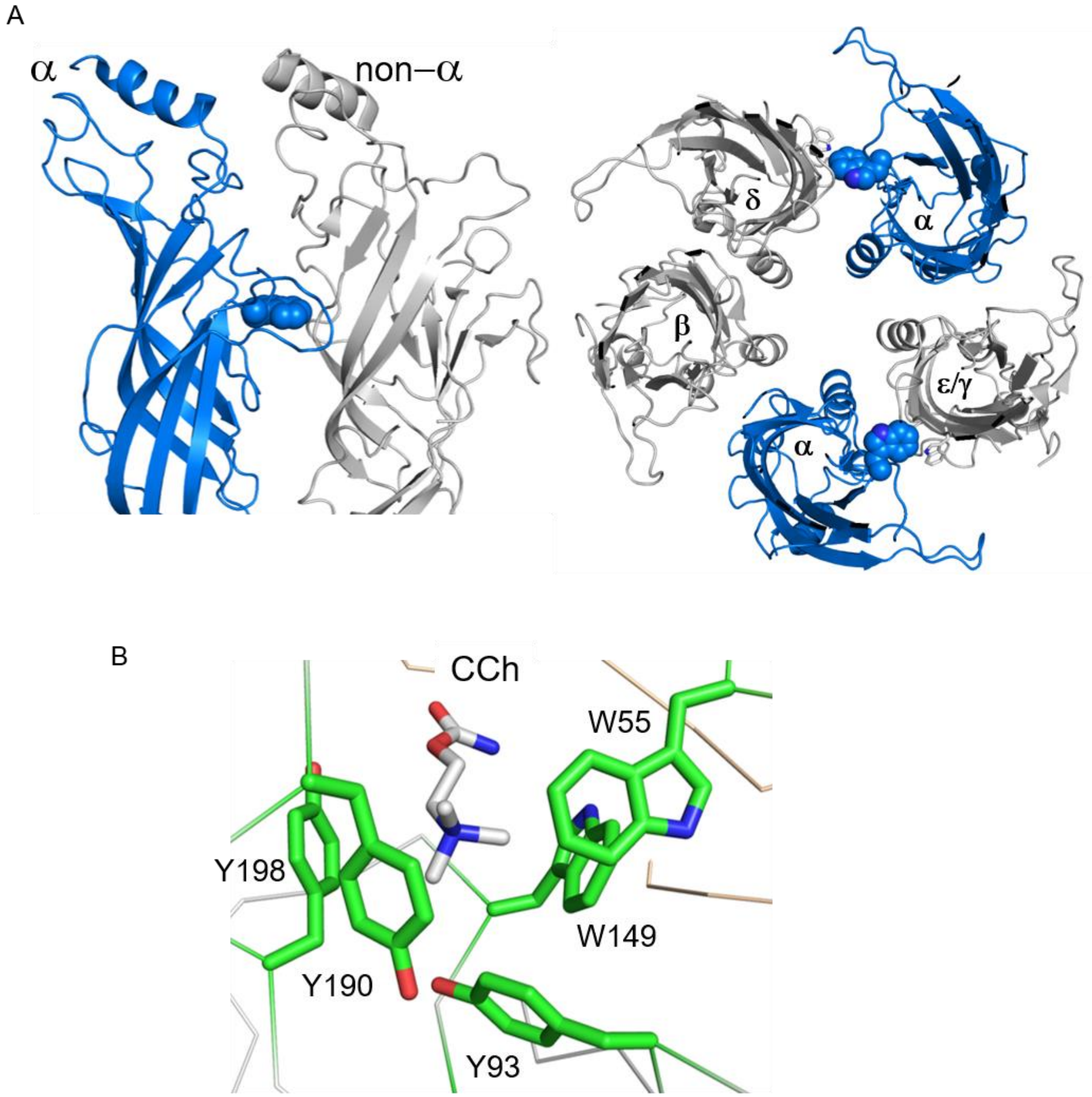

Figure 7.1: Structure of agonist binding site. A. Side and top views of a muscle-type AChR (Torpedo marmorata; pdb accession number 2BG9). subunits are blue. The two agonist sites are in the extracellular domain at αδ and αε/γ subunit interfaces (location identified by spheres, W149). B. High resolution view of the ligand binding site of an acetylcholine binding protein occupied by carbamylcholine (CCh) (*Lymnaea stagnalis*; pdb accession number 1UV6). Aromatic residues are labelled using mouse AChR numbering (W55 is in the non-α subunit).

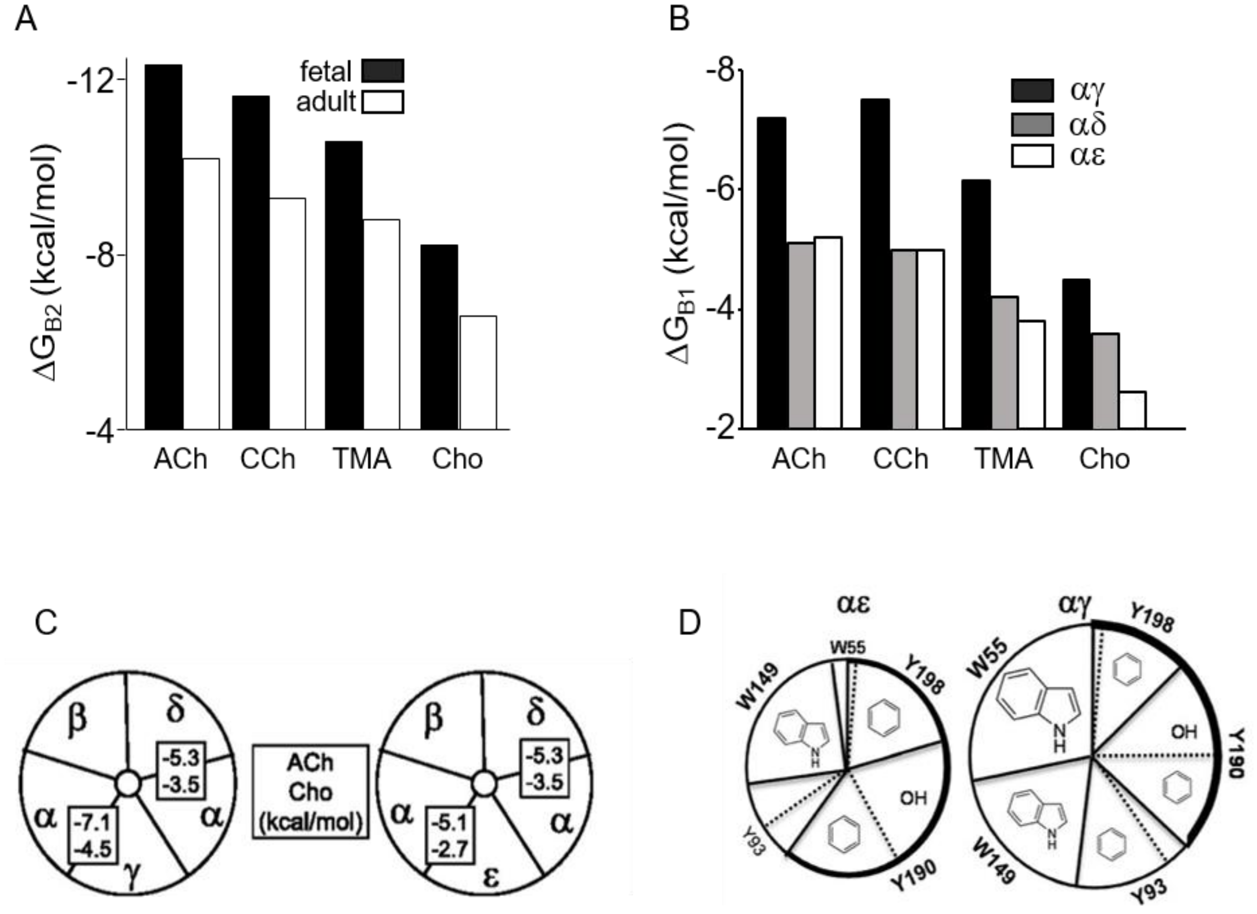

Figure 7.2: Experimentally obtained energies from different agonists. A. Total binding energies for 2-site fetal vs. adult AChRs (WT), for different agonists. For all ligands G_{B2} is ~-2 kcal/mol more-favorable in fetal. B. Binding energies for 1-site AChRs (WT), for different agonists. For all ligands, G_{B1} at αγ is the most-favorable. C. ΔG_{B1}^{ACh} and ΔG_{B1}^{Cho} at each site. D. Pie chart of contribution of functional groups to ΔG_{B1}^{ACh}. The area of each slice is approximately proportional to the free energy lost on removal of each functional group. At αε and αγ, the aromatic groups of αW149, αY190, and αY198 and the hydroxyl of αY190 make approximately equal contributions. At αγ, W55 mes a huge contribution (~ -4.5 kcal.M^{-1}), and the aromatic group of αY93 contributes about as much as αY198. Thick line, loop C contribution. (References given in Appendix 2)

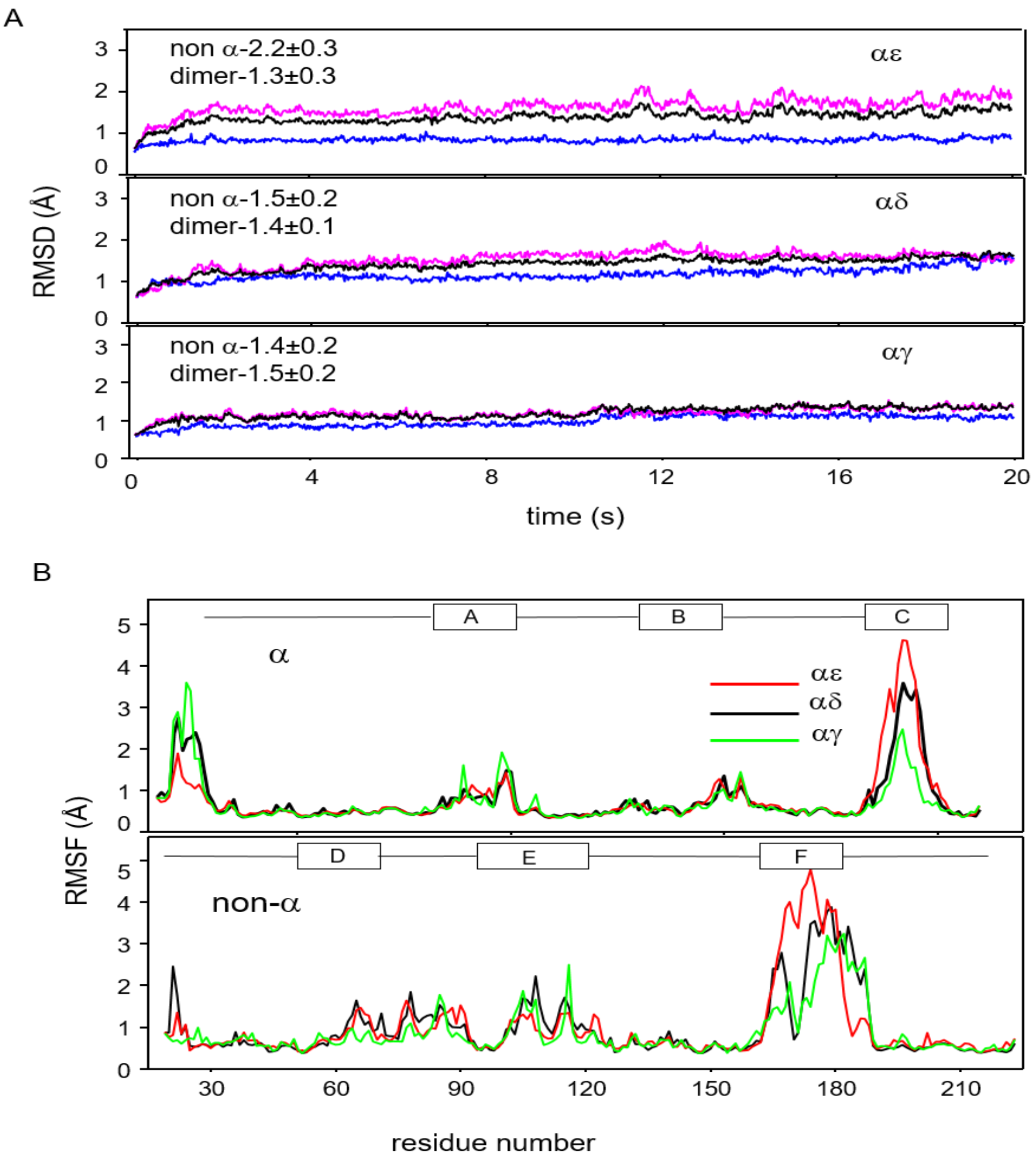

Figure 7.3: Comparison of global, simulated structures of each binding sites. A. Representative MD simulation trajectories showing the time evolution of the root-mean-square deviation (RMSD) of the protein backbone atoms for αε, αδ, and αγ dimers (black, dimer; blue, α subunit; magenta, non-α subunit), which equilibrated in less than 6 ns. The values given (inset) are the average RMSD (Å) for 4 trajectories ± S.D. The average RMSD for the α side was intermediate between the dimer and the non- α side. B. Comparison of residue-wise root-mean-square fluctuation (RMSF) values for α (top) and non-α (bottom) subunits. Average RMSF for the non-α residues was greater than the α-side. The approximate positions of loops (A-F) are shown as blocks above the traces. As expected, the RMSF was relatively higher at the loops.

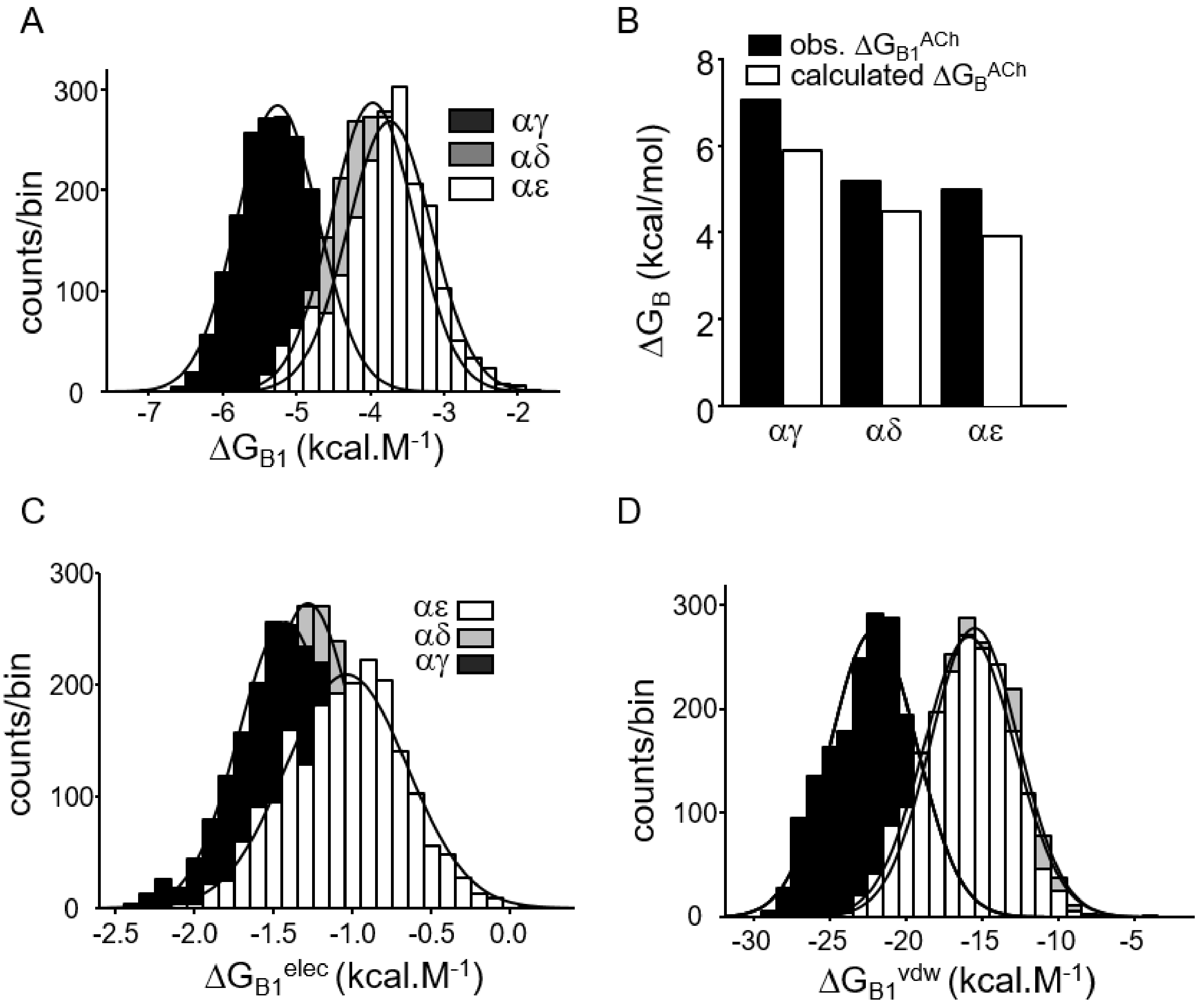

Figure 7.4: ACh binding energies calculated from MD simulations. A. ACh binding energy distributions obtained from the last 10 ns of each MD trajectory. The solid lines are Gaussian fits. The mean energy at αγ is ~33% more favorable than at αδ and αε (Table 7.1). B. Comparison of experimental and calculated ACh binding energies at each site (αγ > αδ > αε). C. Distribution of the electrostatic component ΔG_{elec} (kcal.M^{-1}) of the ACh-protein binding energy, obtained from the last 10 ns of MD simulations for αε, αδ, and αγ sites. The distributions were fitted to Gaussian functions. ΔG_{elec} are comparable for all of the binding sites. b. Distribution of van der Waals energy contribution, E_{VDW} at each site. ΔG_{B1}^{VDW} is significantly different at αγ vs αε/αδ.

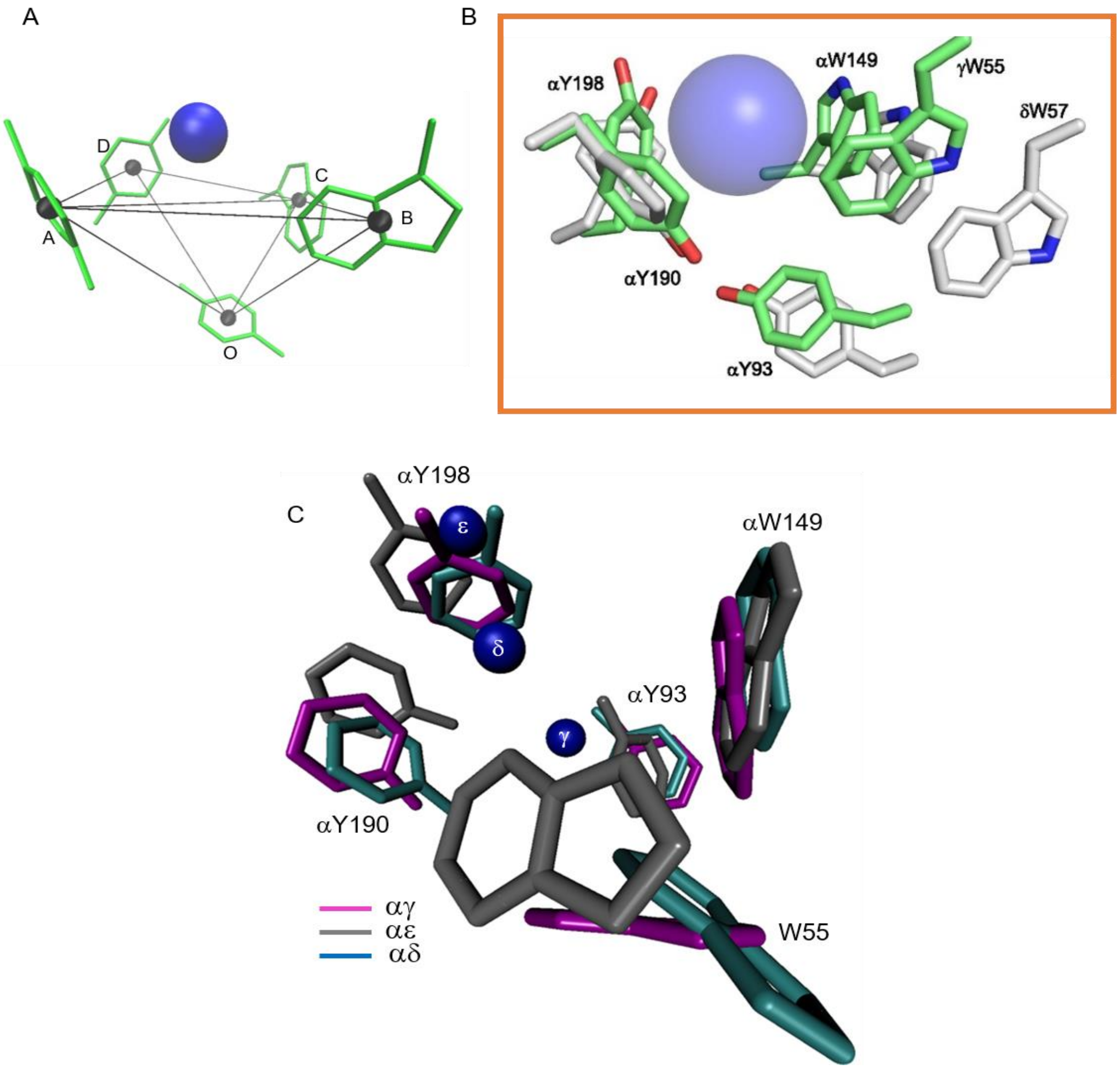

Figure 7.5: Simulated structures of the binding sites. A. Model of the αγ site showing 2 virtual tetrahedra AOCB and ADCO, with O as the common vertex. Pocket volume was calculated from the sum of these two tetrahedra. B. Representative snapshots of αγ and αδ (smallest RMSD from mean structure from last 10 ns of pentamer simulations). Blue sphere, QA of ACh (approximately as a van der Waals surface). At αγ (green), W55, αY93 and αW149 are closer to the QA compared to that at αδ (white). These amino acids also show the largest differences in experimental ΔG_{B1}^{ACh} between sites (-1.7, -0.8 and -4.5 kca.lM^{-1}, respectively). The orientations of αY198 and αY190 relative to the QA are similar at both sites, as are the effects of mutations of these residues on ΔG_{B1}^{ACh}. C. Top view of overlay of the structural models at the αγ (magenta), αδ (cyan) and αε (grey) binding sites, with the Cα carbon atoms of the backbones aligned. Filled blue sphere: N of the QA of ACh. Note the orthogonal disposition of αW149 and W55 and a more-compact binding pocket at αγ vs αε and αδ.

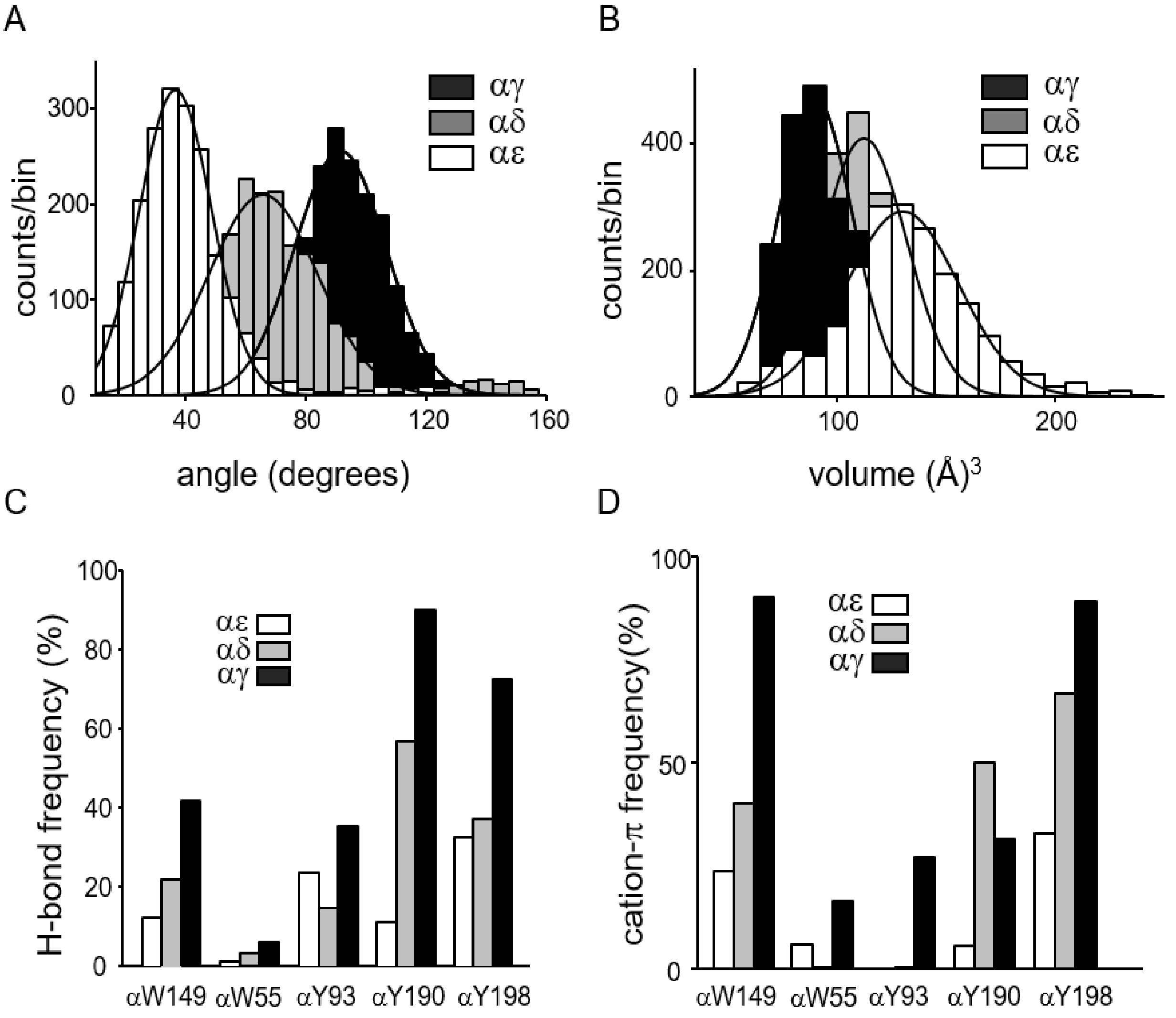

Figure 7.6: Geometric parameters from MD simulations. A. Distributions of the angle between the indole rings of W55 and W149. The rings are orthogonal only at αγ. B. Distributions of the volumes of the binding pockets. αγ is most compact. C. Percentage occurrence of hydrogen bond interactions (SI methods) between ACh and the aromatic side chains in the binding pocket, as calculated by geometric criteria (Methods). At αγ, side chains have higher probability to form H-bonds with ACh. D. Percentage occurrence of cation-π interactions between the QA and the aromatic residues. αW149 and αY198 maximally participate in cation-π at all the sites, but αY93 and γW55 only do so at αγ.

Table 7.1: Ligand binding energy calculated from MD simulations

site	unscaled VDW interaction	electrostatic interaction	ΔG(continuum -solvent)	ΔG (MMPBSA)	ΔG (Autodock)	ΔG_{B1} (experiment)
αδ	-15.7 ± 2.8	-1.3 ± 0.3	-4.0 ± 0.5	-18.8 ± 2.8	-3.4 ± 0.6	-5.3
αε	-16.1 ± 2.9	-1.1 ± 0.4	-3.8 ± 0.6	-19.0 ± 2.9	-3.3 ± 0.7	-5.0
αγ	-22.2 ± 2.8	-1.4 ± 0.3	-5.2 ± 0.5	-35.4 ± 2.7	-4.8 ± 0.7	-7.1

Ligand (ACh) binding energy, ΔG (kcal.M^{-1}), was calculated by the continuum solvent method, MMPBSA method and using the epdb module of Autodock (see methods). ΔG is the sum of the electrostatic (ΔG_{Elec}) and the rescaled van der Waal energy (E_{VDW}) components. ΔG (continuum solvent) = $\Delta G_{Elec}+\lambda E_{VDW}$, where λ is a empirically determined scaling factor (0.17). Note the difference in ΔG between αγ vs αε and αδ sites, irrespective of the method of choice. Experimentally measured ΔG_{B1} is provided for reference.

Table 7.2: Structural parameters from MD simulations

Parameter	αδ	αε	αγ
Trp angle (degree)	68.7 ± 23.7	40.04 ± 17.1	89.11 ± 16.6
Ligand pocket volume ($Å^3$)	115.3 ± 18.7	131.9 ± 30.9	92.80 ± 16.1

Trp angles: the angle between the normal to the aromatic rings of W55 and W149. Note the orthogonality at αγ only. The volume of the binding pocket is also smallest in αγ, indicating compactness. Values are + S.D.

Table 7.3: ACh distances from aromatic residues in the binding pocket

A.

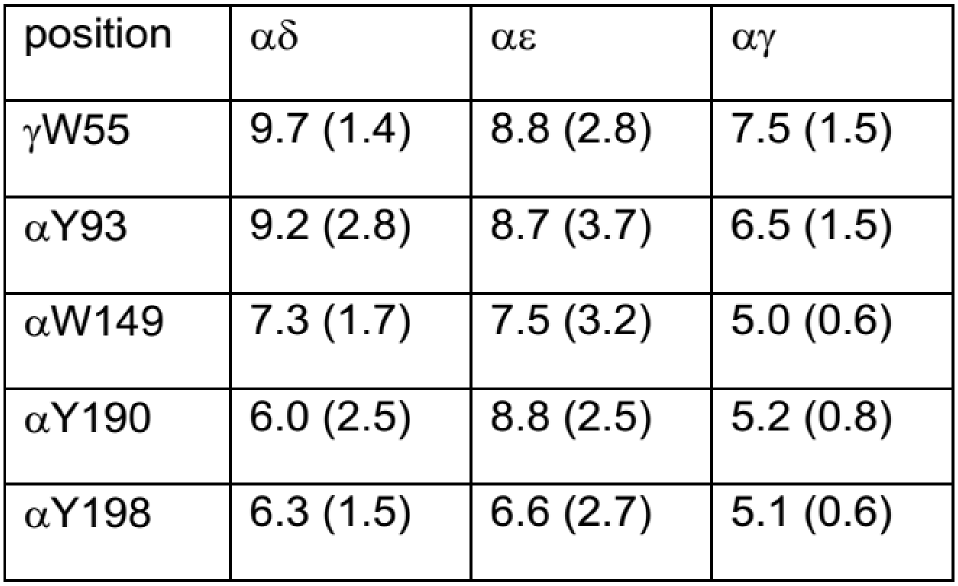

position	αδ	αε	αγ
γW55	9.7 (1.4)	8.8 (2.8)	7.5 (1.5)
αY93	9.2 (2.8)	8.7 (3.7)	6.5 (1.5)
αW149	7.3 (1.7)	7.5 (3.2)	5.0 (0.6)
αY190	6.0 (2.5)	8.8 (2.5)	5.2 (0.8)
αY198	6.3 (1.5)	6.6 (2.7)	5.1 (0.6)

B.

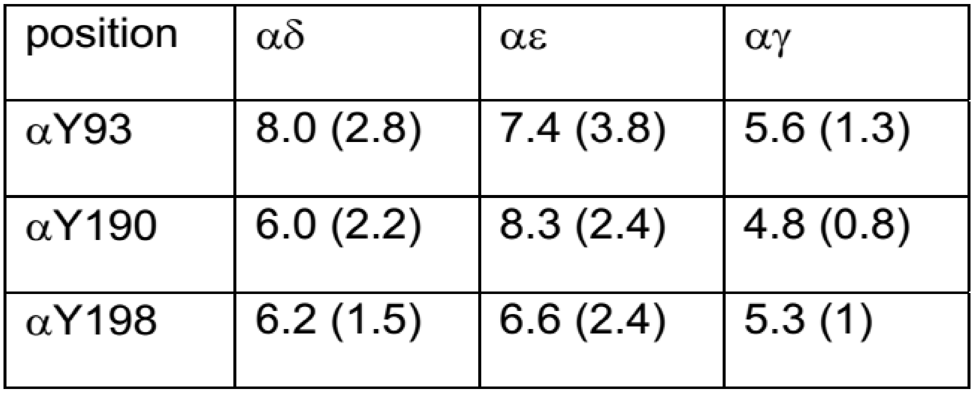

position	αδ	αε	αγ
αY93	8.0 (2.8)	7.4 (3.8)	5.6 (1.3)
αY190	6.0 (2.2)	8.3 (2.4)	4.8 (0.8)
αY198	6.2 (1.5)	6.6 (2.4)	5.3 (1)

A. Average (S.D.) distances in Å are between the geometric center of aromatic residues and the QA of ACh at the binding sites. B. Average (S.D.) distances are between the –OH of the tyrosines and the QA of ACh. In general, the average distances are smaller at αγ vs αε/αδ.

Chapter 8:

Structural correlates of affinity in fetal versus adult endplate nicotinic receptors*

Tapan Kumar Nayak†, Srirupa Chakraborty†, Wenjun Zheng, Anthony Auerbach**

*This chapter has been published:

Nature Communications **7**, 11352, doi:10.1038/ncomms11352 (2016)

† These authors contributed equally to this work. S.C. performed the computational simulations, T.K.N. performed the electrophysiology experiments

** primary editor of paper

ABSTRACT

Adult-type nicotinic acetylcholine receptors (AChRs) mediate signaling at mature neuromuscular junctions and fetal-type AChRs are necessary for proper synapse development. Each AChR has two neurotransmitter binding sites located at the interface of a principal and a complementary subunit. Although all agonist binding sites have the same core of five aromatic amino acids, the fetal site has ~30-fold higher affinity for the neurotransmitter ACh. Here we use molecular dynamics simulations of adult versus fetal homology models to identify complimentary-subunit residues near the core that influence affinity, and use single-channel electrophysiology to corroborate the results. Four residues in combination determine adult versus fetal affinity. Simulations suggest that at lower-affinity sites, one of these unsettles the core directly and the other three (in loop E) increase backbone flexibility to unlock a key, complementary tryptophan from the core. Swapping only four amino acids is both necessary and sufficient to exchange function between adult and fetal AChRs.

8.1 - Introduction

Endplate AChRs are heteropentamers that have two α(1) subunits and one each of β, δ and either γ or ε. Each receptor has two functional neurotransmitter binding sites located in the extracellular domain at subunit interfaces, either αδ+αγ (fetal) or αδ+αε (adult) (Figure 8.1a, inset). Agonist affinities in mouse AChRs have been measured for these sites, both separately and as pairs [91, 122, 276, 277]. The resting equilibrium dissociation constant for ACh (K_d^{ACh}) is ~30-fold lower at αγ compared to αδ or αε. The affinity of the fetal, αγ site is similar to that of the *Lymnaea stagnalis* acetylcholine binding protein (AChBP) [89].

The fetal γ-subunit is required for the proper maturation of the neuromuscular synapse [255, 256, 278]. In mice, γ-null mutations are lethal [134] and in humans, γ-subunit mutations cause both lethal and non-lethal (Escobar) types of multiple pterygium syndromes [135-137]. The reason(s) for the γ subunit requirement in synaptogenesis is not known, but possibilities include the higher agonist affinity, smaller single-channel conductance, longer open-channel lifetime, smaller gating voltage-dependence, lower Ca^{++} permeability and lower probability of opening constitutively of fetal AChRs [77, 91, 139]. Physiologically, the higher affinity of the fetal agonist binding site for both ACh and choline will lead to larger cellular responses [91, 279] at the low concentrations of these agonists that prevail at developing neuromuscular synapses [280].

There are ~250 side chain differences between adult ε- and fetal γ-subunits. Mutational correlates of differences between fetal and adult AChR function have been investigated previously. Mice expressing AChRs having an ε-γ subunit chimera joined at a conserved glycine in loop E, γ(≤113)+ε(≥114), have a fetal-like open-channel lifetime and adult-like conductance [256].

Synapses expressing these AChRs undergo normal endplate differentiation but show altered innervation patterns. In mouse AChRs the M3-M4 linker has been shown to influence fetal vs. adult open-channel lifetime [281]. In *Xenopus* AChRs residues at positions 6'/7' in M2 (N/I in γ vs. S/V in ε) were implicated in setting fetal vs. adult conductance [282], and in rat AChRs swapping the M2-20' amino acid from K to Q results in a partial exchange of conductance [138]. None of the above studies investigated the structural basis of fetal vs. adult affinity, which is the topic we address here.

At all 3 kinds of agonist site (αδ, αε and αγ) ACh is stabilized in the binding pocket by a core of 5 aromatic residues (Figure 8.1a). Based on their individual contributions to affinity, these can be divided into 2 working groups, an 'aromatic triad' and a 'special pair' [283]. The triad is αW149 (indole ring), αY198 (benzene ring) and αY190 (benzene ring and hydroxyl). The 4 functional groups of these 3 amino acids each make a similar contribution to ACh binding energy at all 3 agonist sites [279, 284]. In adult AChRs, these groups provide almost all of the neurotransmitter binding energy, which is equal to $+0.59\ln K_d$ (23 ^{o}C). Together, these groups stabilize ACh by ~-5.1 kcal·M^{-1}/site (-10.2 kcal·M^{-1} for αδ+αε sites combined). The action of the triad is led by αY190, because the ring and –OH each contribute ~-2 kcal·M^{-1} at αδ, αε and αγ.

A second working part of the agonist site apparatus is the special pair, αY93 (benzene ring) and ε/γW55 (δW57; indole ring). At αε and αδ these 2 groups make only a small contribution to ACh affinity but at the fetal αγ site the aromatic rings contribute significantly, to bring the single-site-total to ~-7.1 kcal·M^{-1} and the αδ+αγ total to -12.2 kcal·M^{-1} [279]. Moreover, at αγ the effects of alanine substitutions of this pair are not independent, as removing either ring interferes substantially with the other's ability to stabilize ACh. The energy contribution of this tryptophan differs massively between fetal and adult sites. At αγ the γW55A mutation decreases affinity by ~2000-fold, whereas the homologous substitution at αε reduces it by only ~13-fold and at αδ it actually *increases* affinity by ~2-fold.

Because the aromatic core has the same composition at all three kinds of agonist site, the difference in affinity between fetal and adult AChRs can be attributed to residues in the complementary, non-α subunit (δ, ε or γ). Our approach to finding these amino acids was to use molecular dynamics (MD) simulations of homology models based on AChBP to identify complementary-subunit amino acids near the core that influence the contribution of the special pair to affinity. Then, we exchanged those side chains *in vitro* (δ and ε↔γ) and estimated affinity from single-channel currents of AChRs expressed in cells. The results indicate that four residues in combination determine adult vs. fetal resting affinity, 3 in loop E (111-113; γ subunit numbers) and 1 in the β5-β5' linker (104). In the β5'-β6 hairpin region, mutations of the human γ subunit (V108, S111, P112 and P121) cause multiple pterygium and Escobar syndromes [135]. The simulations suggest that these amino acids influence core properties by changing the structure and dynamics of the β5-β5' linker and the complementary β-sheet, to effect the action of the special pair and the affinity for the agonist. Swapping the four side chains is both necessary and sufficient to exchange fetal vs. adult affinities and open-channel lifetimes.

The results are presented in 5 sections. First, we build and test homology models for fetal and adult agonist sites. Second, we use the models to identify residues in the complementary subunit that influence ACh affinity *in silico*. Third, we use electrophysiology (performed by Dr. T. K. Nayak; also see Appendix 2) to measure *in vitro* affinities of AChRs having the identified residues swapped, fetal↔adult. Fourth, we report the effects of point mutations on affinity, from the identified group and of a critical, complementary-side tryptophan. Fifth, we analyze the simulated structures and develop hypotheses for the mechanisms that undergird the fetal vs. adult affinity difference.

8.2 - Methods

8.2.1 - Homology Model

We improved the dimer model used in Chapter 7, by building a homology model of the extracellular domain of the fetal-type AChR, using MODELLER [219]. The template used was the *Aplysia californica* ACh binding protein (AChBP) crystal structure bound to epibatidine (pdb ID: 2BYQ). The sequences of AChBP and AChR subunits were aligned using CLUSTALX [285] (Figure 8.2a). The AChR subunits share ~20 % sequence identity with *Aplysia* AChBP**.** AChR subunits were modelled simultaneously so that spatial reciprocity was maintained at the interfaces. Residues 128 and 142 in the α subunit and the corresponding residues in other subunits were constrained as disulfide bonds. A protocol of conjugate gradient optimization, simulated annealing and molecular dynamics were used to refine the structure.

First, 100 structural models were generated. MODELLER has various assessment methods and objective functions to test the validity of a homology model (such as molpdf and DOPE scores) but these are not recommended to be used for multi-chain proteins [286]. Therefore we used PROCHECK scores based on G-factor [287] to rank the models. The model with the best G-factor score was chosen for docking and simulations [288]. The top 5 models based on G-factor were similar in both structure (backbone RMSD <0.7 Å; the equilibrated structure RMSD from the simulations was 1.2 Å) and scores. The selected model also ranked high in the MODELLER scores (1st in molpdf and 5th in DOPE score), bad contacts (3rd) and Ramachandran criteria (3rd). Further minimization of the selected model reduced the bad contacts to zero.

8.2.2 - Ligand docking

ACh and TMA were docked at the $\alpha\delta$ and $\alpha\gamma$ binding sites using the Lamarckian genetic algorithm in AUTODOCK [264]. ACh and the core aromatic residues were allowed to be flexible, and 30 Å cubic search grid was used at the expected binding site with 0.375 Å grid spacing. Docked structures were analyzed and selected on the basis of lowest energy and RMSD clustering. The CHARMM force field parameters for ACh and TMA were obtained from the CHARMM Generalized Small Molecule Force Field webserver (CGenFF) [289, 290].

8.2.3 - MD simulations

Point mutations were introduced *in silico* using the VMD *mutator* plug-in [224]. AChRs with ligands or mutations were optimized and equilibrated by using energy minimization and MD simulation. The system was solvated in a water box with TIP3P water model [265] and the box boundary was extended at least to 10 Å from the periphery of the protein in each dimension. Na^+ and Cl^- ions were added to neutralize the system and bring it to an ionic concentration of 150 mM NaCl.

Molecular dynamics simulations were run using NAMD [225] version 2.8, with the CHARMM27 force field [146]. First, a 20,000-step minimization was done using the steepest descent method, and with gradual release of restraints on the protein backbone. The system was heated to 300K over 100 ps, a 500 ps equilibration run was performed in the NVT ensemble and then 20 ns MD simulations were performed in the NPT ensemble at a temperature of 300K and pressure of 1 atm using the Nosé-Hoover method [266]. Following minimization, harmonic constraints (force constant=1 $kcal.M^{-1}/Å^2$) were applied on the $C\alpha$ atoms of residues which were

>25 Å away from the ligand. These restraints maintained the global backbone conformation of the model while allowing relaxation of all side chains.

Periodic boundary conditions were applied. A 10 Å switching distance and a 12 Å cutoff distance were used for non-bonded interactions. The particle mesh Ewald (PME) method [267] was used to calculate long-range electrostatic interactions. The SHAKE algorithm [268] was used to constrain bond lengths of hydrogen-containing bonds, which allows a time step of 2 fs for MD simulations. Four MD simulation trajectories were obtained for each system. The coordinates of the systems were saved every 1 ps during MD simulations for later analysis. The protein RMSD became stable by the first 10 ns (Figure 8.2b). All analyses and binding energy calculations were done on snapshots extracted every 20 ps over the last 10 ns of each trajectory. The ensemble for each system therefore contained 2000 snapshots of the system.

8.2.4 - Calculation of affinity

A total ligand-protein binding energy (ΔE) was estimated as described elsewhere [230] . In brief, this energy was calculated using a continuum solvent model from an ensemble of 2000 snapshots:

$$\Delta E = \alpha E_{VdW} + \beta \Delta E_{elec}$$

………………………. Eq. 9.1

where E_{VdW} is the Van der Waals contribution and ΔE_{elec} and is the electrostatic contribution calculated using the Poisson−Boltzmann (PB) method (PBEQ module of CHARMM [291] in a salt concentration of 140 mM). The molecular dielectric surface was defined by a probe radius of 1.4 Å. Previously-optimized atomic Born radii [269] for the 20 amino acids were used to estimate the electrostatic free energy in explicit water molecules. The dielectric constant of the protein interior and the aqueous environment were set to 4 and 80, respectively.

The coefficients α and β in Eq. 9.1 were evaluated by comparing simulated and experimental ΔE values for alanine mutations and optimizing the coefficients to reproduce the experimental energies (Figure 8.1b). We calculated *in silico* binding energies for the WT (with ACh/TMA) and Ala mutations at each of the core aromatic residues (α93, α149, α190, α198 and δ55), as described above. Values of α and β were scanned within a range of 0-2 to minimize the root-mean-square error (RMSE) between simulated and experimental energies for total 13 sample points:

$$RMSE = \left[\frac{1}{N}\sum_{n}\left(\Delta E_n - \Delta E_{exp,n}\right)^2\right]^{1/2}$$

………………………. Eq. 9.2

where n is each sample point and N=13. The overall fitting quality was tested by the coefficient of multiple determination R^2. The result was α=0.22 and β=1.24. The α and β values for barnase-barstar (0.17 and 1 [230]) were shown previously to reproduce the fetal vs. adult ACh binding energy difference [279]. The small α is possibly due to the loss of protein-water VdW contacts in the AChR, whereas the larger β (>1) may be due to cation-π interactions between the quaternary ammonium group of the ligand and the binding site aromatics, which is unaccounted for by the classical force field. With these values of α and β, the RMSE between simulated and experimental results were at a minimum (0.34 $\text{kcal}\cdot\text{M}^{-1}$; R^2=0.92), with a correlation coefficient of 0.97. To test the generality of these parameters, we plotted simulated and experimental affinities for two additional, non-alanine mutations (δY106L and γL104Y) in Figure 8.1b. These fell on the same regression line.

The approximate binding energy calculated from MD simulations using the above method (ΔE) and the free energy estimated from single-channel currents ($+0.59\ln(K_d)$) are not equivalent. However, the entropy contribution to ligand binding energy has been experimentally shown to be negligible in case of muscle-type AChRs [130], and here we show that changes in these quantities can be compared for the purpose of engineering biological AChRs. In the text we use “affinity” for both the *in silico* and *in vitro* binding energy estimates.

8.2.5 - Structure analyses

The geometric centers of the aromatic rings of interest and the ACh quaternary amine (QA) nitrogen were used as reference points. Structural analyses were done using the last 10 ns of each trajectory for the hetro-pentamer simulations. We measured all the distances and angles using VMD.

The volume of the ligand binding pocket was calculated by joining the centroids of the aromatic rings to form two adjoining tetrahedrons. The volume of each tetrahedron was calculated using the 3-simplex determinant method from the coordinates of the vertices, as described elsewhere [279]. The β-hairpin twist was measured from the angle between the central axial vectors of β5' and β6. The central axis was defined by the least squares linear regression fit of the coordinates of the backbone atoms of residues 107-110 in β5' and residues 115-118 in β6 (γ subunit numbers). The regression fit was calculated by singular value decomposition of the coordinates.

To identify a hydrogen bond between two atoms (i.e., acceptor and donor) a donor-acceptor distance of <3.5 Å and an donor-H-acceptor angle of <60° were used as criteria [257]. We used VMD to identify and calculate the occupancies of all H-bonds within the last 10 ns ensemble**.**

8.2.6 - RMSD and RMSF analyses

To assess the conformational stability of the MD simulations, we calculated the root-mean-square deviation (RMSD) of all backbone atoms in the α plus complimentary subunit relative to the starting structures. The RMSD plots showed a small amount of drift over time in some of the trajectories (Figure 8.2b, left). We determined that most of this drift came from the complimentary-side loop F, which was highly flexible and disorganized. We repeated the RMSD analyses after removing part of loop F from the calculation (residues 166-183 in γ and 164-177 in δ), and both the drift and variance in the RMSD were reduced significantly (Figure 8.2b, center). The plots show that the system stabilized within ~10 ns. This region of loop F had been modeled *ab-initio* into the homology model because there is no corresponding region in AChBP. To test the role of loop F in affinity, we partitioned the binding energy (Eq. 9.1) into contributions from individual residues using CHARMM. None of the loop F residues that were excluded from the RMSD calculations were in the top 5% (n~25) of those contributing to affinity, which comprise ~98% of the total binding energy. The choice of 5% corresponds to a *p*-value of 0.05.

As a further test of stability, we calculated a running average on the RMSD (without loop F) using a rolling window of 5 ns (Figure 8.2b, right-inset). The slopes of the regression lines fitted to the last 10 ns were small. The overall mean absolute slope-value was 0.002±0.001 Å/ns (±s.d) for all 4 constructs combined (n=16 trajectories). In addition, we calculated the average RMSD for the four trajectories for each construct (Figure 8.2b, right; s.d. calculated from 5 ns bins). The drifts in these averages during the last 10 ns (~0.02 Å) were smaller than the standard deviations of the fluctuations (~0.07 Å). These tests establish that all of the systems became stable within 10 ns and could be used for affinity estimation.

To compare the flexibility of ligand binding interface between the two states, we performed root-mean-square fluctuation (RMSF) analysis on the backbone atoms based on the last 10 ns of the MD simulations. RMSF of each residue was calculated with respect to the average structure of the ensemble using VMD version-1.9. This gives a residue-wise average of all possible fluctuations in the trajectories.

8.3 - Results

8.3.1 - Tuning the model

Our approach was to use MD simulations to guide mutagenesis, and electrophysiology experiments to measure *in vitro* affinities. We used an empirical and computationally-inexpensive method of estimating agonist binding energy *in silico* (see Methods). By adjusting the free parameters for van der Waals and electrostatic contributions in the calculations, simulated and experimental affinities could be correlated (Figure 8.1b). This was possible, in part, because in AChRs the entropy component of affinity is small [130, 292].

The circles in Figure 8.1b are simulated vs. experimental ACh binding energies for αγ and αδ agonist sites with mutations of core residues. The free parameters in the binding energy calculation (Eq. 9.1, Methods) were obtained only from the alanine mutations. Two non-alanine substitutions fell on the same regression line. The arrows indicate that the large and opposite effect of an alanine substitution of the complementary tryptophan on affinity at αγ vs. αδ that is apparent *in vitro* was reproduced *in silico*. Also, in both simulations and experiments the $\alpha\gamma^{WT}$ site showed ~40% more favorable binding energy for ACh and tetramethylammonium (TMA) compared to the $\alpha\delta^{WT}$ site (Figure 8.1c). These results suggest that brief simulations and approximate binding energy estimates can be used to screen for amino acids that influence affinity.

8.3.2 - C4 in silico

The first goal was to identify residues in the complementary, γ vs. δ subunit that are responsible for the 30-fold higher affinity for ACh in αγ vs. αδ. We used two criteria to select candidate residues to be exchanged *in silico*. We chose side chains that in the model were within 20 Å of the quaternary ammonium (QA) group of ACh *and* were different between γ vs. δ but homologous between ε and δ. A total of 10 amino acids satisfied both of these criteria (C10; Figure 8.3a).

In the first set of simulations, all C10 side chains were swapped, γ→δ and δ→γ, and ACh binding energies were calculated. The results were that the C10-mutated αδ site provided about the same binding energy as the $\alpha\gamma^{WT}$ site, and the C10-mutated αγ site provided about the same as the $\alpha\delta^{WT}$ site (Figure 8.3b). This suggested that the mutation(s) we were seeking were within the C10 group.

We then winnowed the mutation list. First, each member of the C10 group was dropped, one at a time. The result of these 9-swap simulations was that the affinities no longer reversed when one of 4 of the original 10 amino acids was omitted. When γ(L104, S111, P112 or D113) or δ(Y106, Y113, D114 or S115) side chains remained as in the parent subunit, the full affinity-reversal observed for C10 was incomplete. We call this set of four complementary subunit side chains C4.

Next, we simulated affinities using models in which only the C4 amino acids were exchanged as a group, to make constructs $\alpha\gamma^{C4\delta}$ and $\alpha\delta^{C4\gamma}$ (regular text is parent and superscript is target). Swapping all C4 side chains was sufficient to make the αγ-site have an affinity like $\alpha\delta^{WT}$ and the αδ-site to have an affinity like $\alpha\gamma^{WT}$. *In silico*, exchanging the C4 set of side chains was sufficient to exchange affinities, stably (Figure 8.3b).

In the next set of simulations, each of the 6 other residues of the C10 starting set was added to C4, one at a time. None of these made a significant difference in the magnitude of the affinity swap. Finally, we dropped each mutation from the C4 set, one at a time, and estimated ACh affinity. Unlike in the above simulations, the trajectories of these 3-mutant swaps were not stable (both fluctuating and divergent root mean square deviation, which made analysis of trajectories difficult). *In silico*, C4 was the minimum construct required for exchanging stably αγ and αδ binding energies.

8.3.3 - C4 in vitro for comparison (experiments performed by Dr. T. K. Nayak)

Next, corresponding experimental measurements of ACh affinity (K_d) were made from single-channel currents recorded from AChRs expressed in HEK cells (Figure 8.4). The C4 residues were investigated at αγ, αδ and αε binding interfaces. In these experiments, the constructs were $\alpha\delta^{C4\gamma}$ (δY106L + δY113S + δD114P + δS115D), $\alpha\varepsilon^{C4\gamma}$ (εY104L + εY111S + εE112P + εG113D) and $\alpha\gamma^{C4\delta}$ (γL104Y + γS111Y + γP112D + γD113S).

First, the *in vitro* measurements were made using AChRs that had only 1 functional binding site, its companion being knocked out by a mutation(s) [293]. The results were that the C4 ε→γ and δ→γ exchanges resulted in a nearly-complete swap of affinity (Figure 8.4a). The $\alpha\varepsilon^{C4\gamma}$ and $\alpha\delta^{C4\gamma}$ constructs each had the dose-response profile and affinity of the target, $\alpha\gamma^{WT}$ site. The K_d^{ACh} values for $\alpha\varepsilon^{C4\gamma}$ and $\alpha\delta^{C4\gamma}$ are shown in Table 8.1.

The behavior of $\alpha\gamma^{C4\delta}$ was more complex (Figure 8.4b). This construct alternated between two distinct modes of single-channel activity. One mode retained the high-affinity (Table 8.1) and longer open-channel lifetime characteristic of the parent ($\alpha\gamma^{WT}$) and the other had the low-affinity and briefer open-channel lifetime characteristic of the target ($\alpha\delta^{WT}$). The prevalence of each mode was approximately equal (isoenergetic), with a switching time constant of ~20 ms. The C4 γ→δ affinity exchange *in silico* was stable, but *in vitro* the swap in binding and gating functions was bimodal.

In addition to decreasing the ACh equilibrium dissociation constant (increasing affinity), the $\alpha\varepsilon/\delta^{C4\gamma}$ mutations generated a fetal-like, slower channel-closing rate constant in the presence of the neurotransmitter ACh. The effects of these C4γ mutations in the absence of agonists or in the presence of saturating [ACh] are shown in Figure 8.5 a, b, with the results summarized in Figure 8.6a and Table 8.1. The C4 substitutions were effective in exchanging ACh affinity. We also measured affinity for the partial agonists carbamylcholine (CCh), TMA and choline. These exchanged affinity partially with C4 mutations. On average, the low→high affinity C4 swaps were ~90% effective and the high→low affinity swaps were ~70% effective.

We also made *in vitro* measurements from AChRs having only 3 of the C4 side chain exchanges. The kinetic properties of these C3 receptors were complex and we did not attempt to estimate affinity.

The two WT AChR agonist sites act nearly independently in so far as binding energies measured from two-sites combined are approximately the sums of single-site energies [279]. In the next set of experiments we examined *in vitro* two different mutated, adult AChRs (both sites functional), $\alpha\varepsilon^{C4\gamma}+\alpha\delta^{WT}$ and $\alpha\varepsilon^{C4\gamma}+\alpha\delta^{C4\gamma}$. The prediction was that the first would have a fetal-type affinity and the second would be a 'super' AChR having the high, fetal-type affinity at both agonist sites. These expectations were confirmed, approximately (Figure 8.6b, c).

8.3.4 - Point mutations *(experiments performed by Dr. T. K. Nayak)*

The effects of point mutations of each C4 residue at each agonist site are shown in Figure 8.6d. In experiments, none of these single exchanges had a large (>1 $kcal \cdot M^{-1}$) effect on affinity or gating without agonists. With regard to affinity, the sum of the $\delta \rightarrow \gamma$ single-residue C4 swaps was -2.8 $kcal \cdot M^{-1}$ which is close to that for the $\alpha\delta^{C4\gamma}$ combination, but the sum of the $\gamma \rightarrow \delta$ single-residue swaps was only ~+0.5 $kcal \cdot M^{-1}$. With regard to the allosteric constant, none of the C4 swap sums were sufficient to account for the ~14-fold smaller unliganded gating equilibrium constant (+1.6 $kcal \cdot M^{-1}$) apparent in fetal vs. adult AChRs at -100 mV [91].

The mouse AChR ε-γ chimera was joined at a conserved glycine in loop E [256]. We were unable to record single-channel currents from AChRs having a point substitution here (γG114 to A, L or P) because these receptors either failed to express or open.

The action of the complementary, special pair tryptophan is the main distinction between αγ vs. αδ sites [261, 262, 279]. The huge difference in the effect of an alanine substitution at W55 in γ vs. δ *in vitro* was also apparent *in silico* (Figure 8.1b). To further test both the model and the ability of C4 to swap the properties of the aromatic core, we compared simulated and experimental ACh binding energies for the C4 constructs in the presence of the point mutation γ/εW55A or δW57A. If C4 was completely responsible for the different contributions of the special pair, we expected that an alanine substitution would have either no or little effect at $\alpha\gamma^{C4\delta/\varepsilon}$ (as in $\alpha\delta/\varepsilon^{WT}$), but would cause a large decrease in affinity at $\alpha\delta/\varepsilon^{C4\gamma}$ (as in $\alpha\gamma^{WT}$). The results agreed with these predictions, but partially (Figure 8.7). We did not test $\alpha\gamma^{C4\delta}$(+δW55A) in electrophysiology experiments because $\alpha\gamma^{C4\delta}$ gave rise to complicated, heterogeneous responses without the tryptophan mutation (Figure 8.4).

8.3.5 - Analyses of structures

The modeling and electrophysiology results suggest that the β sheet of the complementary surface of the agonist site can fold stably into, or isomerize between (Figure 8.4b), either of 2 ~isoenergetic configurations to produce a high, γ-like or a low, δ-like *resting* affinity (HA or LA, not to be confused with active-state vs resting-state affinities). Further, they suggest that the C4 side chains bias which of these super-secondary structures is adopted. Because there are no atomic-resolution structures of fetal or adult AChR agonist sites with agonist bound, we analyzed structures generated in the MD simulations in order to explore possible difference between the alternate conformations.

The two regions of interest were the core and the complementary β sheet. Figure 8.8 shows representative snapshots from C4-swapped trajectories and Figure 8.9a shows quantitative analyses of the HA vs. LA structures. The structural parameters estimated from C4-swapped constructs were similar to those from the parent subunits of corresponding affinity.

Representative snapshots of the core from $\alpha\gamma^{C4\delta}$ and $\alpha\delta^{C4\gamma}$ trajectories are shown in Figure 8.10a. In LA vs. HA structures, the β5’ linker residue Y104 is close and face on with αW149, and β2 residue W55 is distant and not orthogonal to either αW149 or αY93. The structural differences of the α subunit aromatic triad were less pronounced, but in the LA structures these side chains were all further from the agonist's quaternary amine (QA). Overall, the simulations indicate that the HA core is more compact, organized and stable.

In AChBP there is a structural water within the core that is H-bonded to ACh and the backbones of β5' and β6 [67, 292, 294] (Figure 8.1a). In the simulations, both this water and ACh were dynamic (Figure 8.10c). The water-β6 H-bond had the same propensity in both HA and LA structures, but the H-bonds with ACh and β5 were less prevalent in LA trajectories (Table 8.2). In the simulations the N-C-C-O dihedral angle (τ2) of the neurotransmitter was bimodal, being either -60^o or $+60^o$ (Figures 9.9a and 9.10a). The $+60^o$ configuration was ~5 times more common in LA trajectories.

We also estimated structural parameters for the complementary surface, which is made up of the β5' linker, the β5'-β6 hairpin (that includes loop E) and strand β2 (Figure 8.1a). Figure 8.10b (top) shows inter-strand backbone H-bonds for the hairpin. In LA vs. HA structures, loop E had 3 vs. 4 residues, because with the HA C4 amino acids (SPD) the pre-proline backbone 111(O) is rotated out of the hairpin plane and fails to form an H-bond with the post-glycine backbone 115(N) (Table 8.2). With LA amino acids (YDS), the 111-115 amide-oxygen H bond is present so that the first residue is part of the hairpin rather than the loop. Also, in HA structures the S111 side chain has an appropriate distance and geometry to H-bond with the loop E backbone (D113 or G114). The other difference in H-bonds is near the base of the hairpin, where the 109(N)-117(O) bond is less prevalent in LA structures. Figure 8.10b (bottom) shows that in the simulations, the overall hairpin is more upright (by $\sim 8^o$) and less twisted (by $\sim 9^o$; Figure 8.9a) in LA structures.

There were fewer H-bonds between the W55 backbone and neighboring residues in LA structures (Figure 8.10c and Table 8.2). Although the β2-β1 strand bond W55(N)-T36(O) was equally likely in LA and HA structures, the backbone H-bonds between W55(O)-T36(N) and W55(O)-E57(N) were less prevalent in LA.

Finally, we used RMSF analyses to estimate the dynamics of the complementary β sheet backbone (Figure 8.9b). The results are summarized in Figure 8.10c. In LA structures, the RMSF of the β5’ linker and loop E (that is, all C4 residues) was significantly smaller than in HA structures. This relative stability was accompanied by higher dynamics in other regions, in particular in the bottom half of the β hairpin and the β2 strand in the vicinity of W55. These differences in backbone dynamics correlate with the lower probability of H-bonds in LA structures at the base of the β-hairpin, with β5 and ACh and in β2 (Table 8.2). In summary, in the simulations lower affinity was associated with a straighter hairpin, a less-dynamic β5’ linker, a shorter and less-dynamic loop E, and a more-dynamic backbone near the core (base of hairpin, structural water and W55).

8.4 - Discussion

8.4.1 - Adult vs. fetal function

It was possible to swap *in vitro* the affinities of the fetal and adult agonist sites based on mutations identified *in silico*. Apparently, (i) the *Aplysia* AChBP is a good model of the endplate AChR resting αγ agonist site, (ii) classical force fields, short simulation times and approximate estimates of binding energy are adequate, and (iii) other structural elements of the biological AChR (transmembrane and intracellular domains, lipid bilayer, post-translational modifications) are not major determinants of ACh affinity. The results suggest that simulations that are not state-of-the-art can nonetheless be used effectively as an engineering tool.

The C4 set of residues determines some of the functional differences between fetal vs. adult AChRs. Swapping just these 4 side chains exchanges fetal vs. adult AChR affinities and open-channel lifetimes. This suggests that the complementary, super-secondary β-sheet can adopt either a fetal-type (HA) or an adult-type (LA) conformation. The C4 mutation set does not, however, account for fetal vs. adult differences in the unliganded gating equilibrium constant, gating voltage-dependence, single-channel conductance or ion selectivity. Nonetheless, it is now possible to control by C4 mutation(s) an AChR's affinity for the neurotransmitter and, by other mutations the allosteric constant, open-channel lifetime and, to some extent, single-channel conductance. This ability may lead to a better understanding of the reasons for the requirement of the γ subunit in synaptogenesis.

The ability of the C4 mutation to swap open-channel lifetime was not expected because in adult AChRs most α subunit mutations near the agonist sites have little or no influence on the open channel life time [295]. The slope of a log-log plot of opening rate vs. gating equilibrium constant for a series of point mutations (ϕ) informs of whether the substitutions change the closed vs. open lifetime, on a scale from 1 to 0 [296-298]. From the two sets of gating rate constants in the bimodal construct $\alpha\gamma^{C4\delta}$ (Figure 8.4b) we estimate that $\phi=0.57$, a value that is characteristic of many residues in the α subunit transmembrane domain [129]. We do not know if this low ϕ-value can be attributed in general to complementary-side residues or to a difference between γ and ε subunits. An in-depth exploration of amino acid ϕ-values on the complementary surface and in the $\alpha\gamma$ core will be taken up, elsewhere.

The C4 mutation set does not account completely for differences in fetal vs. adult AChR affinity. First, simulations showed a stable, high-to-low affinity exchange in $\alpha\gamma^{C4\delta}$ but in electrophysiology experiments the behavior of this construct was bimodal (Figure 8.4b). Apparently, with this swap the energy barrier separating the alternative, complementary β-sheet folds was low enough to allow a reversible isomerization on the ~20 ms time scale, which is far beyond the simulation time frame. Second, the effect of C4-swaps was only partial with regard to the affinity of W55A (both *in silico* and *in vitro*; Figure 8.7). Third, the affinities of the C4-constructs for the partial agonists choline and TMA were not completely swapped (Table 8.1). These results suggest that the C4 group does not fully account for all differences in fetal vs. adult binding properties. Adding mutations to C4, either from the original C10 set or elsewhere in the extracellular domain, might improve the fetal vs. adult match in function. Also, some of the differences between simulated and experimental results may arise from long-range interactions that were not modeled.

Although the C4 combination was sufficient to exchange affinities, we cannot be sure that this set of substitution is unique in this regard. There are 1023 possible mutant combinations for the starting set of 10, of which we examined only 84 *in silico*. It is possible that other combinations could also generate the affinity swap. Also, the original selection criteria could have left out important residues from the starting set. For example, γE57/εG57/δD59 in the complementary β2 strand were not included in the starting set because the ε and δ side chains are not homologous. Nonetheless, the ability of the C4 combination to swap affinity and lifetime suggests that the C4 residues are an important basis for the functional differences between fetal vs. adult endplate AChRs.

Recently, it was found that in α4β2 neuronal nicotinic AChRs three complementary-subunit residues determine differential agonist potency of α4-α4 vs. α4-β2 binding sites [299]. The corresponding positions in the endplate AChR γ subunit are L109, Y117 (in C10) and L119, none of which belong to the affinity-changing C4 group. This lack of correspondence may reflect a difference between these neuronal vs. endplate AChRs, or may be traced to the benchmark of potency vs. affinity. Nonetheless, the approach of combining simple and rapid simulations with *in vitro* energy estimates could be useful in general for revealing affinity-influencing amino acids in zones surrounding the core of ligand-binding sites in other ligand-gated ion channels.

8.4.2 - Structure and dynamics

In the simulations, the C4 mutations caused changes in structure that paralleled those that distinguished LA, $\alpha\delta^{WT}$ and HA, $\alpha\gamma^{WT}$ sites (Figure 8.9a). One of the C4 residues is in the β5’ linker, adjacent to the core, and the other 3 are in loop E and far from the core. Hence, the effects of the C4 side chains appear to take place by both local and non-local mechanisms, to generate a core that is more compact in HA vs. LA structures (Figure 8.10a).

The primary features that distinguish the complementary subunit in LA vs. HA structures were as follows. (i) The β5' linker is less dynamic, with the aromatic Y104 side chain close and face-on to αW149 and suggestive of a direct, π–π interaction. (ii) Loop E is 1 residue shorter. (iii) There are fewer H-bonds near the core, at base of the hairpin with ACh and near W55 in β2. (iv) The W55 side chain is displaced from the core and not orthogonal to αW149 or αY93. (v) The loop E backbone is less-dynamic and the β2 backbone near W55 is more-dynamic. Overall, these differences suggest that three processes are required for C4 residues to generate a low affinity - unsettling the core by a local effect of the linker (104) side chain with αW149, loosening the β-sheet near the core by reducing the probability of H-bonds, and increasing the dynamics of the W55 backbone to unlock the special pair from the core.

We hypothesize that the dynamics and orientation of 104 are both determined by the aromatic vs. aliphatic character of the side chain, which in LA is Y and in HA is L. The apparent π-stacking of the δY104 and αW149 aromatic rings (Figure 8.10a, left) likely affects core architecture directly. This interaction may influence that between αW149 and ACh (~0.7 kcal·M^{-1} less favorable at adult sites [279]) and could also be a reason for the lower dynamics of the β5' linker. The unsettling of the core by the linker Y is, however, not sufficient to lower affinity completely because the effect of the point, L↔Y mutation is relatively small (Figure 8.6d), perhaps because γW55 remains locked in place. Recently, we showed that the $\alpha\delta^{C4\gamma}$ mutations reduce modal changes in affinity induced by loop C mutations at the αδ site [300]. It is possible that increased compactness of the site, along with the loss of a π–π interaction with αW149 stabilizes the aromatic triad and affinity.

In LA constructs the β5’-β6 hairpin is straighter, and loop E is shorter and less dynamic. It is possible that these differences affect interactions between core residues and the agonist directly, but more likely they influence affinity indirectly by changing the H-bond network of the β-sheet to increase backbone dynamics near the core. The simulations suggest that in LA structures the bottom half of the β-hairpin and near W55, locations that have fewer H-bonds, are more dynamic (Figure 8.10c). Our hypothesis is that the loop E C4 residues unlock indirectly the W55 backbone and allow this side chain to move away from the core, reducing its interaction with its partner αY93 and diminishing the contribution of the special pair towards affinity.

The simulations also showed differences in the ACh molecule between LA and HA constructs. In LA structures, the ACh τ2 dihedral angle is +60^o rather than -60^o, perhaps because the H-bond with water is less probable as a consequence of the greater backbone dynamics nearby. However, the extent to which the differences in agonist orientation and H-bonding relate to fetal vs. adult affinity is uncertain. The agonist sites show a similar affinity-difference for TMA (Figure 8.1c, bottom), but this ligand does not have a rotatable bond and is too distant from the water to form an H-bond. We suspect that the core water is a factor that sets the higher affinity for ACh vs. TMA, but may not be critical in determining the relative affinity of fetal vs. adult sites.

The results suggest that both the structure and dynamics of complementary β sheet are influenced by the C4 amino acids as a group, and that these residues are the bases, in part, for adult vs. fetal endplate receptor function. At the agonist-site core, the orientation of the 104 side chain and dynamics of the W55 backbone together appear to generate the ~30-fold affinity difference for the neurotransmitter. The simulations suggest that alternative conformations of the complementary β sheet influence the architecture and affinity of the core. Further analyses of loop

E interactions with loops A, B and C in the α subunit (that hold other core aromatics) and with nearby residues in β2-β3 linker (the MIR) may further illuminate affinity mechanisms in AChRs.

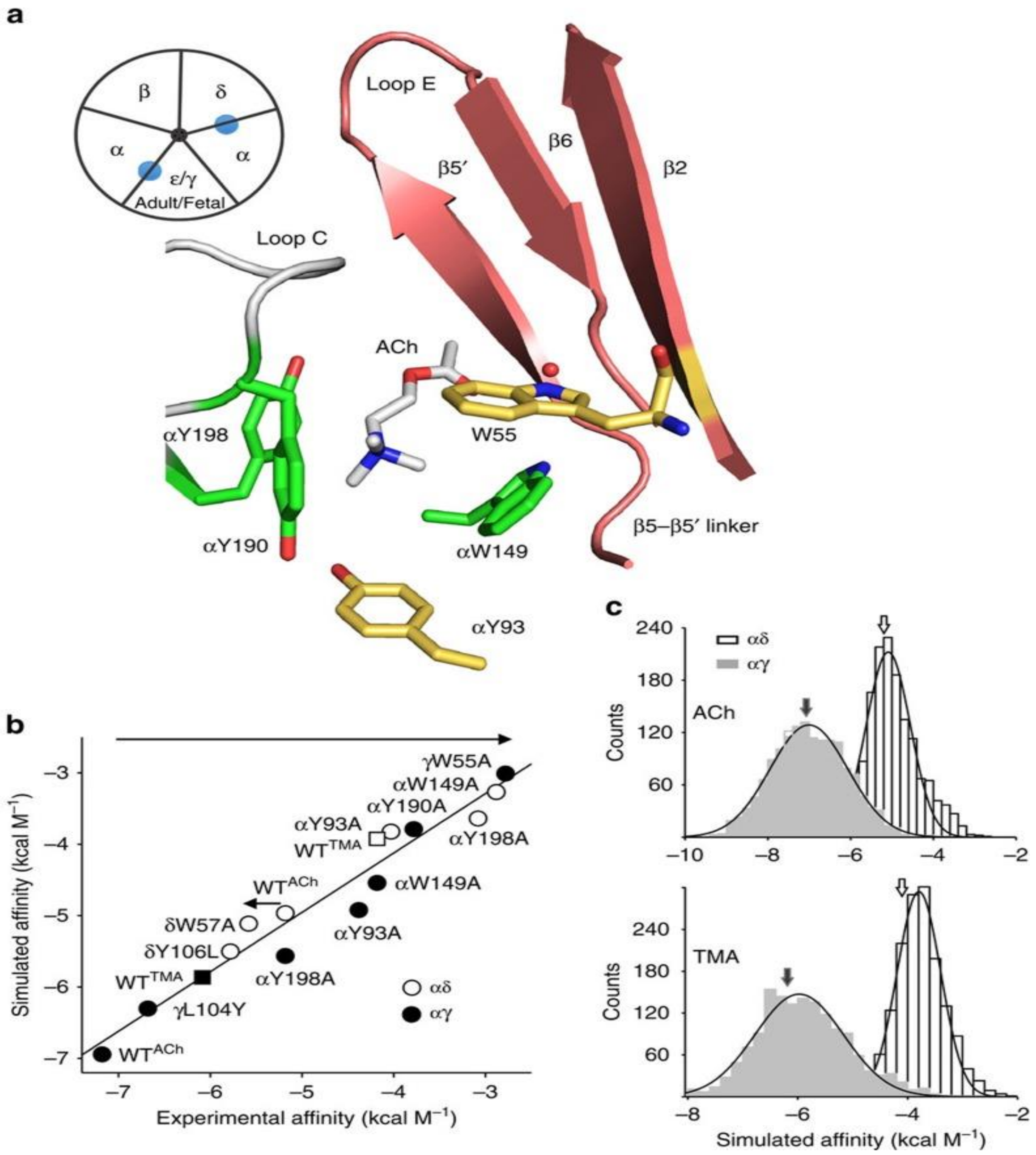

Figure 8.1: Ligand binding site and affinities. a. The principal subunit (α in AChRs) is left (white) and the complementary subunit (δ, ε or γ) is right (pink; *Lymenea stagnalis,* pbd accession number 3WIP[67]). Aromatic triad, green; special pair, yellow; structural water, red sphere. Inset: in endplate AChRs only 2 of the 5 subunit interfaces are functional binding sites (blue). b. Affinity estimates from simulations and electrophysiology experiments are correlated. Circles, ACh (alanine mutations of core aromatics except where marked); squares, TMA (WT only). In both simulations and electrophysiology experiments, there is a large loss in binding energy with αW55A and a small gain with δW57A (arrows). c. Distributions of binding energies from WT AChR simulations. Arrows mark the corresponding *in vitro* affinities estimated from electrophysiology experiments.

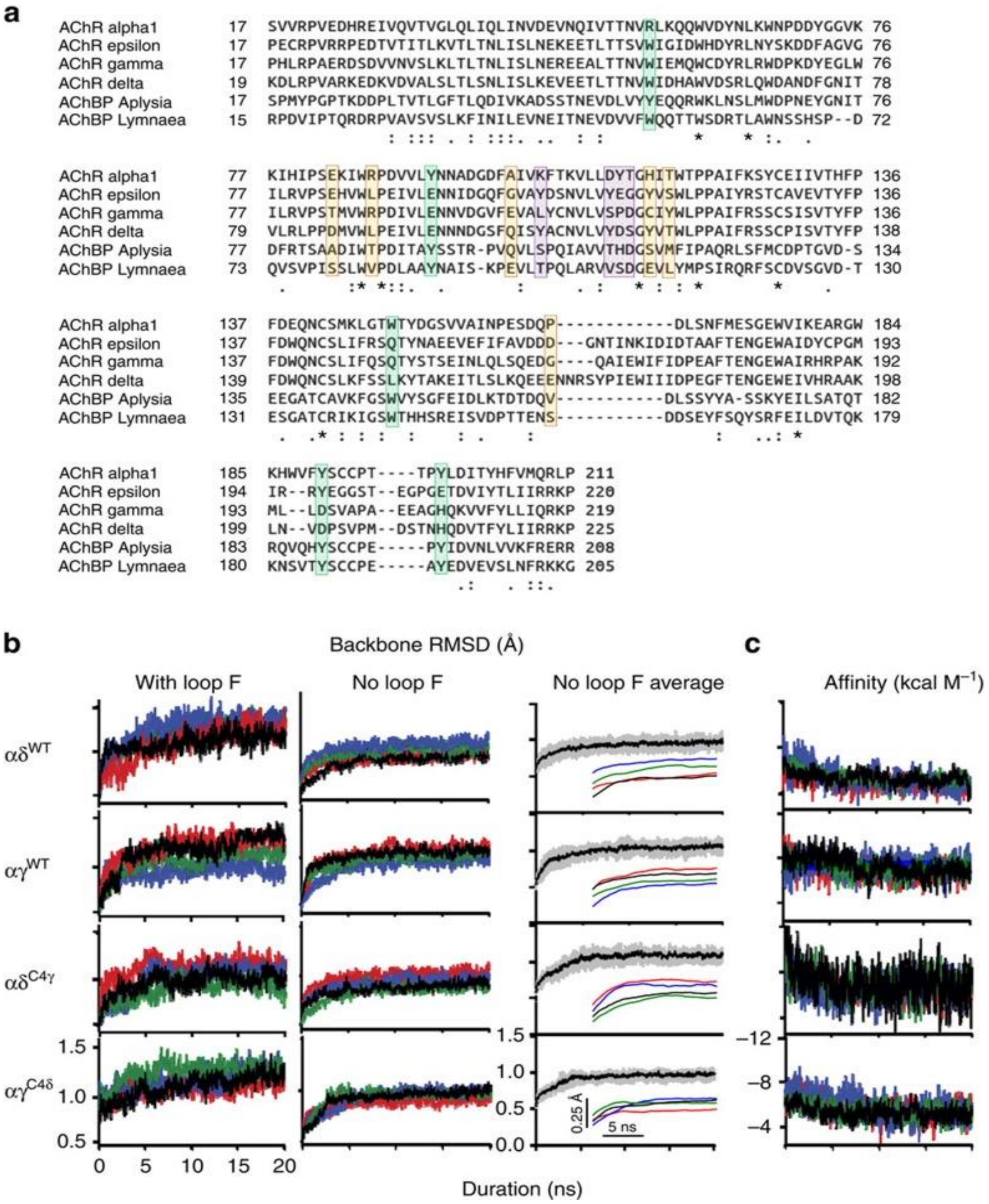

```
AChR alpha1      17  SVVRPVEDHREIVQVTVGLQLIQLINVDEVNQIVTTNVRLKQQWVDYNLKWNPDDYGGVK 76
AChR epsilon     17  PECRPVRRPEDTVTITLKVTLTNLISLNEKEETLTTSVWIGIDWHDYRLNYSKDDFAGVG 76
AChR gamma       17  PHLRPAERDSDVVNVSLKLTLTNLISLNEREEALTTNVWIEMQWCDYRLRWDPKDYEGLW 76
AChR delta       19  KDLRPVARKEDKVDVALSLTLSNLISLKEVEETLTTNVWIDHAWVDSRLQWDANDFGNIT 78
AChBP Aplysia    17  SPMYPGPTKDDPLTVTLGFTLQDIVKADSSTNEVDLVYYEQQRWKLNSLMWDPNEYGNIT 76
AChBP Lymnaea    15  RPDVIPTQRDRPVAVSVSLKFINILEVNEITNEVDVVFWQQTTWSDRTLAWNSSHSP--D 72
                                 : ::: . : :::. ..  : :         *    * :.  .

AChR alpha1      77  KIHIPSEKIWRPDVVLYNNADGDFAIVKFTKVLLDYTGHITWTPPAIFKSYCEIIVTHFP 136
AChR epsilon     77  ILRVPSEHVWLPEIVLENNIDGQFGVAYDSNVLVYEGGYVSWLPPAIYRSTCAVEVTYFP 136
AChR gamma       77  ILRVPSTMVWRPDIVLENNVDGVFEVALYCNVLVSPDGCIYWLPPAIFRSSCSISVTYFP 136
AChR delta       79  VLRLPPDMVWLPEIVLENNNDGSFQISYACNVLVYDSGYVTWLPPAIFRSSCPISVTYFP 138
AChBP Aplysia    77  DFRTSAADIWTPDITAYSSTR-PVQVLSPQIAVVTHDGSVMFIPAQRLSFMCDPTGVD-S 134
AChBP Lymnaea    73  QVSVPISSLWVPDLAAYNAIS-KPEVLTPQLARVVSDGEVLYMPSIRQRFSCDVSGVD-T 130
                      .      :* *::.  .       :     . :   * : : *       *    .

AChR alpha1     137  FDEQNCSMKLGTWTYDGSVVAINPESDQP------------DLSNFMESGEWVIKEARGW 184
AChR epsilon    137  FDWQNCSLIFRSQTYNAEEVEFIFAVDDD---GNTINKIDIDTAAFTENGEWAIDYCPGM 193
AChR gamma      137  FDWQNCSLIFQSQTYSTSEINLQLSQEDG----QAIEWIFIDPEAFTENGEWAIRHRPAK 192
AChR delta      139  FDWQNCSLKFSSLKYTAKEITLSLKQEEENNRSYPIEWIIIDPEGFTENGEWEIVHRAAK 198
AChBP Aplysia   135  EEGATCAVKFGSWVYSGFEIDLKTDTDQV-----------DLSSYYA-SSKYEILSATQT 182
AChBP Lymnaea   131  ESGATCRIKIGSWTHHSREISVDPTTENS-----------DDSEYFSQYSRFEILDVTQK 179
                      .  .* : :  :    : .    :                  :   ..: *

AChR alpha1     185  KHWVFYSCCPT----TPYLDITYHFVMQRLP 211
AChR epsilon    194  IR--RYEGGST--EGPGETDVIYTLIIRRKP 220
AChR gamma      193  ML--LDSVAPA--EEAGHQKVVFYLLIQRKP 219
AChR delta      199  LN--VDPSVPM--DSTNHQDVTFYLIIRRKP 225
AChBP Aplysia   183  RQVQHYSCCPE-----PYIDVNLVVKFRERR 208
AChBP Lymnaea   180  KNSVTYSCCPE-----AYEDVEVSLNFRKKG 205
                                        .:   . ::.
```

Figure 8.2: Sequence alignment and stability of models. a. Sequence alignment of the extracellular domain of AChR subunits (mouse) and AChBPs. Highlighted residues are: core aromatics, green; C4, violet; other members of C10, orange. b. Temporal evolution of simulated root-mean-square-deviation (RMSD) in WT and C4-swapped constructs. Left, total RMSD; each color is a different trajectory. Center, RMSD after removing a section of loop F. Right, average (black) ± s.d. (grey) of all four trajectories (loop F removed; inset is rolling 5 ns average of each trajectory). All three plots show that the structure is stabilized by ~10 ns. c. Temporal evolution of simulated ACh binding energy (loop F included).

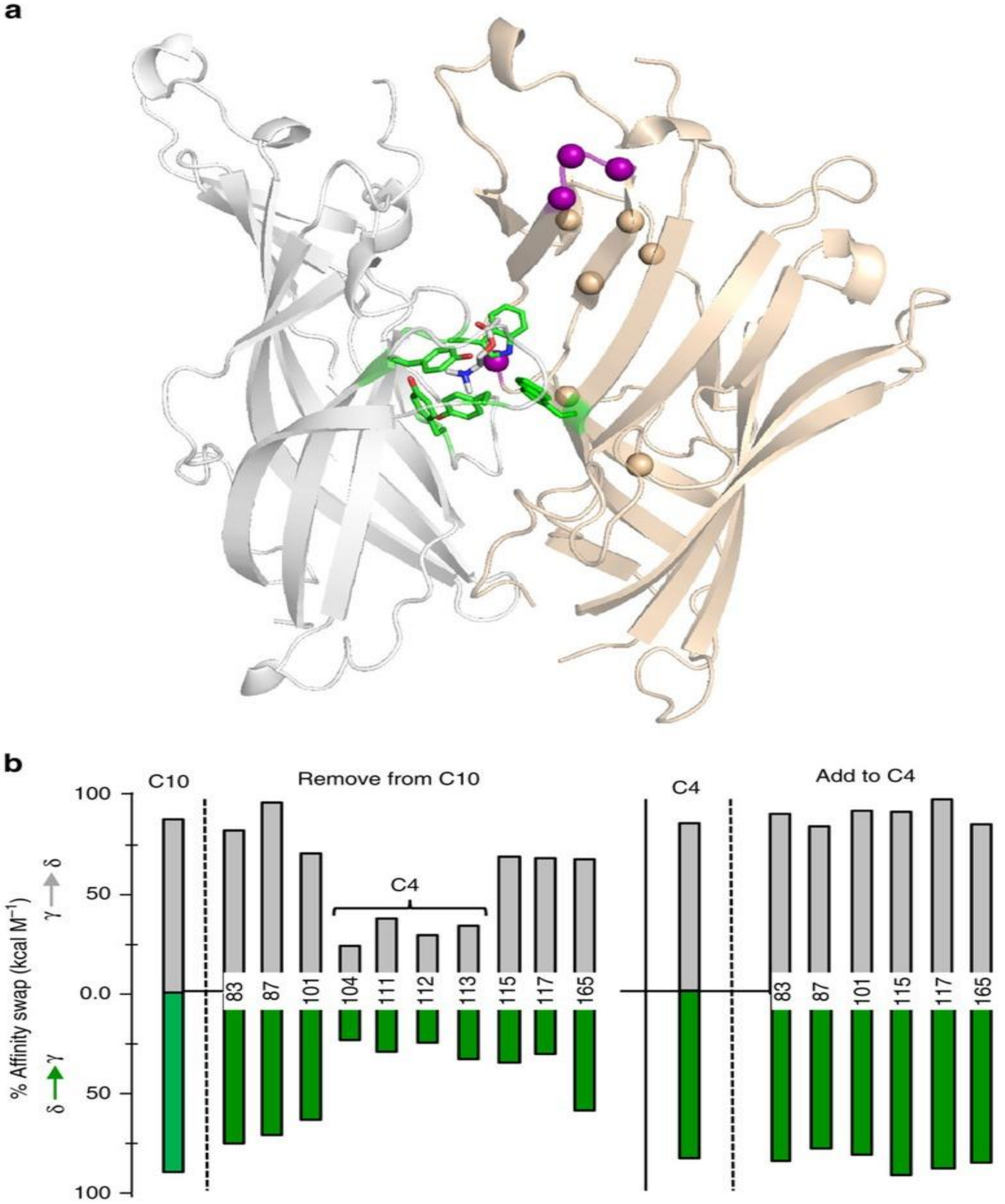

Figure 8.3: Simulations identify affinity-influencing side chains. a. 10 residues in the complementary subunit (tan) are within 20 Å of the ACh quaternary amine and are different in γ vs. δ≈ε (large spheres; C10). Core, green; C4 residues, violet. b. Affinity changes calculated *in silico* for different combinations of side-chain swaps. Residue numbers pertain to the γ subunit. Left-to-right: swapping all C10 residues almost completely exchanges affinity; dropping any one of 4 residues from C10 reduces the magnitude of the affinity change (C4; violet spheres in panel a); swapping all C4 side chains together is sufficient to exchange affinity; adding residues does not improve significantly the effect of the C4 swap.

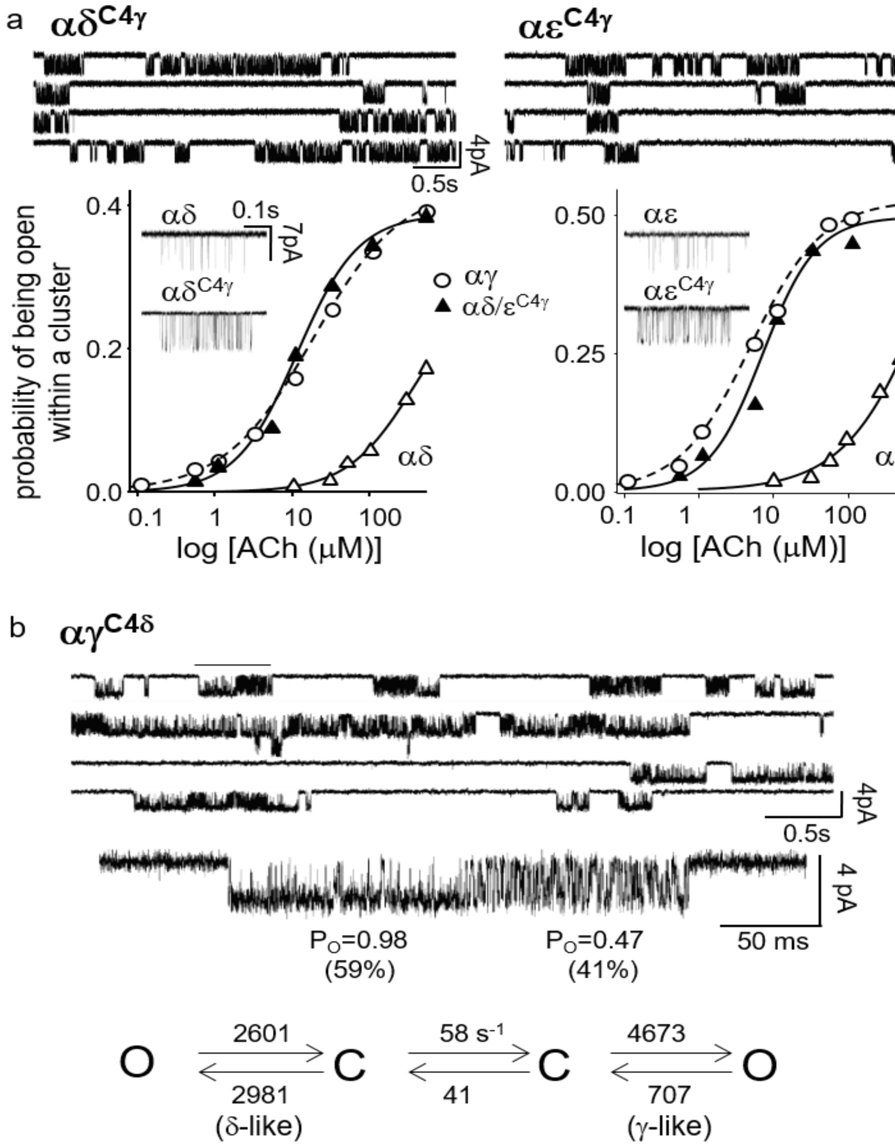

Figure 8.4: Electrophysiology measurements corroborate simulations (Experiments performed by Dr. T. K. Nayak). a. Replacing all of the δ/ε C4 side chains with those of γ ($\alpha\delta/\varepsilon^{C4\gamma}$) fully-exchanges ACh affinity. In all traces openings are down. Top, low time-resolution view of single-channel currents. The long gaps between clusters of openings are sojourns in desensitized states; affinity was estimated from the intra-cluster interval durations; membrane potential was +70 mV to reduce channel block by ACh (100 mM); only one agonist site was functional. Bottom, dose-response curves. Inset, example clusters (10 μM ACh, V_m=-100 mV, no channel block). b. Top, replacing all of the γ C4 side chains with those of δ ($\alpha\gamma^{C4\delta}$) generates AChRs that switch between fetal and adult affinity and open-channel lifetime (100 mM ACh, V_m=+70 mV). Bottom, bimodal kinetics of single channel intra-cluster interval duration showing the αγ↔αδ switch in behavior.

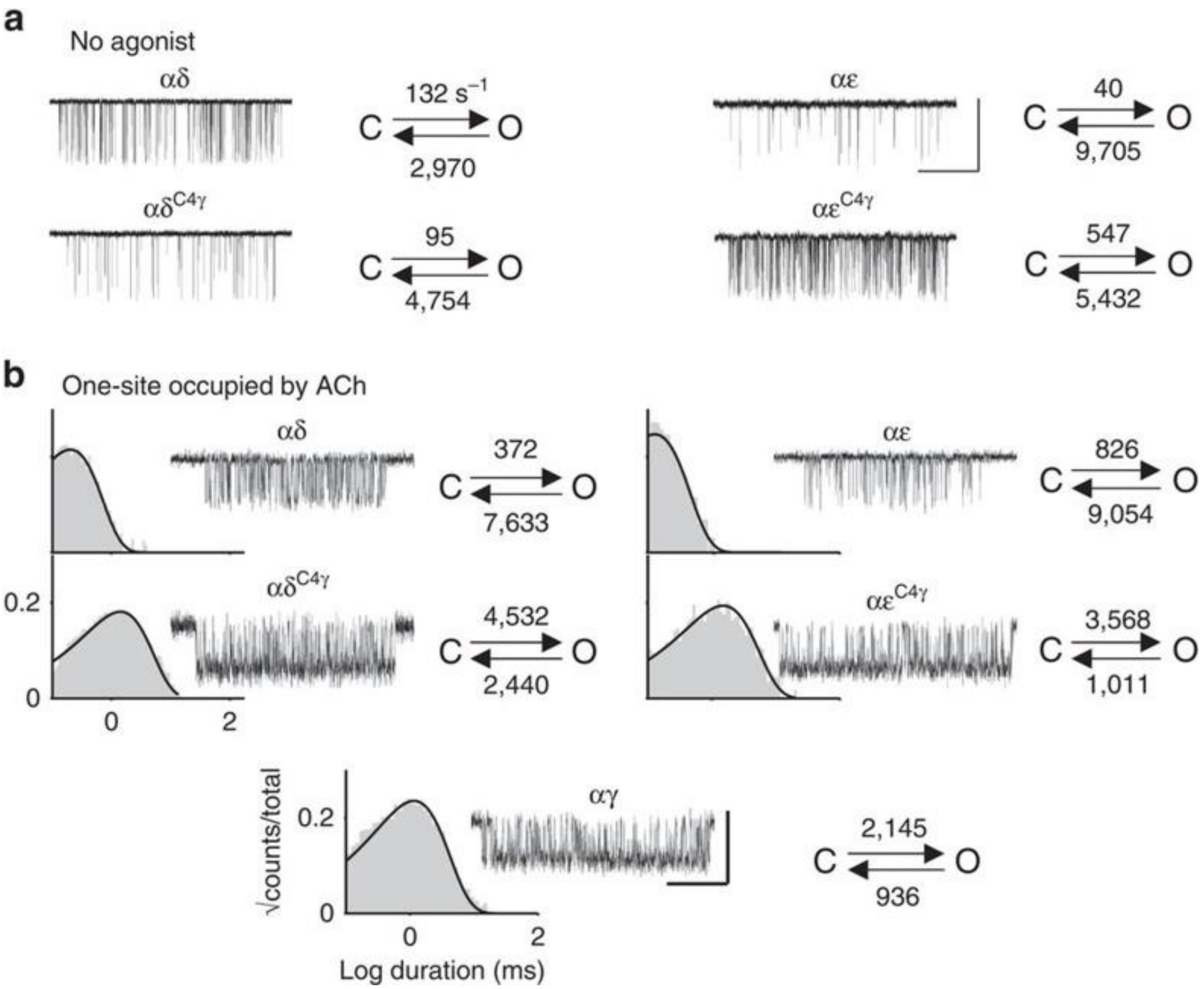

Figure 8.5: C4 mutations swap fetal vs. adult gating kinetics (Experiments performed by Dr. T. K. Nayak). a. Gating without agonists (opening are down; V_m=-100 mV). At αδ and αε the effects of the C4γ mutations are <2-fold except for the αε opening rate constant. C4 mutations have a small effect on unliganded gating. b. Gating with one functional agonist binding site occupied by ACh (100 mM; V_m=+70 mV to reduce channel block). At αδ and αε the C4γ mutations cause the channel-closing rate constant to become like that of the target subunit. Histograms are open-channel lifetime distributions. See Figure 8.6a for summary.

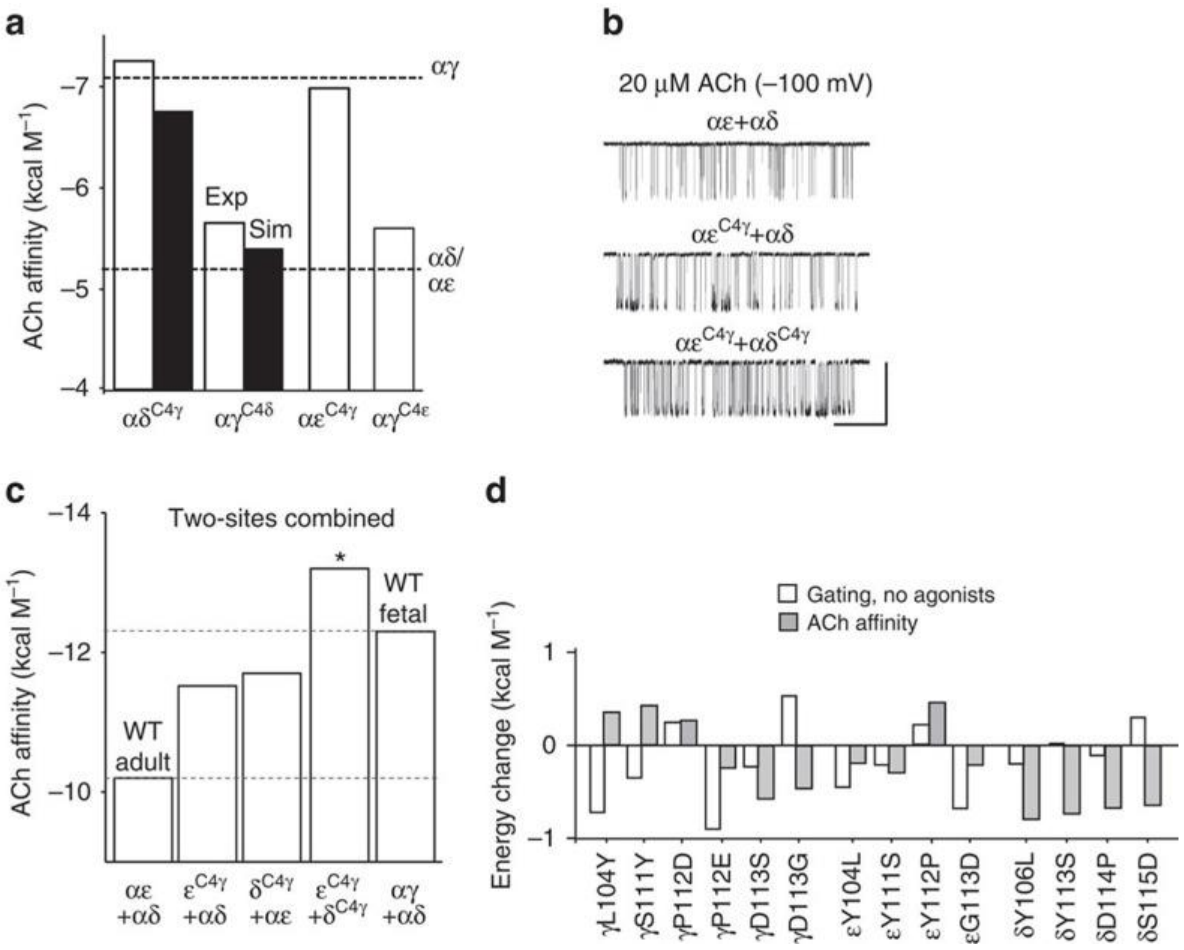

Figure 8.6: ACh affinities for 1- and 2-site AChRs (Experiments performed by Dr. T. K. Nayak)**.** a. ACh affinities (+0.59lnK_d) of C4-swapped constructs in AChRs having a single functional agonist binding site (exp, from electrophysiology; sim, from MD simulations; see Table 8.1). Dashed lines, WT affinities measured by using electrophysiology[279]. The C4 mutations exchange affinity. b. Swapping C4 at both adult sites (αε+αδ) in 2-site AChRs. Example single-channel currents (openings are down). c. Total ACh binding energy from both sites combined; *, the doubly-swapped adult AChR (ε^{C4γ}+δ^{C4γ}) has even-more favorable ACh binding energy than the WT fetal AChR. d. Effects of swapping C4 side chains one at a time in 1-site receptors.

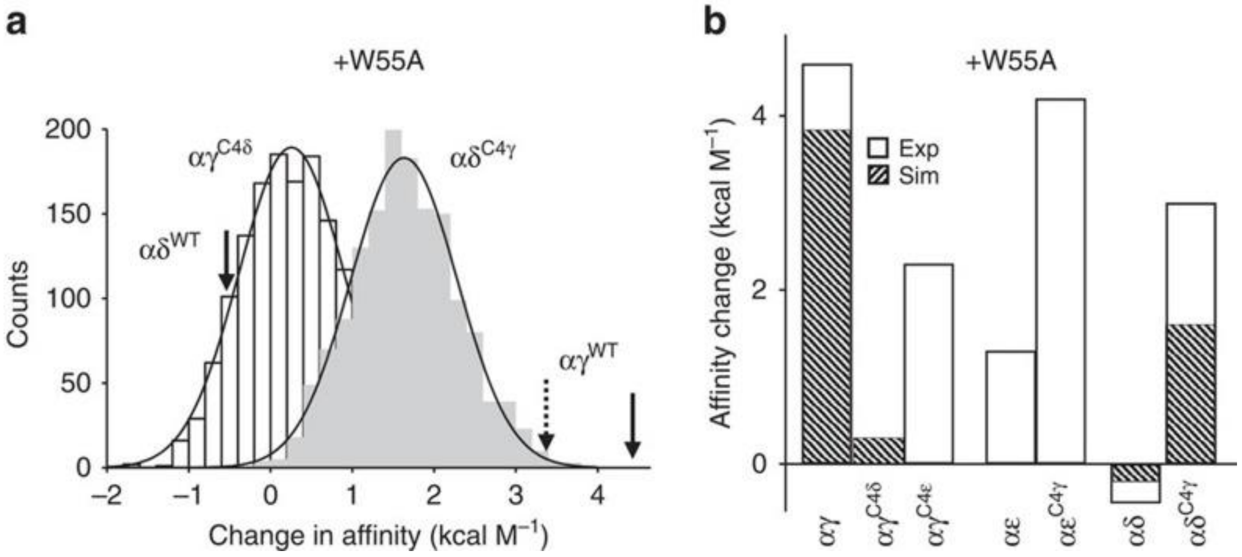

Figure 8.7: The action of W55 in C4-swapped constructs. a. Change in ACh affinity with an added W55A mutation. Histograms simulated from C4-swapped constructs; solid arrows, electrophysiology results in WT background (see Figure 8.1b). Left, for the $\alpha\gamma^{C4\delta}$ and $\alpha\delta^{WT}$ backgrounds, the change in affinity was similar and small in both simulations and experiments. Right, for the $\alpha\delta^{C4\gamma}$ and $\alpha\gamma^{WT}$ backgrounds, the simulated change in affinity was smaller than observed in experiments. Dashed line, simulated change in affinity for the $\alpha\gamma^{WT}$ background. b. Summary of W55A mutational effects on ACh affinity. In both simulations and experiments the energy change was partial for $\alpha\gamma^{C4\delta}$ and $\alpha\delta^{C4\gamma}$ but nearly complete for $\alpha\varepsilon^{C4\gamma}$.

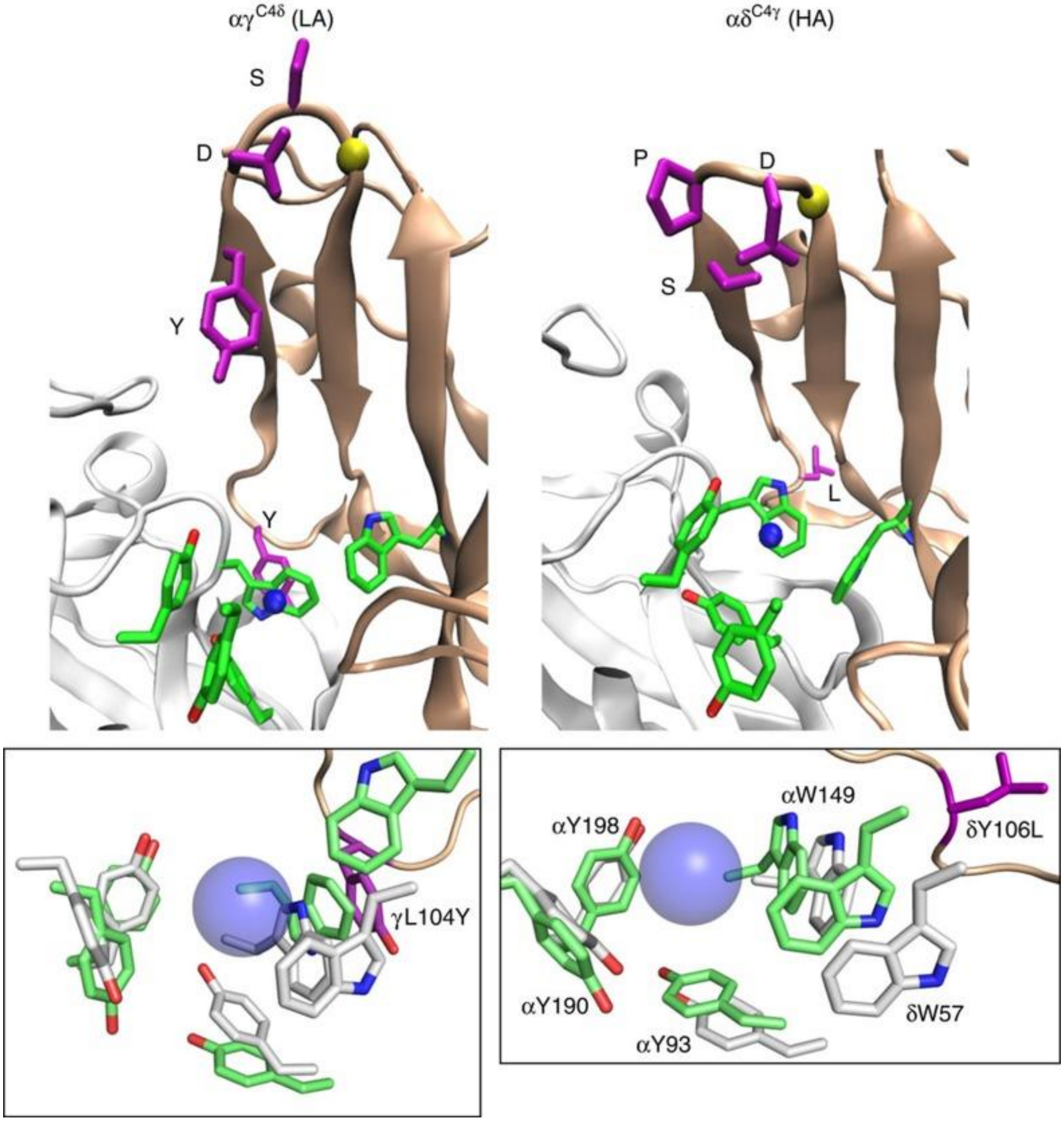

Figure 8.8: Representative snapshots of C4-swapped constructs. The snapshots have the lowest RMSD from the mean. Top: Low-resolution views; α subunit, white; complementary subunit, tan; core aromatics, green; C4 amino acids, violet; ACh nitrogen, blue sphere; αC of conserved loop E glycine, yellow. Bottom: High-resolution view of core in the parent (white) and C4-swapped (green) constructs. In the higher affinity (HA) structures the binding pocket is more compact and W55 is closer to agonist (quaternary ammonium group, large blue sphere).

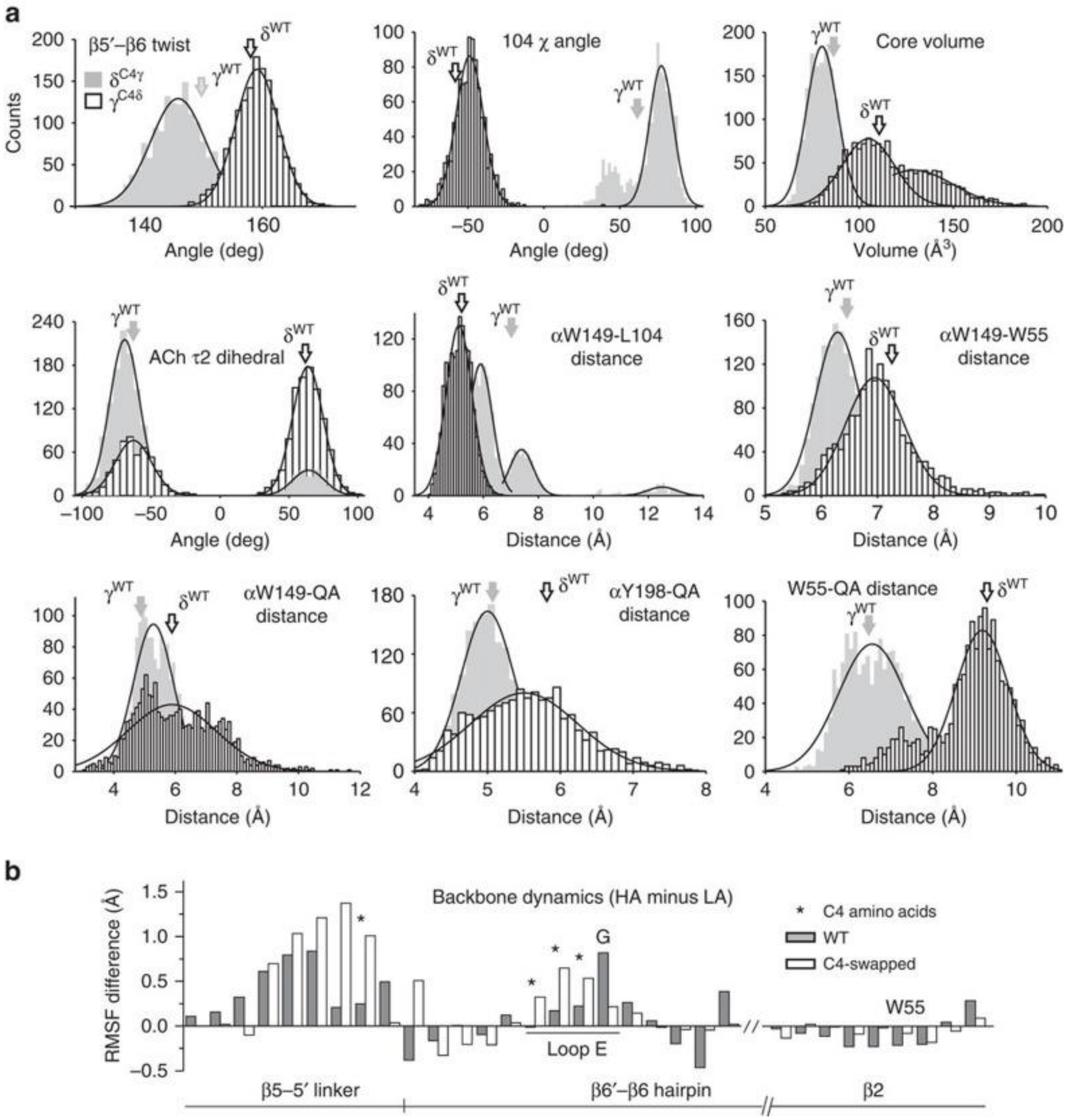

Figure 8.9: Quantitative analyses of MD results. a. Structural parameters estimated from trajectories. Histograms are from C4-swaps; arrows are mean values from WT trajectories. b. HA RMSF minus LA. WT, grey (αγ minus αδ) and C4-swap, white ($\alpha\delta^{C4\gamma}$ minus $\alpha\gamma^{C4\delta}$). The β5-β5’ linker and loop E are more flexible in HA structures, whereas the base of the hairpin and β2 near W55 are more flexible in LA structures (see Figure 8.10c).

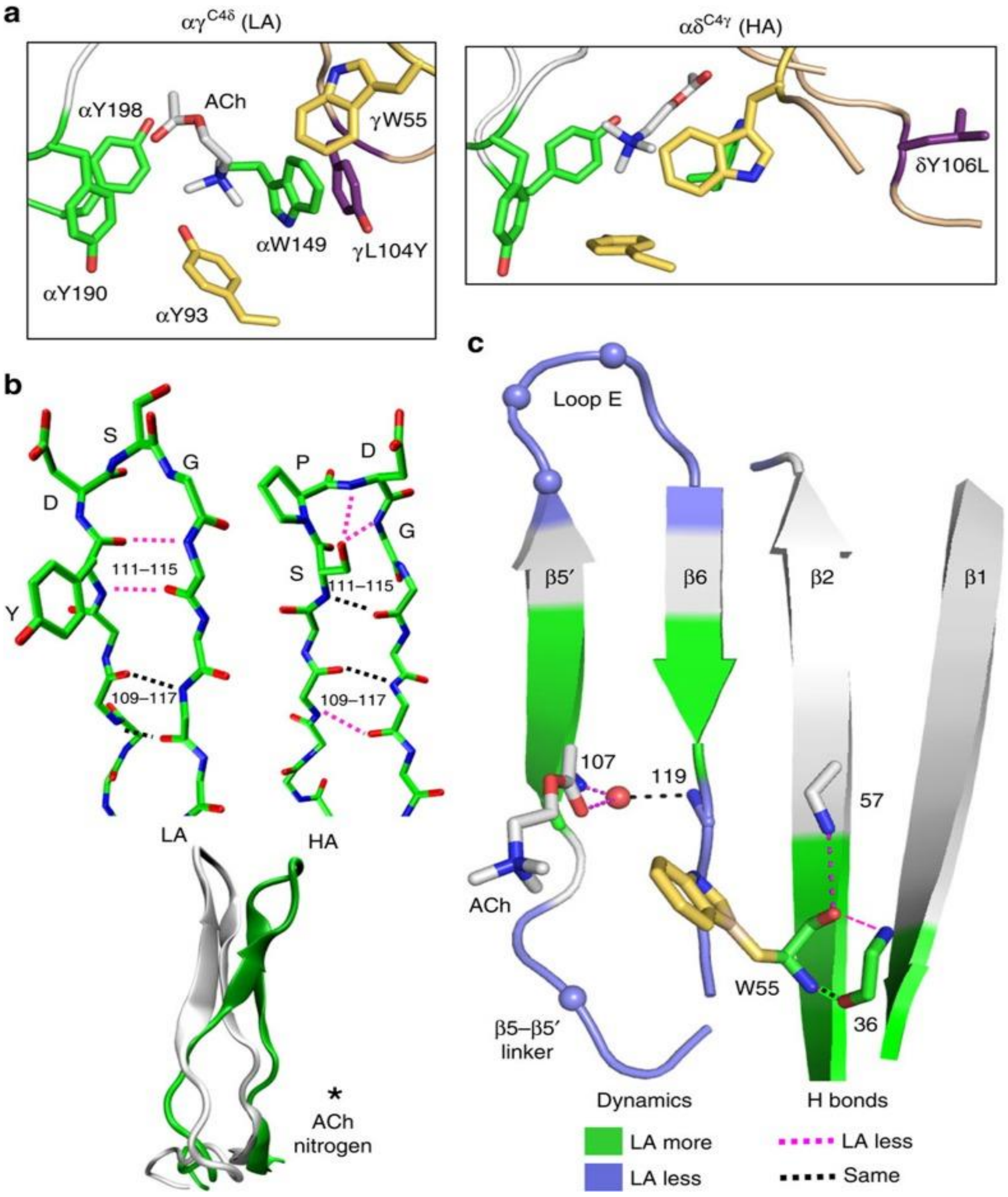

Figure 8.10: Structures suggest a mechanism for fetal vs. adult affinity. a. Representative snapshots of C4-swapped cores (LA, low affinity $\alpha\delta^{WT}/\alpha\gamma^{C4\delta}$ and HA, high affinity $\alpha\gamma^{WT}/\alpha\delta^{C4\gamma}$). Left, the LA core is spread, γW55 is far from ACh, C4 residue γL104Y (purple) is face-on to αW149 and ACh is bent. Right, the HA core is compact, δW57-αW149-αY93 are orthogonal, δY106L points away from the agonist and ACh is straight. b. H-bonds of the β5'-β6 hairpin. Top, dotted lines are H-bonds. Pink, bonds that correlate with affinity (are ~2x more prevalent in simulations of LA or HA sites); black, bonds that are equally-prevalent in LA and HA trajectories (Table 8.2). Loop E (bold side chain labels) is one residue shorter in LA structures. Bottom, in LA constructs the hairpin is straighter and less twisted. c. Relative dynamics of the β-sheet backbone. LA is associated with a smaller RMSF (light blue) in the β5' linker and loop E, and a greater RMSF (green) at the bottom half of the hairpin and regions surrounding W55. αC of the C4 amino acids, light blue spheres; structural water oxygen, red sphere; H-bonds, dashed lines; numbers are after γ-subunit. PDB accession number 3WIP; see Figure 8.9 and Table 8.2 for quantitative analyses.

Table 8.1. ***In vitro*** **affinities from electrophysiology experiments**

WT→C4	agonist	K_d (μM)		free energy (kcal·M^{-1})		% success
		WT	swapped	WT	swapped	
αδ→αγ	ACh	125	3.6	-5.3	-7.4	116
	TMA	810	45	-4.2	-5.9	88
αε→αγ	ACh	175	7.0	-5.1	-7.0	93
	TMA	1350	175	-3.9	-5.1	54
	Cho	10300	810	-2.7	-4.2	83
αγ→αδ	ACh*	6.0	75	-7.1	-5.6	83
	TMA	30	350	-6.2	-4.7	76
	CCh	3.0	45	-7.5	-5.9	64
αγ→αε	ACh	6.0	90	-7.1	-5.5	80
	TMA	30	250	-6.2	-4.9	56
	Cho	490	2650	-4.5	-3.5	56

Free energy (kcal·M^{-1})=+0.59lnK_d (in M). % success is with regard to energy and is equal to [(swapped-WT)/(WT^{target}-WT)]×100, where WT^{target} is the energy of the C4-intended site (for example, αγ-site energy in $\alpha\delta^{C4\gamma}$). *, estimated from the low P_O cluster population (see Figure 8.4b).

Table 8.2. H-bonds

Atoms (γ subunit)	$\alpha\delta^{WT}$(LA)	$\alpha\gamma^{WT}$(HA)
L109 (N) - Y117 (O)	0.5	1.0
L109 (O) - Y117 (N)	0.8	0.8
S111 (N) - C115 (O)	1.0	0.5
S111 (O) - C115 (N)	0.4	0.0
S111 (O) – G114 (N)	0.3	0.0
S111 (OG) - G114 (N)	-	0.9
S111 (OG) - D113 (N)	-	0.8
W55 (O) - E57 (N)	0.0	0.4
T36 (N) - W55 (O)	0.1	0.5
T36 (O) - W55 (N)	1.0	0.9
N107 (N) - O (water)	0.5	1.0
L119 (N) - O (water)	0.8	0.7
ACh (O) - O (water)	0.3	0.7

Fraction of trajectories in which each H-bond is present.

Chapter 9:

Role of M1 π-helix in ligand gated ion channel activation and desensitization*

* Parts of this chapter has been published in the article:

J Physiol. 2015 593: 2851-2866

The structural study from the paper along with some further analysis is discussed here.

ABSTRACT

Nicotinic acetylcholine receptors (AChRs) switch on/off to generate transient membrane currents (C↔O; ‘gating’) and enter/recover from long-lived, refractory states (O↔D; ‘desensitization’). The M1, transmembrane helix of the muscle endplate AChR is linked to a β-strand of the extracellular domain that extends to a neurotransmitter binding site. Electrophysiology experiments have shown that mutations of amino acids that are located at proline kink in M1, at both α (N217, V218 and P221) and non-α subunits, affect gating and desensitization. The M1 domain has a conserved proline that separates π- and α-helices. In related receptors, the kink is straighter and more stable in O vs. C structures (gating is ‘spring-loaded’). There is a discrete break in the character of the gating transition state between αN217 and αV218, indicating that the π-helix is a border between extracellular- and transmembrane-domain function. Structural analyses suggest that bending of the π-helix is correlated to motions of the M2 helix that can bring about gate opening and desensitization.

9.1 - Introduction

The muscle AChR has an equatorial gate in the transmembrane domain (TMD) that regulates ion conductance, and two sites in the extracellular domain (ECD) that can bind agonists to influence the gating equilibrium constant [60, 301-303]. Of the 4-helix bundle (M1-M4) of the TMD, M2 lines the pore and bends to open/close the gate [72]. M1 has a proline kink and a π-helix [74] that are conserved in all pentameric ligand-gated ion channels (pLGICs).

M1 is linked covalently to the β_{10} strand of the ECD that projects to an agonist site (Figure 9.1A). The kink is located just above the level of the TMD equator, close to a binding site for the anesthetic propofol in a prokaryotic pLGIC (Figure 9.1B) [86]. It has been proposed [304] and questioned [305] that the principal pathway for the channel-opening transition starts with movements of ligands at agonist sites that perturb the β_{10} backbone and a salt bridge at its base to control the M2 gate. The relative position of the peak free energy change experienced by a side chain within a reaction (for instance, C↔O or O↔D) is given by phi, the slope of a rate-equilibrium free energy relationship (REFER). In muscle AChRs residues in the αECD have a relatively early gating transition state (phi~0.8), most of those in the αTMD reach theirs approximately mid-reaction (phi~0.6) and those at the gate change energy (structure) near the end of the opening process (phi~0.3)[129] (Figure 9.1A). This pattern led to the proposal that the channel-opening transition occurs as a longitudinal conformational 'wave' [306], but some results suggest that this process starts at the ECD-TMD interface rather than at the agonist sites [307, 308].

As discussed earlier (page 33-34), at first approximation, AChRs have only two stable conformations, C (without agonists) and D. These have lifetimes of ~minutes, whereas all others have sub-ms lifetimes. Hence, the O state is a transient intermediate within C↔D that is, however, the source of the physiological response. It is known that in AChRs, desensitization proceeds mainly from O states [309, 310]. Hence, an agonist molecule can be thought of as a catalyst that reduces the activation energy of the C↔D transition state by increasing the stability of the O intermediate. Little is known about the structural changes that comprise AChR desensitization, but a structure of a possibly-desensitized GABA receptor suggests that in addition having conductance regulated by the equatorial gate, the pore can be occluded at its base by a constriction of the M2 helices [95].

Interesting observations regarding AChR gating function have been made previously regarding the M1 kink amino acids. The mutation αN217K causes a congenital myasthenic syndrome (CMS) [311]. Many side chains throughout the protein change energy between C and O. The largest range of energy change measured so far is for αV218, where an A-to-Y substitution (in both α subunits) increases the gating equilibrium constant more than a million-fold [129]. αP221 is conserved absolutely across the entire pentameric ligand-gated ion channel superfamily. Substitutions of natural side chains here that are expected to reduce kinking reduce or eliminate AChR currents, whereas ester backbone substitutions that allow kinking do not [312]. Single-channel electrophysiology done by our group to assess the effects of mutations at 3 kink positions (αN217, αV218 and αP221) with regard to gating and desensitization led to the findings [308]: (i) mutations of the kink residues (only in the α subunit) change the unliganded (allosteric) gating equilibrium constant substantially but have no detectable effect on either low- and high-affinity agonist binding; (ii) there is a sharp discontinuity in gating phi-values in the π-helix. The αN217-αV218 backbone bond is a border that divides ECD and TMD gating function; (iii) mutations of αP221 are with regard to gating but unusual because they increase desensitization, as does the anesthetic propofol.

π-helix is a relatively rare secondary structure. A 2010 study [313] of all the protein structures available in PDB database showed that it is present in ~15% of known protein chains. However, in 84% of the proteins where it is present, there is only a single π-helix per chain. A π-helix is characterized mainly by the presence of (n-n_{+5}) backbone hydrogen bonds instead of the typical (n-n_{+4}) bonding nature of α-helix [314], and occurs predominantly due to the insertion of a proline residue (where the backbone nitrogen cannot act as a H-donor) in an α-helix. Because π-helix formation by a proline insertion destabilizes a α-helix by 3-6 kcal.M^{-1} [315-317], its occurrence is thought to have an evolutionary rationale only in the case of a functional advantage [318]. These facts, along with the electrophysiology results suggest that the M1 π–helix is an important moving part in AChR gating and also related to receptor desensitization. Here we study the structural correlations between this π-helix and the gate lining M2 motions.

9.2 - Methods

π-helix identification: We used the following criteria for identifying a π-helix [313]. i) At least 2 (n-n_{+5}) backbone H-bonds (in AChR α subunits, between positions 214-219 and 215-220). ii) Dihedral angles: (ψ_n+ϕ_{n+1})~-125° in the π-helix region (~-105° in the α-helix region). This sum for the first residue of the π -helix is ~-95°. iii) 7 amino acids, with those in the αAChR π-helix (FIINVII) being characteristic [314]. We cross-checked our π helix identification using the pi-HUNT code [313].

M1 tilt angle: The π–α tilt angle was that between the central axes of the helices. The central axis was defined by the least squares linear regression fit of the coordinates of the backbone atoms. The regression fit was calculated by a Singular Value Decomposition technique. Residues 214-220 and 223-236 (AChR α subunit numbers) were used for the π and α axes.

Dihedral angles: The dihedral angles ϕ and ψ were obtained from the Ramachandran plot using VMD version V1.9 [224]. All M1 residues (including the proline) are in the trans-conformation in all pLGIC structures. Therefore, the rotation angle Ω per residue in the helix could be calculated by using:

$$3\cos\Omega = 1 - 4cos^2[(\phi + \psi)/2]$$

………………………. Eq. 10.1

Backbone bond energy: The conformational energy of the backbone of the M1 helix was calculated using CHARMM [319]. The bonded energy terms (the bond, angle, Urey-Bradley, dihedral and improper energy) were calculated using the CHARMM27 force field [146] with CMAP corrections.

Principal Component Analysis: To check if the M1 kink and the M2 positions are correlated, we performed principal component analysis on 28 different LGIC structures obtained from PDB, in various gating conformations. The PDB ids of the analyzed dataset is given in Table 9.1. These were selected based on the fact that all of these have a π-helix in M1, and do not have any mutations in the TMD region. PCA was done only on the M1 and M2 regions of the structures to prevent biasing of results by orientations of surrounding loops. The residue ranges by AChR-α numbering are 214-233 for M1 and 244-260 for M2. The method of PCA used is similar to that described in page 69.

Coarse-grained Elastic Network Modeling: Due to time and computational power constraints, the all-atom MD simulations that we can perform is limited to the order of nanosecond time-scale, while physiologically, the actual transition takes tens of microseconds. Therefore, as an initial test of our hypothesis that M1 kinking is correlated to M2 gating at the TMD, we employed the more time-efficient elastic network modeling method to elucidate allosterically coupled motions between M1 and M2. Various studies have established the usefulness of the Elastic Network Model (ENM) to extract functionally relevant structural dynamics in proteins [320, 321]. ENM is a coarse-grained modeling technique which represents the structure of a protein as a network of Cα atoms connected by springs [199], with a distance-dependent force constant. In this, the protein's minimal-energy equilibrium conformation is obtained from a model or a pdb structure. A harmonic potential is used to define the interaction between two Cα atoms that lie within a cutoff distance R_C (10Å as used in [200]). The potential energy function of ENM is [322]:

$$E_{ENM} = \frac{1}{2}\sum_{i=2}^{N}\sum_{j=1}^{i-1} C_{ij}\theta(R_c - d_{ij}^0)(d_{ij} - d_{ij}^0)^2$$

………………………. Eq. 10.2

where d_{ij} is the distance between the i-th and j-th C_α atoms, d^0_{ij} is the value of d_{ij} in the starting structure, N is the number of C_α atoms, and $\theta(x)$ is the Heaviside step function. C_{ij} is the force constant of the spring between atoms i and j, set to 10 for bonded atoms and 1 for non-bonded atoms [126]. A normal mode analysis is performed on this ball-spring system. The eigenvalue problem for this system of springs is solved for the Hessian matrix H. H is defined by the the second derivatives of ENM potential energy equation 10.2 [126]:

$$HW_m = \lambda_m W_m$$

……………………… Eq. 10.3

where λ_m and W_m are the eigenvalue and eigenvector corresponding to mode m. Despite the simplifications, the normal mode analysis of ENM often supplies a number of low-frequency modes that represent collective motions between structures, determined by the global conformations of the structures.

Top 20 non-zero modes of GluCl Closed structure (4TNV) were compared with the observed structural changes X_{obs} in the coordinates from GluCl Open structure (3RIF).

An overlap value I_m gives a measure of fractional contribution of mode *m* to X_{obs} [323].

$$I_m = \frac{|X^T_{obs}.W_m|}{|X_{obs}|.|W_m|}$$

……………………… Eq. 10.4

I_m can take values between 0 and 1, with higher value meaning greater similarity.

Since we are interested in the M1-M2 correlated motions instead of the entire global structural correlates (for example, between ECD and TMD; between subunits; etc), we performed the normal mode analysis only in the TMD of a single subunit – the M1-M2-M2-M4 system. This shorter sub-system will help in identifying and amplifying those modes which would otherwise have been low-amplitude modes in the ENM of the entire system. The normal mode analysis calculations were done using the AD-ENM program [324] (http://enm.lobos.nih.gov/).

9.3 - Results

M1 structures

The M1 kink proline (αP221 in AChRs) separates a π-helix (α214-α220) and a α-helix (α221-α233). π-helices are common secondary structures that are often located at active sites [313]. The M1 backbone of all the structures listed in Table 9.1, (GLIC [71], GluCl [74], ELIC [325], GlyR [326] and a $GABA_A$ receptor [95] fits the definition: 7 residues, 2 n+5 backbone H-bonds, (psi_n+phi_{n+1})~125°, characteristic side chains and a following proline [314]. We tested that the M1 π-helix is present in all pLGIC x-ray structures reported so far, with the possible exception of $5\text{-}HT_3$ [327]. Our search did not identify any other π-helices in GluCl, GLIC, ELIC or GABA structures, but one is present in the intracellular domain of the $5HT_3$ receptor, just before M4 (positions 321-329).

The proline causes M1 to kink at the π−α helix boundary (Figure 9.2A). In GluCl C→O [73, 74], the kink angle becomes shallower by ~7°. This kink is present in other pentameric LGIC structures too, some of which are shown in Figure 9.2C. The general trend is C structures are more bent than O, with the D-state GABA structure having the least bending. Figure 9.2B shows that the conformational energy of the backbone is lower (more stable) in O, in particular at the π−α boundary (α220- α221; AChR α subunit numbers). The π−α boundary is more strained in Closed. The AChR channel-opening conformational change appears to be 'spring-loaded' in so far as the M1 kink relaxes, C→O.

Mutations of M1 α helix residues αV218, αC222, αF225, αS226 and αL228 have large effects on the diliganded gating equilibrium constant [129]. This indicates that the gating rearrangement of the αTMD helix bundle alters the local environments of these M1 side chains, with significant energy consequences. Figure 9.2A shows the position of the M1 α helix relative to M2 in GluCl. We speculate that the ~2 Å upward relative displacement of M2, O vs. C, is the basis for the large gating energy changes in the αM1 side chains.

The helical nature of secondary structure is fundamentally determined by the dihedral angles of the backbone atoms. Comparing the phi-psi angles between the O and C structures in both GluCl and GLIC (Figure 9.3), it is observed that the phi angles are very similar between O and C. However, interestingly, the psi angles which are similar in the two different O structures (for both receptors) deviates considerably in the C structures compared to O, especially around the π-helix forming proline residue. This supports our hypothesis that M1 structural changes are correlated with channel opening by the M2 helix.

Principal Component Analysis: The principal components of the structural variations within our selected ensemble of PDB conformations (Table 9.1) were obtained to see if there are any structural correlations between various different crystal structures of PLGICs. 28 different PLGIC structures were chosen as our dataset, in various different gate conformations. PC modes 1 and 2 done on M1-M2 domain showed that two of these structures (Torpedo AChR 2BG9 and GlyR α1 TM monomer) are vastly different in conformation than the rest of the dataset (Figure 9.4A). Therefore, the PCA was repeated after removing these two structures from the set (Figure 9.4B). Now, with a set of 26, the open structures formed a clear cluster with the top two modes. The closed structures were more scattered, with the locally closed conformations forming a separate cluster of their own. The two putative desensitized structures were more similar to the open than closed. The PC analysis was repeated with just the M1 domain to make sure the clustering discussed above were not solely due to the M2 variations.

PC mode 1 did not seem to form any particular clusters between O or C structures (Figure 9.4C). However, modes 2 and 3 seemed to cluster M1 of the O structures to a reasonable extent (Figures 9.4C and 9.4D). The desensitized state M1 however, did not seem to cluster well. The PCA results corroborate our hypothesis that M1 conformations are linked to M2 motions, leading to the gating action of the channel.

Normal Mode Analysis: The TMD of GluCl Closed (4TNV) and Open (3RIF) have an RMSD of 1.6 Å between them. A coarse grained elastic network model as described by equations 10.2 and 10.3 was used to perform normal mode analysis on the TMD helices of the Closed GluCl (4TNV) structure. After eliminating the 6 zero eigenvalue modes that describe the global translational and rotational motions, we kept the lowest 20 modes. The eigenvalues of these modes are shown in Figure 9.5A). These 20 modes from C state were projected on the O state (3RIF) of the TMD and the overlap calculated using equation 10.4. It was found that these 20 modes could cumulatively capture ~83% (0.83) of the observed conformational change from C to O structure (Figure 9.5B).

Modes 2 and 6 from C-state have the highest overlap (Figure 9.5) with the O-state. Mode 2 involves a hinge-like motion at M1 π-helix, coupled with M2 retracting from the pore (Figure 9.6A). Mode 6 also has a hinge-like motion of the π-helix, but orthogonal to mode 2 (Figure 9.6B). Here too, the M2 helix seems to move away from the pore. The 9' residue Leu 254 (Leu 251 in αAChR) is known to form the most constricted region of the pore. The radius of the pore increases from 1.4 Å to 2.4 Å between C and O GluCl crystal structures. Both modes 2 and 6 which involve bending of M1, cause the 9' region to move away from the pore (Figure 9.6).

9.4 - Discussion

Without agonists the highest phi-values (earliest transition states) are in the αM2-3 linkers (~0.95), followed by residues at the agonist sites [104] and the rest of the αECD (~0.8), most of the αTMD (~0.6) and the M2 equator (~0.3). This map suggests that AChR opening starts with a spontaneous fluctuation in the αM2-3 backbone [126, 307], followed by a tilt/twist of the αECD and the π helix, a bend in M2 and then expansion of the gate. The high phi value for αN217 suggests that the decrease in the π−α tilt angle precedes M2 bending and, hence, that it is a cause rather than a consequence. Our ENM model suggests that the M1 kinking action is correlated to the channel opening by M2 and the PCA of existing PDB structures corroborates this finding. Though the GlyR Open structure seems to be an outlier in the PCA results (Figure 9.4), there has been some contention with this recently obtained O-structure. The M23 linker, the inter-subunit distance at the binding site and the M1 kink all seem to be different from other established Open structures in PDB.

αP221 mutations alter the desensitization process. With αP221A and βP232A, the rate constant for entry into a desensitized state is >10 times faster than without the mutation [308]. This translates to a desensitization phi-value ~1, which implies that these positions reach their transition state near the onset of this reaction.

The mutation of the M1 proline is expected to modify both the π−α angle and the α helix twist. Because the O conformation is a necessary intermediate for desensitization, we hypothesize that the straightening of M1 in C→O apparent in GluCl continues in O→D (and, perhaps, propofol-inhibition). The high desensitization phi-value for some αP221 mutants suggests that changes in energy (structure) occur at the M1 $\pi-\alpha$ border early in the desensitization process, and, hence, may be a trigger. The PC analysis did not resolve the putative D-state structures into a cluster. Even visual checking of the structures show that both M1 and M2 are very different between the two structures. But both the structures have the lowest pore radius at the bottom of M1. It is possible that D-state can be reached in a number of different paths from the O-state. One of them seem to be by further straightening of M1 that allows M2 to bend and occlude the bottom of the pore. This study lays the groundwork for further future research to test the M1M2 gating correlations by performing all-atom MD simulations of the entire AChR structure and to study the transition state by applying steered and targeted MD.

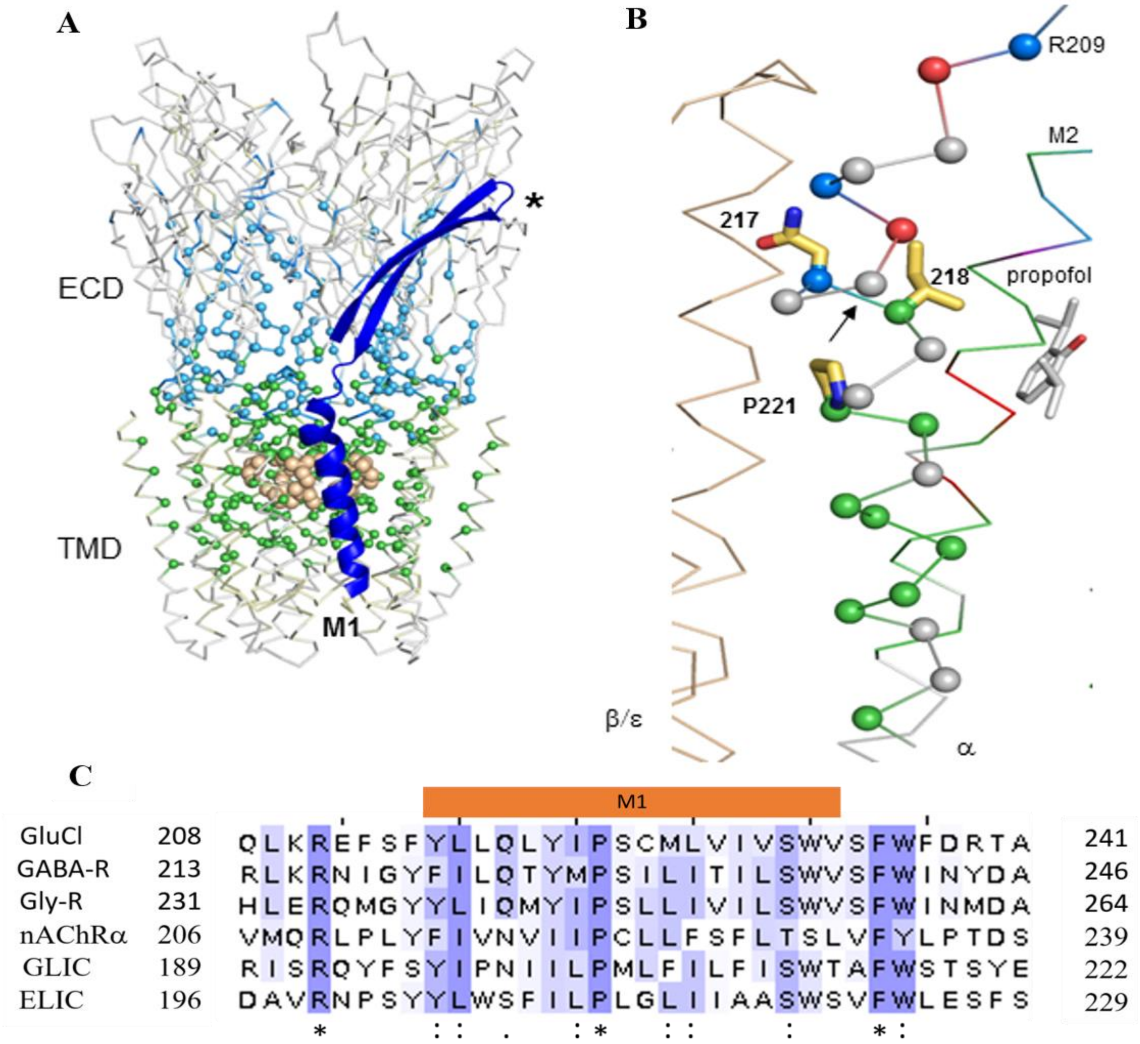

GluCl	208	QLKREFSFYLLQLYIPSCMLVIVSWVSFWFDRTA	241
GABA-R	213	RLKRNIGYFILQTYMPSILITILSWVSFWINYDA	246
Gly-R	231	HLERQMGYYLIQMYIPSLLIVILSWVSFWINMDA	264
nAChRα	206	VMQRLPLYFIVNVIIPCLLFSFLTSLVFYLPTDS	239
GLIC	189	RISRQYFSYIPNIILPMLFILFISWTAFWSTSYE	222
ELIC	196	DAVRNPSYYLWSFILPLGLIIAASWSVFWLESFS	229
		* : : . : * : : : * :	

Figure 9.1: M1 structure and sequence. A. Side view of the AChR homolog GLIC (pdb accession number 3P50; [86]. ECD, extracellular domain; TMD, transmembrane domain; blue, $\beta_{9\text{-}10}$-M1; tan spheres, equatorial M2 gate; *, neurotransmitter binding site (AChR α subunit). The αC atoms are colored by gating phi value (AChR α subunit). The ECD is mostly ~0.8 (cyan) and the TMD is mostly ~0.6 (green). B. Close-up of M1 (αAChR numbering). αN217-αV218 is a gating phi-value border (arrow). The N-terminal residue of the π helix, αF214, has a phi ~0.3 (red). C. Sequence alignment of M1 region (marked by orange bar). The M1 proline is conserved throughout the family. Color scheme: BLOSUM62 identity score.

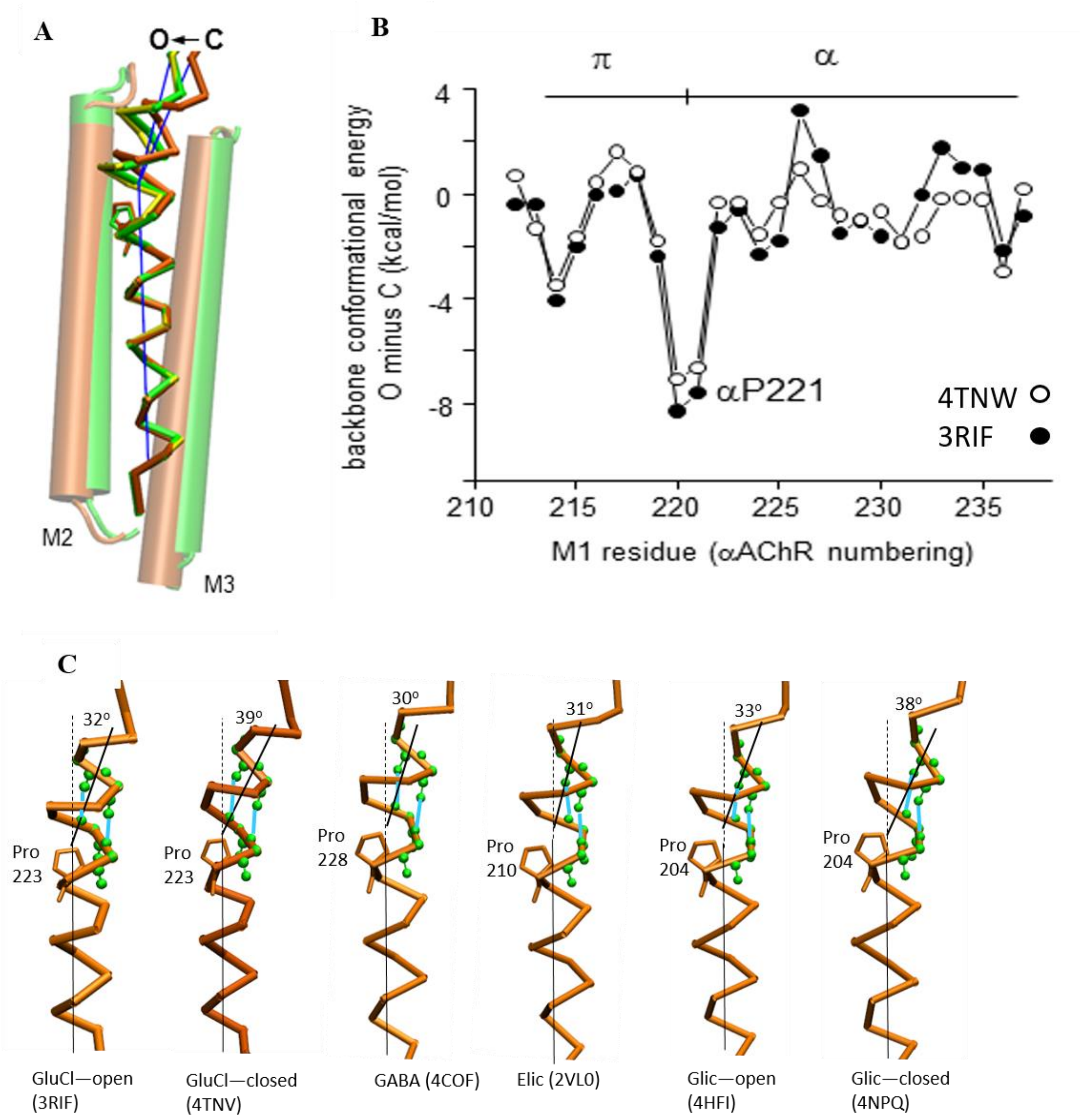

Figure 9.2: π-helix bend and energy: A. M1, O vs. C (GluCl) [73, 74]. The π–α tilt angle is ~7° shallower in O (green; 3RIF) vs. C (orange; 4TNV) and even shallower in a possibly-desensitized GABAR structure (yellow; 4COF [95]). B. The difference in M1 backbone conformational energy, O minus C (GluCl). The π–α boundary is more strained in Closed. C. π–α tilt angle in different pentameric ligand gated ion channels. The pi-helix forming Proline residue is shown by orange sticks. The n—n+5 backbone hydrogen bonds shown by cyan lines. The closed structures have greater angle of kink than the open structures. The GABA structure, which is in a possibly desensitized state, has the smallest angle of kink.

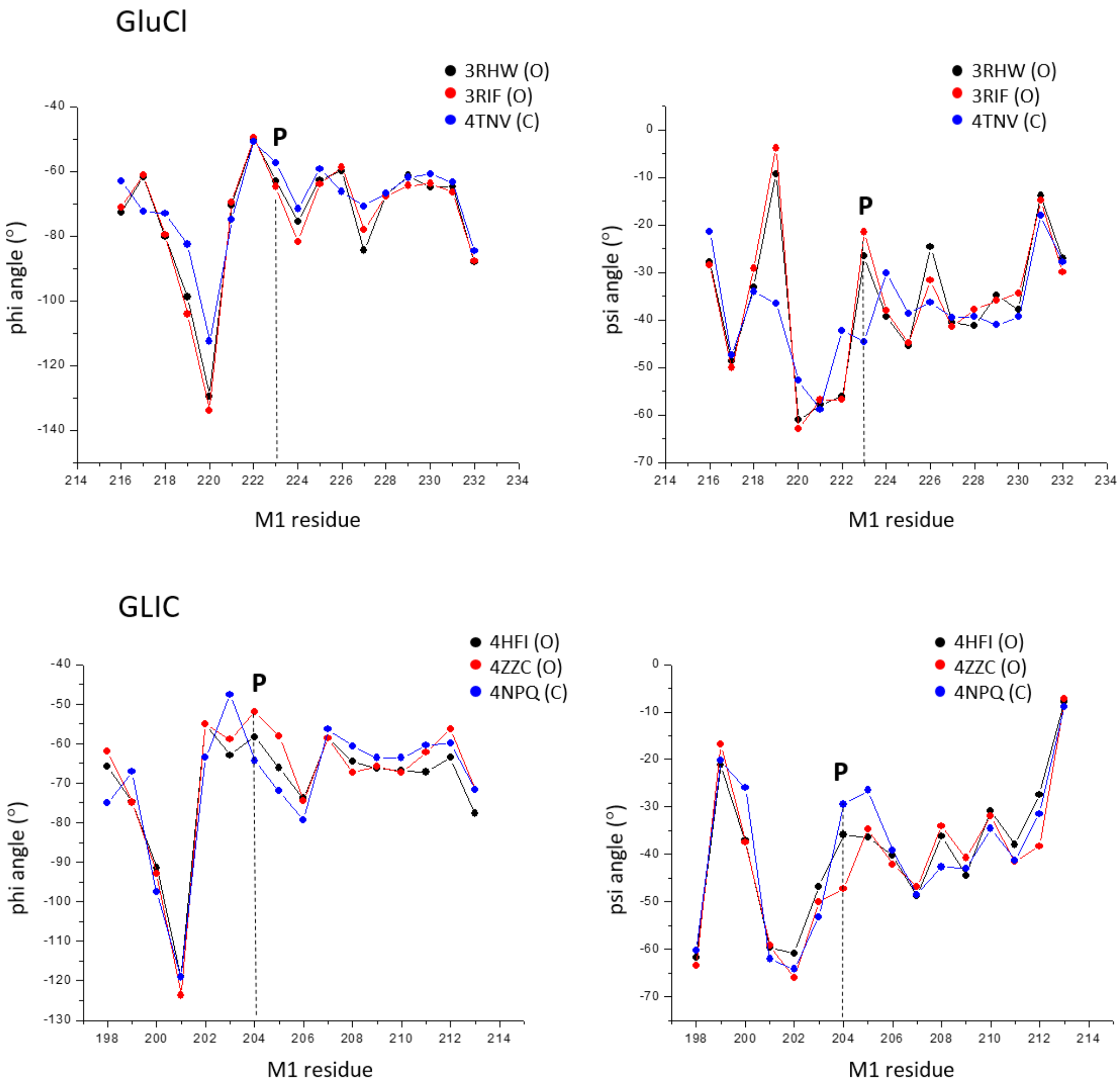

Figure 9.3: Dihedral angles of M1 helix. Backbone dihedral angles of GluCl (top) and GLIC (bottom) structures. Black and red are the Open conformations and blue are the Close conformations. The phi angles (left) seem to be similar in general between the O and C structures. But the psi angles (right) are different between O and C.

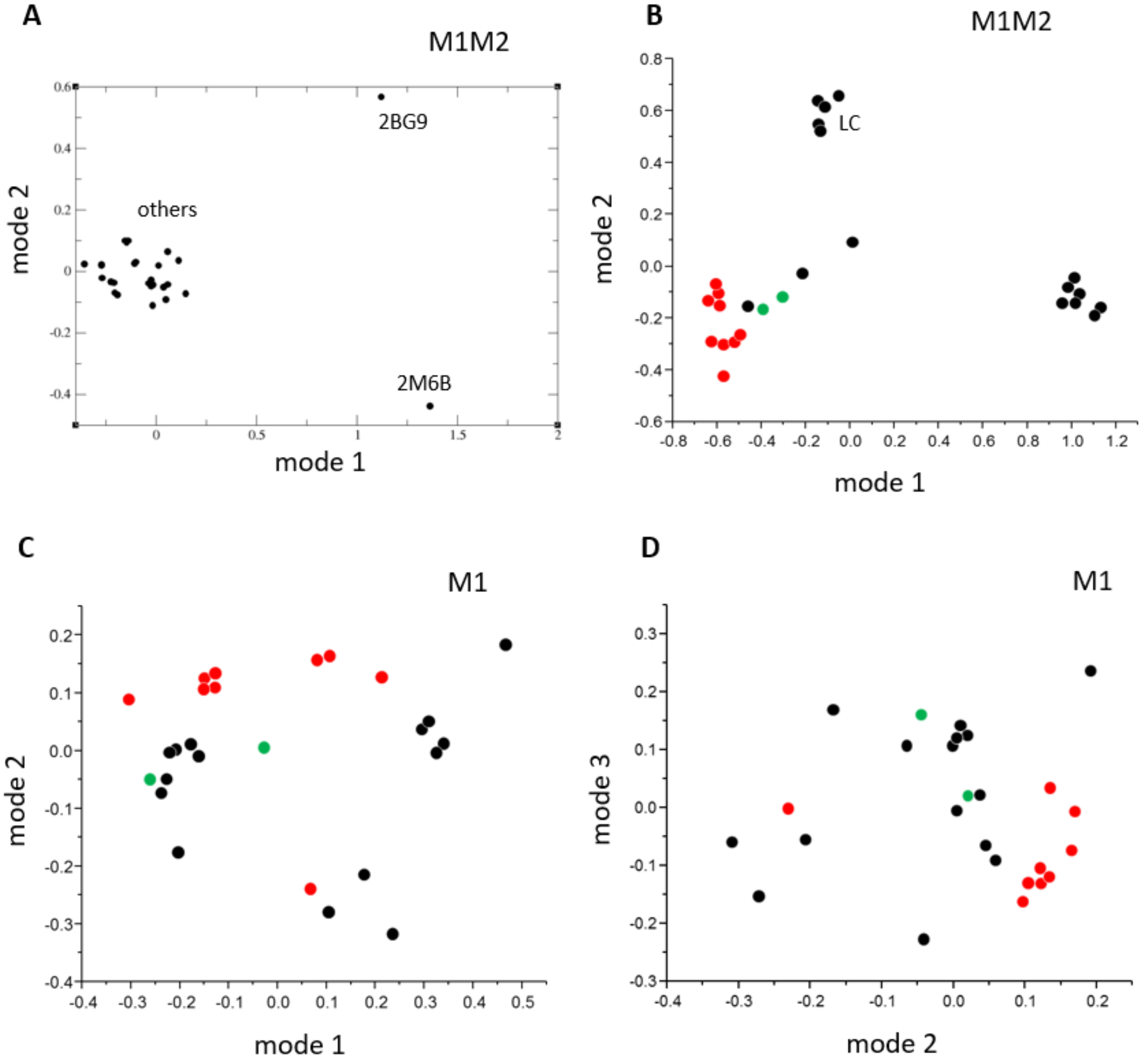

Figure 9.4: Principal Component Analysis of different PDB structures. Red, Open; black, Closed; Green, putative Desensitized. A. PCA of M1M2 domain on all 28 structures of Table 9.1. 2BG9 and 2M6B are clear outliers, and hence not used for the rest of the analysis. B. PCA of M1M2 domain on 26 structures. All the Open structures form a cluster by both the top two modes. C. PCA of M1 on 26 structures, mode 2 vs. mode 1. D. PCA of M1 on 26 structures, mode 3 vs. mode 2.

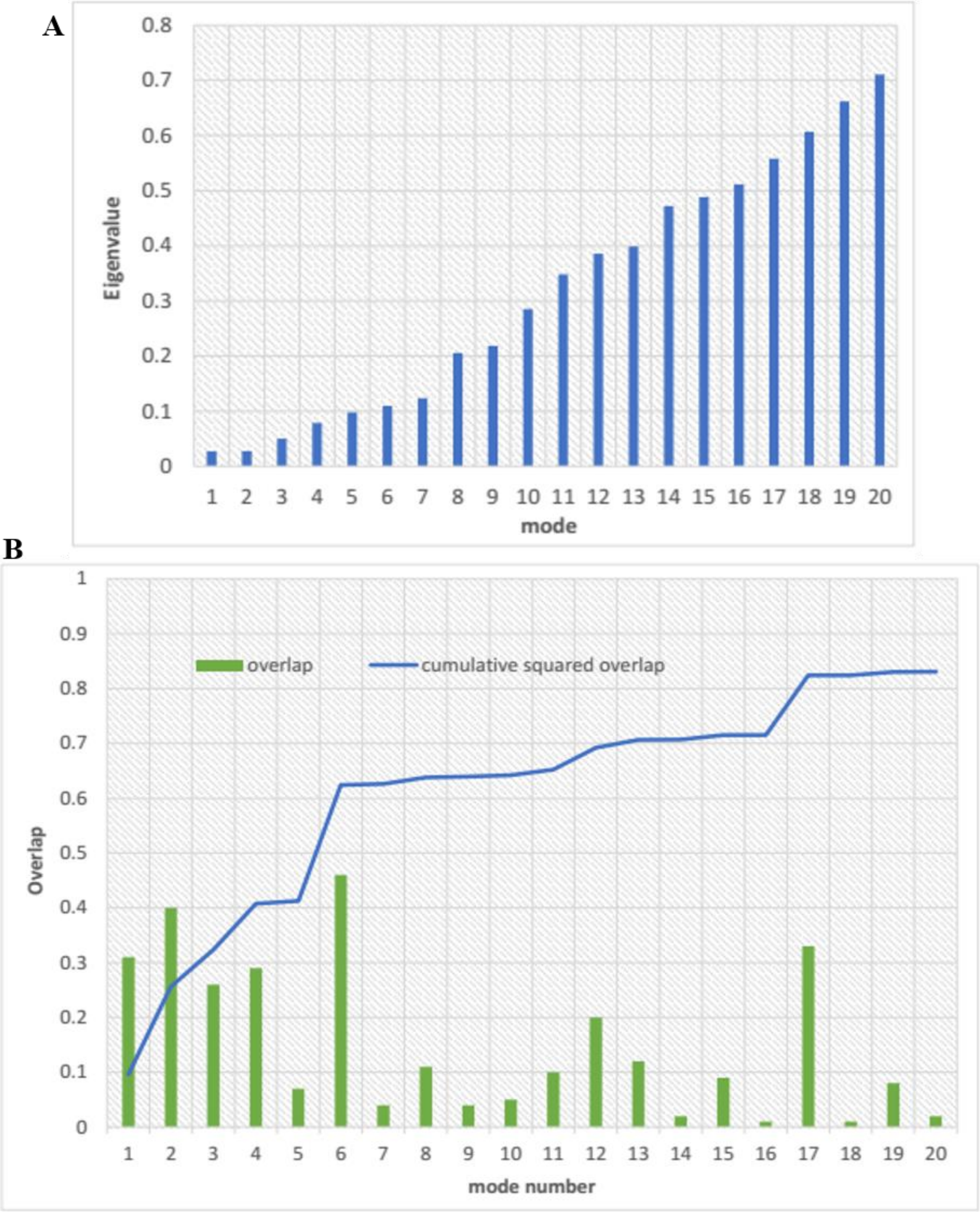

Figure 9.5: Normal Mode Analysis of TMD helices. A. The lowest 20 non-zero eigenvalues of NMA analysis on GluCl Closed structure (4TNV). B. The overlap of each mode on GluCl Open structure (3RIF). The cumulative squared overlap for the 20 modes (blue line) is a significantly high ~83%. Modes 2 and 6 have the highest overlap at ~ 40% and ~45% respectively.

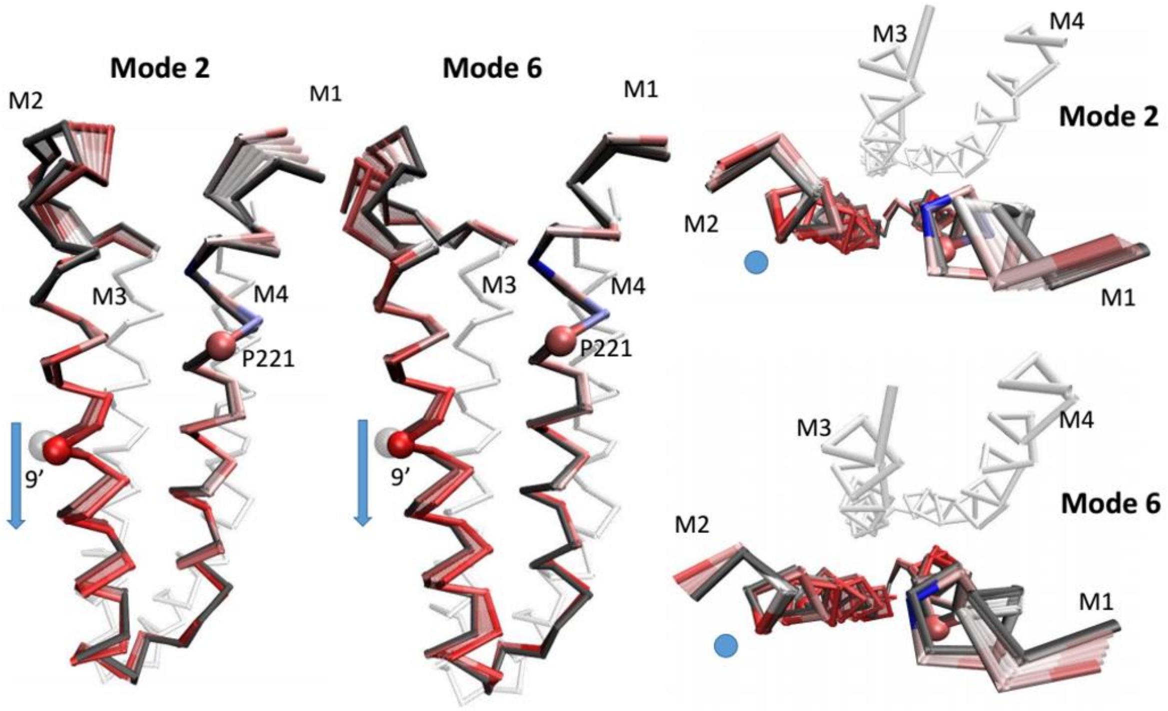

Figure 9.6: Structural details of top-overlap modes. Side view (left) and top view (right) of modes 2 and 6. Both the modes involve a bending motion of the p-helix, with a simultaneous withdrawal of M2 from the channel pore. Pore location indication by light blue light (left) and circle (right). M1 proline and gate 9’ residue shown by spheres. A corresponding M23 linker motion was also observed, which will be a part of a future study.

Ref. No.	PDB id	Receptor type	State
1	3RHW	GluCl + ivermectin	O
2	3RIF	GluCl + ivermectin + glutamate	O
3	3RI5	GluCl + ivermectin + picrotoxin	O
4	3RIA	GluCl + ivermectin + iodide	O
5	4TNW	GluCl+POPC, lipid modulated	O
6	4TNV	GluCl, apo	C
7	5HCJ	GLIC	LC
8	4ZZB	GLIC + Xenon ion	LC
9	4ZZC	GLIC + Xenon ion	O
10	4NPQ	GLIC	C
11	4NPP	GLIC	O/LC
12	4HFI	GLIC	O
13	4YEU	ELIC-GLIC chimera	C
14	4Z90	ELIC + isoflurane	C
15	4Z91	ELIC	C (2nd)
16	4TWD	ELIC + memantine	C (PB)
17	4TWF	ELIC + bromomemantine	C (PB)
18	3RQU	ELIC	C
19	3RQW	ELIC + acetylcholine	C
20	2VL0	ELIC	C
21	2BG9	Torpedo nAChR	C
22	4COF	GABA$_A$-R β3	D
23	3JAD	GlyR α1 + strychnine	C
24	3JAE	GlyR α1 + glycine	O
25	3JAF	GlyR α1 + glycine + ivermectin	D
26	2M6B	GlyR α1 TM monomer	O
27	5CFB	GlyR α3 + strychnine	C
28	4X5T	GLIC- GlyR(α1) chimera	C

Table 9.1: Dataset from PDB used for PCA analysis. States: O – open; C – closed; C (2nd) – a second closed conformation; PB – pore blocked; D – desensitized.

Appendix 1

Hydrogen bond analysis in primary biochemical states of kinesin-microtubule system

METHOD:

Hydrogen bonds (HB) between two polar atoms (i.e., as acceptor and donor) were identified by the VMD program [224] using the geometric criteria: a donor–acceptor distance of <3.5 Å and a donor–hydrogen–acceptor angle of <60° [328]. The HBs were identified in all the 2500 snapshots of the last 50ns ensemble for each state, and their fractional occupancies calculated (fraction of total snapshots where a given HB is present). The mean occupancies of each HB over 4 trajectories is given in Table A1. Only those residue pairs with average HB occupancy > 0.3 were considered. Since multiple HBs may form between two residues through different H-atoms and donor-acceptor pairs, the average HB occupancy may be greater than 1. We focused on those HBs involving the kinesin-tubulin interface and the nucleotide-binding pocket.

RESULT:

HBs involving nucleotide-binding motifs (see Table A1 and Figure 6.10)

a. HBs between kinesin and nucleotide: In ADP and ATP state, ADP forms HBs mainly with residues 88-93 of P-loop. In ADP state, no HB forms between ADP and switch I or II due to an open nucleotide-binding pocket (see Figure 6.4(d) and Table 6.5). In ATP state, in addition to an

HB between ADP and N198 of switch I as found previously [217], more HBs form between AlF_4 and residues S201, S202, R203 of switch I and G234 of switch II. Among them, two HBs involving S202 [180, 329] and G234 [180] are known to be important for ATP hydrolysis, which were not observed with high occupancy in our previous study [217].

b. HBs between nucleotide-binding motifs: Between P-loop and switch II, 2 HBs form in each state. For example, an HB between T87 and E236, together with another HB between T92 and D231, was observed in ADP and ATP state but not in APO state, which is consistent with the finding of open switch II in APO state (see Figure 6.4(d) and Table 6.5). The importance of this HB to the closure of nucleotide-binding pocket was supported by the finding that a mutation of T436 in NCD (corresponding to T87 of kinesin-1) caused faster ADP release and uncoupling of ATPase from force generation [330]. Two HBs between K91 and D231/L232 only form in APO state after the release of K91 from ADP coordination. Between switch I and II, 3, 2, and 2 HBs form in APO, ADP, and ATP state, respectively. An HB (also a salt bridge) forms between R203 and E236 in all three states with different occupancy. This salt bridge was thought to be essential to ATP hydrolysis by closing the backdoor of nucleotide-binding pocket [240], and its disruption leads to Pi release [180] as supported by mutational studies [331, 332]. S202 forms an HB with D231 in APO state and with G234 in ADP state. An HB forms between R190 and D231 in APO and ATP state, which may be involved in stabilizing a more ordered switch II in these states than ADP state. An alternative role of R190-D231 HB in Mg dissociation was also proposed [239]. Between switch I and P-loop, only one HB forms in ATP and APO state but not in ADP state, which is consistent with a more open and less extended switch-I conformation in ADP state (see Figure 6.4(d)).

c. HBs between nucleotide-binding motifs and tubulin-binding motifs (including loop L7, loop L11, α4 helix, and α6 helix): In ADP state, switch I forms 2 HBs with loop L11 and 3 HBs with loop L7. One HB between R203 of switch I and E250 of L11 also forms in APO and ATP state. Consistent with the functional importance of this HB, a E250A mutation resulted in defective MT-activated ATPase [333]. However, our finding of this HB in all three states does not support the proposal that it stabilizes a raised conformation of L11 that contributes to weak MT binding [180] and stabilization of Mg binding in ADP state [181]. Two HBs between switch I (involving R190 and S200) and L7 (involving E136) are unique to ADP state, which are likely to stabilize the weak MT-binding conformation of L7. In a structural study of KIF1A, a tri-residue Mg stabilizer (involving E148, R203, and D248 of KIF1A, corresponding to E136, R190, and D248 of kinesin-1) was proposed to stabilize Mg binding in ADP state [181] . In ATP state, switch I forms 1 HB with loop L11 and 2 HBs with loop L7, switch II forms 2 HBs with L11/α4, and P-loop forms 2 HBs with α6 helix. An HB between E236 of switch II and N255 of α4 helix is also present in APO state but not in ADP state. In support of a role of this HB in coupling MT binding with ADP release, two decoupling mutations N650K and E631A were found in KAR3 (corresponding to N255 and E236 of human kinesin-1) [251], and an N256K mutation of rat kinesin-1 (corresponding to N255 of human kinesin-1) was found to block MT stimulation of ADP release and ATP hydrolysis [331]. An HB between H191 of switch I and E136 of L7 only forms in ATP and APO state, which is likely involved in stabilizing the strong MT-binding conformation of L7. In APO state, switch I forms 1 HB with loop L11 and 3 HBs with loop L7, switch II forms 1 HB with α4 helix, and P-loop forms 2 HBs with α6 helix. Some of them are unique to APO state (such as an HB between T87 of P-loop and E311 of α6 helix). In sum, we have found the above HBs potentially mediating communication between the nucleotide-binding pocket and the MT-binding site following three possible paths: 1. via switch I→loop L7 (see ref [235] and ref [214]); 2. via switch I and II→loop L11 and α4 helix (see ref [235]); 3. via P-loop→α6 helix (see ref [334]).

HBs involved in kinesin-tubulin binding (see Table A1 and Figure 6.10)

We found that 16, 26, and 26 HBs form between kinesin and αβ-tubulin in ADP, APO, and ATP state, respectively. The finding of fewer HBs in ADP state than ATP or APO state is consistent with weak MT binding in ADP state and strong MT binding in ATP and APO state. Next, we focused on HBs involving the following tubulin-binding motifs:

- 1 HB forms between K141 of loop L7 and E159 of β-tubulin in APO state, and in ATP state with lower occupancy, supporting its role in strong MT binding which triggers Mg-ADP release [181]. The importance of this HB to MT-activated Mg-ADP release was supported by the finding that an R153A mutant of KIF1A (corresponding to K141 of kinesin-1) exhibited impaired MT-activated ATPase [181].
- 2, 7, and 5 HBs form between loop L8 (residues H156, E157, D158, K159, and R161) and β-tubulin in ADP, APO, and ATP state, respectively. Unlike ref [217], we found L8 to be more involved in kinesin-tubulin binding (with more HBs) in ATP and APO state than ADP state. We note the above differences in L8-tubulin HBs cannot be detected by inspecting static structures of the three states which showed little change of L8 conformation (see Figure 6.4c and ref [179]).
- 3, 4, and 5 HBs form between loop L11 (residues K237, K240, and E244) and α-tubulin in ADP, APO, and ATP state, respectively. Two HBs between K240 and E244 of L11 and α-tubulin only form in APO and ATP state, and K237 forms HBs with α-tubulin with higher

occupancy in APO and ATP state than ADP state. These interactions may contribute to strong MT binding.

- 2, 3, and 6 HBs form between α4 helix (residues K252, N255, S259, N263, and E270) and αβ-tubulin in ADP, APO, and ATP state, respectively. Of particular interest are two HBs between E270 & N255 and α-tubulin which form in APO and ATP state but not in ADP state, hinting for their role in facilitating strong MT binding.
- 6, 3, and 5 HBs form between loop L12 (residues T273, Y274, R278, and D279) and β-tubulin in ADP, APO, and ATP state, respectively. The finding of more HBs in ADP state than APO and ATP state is consistent with the proposal that L12 is involved in weak MT binding in ADP state [180]. Y274 and R278 are involved in multiple HBs in all three states. The importance of R278 to kinesin-tubulin interaction was supported by an alanine-scanning mutagenesis study [333].
- 3, 5, and 3 HBs form between α6 helix (residues S310, K313, S314, and R321) and α-tubulin in ADP, APO, and ATP state, respectively. An HB forms between R321 and E415 of α-tubulin in all three states. The higher occupancy of this HB in APO and ADP state is consistent with a mutational study that found E415 of α-tubulin as important for coupling MT binding and ADP release [335]. Another mutational study [29] supported the importance of R321 to kinesin's ATPase activities.

Summarizing, we found a network of HBs spanning the kinesin-tubulin interface, which differ significantly between ADP, APO, and ATP state in a way that is consistent with their different MT-binding affinity. The HBs present in APO and ATP state (but not in ADP state) are predicted to be important for enabling high MT-binding affinity.

Table A1. Results of hydrogen bond analysis based on MD simulation in APO, ATP and ADP state.

kinesin-tubulin residue pair		HB occupancy		
		APO state	ATP state	ADP state
K44	E423_α	0.33		
D235	E414_α	0.58		
K237	E414_α	0.90	0.96	0.58
K237	E417_α	0.93	0.74	0.58
K237	E420_α			0.35
K240	E417_α	0.54	0.43	
K240	E420_α		0.53	
E244	K112_α	0.35	0.52	
N255	M413_α	0.80	0.84	
S259	E415_α	1.16	0.77	0.68
N263	R402_α		0.39	
N263	E415_α			0.41
E270	K401_α	0.75	0.49	
E270	R402_α		0.63	
S310	E420_α	0.39	0.88	
K313	E420_α	0.56		0.33
K313	E423_α	0.97	1.31	0.99
S314	E414_α	0.60		
R321	E415_α	0.99	0.49	2.19
K141	E159_β	0.88	0.45	
H156	E420_β	0.82	0.76	
E157	E420_β	0.45	0.49	
E157	S423_β	1.40	1.17	
D158	T419_β	0.44		
K159	E415_β	0.34		
R161	E420_β			1.65
R161	E422_β	1.87	1.26	
R161	D427_β	0.62	1.24	0.34
K252	D163_β		0.34	
T273	Q434_β		0.58	
Y274	R264_β			0.39
Y274	D427_β			0.60
Y274	E431_β	0.83	0.74	
Y274	Q434_β	0.67	0.93	0.38
R278	E196_β			1.28

kinesin residue pair		HB occupancy		
		APO state	ATP state	ADP state
T87	E236		0.34	0.55
S88	N198		0.60	
K91	D231	1.32		
K91	L232	0.67		
T92	H200	0.53		
T92	D231		1.20	0.94
R190	D231	0.62	1.51	
S202	D231	0.73		
S202	G234			0.67
R203	E236	1.16	0.96	0.60
Q86	T312	0.77	0.31	
Q86	T315		0.48	
T87	E311	1.46		
R190	E136			1.55
H191	E136	1.79	2.35	
S200	E136			1.41
R203	E136	0.31		
R203	E244			1.14
R203	E250	1.12	0.68	0.87
S204	E136	1.02	1.00	0.87
E236	T241		0.36	
E236	N255	1.71	1.54	

kinesin-ligand pair		HB occupancy		
		APO state	ALF state	ADP state
S88	ADP	-	0.95	1.02
S89	ADP	-	3.08	1.69
G90	ADP	-	1.85	1.41
K91	ADP	-	2.12	1.84
T92	ADP	-	1.31	1.26
H93	ADP	-	1.14	1.22
N198	ADP	-	0.72	
T87	AlF_4	-	0.82	-
K91	AlF_4	-	1.00	-
S201	AlF_4	-	0.31	-

R278	D427_β	1.94	1.84	0.36		S202	AlF_4	-	0.56	-
D279	R264_β		0.63	0.68		R203	AlF_4	-	0.69	-
R284	E196_β	0.77	1.46			G234	AlF_4	-	0.81	-

For clarity, residues of P-loop, switch I and II are shown in blue, red and green font, respectively, and residues of MT-binding motifs are highlighted by different colors (L7: purple, L8: tan, L11: yellow, L12: pink, α4: dark yellow, α5: cyan, α6: orange). Only HBs with average occupancy >0.3 are shown. Underlined HBs are also shown in Figure 6.10.

Appendix 2

Electrophysiology experimental results for AChR-agonist affinity differences between fetal and adult-type receptors [279].

Electrophysiology Methods

AChRs were expressed in HEK cells by transient transfection of mouse endplate AChR subunits. Mutations were incorporated into AChR subunits using the *QuickChange* site-directed mutagenesis kit (Agilent Technologies, CA) and were verified by nucleotide sequencing. Single-channel currents were recorded in the cell-attached patch configuration (23 ^{o}C). The bath solution was (mM): 142 KCl, 5.4 NaCl, 1.8 $CaCl_2$, 1.7 $MgCl_2$, 10 HEPES/KOH, pH 7.4 and the pipette solution was: 137 NaCl, 0.9 $CaCl_2$, 2.7 KCl, 1.5 KH_2PO_4, 0.5 $MgCl_2$, and 8.1 Na_2HPO_4, pH 7.3. To estimate the fully-liganded gating equilibrium constant, a saturating concentration of agonist (100 mM; >100×K_d) was added to the pipette. The agonists were acetylcholine (ACh), tetrametylammonium (TMA), carbamylcholine (CCh) and choline. Experimental estimates of affinities (K_d) and gating equilibrium constants, E_0 and E_1, were measured using the techniques explained in page 41-42. Electrophysiology analysis was done from single-channel current interval durations by using QUB software [336]. E_1 was estimated as the gating equilibrium constant for a single site at high [agonist] (full-saturation, >5×K_d). E_0 was estimated from the gating equilibrium constant in the absence of any agonists using a constitutively active background [103, 337]. In the cross-concentration approach the membrane was held at -100 mV, and in experiments at high [agonist] the membrane was depolarized to +70 mV in order to reduce channel-block by the agonist. Membrane potential has no effect on K_d [338]. In order to study AChRs having just one functional binding site we added mutations to the ε, γ, δ subunits that eliminate binding at the mutated site [293] (also explained in page 38). To make αγ- or αε-only AChRs, δP123R mutations were applied, and to make αδ-only AChRs, ε/γP121R mutations were applied, sometimes in combination with γW55R. These mutations also change E_0, which was measured and corrected for, in each knock-out construct.

Results

agonist	WT	E_2	ΔG_2^{obs}	ΔG_0^{WT}	ΔG_{B2}
ACh	fetal	58.7	-2.4	9.9	-12.3
	adult	25.4	-1.9	8.3	-10.2
CCh	fetal	16.5 (0.9)	-1.7 (0.03)	9.9	-11.6 (0.3)
	adult	5.33	-1.0	8.3	-9.3
TMA	fetal	4.2 (0.7)	-0.8 (0.09)	9.9	-10.7 (0.3)
	adult	2.54	-0.5	8.3	-8.8
Cho	fetal	0.06 (0.01)	1.7 (0.09)	9.9	-8.2 (0.3)
	adult	0.046	1.8	8.3	-6.5

Agonist energy for AChRs with 2 WT binding sites (ΔG_{B2}) [91, 339]

Agonist energy for AChRs with 1 functional WT binding site (ΔG_{B1}) in kcal.M^{-1}.

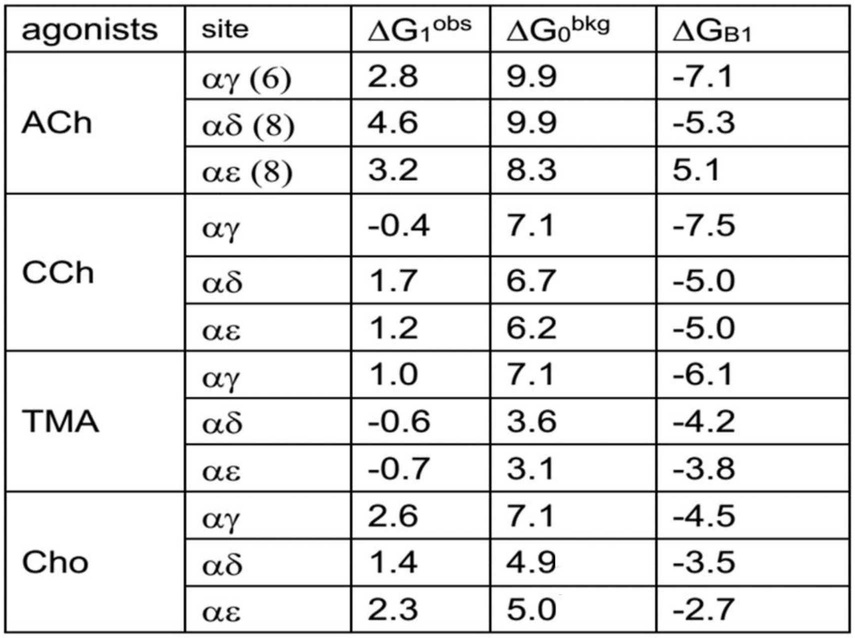

agonists	site	ΔG_1^{obs}	ΔG_0^{bkg}	ΔG_{B1}
ACh	αγ (6)	2.8	9.9	-7.1
	αδ (8)	4.6	9.9	-5.3
	αε (8)	3.2	8.3	5.1
CCh	αγ	-0.4	7.1	-7.5
	αδ	1.7	6.7	-5.0
	αε	1.2	6.2	-5.0
TMA	αγ	1.0	7.1	-6.1
	αδ	-0.6	3.6	-4.2
	αε	-0.7	3.1	-3.8
Cho	αγ	2.6	7.1	-4.5
	αδ	1.4	4.9	-3.5
	αε	2.3	5.0	-2.7

Effects of mutations of core aromatic residues on the agonist energy

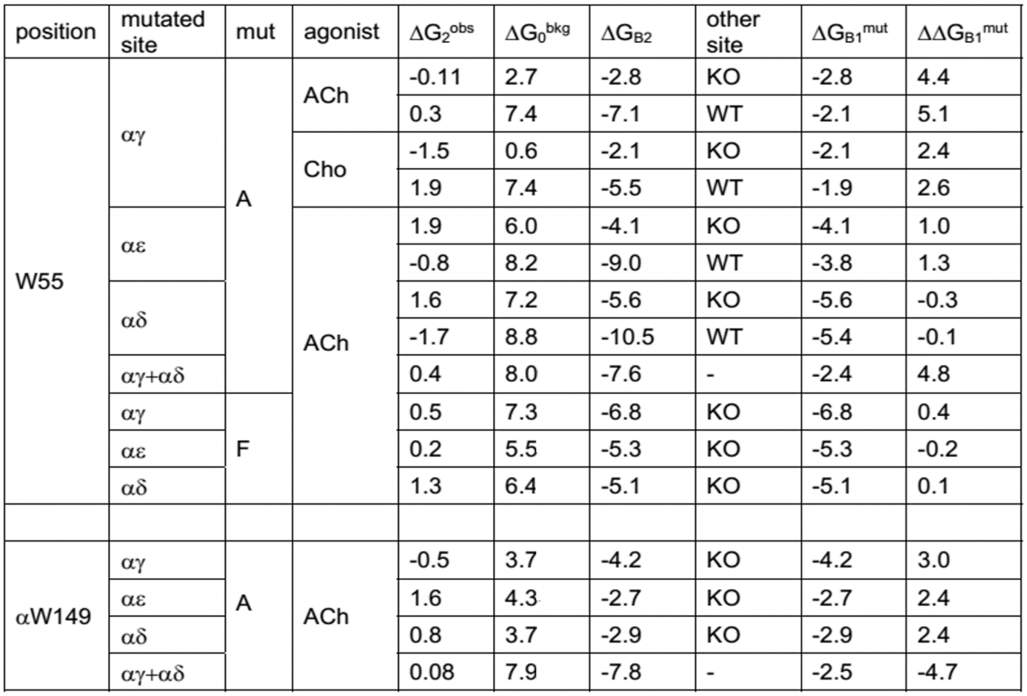

position	mutated site	mut	agonist	ΔG_2^{obs}	ΔG_0^{bkg}	ΔG_{B2}	other site	ΔG_{B1}^{mut}	$\Delta\Delta G_{B1}^{mut}$
W55	αγ	A	ACh	-0.11	2.7	-2.8	KO	-2.8	4.4
				0.3	7.4	-7.1	WT	-2.1	5.1
			Cho	-1.5	0.6	-2.1	KO	-2.1	2.4
				1.9	7.4	-5.5	WT	-1.9	2.6
	αε		ACh	1.9	6.0	-4.1	KO	-4.1	1.0
				-0.8	8.2	-9.0	WT	-3.8	1.3
	αδ			1.6	7.2	-5.6	KO	-5.6	-0.3
				-1.7	8.8	-10.5	WT	-5.4	-0.1
	αγ+αδ			0.4	8.0	-7.6	-	-2.4	4.8
	αγ	F		0.5	7.3	-6.8	KO	-6.8	0.4
	αε			0.2	5.5	-5.3	KO	-5.3	-0.2
	αδ			1.3	6.4	-5.1	KO	-5.1	0.1
αW149	αγ	A	ACh	-0.5	3.7	-4.2	KO	-4.2	3.0
	αε			1.6	4.3	-2.7	KO	-2.7	2.4
	αδ			0.8	3.7	-2.9	KO	-2.9	2.4
	αγ+αδ			0.08	7.9	-7.8	-	-2.5	-4.7

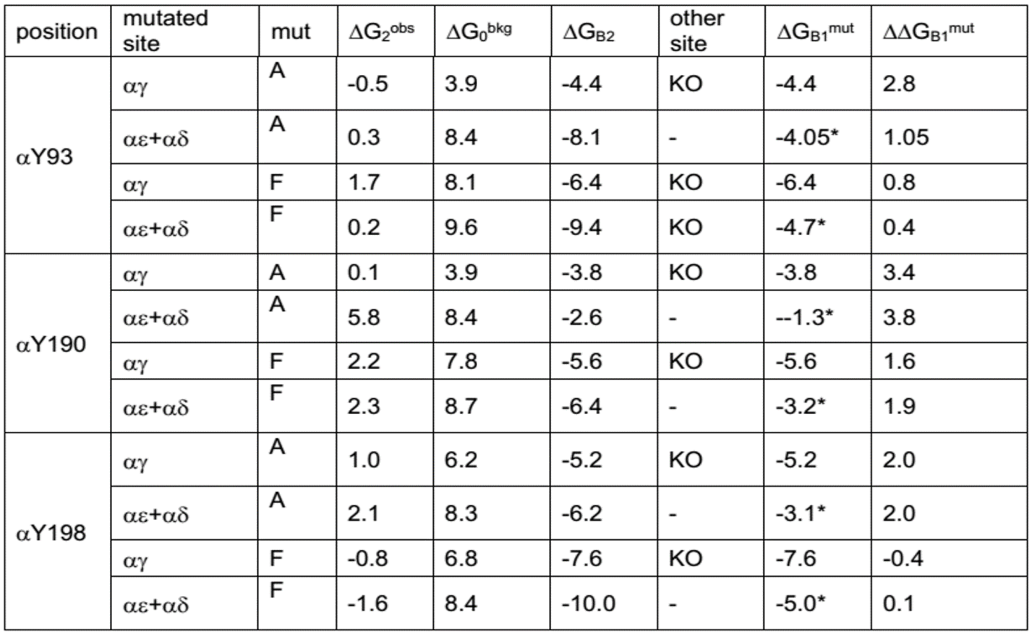

position	mutated site	mut	ΔG_2^{obs}	ΔG_0^{bkg}	ΔG_{B2}	other site	ΔG_{B1}^{mut}	$\Delta\Delta G_{B1}^{mut}$
αY93	αγ	A	-0.5	3.9	-4.4	KO	-4.4	2.8
	αε+αδ	A	0.3	8.4	-8.1	-	-4.05*	1.05
	αγ	F	1.7	8.1	-6.4	KO	-6.4	0.8
	αε+αδ	F	0.2	9.6	-9.4	KO	-4.7*	0.4
αY190	αγ	A	0.1	3.9	-3.8	KO	-3.8	3.4
	αε+αδ	A	5.8	8.4	-2.6	-	--1.3*	3.8
	αγ	F	2.2	7.8	-5.6	KO	-5.6	1.6
	αε+αδ	F	2.3	8.7	-6.4	-	-3.2*	1.9
αY198	αγ	A	1.0	6.2	-5.2	KO	-5.2	2.0
	αε+αδ	A	2.1	8.3	-6.2	-	-3.1*	2.0
	αγ	F	-0.8	6.8	-7.6	KO	-7.6	-0.4
	αε+αδ	F	-1.6	8.4	-10.0	-	-5.0*	0.1

ACh binding energies (kcal.M^{-1}) for A and F mutants of core aromatic residues. For the adult receptor, the agonist energies for the tyrosine to alanine mutations were previously estimated in AChRs with 2-WT binding sites [284]. Assuming that the αδ and αε sites are independent and equivalent, $\Delta G_{B1mut} = \Delta G_{B2}/2$ (*).

REFERENCES

1. Henzler-Wildman, K. and D. Kern, *Dynamic personalities of proteins.* Nature, 2007. **450**(7172): p. 964-72.
2. Anfinsen, C.B., *Principles that govern the folding of protein chains.* Science, 1973. **181**(4096): p. 223-30.
3. Hardy, J.A. and J.A. Wells, *Searching for new allosteric sites in enzymes.* Curr Opin Struct Biol, 2004. **14**(6): p. 706-15.
4. Suel, G.M., et al., *Evolutionarily conserved networks of residues mediate allosteric communication in proteins.* Nat Struct Biol, 2003. **10**(1): p. 59-69.
5. Swain, J.F. and L.M. Gierasch, *The changing landscape of protein allostery.* Curr Opin Struct Biol, 2006. **16**(1): p. 102-8.
6. Goodey, N.M. and S.J. Benkovic, *Allosteric regulation and catalysis emerge via a common route.* Nat Chem Biol, 2008. **4**(8): p. 474-82.
7. Monod, J., *Chance and necessity : an essay on the natural philosophy of modern biology*. 1971, New York: Knopf. xiv, 198 p.
8. Fenton, A.W., *Allostery: an illustrated definition for the 'second secret of life'.* Trends Biochem Sci, 2008. **33**(9): p. 420-5.
9. Changeux, J.P., *50th anniversary of the word "allosteric".* Protein Sci, 2011. **20**(7): p. 1119-24.
10. Bray, D. and T. Duke, *Conformational spread: the propagation of allosteric states in large multiprotein complexes.* Annu Rev Biophys Biomol Struct, 2004. **33**: p. 53-73.
11. Changeux, J.P. and S.J. Edelstein, *Allosteric mechanisms of signal transduction.* Science, 2005. **308**(5727): p. 1424-8.
12. Koshland, D.E., Jr., *Conformational changes: how small is big enough?* Nat Med, 1998. **4**(10): p. 1112-4.
13. Monod, J., J. Wyman, and J.P. Changeux, *On the Nature of Allosteric Transitions: A Plausible Model.* J Mol Biol, 1965. **12**: p. 88-118.
14. Koshland, D.E., Jr., G. Nemethy, and D. Filmer, *Comparison of experimental binding data and theoretical models in proteins containing subunits.* Biochemistry, 1966. **5**(1): p. 365-85.
15. Koshland, D.E., Jr., *Enzyme flexibility and enzyme action.* J Cell Comp Physiol, 1959. **54**: p. 245-58.
16. Weber, G., *Ligand binding and internal equilibria in proteins.* Biochemistry, 1972. **11**(5): p. 864-78.
17. Tsai, C.J. and R. Nussinov, *A unified view of "how allostery works".* PLoS Comput Biol, 2014. **10**(2): p. e1003394.
18. Cooper, A. and D.T. Dryden, *Allostery without conformational change. A plausible model.* Eur Biophys J, 1984. **11**(2): p. 103-9.
19. Gunasekaran, K., B. Ma, and R. Nussinov, *Is allostery an intrinsic property of all dynamic proteins?* Proteins, 2004. **57**(3): p. 433-43.
20. Wand, A.J., *Dynamic activation of protein function: a view emerging from NMR spectroscopy.* Nat Struct Biol, 2001. **8**(11): p. 926-31.
21. Popovych, N., et al., *Dynamically driven protein allostery.* Nat Struct Mol Biol, 2006. **13**(9): p. 831-8.

22. Daily, M.D. and J.J. Gray, *Allosteric communication occurs via networks of tertiary and quaternary motions in proteins.* PLoS Comput Biol, 2009. **5**(2): p. e1000293.
23. Berg, J.S., B.C. Powell, and R.E. Cheney, *A millennial myosin census.* Mol Biol Cell, 2001. **12**(4): p. 780-94.
24. Kühne, W., *Untersuchungen über das Protoplasma und die Contractilität / von W. Kühne*. 1864, Leipzig :: W. Engelmann.
25. Miki, H., Y. Okada, and N. Hirokawa, *Analysis of the kinesin superfamily: insights into structure and function.* Trends Cell Biol, 2005. **15**(9): p. 467-76.
26. Bhabha, G., et al., *How Dynein Moves Along Microtubules.* Trends Biochem Sci, 2016. **41**(1): p. 94-105.
27. Howard, J. and A.A. Hyman, *Microtubule polymerases and depolymerases.* Curr Opin Cell Biol, 2007. **19**(1): p. 31-5.
28. Desai, A. and T.J. Mitchison, *Microtubule polymerization dynamics.* Annu Rev Cell Dev Biol, 1997. **13**: p. 83-117.
29. Grant, B.J., et al., *Electrostatically biased binding of kinesin to microtubules.* PLoS Biol, 2011. **9**(11): p. e1001207.
30. Vale, R.D., T.S. Reese, and M.P. Sheetz, *Identification of a novel force-generating protein, kinesin, involved in microtubule-based motility.* Cell, 1985. **42**(1): p. 39-50.
31. Hirokawa, N., et al., *Kinesin superfamily motor proteins and intracellular transport.* Nat Rev Mol Cell Biol, 2009. **10**(10): p. 682-96.
32. Lawrence, C.J., et al., *A standardized kinesin nomenclature.* J Cell Biol, 2004. **167**(1): p. 19-22.
33. Nishiyama, M., H. Higuchi, and T. Yanagida, *Chemomechanical coupling of the forward and backward steps of single kinesin molecules.* Nat Cell Biol, 2002. **4**(10): p. 790-7.
34. Kull, F.J., R.D. Vale, and R.J. Fletterick, *The case for a common ancestor: kinesin and myosin motor proteins and G proteins.* J Muscle Res Cell Motil, 1998. **19**(8): p. 877-86.
35. Case, R.B., et al., *Role of the kinesin neck linker and catalytic core in microtubule-based motility.* Curr Biol, 2000. **10**(3): p. 157-60.
36. Vale, R.D., et al., *Searching for kinesin's mechanical amplifier.* Philos Trans R Soc Lond B Biol Sci, 2000. **355**(1396): p. 449-57.
37. Gyoeva, F.K., et al., *The tetrameric molecule of conventional kinesin contains identical light chains.* Biochemistry, 2004. **43**(42): p. 13525-31.
38. Block, S.M., L.S. Goldstein, and B.J. Schnapp, *Bead movement by single kinesin molecules studied with optical tweezers.* Nature, 1990. **348**(6299): p. 348-52.
39. Howard, J., A.J. Hudspeth, and R.D. Vale, *Movement of microtubules by single kinesin molecules.* Nature, 1989. **342**(6246): p. 154-8.
40. Schnitzer, M.J. and S.M. Block, *Kinesin hydrolyses one ATP per 8-nm step.* Nature, 1997. **388**(6640): p. 386-90.
41. Schnitzer, M.J., K. Visscher, and S.M. Block, *Force production by single kinesin motors.* Nat Cell Biol, 2000. **2**(10): p. 718-23.
42. Jeppesen, G.M. and J.K. Hoerber, *The mechanical properties of kinesin-1: a holistic approach.* Biochem Soc Trans, 2012. **40**(2): p. 438-43.
43. Hackney, D.D. and M.F. Stock, *Kinesin's IAK tail domain inhibits initial microtubule-stimulated ADP release.* Nat Cell Biol, 2000. **2**(5): p. 257-60.

44. Stock, M.F., et al., *Formation of the compact confomer of kinesin requires a COOH-terminal heavy chain domain and inhibits microtubule-stimulated ATPase activity.* J Biol Chem, 1999. **274**(21): p. 14617-23.
45. Verhey, K.J. and J.W. Hammond, *Traffic control: regulation of kinesin motors.* Nat Rev Mol Cell Biol, 2009. **10**(11): p. 765-77.
46. Endow, S.A., *Kinesin motors as molecular machines.* Bioessays, 2003. **25**(12): p. 1212-9.
47. Cross, R.A., *The kinetic mechanism of kinesin.* Trends Biochem Sci, 2004. **29**(6): p. 301-9.
48. Valentine, M.T. and S.P. Gilbert, *To step or not to step? How biochemistry and mechanics influence processivity in Kinesin and Eg5.* Curr Opin Cell Biol, 2007. **19**(1): p. 75-81.
49. Carter, N.J. and R.A. Cross, *Mechanics of the kinesin step.* Nature, 2005. **435**(7040): p. 308-12.
50. Vale, R.D. and R.A. Milligan, *The way things move: looking under the hood of molecular motor proteins.* Science, 2000. **288**(5463): p. 88-95.
51. Hackney, D.D., *Kinesin ATPase: rate-limiting ADP release.* Proc Natl Acad Sci U S A, 1988. **85**(17): p. 6314-8.
52. Rice, S., et al., *A structural change in the kinesin motor protein that drives motility.* Nature, 1999. **402**(6763): p. 778-84.
53. Gigant, B., et al., *Structure of a kinesin-tubulin complex and implications for kinesin motility.* Nat Struct Mol Biol, 2013. **20**(8): p. 1001-7.
54. Thompson, A.J., H.A. Lester, and S.C. Lummis, *The structural basis of function in Cys-loop receptors.* Q Rev Biophys, 2010. **43**(4): p. 449-99.
55. Le Novere, N. and J.P. Changeux, *Molecular evolution of the nicotinic acetylcholine receptor: an example of multigene family in excitable cells.* J Mol Evol, 1995. **40**(2): p. 155-72.
56. Sine, S.M., *End-plate acetylcholine receptor: structure, mechanism, pharmacology, and disease.* Physiol Rev, 2012. **92**(3): p. 1189-234.
57. Alberts, B., *Molecular biology of the cell*. 4th ed. 2002, New York: Garland Science. xxxiv, 1548 p.
58. Kuffler, S.W. and D. Yoshikami, *The number of transmitter molecules in a quantum: an estimate from iontophoretic application of acetylcholine at the neuromuscular synapse.* J Physiol, 1975. **251**(2): p. 465-82.
59. Taly, A., et al., *Allosteric regulation of pentameric ligand-gated ion channels: an emerging mechanistic perspective.* Channels (Austin), 2014. **8**(4): p. 350-60.
60. Unwin, N., *Nicotinic acetylcholine receptor and the structural basis of neuromuscular transmission: insights from Torpedo postsynaptic membranes.* Q Rev Biophys, 2013. **46**(4): p. 283-322.
61. Karlsson, E., *Chemistry of Protein Toxins in Snake Venoms*, in *Snake Venoms*, C.-Y. Lee, Editor. 1979, Springer Berlin Heidelberg: Berlin, Heidelberg. p. 159-212.
62. Klett, R.P., et al., *The acetylcholine receptor. I. Purification and characterization of a macromolecule isolated from Electrophorus electricus.* J Biol Chem, 1973. **248**(19): p. 6841-53.
63. Cartaud, J. and E.L. Benedetti, *A morphological study of the cholinergic receptor protein from Torpedo marmorata in its membrane environment and in its detergent-extracted purified form.* J Cell Sci, 1978. **29**: p. 313-37.

64. Toyoshima, C. and N. Unwin, *Ion channel of acetylcholine receptor reconstructed from images of postsynaptic membranes.* Nature, 1988. **336**(6196): p. 247-50.
65. Tzartos, S.J. and J.M. Lindstrom, *Monoclonal antibodies used to probe acetylcholine receptor structure: localization of the main immunogenic region and detection of similarities between subunits.* Proc Natl Acad Sci U S A, 1980. **77**(2): p. 755-9.
66. Unwin, N., *Refined structure of the nicotinic acetylcholine receptor at 4A resolution.* J Mol Biol, 2005. **346**(4): p. 967-89.
67. Olsen, J.A., et al., *Molecular recognition of the neurotransmitter acetylcholine by an acetylcholine binding protein reveals determinants of binding to nicotinic acetylcholine receptors.* PLoS One, 2014. **9**(3): p. e91232.
68. Hansen, S.B., et al., *Structures of Aplysia AChBP complexes with nicotinic agonists and antagonists reveal distinctive binding interfaces and conformations.* EMBO J, 2005. **24**(20): p. 3635-46.
69. Hilf, R.J. and R. Dutzler, *X-ray structure of a prokaryotic pentameric ligand-gated ion channel.* Nature, 2008. **452**(7185): p. 375-9.
70. Pan, J., et al., *Structure of the pentameric ligand-gated ion channel ELIC cocrystallized with its competitive antagonist acetylcholine.* Nat Commun, 2012. **3**: p. 714.
71. Sauguet, L., et al., *Structural basis for ion permeation mechanism in pentameric ligand-gated ion channels.* EMBO J, 2013. **32**(5): p. 728-41.
72. Sauguet, L., et al., *Crystal structures of a pentameric ligand-gated ion channel provide a mechanism for activation.* Proc Natl Acad Sci U S A, 2014. **111**(3): p. 966-71.
73. Althoff, T., et al., *X-ray structures of GluCl in apo states reveal a gating mechanism of Cys-loop receptors.* Nature, 2014. **512**(7514): p. 333-7.
74. Hibbs, R.E. and E. Gouaux, *Principles of activation and permeation in an anion-selective Cys-loop receptor.* Nature, 2011. **474**(7349): p. 54-60.
75. Changeux, J.P., et al., *Reconstitution of a functional acetylcholine regulator under defined conditions.* FEBS Lett, 1979. **105**(1): p. 181-7.
76. Reynolds, J.A. and A. Karlin, *Molecular weight in detergent solution of acetylcholine receptor from Torpedo californica.* Biochemistry, 1978. **17**(11): p. 2035-8.
77. Mishina, M., et al., *Molecular distinction between fetal and adult forms of muscle acetylcholine receptor.* Nature, 1986. **321**(6068): p. 406-11.
78. Popot, J.L. and J.P. Changeux, *Nicotinic receptor of acetylcholine: structure of an oligomeric integral membrane protein.* Physiol Rev, 1984. **64**(4): p. 1162-239.
79. Grosman, C., et al., *The extracellular linker of muscle acetylcholine receptor channels is a gating control element.* J Gen Physiol, 2000. **116**(3): p. 327-40.
80. Numa, S., *Molecular basis for the function of ionic channels.* Biochem Soc Symp, 1986. **52**: p. 119-43.
81. Ren, X.Q., et al., *Structural determinants of alpha4beta2 nicotinic acetylcholine receptor trafficking.* J Neurosci, 2005. **25**(28): p. 6676-86.
82. Zhang, H. and A. Karlin, *Contribution of the beta subunit M2 segment to the ion-conducting pathway of the acetylcholine receptor.* Biochemistry, 1998. **37**(22): p. 7952-64.
83. Kim, S., A.K. Chamberlain, and J.U. Bowie, *A model of the closed form of the nicotinic acetylcholine receptor m2 channel pore.* Biophys J, 2004. **87**(2): p. 792-9.
84. Siegel, G.J., et al., *Basic neurochemistry.* 1999.

85. Rogers, S.E., et al. *Opening a hydrophobic gate: the nicotinic acetylcholine receptor as an example*. ArXiv e-prints, 2009. **0902**.
86. Nury, H., et al., *X-ray structures of general anaesthetics bound to a pentameric ligand-gated ion channel.* Nature, 2011. **469**(7330): p. 428-31.
87. Bocquet, N., et al., *X-ray structure of a pentameric ligand-gated ion channel in an apparently open conformation.* Nature, 2009. **457**(7225): p. 111-4.
88. Oswald, R.E. and J.P. Changeux, *Crosslinking of alpha-bungarotoxin to the acetylcholine receptor from Torpedo marmorata by ultraviolet light irradiation.* FEBS Lett, 1982. **139**(2): p. 225-9.
89. Brejc, K., et al., *Crystal structure of an ACh-binding protein reveals the ligand-binding domain of nicotinic receptors.* Nature, 2001. **411**(6835): p. 269-76.
90. Corringer, P.J., N. Le Novere, and J.P. Changeux, *Nicotinic receptors at the amino acid level.* Annu Rev Pharmacol Toxicol, 2000. **40**: p. 431-58.
91. Nayak, T.K. and A. Auerbach, *Asymmetric transmitter binding sites of fetal muscle acetylcholine receptors shape their synaptic response.* Proc Natl Acad Sci U S A, 2013. **110**(33): p. 13654-9.
92. Zhong, W., et al., *From ab initio quantum mechanics to molecular neurobiology: a cation-pi binding site in the nicotinic receptor.* Proc Natl Acad Sci U S A, 1998. **95**(21): p. 12088-93.
93. Auerbach, A., *Activation of endplate nicotinic acetylcholine receptors by agonists.* Biochem Pharmacol, 2015. **97**(4): p. 601-8.
94. Auerbach, A., *Life at the top: the transition state of AChR gating.* Sci STKE, 2003. **2003**(188): p. re11.
95. Miller, P.S. and A.R. Aricescu, *Crystal structure of a human GABAA receptor.* Nature, 2014. **512**(7514): p. 270-5.
96. Karlin, A., *On the application of "a plausible model" of allosteric proteins to the receptor for acetylcholine.* J Theor Biol, 1967. **16**(2): p. 306-20.
97. Jackson, M.B., *Spontaneous openings of the acetylcholine receptor channel.* Proc Natl Acad Sci U S A, 1984. **81**(12): p. 3901-4.
98. Changeux, J.P. and S.J. Edelstein, *Allosteric receptors after 30 years.* Neuron, 1998. **21**(5): p. 959-80.
99. Auerbach, A., *Thinking in cycles: MWC is a good model for acetylcholine receptor-channels.* J Physiol, 2012. **590**(1): p. 93-8.
100. Chakrapani, S. and A. Auerbach, *A speed limit for conformational change of an allosteric membrane protein.* Proc Natl Acad Sci U S A, 2005. **102**(1): p. 87-92.
101. Neubig, R.R., N.D. Boyd, and J.B. Cohen, *Conformations of Torpedo acetylcholine receptor associated with ion transport and desensitization.* Biochemistry, 1982. **21**(14): p. 3460-7.
102. Zhou, M., A.G. Engel, and A. Auerbach, *Serum choline activates mutant acetylcholine receptors that cause slow channel congenital myasthenic syndromes.* Proc Natl Acad Sci U S A, 1999. **96**(18): p. 10466-71.
103. Purohit, P. and A. Auerbach, *Unliganded gating of acetylcholine receptor channels.* Proc Natl Acad Sci U S A, 2009. **106**(1): p. 115-20.
104. Purohit, P. and A. Auerbach, *Energetics of gating at the apo-acetylcholine receptor transmitter binding site.* J Gen Physiol, 2010. **135**(4): p. 321-31.

105. Gupta, S., P. Purohit, and A. Auerbach, *Function of interfacial prolines at the transmitter-binding sites of the neuromuscular acetylcholine receptor.* J Biol Chem, 2013. **288**(18): p. 12667-79.
106. Jha, A. and A. Auerbach, *Acetylcholine receptor channels activated by a single agonist molecule.* Biophys J, 2010. **98**(9): p. 1840-6.
107. Pathria, R.K., *Statistical mechanics*. 2nd ed. 1996, Oxford ; Boston: Butterworth-Heinemann. 529 p.
108. Jadey, S. and A. Auerbach, *An integrated catch-and-hold mechanism activates nicotinic acetylcholine receptors.* J Gen Physiol, 2012. **140**(1): p. 17-28.
109. Purohit, P., et al., *Catch-and-hold activation of muscle acetylcholine receptors having transmitter binding site mutations.* Biophys J, 2014. **107**(1): p. 88-99.
110. Auerbach, A., *The energy and work of a ligand-gated ion channel.* J Mol Biol, 2013. **425**(9): p. 1461-75.
111. Auerbach, A., *The gating isomerization of neuromuscular acetylcholine receptors.* J Physiol, 2010. **588**(Pt 4): p. 573-86.
112. Neher, E., B. Sakmann, and J.H. Steinbach, *The extracellular patch clamp: a method for resolving currents through individual open channels in biological membranes.* Pflugers Arch, 1978. **375**(2): p. 219-28.
113. Hamill, O.P., et al., *Improved patch-clamp techniques for high-resolution current recording from cells and cell-free membrane patches.* Pflugers Arch, 1981. **391**(2): p. 85-100.
114. Sigworth, F.J., H. Affolter, and E. Neher, *Design of the EPC-9, a computer-controlled patch-clamp amplifier. 2. Software.* J Neurosci Methods, 1995. **56**(2): p. 203-15.
115. Calimet, N., et al., *A gating mechanism of pentameric ligand-gated ion channels.* Proc Natl Acad Sci U S A, 2013. **110**(42): p. E3987-96.
116. Cheng, X., et al., *Molecular-dynamics simulations of ELIC-a prokaryotic homologue of the nicotinic acetylcholine receptor.* Biophys J, 2009. **96**(11): p. 4502-13.
117. Henchman, R.H., et al., *Asymmetric structural motions of the homomeric alpha7 nicotinic receptor ligand binding domain revealed by molecular dynamics simulation.* Biophys J, 2003. **85**(5): p. 3007-18.
118. Law, R.J., R.H. Henchman, and J.A. McCammon, *A gating mechanism proposed from a simulation of a human alpha7 nicotinic acetylcholine receptor.* Proc Natl Acad Sci U S A, 2005. **102**(19): p. 6813-8.
119. Cheng, X., et al., *Targeted molecular dynamics study of C-loop closure and channel gating in nicotinic receptors.* PLoS Comput Biol, 2006. **2**(9): p. e134.
120. Liu, X., et al., *Unbinding of nicotine from the acetylcholine binding protein: steered molecular dynamics simulations.* J Phys Chem B, 2008. **112**(13): p. 4087-93.
121. Nury, H., et al., *One-microsecond molecular dynamics simulation of channel gating in a nicotinic receptor homologue.* Proc Natl Acad Sci U S A, 2010. **107**(14): p. 6275-80.
122. Sine, S.M., T. Claudio, and F.J. Sigworth, *Activation of Torpedo acetylcholine receptors expressed in mouse fibroblasts. Single channel current kinetics reveal distinct agonist binding affinities.* J Gen Physiol, 1990. **96**(2): p. 395-437.
123. Cheng, X., et al., *Channel opening motion of alpha7 nicotinic acetylcholine receptor as suggested by normal mode analysis.* J Mol Biol, 2006. **355**(2): p. 310-24.

124. Samson, A.O. and M. Levitt, *Inhibition mechanism of the acetylcholine receptor by alpha-neurotoxins as revealed by normal-mode dynamics.* Biochemistry, 2008. **47**(13): p. 4065-70.

125. Taly, A., et al., *Normal mode analysis suggests a quaternary twist model for the nicotinic receptor gating mechanism.* Biophys J, 2005. **88**(6): p. 3954-65.

126. Zheng, W. and A. Auerbach, *Decrypting the sequence of structural events during the gating transition of pentameric ligand-gated ion channels based on an interpolated elastic network model.* PLoS Comput Biol, 2011. **7**(1): p. e1001046.

127. Le Novere, N., T. Grutter, and J.P. Changeux, *Models of the extracellular domain of the nicotinic receptors and of agonist- and Ca2+-binding sites.* Proc Natl Acad Sci U S A, 2002. **99**(5): p. 3210-5.

128. Sine, S.M., H.L. Wang, and N. Bren, *Lysine scanning mutagenesis delineates structural model of the nicotinic receptor ligand binding domain.* J Biol Chem, 2002. **277**(32): p. 29210-23.

129. Purohit, P., et al., *Functional anatomy of an allosteric protein.* Nat Commun, 2013. **4**: p. 2984.

130. Gupta, S. and A. Auerbach, *Temperature dependence of acetylcholine receptor channels activated by different agonists.* Biophys J, 2011. **100**(4): p. 895-903.

131. Liu, Y., et al., *Postsynaptic development of the neuromuscular junction in mice lacking the gamma-subunit of muscle nicotinic acetylcholine receptor.* J Mol Neurosci, 2010. **40**(1-2): p. 21-6.

132. Koenen, M., et al., *Acetylcholine receptor channel subtype directs the innervation pattern of skeletal muscle.* EMBO Rep, 2005. **6**(6): p. 570-6.

133. Jin, T.E., A. Wernig, and V. Witzemann, *Changes in acetylcholine receptor function induce shifts in muscle fiber type composition.* FEBS J, 2008. **275**(9): p. 2042-54.

134. Takahashi, M., et al., *Spontaneous muscle action potentials fail to develop without fetal-type acetylcholine receptors.* EMBO Rep, 2002. **3**(7): p. 674-81.

135. Vogt, J., et al., *CHRNG genotype-phenotype correlations in the multiple pterygium syndromes.* J Med Genet, 2012. **49**(1): p. 21-6.

136. Hoffmann, K., et al., *Escobar syndrome is a prenatal myasthenia caused by disruption of the acetylcholine receptor fetal gamma subunit.* Am J Hum Genet, 2006. **79**(2): p. 303-12.

137. Morgan, N.V., et al., *Mutations in the embryonal subunit of the acetylcholine receptor (CHRNG) cause lethal and Escobar variants of multiple pterygium syndrome.* Am J Hum Genet, 2006. **79**(2): p. 390-5.

138. Herlitze, S., et al., *Structural determinants of channel conductance in fetal and adult rat muscle acetylcholine receptors.* J Physiol, 1996. **492 (Pt 3)**: p. 775-87.

139. Villarroel, A. and B. Sakmann, *Calcium permeability increase of endplate channels in rat muscle during postnatal development.* J Physiol, 1996. **496 (Pt 2)**: p. 331-8.

140. Scimemi, A. and M. Beato, *Determining the neurotransmitter concentration profile at active synapses.* Molecular neurobiology, 2009. **40**(3): p. 289-306.

141. Alder, B. and T. Wainwright, *Phase transition for a hard sphere system.* The Journal of chemical physics, 1957. **27**(5): p. 1208.

142. Alder, B.J. and T. Wainwright, *Studies in molecular dynamics. I. General method.* The Journal of Chemical Physics, 1959. **31**(2): p. 459-466.

143. Rahman, A., *Correlations in the motion of atoms in liquid argon.* Physical Review, 1964. **136**(2A): p. A405.

144. Rahman, A. and F.H. Stillinger, *Propagation of sound in water. A molecular-dynamics study*. Physical Review A, 1974. **10**(1): p. 368.
145. McCammon, J.A., B.R. Gelin, and M. Karplus, *Dynamics of folded proteins.* Nature, 1977. **267**(5612): p. 585-90.
146. MacKerell, A.D., et al., *All-atom empirical potential for molecular modeling and dynamics studies of proteins.* J Phys Chem B, 1998. **102**(18): p. 3586-616.
147. Adcock, S.A. and J.A. McCammon, *Molecular dynamics: survey of methods for simulating the activity of proteins.* Chem Rev, 2006. **106**(5): p. 1589-615.
148. Leach, A.R., *Molecular modelling : principles and applications*. 2nd ed. 2001, Harlow, England ; New York: Prentice Hall. xxiii, 744 pages, 16 pages of plates.
149. Zimmermann, K., *ORAL: all purpose molecular mechanics simulator and energy minimizer.* Journal of computational chemistry, 1991. **12**(3): p. 310-319.
150. Berendsen, H.J.C. and W.F. van Gunsteren *Practical algorithms for dynamics simulations*. Proceedings of the International School of Physics "Enrico Fermi", course 97, 1986. 43-65.
151. Verlet, L., *Computer" experiments" on classical fluids. I. Thermodynamical properties of Lennard-Jones molecules.* Physical review, 1967. **159**(1): p. 98.
152. Bekker, H., et al., *An efficient, box shape independent non-bonded force and virial algorithm for molecular dynamics.* Molecular Simulation, 1995. **14**(3): p. 137-151.
153. Steinbach, P.J. and B.R. Brooks, *New spherical‐cutoff methods for long‐range forces in macromolecular simulation.* Journal of computational chemistry, 1994. **15**(7): p. 667-683.
154. Schlitter, J., M. Engels, and P. Krüger, *Targeted molecular dynamics: a new approach for searching pathways of conformational transitions.* Journal of molecular graphics, 1994. **12**(2): p. 84-89.
155. Hamelberg, D., J. Mongan, and J.A. McCammon, *Accelerated molecular dynamics: a promising and efficient simulation method for biomolecules.* The Journal of chemical physics, 2004. **120**(24): p. 11919-11929.
156. Isralewitz, B., S. Izrailev, and K. Schulten, *Binding pathway of retinal to bacterio-opsin: a prediction by molecular dynamics simulations.* Biophys J, 1997. **73**(6): p. 2972-9.
157. Kosztin, D., S. Izrailev, and K. Schulten, *Unbinding of retinoic acid from its receptor studied by steered molecular dynamics.* Biophys J, 1999. **76**(1 Pt 1): p. 188-97.
158. Lu, H. and K. Schulten, *Steered molecular dynamics simulations of force-induced protein domain unfolding.* Proteins, 1999. **35**(4): p. 453-63.
159. Baker, D. and A. Sali, *Protein structure prediction and structural genomics.* Science, 2001. **294**(5540): p. 93-6.
160. Carrillo, H. and D. Lipman, *The Multiple Sequence Alignment Problem in Biology.* Siam Journal on Applied Mathematics, 1988. **48**(5): p. 1073-1082.
161. Lipman, D.J., S.F. Altschul, and J.D. Kececioglu, *A Tool for Multiple Sequence Alignment.* Proceedings of the National Academy of Sciences of the United States of America, 1989. **86**(12): p. 4412-4415.
162. Chothia, C. and A.M. Lesk, *The relation between the divergence of sequence and structure in proteins.* EMBO J, 1986. **5**(4): p. 823-6.
163. Adhikari, A.N., et al., *Modeling large regions in proteins: applications to loops, termini, and folding.* Protein Sci, 2012. **21**(1): p. 107-21.
164. Webb, B. and A. Sali, *Comparative protein structure modeling using Modeller.* Current protocols in bioinformatics, 2014: p. 5.6. 1-5.6. 32.

165. Das, R. and D. Baker, *Macromolecular modeling with Rosetta.* Annual Review of Biochemistry, 2008. **77**: p. 363-382.
166. Lengauer, T. and M. Rarey, *Computational methods for biomolecular docking.* Curr Opin Struct Biol, 1996. **6**(3): p. 402-6.
167. Jorgensen, W.L., *Rusting of the lock and key model for protein-ligand binding.* Science, 1991. **254**(5034): p. 954-5.
168. Halperin, I., et al., *Principles of docking: An overview of search algorithms and a guide to scoring functions.* Proteins, 2002. **47**(4): p. 409-43.
169. Morris, G.M., et al., *Automated docking using a Lamarckian genetic algorithm and an empirical binding free energy function.* Journal of computational chemistry, 1998. **19**(14): p. 1639-1662.
170. Hirokawa, N., Y. Noda, and Y. Okada, *Kinesin and dynein superfamily proteins in organelle transport and cell division.* Curr Opin Cell Biol, 1998. **10**(1): p. 60-73.
171. Hackney, D.D., *Highly processive microtubule-stimulated ATP hydrolysis by dimeric kinesin head domains.* Nature, 1995. **377**(6548): p. 448-50.
172. Endow, S.A. and D.S. Barker, *Processive and nonprocessive models of kinesin movement.* Annu Rev Physiol, 2003. **65**: p. 161-75.
173. Yildiz, A., et al., *Kinesin walks hand-over-hand.* Science, 2004. **303**(5658): p. 676-8.
174. Hackney, D.D., *Biochemistry. Processive motor movement.* Science, 2007. **316**(5821): p. 58-9.
175. Block, S.M., *Kinesin motor mechanics: binding, stepping, tracking, gating, and limping.* Biophys J, 2007. **92**(9): p. 2986-95.
176. Gilbert, S.P., et al., *Pathway of processive ATP hydrolysis by kinesin.* Nature, 1995. **373**(6516): p. 671-6.
177. Ma, Y.Z. and E.W. Taylor, *Kinetic mechanism of a monomeric kinesin construct.* J Biol Chem, 1997. **272**(2): p. 717-23.
178. Moyer, M.L., S.P. Gilbert, and K.A. Johnson, *Pathway of ATP hydrolysis by monomeric and dimeric kinesin.* Biochemistry, 1998. **37**(3): p. 800-13.
179. Kikkawa, M., et al., *Switch-based mechanism of kinesin motors.* Nature, 2001. **411**(6836): p. 439-45.
180. Nitta, R., et al., *KIF1A alternately uses two loops to bind microtubules.* Science, 2004. **305**(5684): p. 678-83.
181. Nitta, R., Y. Okada, and N. Hirokawa, *Structural model for strain-dependent microtubule activation of Mg-ADP release from kinesin.* Nat Struct Mol Biol, 2008. **15**(10): p. 1067-75.
182. Kikkawa, M. and N. Hirokawa, *High-resolution cryo-EM maps show the nucleotide binding pocket of KIF1A in open and closed conformations.* EMBO J, 2006. **25**(18): p. 4187-94.
183. Hirose, K., et al., *Large conformational changes in a kinesin motor catalyzed by interaction with microtubules.* Mol Cell, 2006. **23**(6): p. 913-23.
184. Sindelar, C.V. and K.H. Downing, *The beginning of kinesin's force-generating cycle visualized at 9-A resolution.* J Cell Biol, 2007. **177**(3): p. 377-85.
185. Goulet, A., et al., *The structural basis of force generation by the mitotic motor kinesin-5.* J Biol Chem, 2012. **287**(53): p. 44654-66.
186. Sindelar, C.V. and K.H. Downing, *An atomic-level mechanism for activation of the kinesin molecular motors.* Proc Natl Acad Sci U S A, 2010. **107**(9): p. 4111-6.

187. Goulet, A., et al., *Comprehensive structural model of the mechanochemical cycle of a mitotic motor highlights molecular adaptations in the kinesin family.* Proc Natl Acad Sci U S A, 2014. **111**(5): p. 1837-42.
188. Jolley, C.C., et al., *Fitting low-resolution cryo-EM maps of proteins using constrained geometric simulations.* Biophys J, 2008. **94**(5): p. 1613-21.
189. Topf, M., et al., *Protein structure fitting and refinement guided by cryo-EM density.* Structure, 2008. **16**(2): p. 295-307.
190. Velazquez-Muriel, J.A., et al., *Flexible fitting in 3D-EM guided by the structural variability of protein superfamilies.* Structure, 2006. **14**(7): p. 1115-26.
191. Tan, R.K., B. Devkota, and S.C. Harvey, *YUP.SCX: coaxing atomic models into medium resolution electron density maps.* J Struct Biol, 2008. **163**(2): p. 163-74.
192. Schroder, G.F., A.T. Brunger, and M. Levitt, *Combining efficient conformational sampling with a deformable elastic network model facilitates structure refinement at low resolution.* Structure, 2007. **15**(12): p. 1630-41.
193. Tama, F., O. Miyashita, and C.L. Brooks, 3rd, *Normal mode based flexible fitting of high-resolution structure into low-resolution experimental data from cryo-EM.* J Struct Biol, 2004. **147**(3): p. 315-26.
194. Suhre, K., J. Navaza, and Y.H. Sanejouand, *NORMA: a tool for flexible fitting of high-resolution protein structures into low-resolution electron-microscopy-derived density maps.* Acta Crystallogr D Biol Crystallogr, 2006. **62**(Pt 9): p. 1098-100.
195. Zheng, W., *Accurate flexible fitting of high-resolution protein structures into cryo-electron microscopy maps using coarse-grained pseudo-energy minimization.* Biophys J, 2011. **100**(2): p. 478-88.
196. DiMaio, F., et al., *Refinement of protein structures into low-resolution density maps using rosetta.* J Mol Biol, 2009. **392**(1): p. 181-90.
197. Trabuco, L.G., et al., *Flexible fitting of atomic structures into electron microscopy maps using molecular dynamics.* Structure, 2008. **16**(5): p. 673-83.
198. Trabuco, L.G., et al., *Molecular dynamics flexible fitting: a practical guide to combine cryo-electron microscopy and X-ray crystallography.* Methods, 2009. **49**(2): p. 174-80.
199. Zheng, W. and B.R. Brooks, *Normal-modes-based prediction of protein conformational changes guided by distance constraints.* Biophys J, 2005. **88**(5): p. 3109-17.
200. Zheng, W., B.R. Brooks, and G. Hummer, *Protein conformational transitions explored by mixed elastic network models.* Proteins, 2007. **69**(1): p. 43-57.
201. Zheng, W. and S. Doniach, *A comparative study of motor-protein motions by using a simple elastic-network model.* Proc Natl Acad Sci U S A, 2003. **100**(23): p. 13253-8.
202. Zheng, W. and M. Tekpinar, *Large-scale evaluation of dynamically important residues in proteins predicted by the perturbation analysis of a coarse-grained elastic model.* BMC Struct Biol, 2009. **9**: p. 45.
203. Hyeon, C. and J.N. Onuchic, *Mechanical control of the directional stepping dynamics of the kinesin motor.* Proc Natl Acad Sci U S A, 2007. **104**(44): p. 17382-7.
204. Jana, B., C. Hyeon, and J.N. Onuchic, *The origin of minus-end directionality and mechanochemistry of Ncd motors.* PLoS Comput Biol, 2012. **8**(11): p. e1002783.
205. Zhang, Z. and D. Thirumalai, *Dissecting the kinematics of the kinesin step.* Structure, 2012. **20**(4): p. 628-40.
206. Kanada, R., et al., *Structure-based molecular simulations reveal the enhancement of biased Brownian motions in single-headed kinesin.* PLoS Comput Biol, 2013. **9**(2): p. e1002907.

207. Behnke-Parks, W.M., et al., *Loop L5 acts as a conformational latch in the mitotic kinesin Eg5.* J Biol Chem, 2011. **286**(7): p. 5242-53.
208. Zhang, W., *Exploring the intermediate states of ADP-ATP exchange: a simulation study on Eg5.* J Phys Chem B, 2011. **115**(5): p. 784-95.
209. Harrington, T.D., et al., *Analysis of the interaction of the Eg5 Loop5 with the nucleotide site.* J Theor Biol, 2011. **289**: p. 107-15.
210. Naber, N., et al., *Multiple conformations of the nucleotide site of Kinesin family motors in the triphosphate state.* J Mol Biol, 2011. **408**(4): p. 628-42.
211. Hwang, W., M.J. Lang, and M. Karplus, *Force generation in kinesin hinges on cover-neck bundle formation.* Structure, 2008. **16**(1): p. 62-71.
212. Lakkaraju, S.K. and W. Hwang, *Hysteresis-based mechanism for the directed motility of the Ncd motor.* Biophys J, 2011. **101**(5): p. 1105-13.
213. Krukau, A., V. Knecht, and R. Lipowsky, *Allosteric control of kinesin's motor domain by tubulin: a molecular dynamics study.* Phys Chem Chem Phys, 2014. **16**(13): p. 6189-98.
214. Scarabelli, G. and B.J. Grant, *Mapping the structural and dynamical features of kinesin motor domains.* PLoS Comput Biol, 2013. **9**(11): p. e1003329.
215. Aprodu, I., M. Soncini, and A. Redaelli, *Interaction forces and interface properties of KIF1A kinesin-alphabeta tubulin complex assessed by molecular dynamics.* J Biomech, 2008. **41**(15): p. 3196-201.
216. Li, M. and W. Zheng, *Probing the structural and energetic basis of kinesin-microtubule binding using computational alanine-scanning mutagenesis.* Biochemistry, 2011. **50**(40): p. 8645-55.
217. Li, M. and W. Zheng, *All-atom structural investigation of kinesin-microtubule complex constrained by high-quality cryo-electron-microscopy maps.* Biochemistry, 2012. **51**(25): p. 5022-32.
218. Kull, F.J., et al., *Crystal structure of the kinesin motor domain reveals a structural similarity to myosin.* Nature, 1996. **380**(6574): p. 550-5.
219. Eswar, N., et al., *Protein structure modeling with MODELLER.* Methods Mol Biol, 2008. **426**: p. 145-59.
220. Parke, C.L., et al., *ATP hydrolysis in Eg5 kinesin involves a catalytic two-water mechanism.* J Biol Chem, 2010. **285**(8): p. 5859-67.
221. Muller, J., et al., *The structure of the nucleotide-binding site of kinesin.* Biol Chem, 1999. **380**(7-8): p. 981-92.
222. Fiser, A. and A. Sali, *ModLoop: automated modeling of loops in protein structures.* Bioinformatics, 2003. **19**(18): p. 2500-1.
223. Pettersen, E.F., et al., *UCSF Chimera--a visualization system for exploratory research and analysis.* J Comput Chem, 2004. **25**(13): p. 1605-12.
224. Humphrey, W., A. Dalke, and K. Schulten, *VMD: visual molecular dynamics.* J Mol Graph, 1996. **14**(1): p. 33-8, 27-8.
225. Phillips, J.C., et al., *Scalable molecular dynamics with NAMD.* J Comput Chem, 2005. **26**(16): p. 1781-802.
226. Foloppe, N. and A.D. MacKerell Jr, *All‐atom empirical force field for nucleic acids: I. Parameter optimization based on small molecule and condensed phase macromolecular target data.* Journal of computational chemistry, 2000. **21**(2): p. 86-104.

227. Deserno, M. and C. Holm, *How to mesh up Ewald sums. I. A theoretical and numerical comparison of various particle mesh routines.* The Journal of chemical physics, 1998. **109**(18): p. 7678-7693.
228. Brünger, A., C.L. Brooks, and M. Karplus, *Stochastic boundary conditions for molecular dynamics simulations of ST2 water.* Chemical physics letters, 1984. **105**(5): p. 495-500.
229. Martyna, G.J., A. Hughes, and M.E. Tuckerman, *Molecular dynamics algorithms for path integrals at constant pressure.* The Journal of chemical physics, 1999. **110**(7): p. 3275-3290.
230. Eriksson, M.A. and B. Roux, *Modeling the structure of agitoxin in complex with the Shaker K+ channel: a computational approach based on experimental distance restraints extracted from thermodynamic mutant cycles.* Biophys J, 2002. **83**(5): p. 2595-609.
231. Gilson, M.K. and B.H. Honig, *Energetics of charge–charge interactions in proteins.* Proteins: Structure, Function, and Bioinformatics, 1988. **3**(1): p. 32-52.
232. Im, W., D. Beglov, and B. Roux, *Continuum solvation model: computation of electrostatic forces from numerical solutions to the Poisson-Boltzmann equation.* Computer Physics Communications, 1998. **111**(1): p. 59-75.
233. Brooks, B.R., et al., *CHARMM: the biomolecular simulation program.* Journal of computational chemistry, 2009. **30**(10): p. 1545-1614.
234. Hirokawa, N., R. Nitta, and Y. Okada, *The mechanisms of kinesin motor motility: lessons from the monomeric motor KIF1A.* Nat Rev Mol Cell Biol, 2009. **10**(12): p. 877-84.
235. Kull, F.J. and S.A. Endow, *Force generation by kinesin and myosin cytoskeletal motor proteins.* J Cell Sci, 2013. **126**(Pt 1): p. 9-19.
236. Sack, S., F.J. Kull, and E. Mandelkow, *Motor proteins of the kinesin family. Structures, variations, and nucleotide binding sites.* Eur J Biochem, 1999. **262**(1): p. 1-11.
237. Le Grand, S.M. and K.M. Merz, *Rapid approximation to molecular surface area via the use of Boolean logic and look‐up tables.* Journal of Computational Chemistry, 1993. **14**(3): p. 349-352.
238. Sosa, H., et al., *ADP-induced rocking of the kinesin motor domain revealed by single-molecule fluorescence polarization microscopy.* Nat Struct Biol, 2001. **8**(6): p. 540-4.
239. Song, Y.H., et al., *Structure of a fast kinesin: implications for ATPase mechanism and interactions with microtubules.* EMBO J, 2001. **20**(22): p. 6213-25.
240. Chang, Q., et al., *Structural basis for the ATP-induced isomerization of kinesin.* J Mol Biol, 2013. **425**(11): p. 1869-80.
241. Rice, S., *Structure of kif14: an engaging molecular motor.* J Mol Biol, 2014. **426**(17): p. 2993-6.
242. Arora, K., et al., *KIF14 binds tightly to microtubules and adopts a rigor-like conformation.* J Mol Biol, 2014. **426**(17): p. 2997-3015.
243. Grant, B.J., et al., *Multivariate analysis of conserved sequence-structure relationships in kinesins: coupling of the active site and a tubulin-binding sub-domain.* J Mol Biol, 2007. **368**(5): p. 1231-48.
244. Kull, F.J. and S.A. Endow, *Kinesin: switch I & II and the motor mechanism.* J Cell Sci, 2002. **115**(Pt 1): p. 15-23.
245. Kaan, H.Y., D.D. Hackney, and F. Kozielski, *The structure of the kinesin-1 motor-tail complex reveals the mechanism of autoinhibition.* Science, 2011. **333**(6044): p. 883-5.
246. Zhao, Y.C., F.J. Kull, and J.C. Cochran, *Modulation of the kinesin ATPase cycle by neck linker docking and microtubule binding.* J Biol Chem, 2010. **285**(33): p. 25213-20.

247. Ma, Y.Z. and E.W. Taylor, *Mechanism of microtubule kinesin ATPase.* Biochemistry, 1995. **34**(40): p. 13242-51.

248. Li, M. and W. Zheng, *All-atom molecular dynamics simulations of actin-myosin interactions: a comparative study of cardiac alpha myosin, beta myosin, and fast skeletal muscle myosin.* Biochemistry, 2013. **52**(47): p. 8393-405.

249. Coureux, P.D., et al., *A structural state of the myosin V motor without bound nucleotide.* Nature, 2003. **425**(6956): p. 419-23.

250. Reubold, T.F., et al., *A structural model for actin-induced nucleotide release in myosin.* Nat Struct Biol, 2003. **10**(10): p. 826-30.

251. Yun, M., et al., *A structural pathway for activation of the kinesin motor ATPase.* EMBO J, 2001. **20**(11): p. 2611-8.

252. Yildiz, A., et al., *Intramolecular strain coordinates kinesin stepping behavior along microtubules.* Cell, 2008. **134**(6): p. 1030-41.

253. Uemura, S. and S. Ishiwata, *Loading direction regulates the affinity of ADP for kinesin.* Nat Struct Biol, 2003. **10**(4): p. 308-11.

254. Zeisel, S.H. and M.D. Niculescu, *Perinatal choline influences brain structure and function.* Nutr Rev, 2006. **64**(4): p. 197-203.

255. Jaramillo, F., S. Vicini, and S.M. Schuetze, *Embryonic acetylcholine receptors guarantee spontaneous contractions in rat developing muscle.* Nature, 1988. **335**(6185): p. 66-8.

256. Witzemann, V., et al., *Acetylcholine receptor epsilon-subunit deletion causes muscle weakness and atrophy in juvenile and adult mice.* Proc Natl Acad Sci U S A, 1996. **93**(23): p. 13286-91.

257. Ashby, J.A., et al., *GABA binding to an insect GABA receptor: a molecular dynamics and mutagenesis study.* Biophys J, 2012. **103**(10): p. 2071-81.

258. Cohen, J.B., S.D. Sharp, and W.S. Liu, *Structure of the agonist-binding site of the nicotinic acetylcholine receptor. [3H]acetylcholine mustard identifies residues in the cation-binding subsite.* J Biol Chem, 1991. **266**(34): p. 23354-64.

259. Kearney, P.C., et al., *Dose-response relations for unnatural amino acids at the agonist binding site of the nicotinic acetylcholine receptor: tests with novel side chains and with several agonists.* Mol Pharmacol, 1996. **50**(5): p. 1401-12.

260. Chiara, D.C. and J.B. Cohen, *Identification of amino acids contributing to high and low affinity d-tubocurarine sites in the Torpedo nicotinic acetylcholine receptor.* J Biol Chem, 1997. **272**(52): p. 32940-50.

261. Xie, Y. and J.B. Cohen, *Contributions of Torpedo nicotinic acetylcholine receptor gamma Trp-55 and delta Trp-57 to agonist and competitive antagonist function.* J Biol Chem, 2001. **276**(4): p. 2417-26.

262. Bafna, P.A., A. Jha, and A. Auerbach, *Aromatic Residues {epsilon}Trp-55 and {delta}Trp-57 and the Activation of Acetylcholine Receptor Channels.* J Biol Chem, 2009. **284**(13): p. 8582-8.

263. Nowak, M.W., et al., *Nicotinic receptor binding site probed with unnatural amino acid incorporation in intact cells.* Science, 1995. **268**(5209): p. 439-42.

264. Morris, G.M., et al., *Autodock4 and AutoDockTools4: automated docking with selective receptor flexiblity.* J. Computational Chemistry 2009. **16**: p. 2785-2791.

265. Foloppe, N. and A.D. Mackerell, *All-atom empirical force field for nucleic acids: I. Parameter optimization based on small molecule and condensed phase macromolecular target data.* Journal Computational Chemistry 2000. **21**: p. 86-104.

266. Martyna, G.J., A. Hughes, and M.E. Tuckerman, *Molecular dynamics algorithms for path integrals in constant pressure.* Journal of Chemical Physics, 1999. **110**: p. 3275-3290.
267. Deserno, M. and C. Holm, *How to mesh up Ewald sums. I. A theoretical and numerical comparison of various particle mesh routines.* Journal Chemical Physics, 1998. **109**: p. 7678-7693.
268. Hoover, W.G., *Canonical dynamics: Equilibrium phase-space distributions.* Phys Rev A, 1985. **31**(3): p. 1695-1697.
269. Nina, M., D. Beglov, and B. Roux, *Atomic radii for continuum electrostatics calculations based on molecular dynamics free energy simulations.* J. Phys. Chem. B 1997. **101**: p. 5239-5248.
270. Kuhn, B. and P.A. Kollman, *Binding of a diverse set of ligands to avidin and streptavidin: an accurate quantitative prediction of their relative affinities by a combination of molecular mechanics and continuum solvent models.* J Med Chem, 2000. **43**(20): p. 3786-91.
271. Grazioso, G., et al., *Alpha7 nicotinic acetylcholine receptor agonists: prediction of their binding affinity through a molecular mechanics Poisson-Boltzmann surface area approach.* J Comput Chem, 2008. **29**(15): p. 2593-602.
272. Samanta, U., D. Pal, and P. Chakrabarti, *Packing of aromatic rings against tryptophan residues in proteins.* Acta Crystallogr D Biol Crystallogr, 1999. **55**(Pt 8): p. 1421-7.
273. Tsunoyama, K. and T. Gojobori, *Evolution of nicotinic acetylcholine receptor subunits.* Mol Biol Evol, 1998. **15**(5): p. 518-27.
274. Ortells, M.O. and G.G. Lunt, *Evolutionary history of the ligand-gated ion-channel superfamily of receptors.* Trends Neurosci, 1995. **18**(3): p. 121-7.
275. Zeisel, S.H., *Choline: critical role during fetal development and dietary requirements in adults.* Annu Rev Nutr, 2006. **26**: p. 229-50.
276. Jackson, M.B., *Dependence of acetylcholine receptor channel kinetics on agonist concentration in cultured mouse muscle fibres.* J Physiol, 1988. **397**: p. 555-83.
277. Salamone, F.N., M. Zhou, and A. Auerbach, *A re-examination of adult mouse nicotinic acetylcholine receptor channel activation kinetics.* J Physiol, 1999. **516 (Pt 2)**: p. 315-30.
278. Liu, Y., et al., *Essential roles of the acetylcholine receptor gamma-subunit in neuromuscular synaptic patterning.* Development, 2008. **135**(11): p. 1957-67.
279. Nayak, T.K., et al., *Functional differences between neurotransmitter binding sites of muscle acetylcholine receptors.* Proc Natl Acad Sci U S A, 2014. **111**(49): p. 17660-5.
280. Polak, R.L., L.C. Sellin, and S. Thesleff, *Acetylcholine content and release in denervated or botulinum poisoned rat skeletal muscle.* J Physiol, 1981. **319**: p. 253-9.
281. Bouzat, C., N. Bren, and S.M. Sine, *Structural basis of the different gating kinetics of fetal and adult acetylcholine receptors.* Neuron, 1994. **13**(6): p. 1395-402.
282. Sullivan, M.P., J.L. Owens, and R.W. Kullberg, *Role of M2 domain residues in conductance and gating of acetylcholine receptors in developing Xenopus muscle.* J Physiol, 1999. **515 (Pt 1)**: p. 31-9.
283. Auerbach, A., *Agonist activation of a nicotinic acetylcholine receptor.* Neuropharmacology, 2015. **96**(Pt B): p. 150-6.
284. Purohit, P., I. Bruhova, and A. Auerbach, *Sources of energy for gating by neurotransmitters in acetylcholine receptor channels.* Proc Natl Acad Sci U S A, 2012. **109**(24): p. 9384-9.

285. Chenna, R., et al., *Multiple sequence alignment with the Clustal series of programs.* Nucleic Acids Res, 2003. **31**(13): p. 3497-500.
286. Shen, M.Y. and A. Sali, *Statistical potential for assessment and prediction of protein structures.* Protein Sci, 2006. **15**(11): p. 2507-24.
287. Engh, R.A. and R. Huber, *Accurate Bond and Angle Parameters for X-Ray Protein-Structure Refinement.* Acta Crystallographica Section A, 1991. **47**: p. 392-400.
288. Laskowski, R.A., et al., *PROCHECK - a program to check the stereochemical quality of protein structures.* Journal of Applied Crystallography, 1993. **26**: p. 283-291.
289. Vanommeslaeghe, K. and A.D. MacKerell, Jr., *Automation of the CHARMM General Force Field (CGenFF) I: bond perception and atom typing.* J Chem Inf Model, 2012. **52**(12): p. 3144-54.
290. Vanommeslaeghe, K., E.P. Raman, and A.D. MacKerell, Jr., *Automation of the CHARMM General Force Field (CGenFF) II: assignment of bonded parameters and partial atomic charges.* J Chem Inf Model, 2012. **52**(12): p. 3155-68.
291. Brooks, B.R., et al., *A Program for Macromolecular Energy, Minimization, and Dynamics Calculations.* . Journal Computational Chemistry, 1983. **4**: p. 187-217.
292. Celie, P.H., et al., *Nicotine and carbamylcholine binding to nicotinic acetylcholine receptors as studied in AChBP crystal structures.* Neuron, 2004. **41**(6): p. 907-14.
293. Gupta, S., P. Purohit, and A. Auerbach, *Function of interfacial prolines at the transmitter binding sites of the neuromuscular acetylcholine receptor.* J Biol Chem, 2013.
294. Amiri, S., M.S. Sansom, and P.C. Biggin, *Molecular dynamics studies of AChBP with nicotine and carbamylcholine: the role of water in the binding pocket.* Protein Eng Des Sel, 2007. **20**(7): p. 353-9.
295. Grosman, C., M. Zhou, and A. Auerbach, *Mapping the conformational wave of acetylcholine receptor channel gating.* Nature, 2000. **403**(6771): p. 773-6.
296. Fersht, A.R., R.J. Leatherbarrow, and T.N.C. Wells, *Quantitative analysis of structure-activity relationships in engineered proteins by linear free-energy relationships.* Nature, 1986. **322**: p. 284-286.
297. Fersht, A.R., R.J. Leatherbarrow, and T.N. Wells, *Structure-activity relationships in engineered proteins: analysis of use of binding energy by linear free energy relationships.* Biochemistry, 1987. **26**: p. 6030-6038.
298. Estell, D.A., et al., *Probing steric and hydrophobic effects on enzyme-substrate interactions by protein engineering.* Science, 1986. **233**(4764): p. 659-63.
299. Shahsavar, A., et al., *AChBP Engineered to Mimic the alpha4-beta4 Binding Pocket in alpha4beta2 Nicotinic Acetylcholine Receptors Reveals Interface Specific Interactions Important for Binding and Activity.* Mol Pharmacol, 2015.
300. Vij, R., P. Purohit, and A. Auerbach, *Modal affinities of endplate acetylcholine receptors caused by loop C mutations.* J Gen Physiol, 2015. **146**(5): p. 375-86.
301. Sine, S.M., *End-Plate Acetylcholine Receptor: Structure, Mechanism, Pharmacology, and Disease.* Physiological Reviews, 2012. **92**(3): p. 1189-1234.
302. Changeux, J.-P., *Protein dynamics and the allosteric transitions of pentameric receptor channels.* Biophysical Reviews, 2014: p. 1-11.
303. Auerbach, A., *Agonist activation of a nicotinic acetylcholine receptor.* Neuropharmacology, 2014.
304. Lee, W.Y. and S.M. Sine, *Principal pathway coupling agonist binding to channel gating in nicotinic receptors.* Nature, 2005. **438**(7065): p. 243-7.

305. Purohit, P. and A. Auerbach, *Loop C and the mechanism of acetylcholine receptor-channel gating.* J Gen Physiol, 2013. **141**(4): p. 467-78.
306. Grosman, C., M. Zhou, and A. Auerbach, *Mapping the conformational wave of acetylcholine receptor channel gating.* Nature, 2000. **403**(6771): p. 773.
307. Bafna, P.A., P.G. Purohit, and A. Auerbach, *Gating at the Mouth of the Acetylcholine Receptor Channel: Energetic Consequences of Mutations in the alpha M2-Cap.* Plos One, 2008. **3**(6).
308. Purohit, P., S. Chakraborty, and A. Auerbach, *Function of the M1 pi-helix in endplate receptor activation and desensitization.* J Physiol, 2015. **593**(13): p. 2851-66.
309. Katz, B. and S. Thesleff, *A study of the desensitization produced by acetylcholine at the motor end-plate.* J Physiol, 1957. **138**(1): p. 63-80.
310. Auerbach, A. and G. Akk, *Desensitization of mouse nicotinic acetylcholine receptor channels. A two-gate mechanism.* J Gen Physiol, 1998. **112**(2): p. 181-97.
311. Wang, H.L., et al., *Mutation in the M1 domain of the acetylcholine receptor alpha subunit decreases the rate of agonist dissociation.* J Gen Physiol, 1997. **109**(6): p. 757-66.
312. England, P.M., et al., *Backbone mutations in transmembrane domains of a ligand-gated ion channel: implications for the mechanism of gating.* Cell, 1999. **96**(1): p. 89-98.
313. Cooley, R.B., D.J. Arp, and P.A. Karplus, *Evolutionary origin of a secondary structure: pi-helices as cryptic but widespread insertional variations of alpha-helices that enhance protein functionality.* J Mol Biol, 2010. **404**(2): p. 232-46.
314. Fodje, M.N. and S. Al-Karadaghi, *Occurrence, conformational features and amino acid propensities for the pi-helix.* Protein Eng, 2002. **15**(5): p. 353-8.
315. Bloom, J.D. and F.H. Arnold, *In the light of directed evolution: pathways of adaptive protein evolution.* Proc Natl Acad Sci U S A, 2009. **106 Suppl 1**: p. 9995-10000.
316. Heinz, D.W., et al., *How amino-acid insertions are allowed in an alpha-helix of T4 lysozyme.* Nature, 1993. **361**(6412): p. 561-4.
317. Worth, C.L., S. Gong, and T.L. Blundell, *Structural and functional constraints in the evolution of protein families.* Nat Rev Mol Cell Biol, 2009. **10**(10): p. 709-20.
318. Weaver, T.M., *The pi-helix translates structure into function.* Protein Sci, 2000. **9**(1): p. 201-6.
319. Brooks, B.R., et al., *CHARMM: the biomolecular simulation program.* J Comput Chem, 2009. **30**(10): p. 1545-614.
320. Bahar, I. and A. Rader, *Coarse-grained normal mode analysis in structural biology.* Current opinion in structural biology, 2005. **15**(5): p. 586-592.
321. Ma, J., *Usefulness and limitations of normal mode analysis in modeling dynamics of biomolecular complexes.* Structure, 2005. **13**(3): p. 373-380.
322. Tirion, M.M., *Large amplitude elastic motions in proteins from a single-parameter, atomic analysis.* Physical review letters, 1996. **77**(9): p. 1905.
323. Zheng, W., *Coarse-grained modeling of the structural states and transition underlying the powerstroke of dynein motor domain.* The Journal of chemical physics, 2012. **136**(15): p. 155103.
324. Zheng, W., B.R. Brooks, and D. Thirumalai, *Low-frequency normal modes that describe allosteric transitions in biological nanomachines are robust to sequence variations.* Proc Natl Acad Sci U S A, 2006. **103**(20): p. 7664-9.
325. Hilf, R.J.C. and R. Dutzler, *X-ray structure of a prokaryotic pentameric ligand-gated ion channel.* Nature, 2008. **452**(7185): p. 375-379.

326. Du, J., et al., *Glycine receptor mechanism elucidated by electron cryo-microscopy.* Nature, 2015. **526**(7572): p. 224-9.
327. Hassaine, G., et al., *X-ray structure of the mouse serotonin 5-HT3 receptor.* Nature, 2014. **512**(7514): p. 276-81.
328. Le, L., et al., *Molecular modeling of swine influenza A/H1N1, Spanish H1N1, and avian H5N1 flu N1 neuraminidases bound to Tamiflu and Relenza.* PLoS Curr, 2009. **1**: p. RRN1015.
329. Smith, C.A. and I. Rayment, *X-ray structure of the magnesium(II).ADP.vanadate complex of the Dictyostelium discoideum myosin motor domain to 1.9 A resolution.* Biochemistry, 1996. **35**(17): p. 5404-17.
330. Heuston, E., et al., *A kinesin motor in a force-producing conformation.* BMC Struct Biol, 2010. **10**: p. 19.
331. Auerbach, S.D. and K.A. Johnson, *Kinetic effects of kinesin switch I and switch II mutations.* J Biol Chem, 2005. **280**(44): p. 37061-8.
332. Farrell, C.M., et al., *The role of ATP hydrolysis for kinesin processivity.* J Biol Chem, 2002. **277**(19): p. 17079-87.
333. Woehlke, G., et al., *Microtubule interaction site of the kinesin motor.* Cell, 1997. **90**(2): p. 207-16.
334. Amos, L.A. and K. Hirose, *A cool look at the structural changes in kinesin motor domains.* J Cell Sci, 2007. **120**(Pt 22): p. 3919-27.
335. Uchimura, S., et al., *Key residues on microtubule responsible for activation of kinesin ATPase.* EMBO J, 2010. **29**(7): p. 1167-75.
336. Nicolai, C. and F. Sachs, *Solving ion channel kinetics with the QuB software.* Biophysical Reviews and Letters, 2013. **08**(03): p. 1-21.
337. Nayak, T.K., P.G. Purohit, and A. Auerbach, *The intrinsic energy of the gating isomerization of a neuromuscular acetylcholine receptor channel.* J Gen Physiol, 2012. **139**(5): p. 349-58.
338. Auerbach, A., et al., *Voltage dependence of mouse acetylcholine receptor gating: different charge movements in di-, mono- and unliganded receptors.* J. Physiol., 1996. **494**: p. 155-170.
339. Jadey, S.V., et al., *Design and control of acetylcholine receptor conformational change.* Proc Natl Acad Sci U S A, 2011. **108**(11): p. 4328-33.